

**Modelling and Simulation of the Transport Mechanisms
in Solid Oxide Fuel Cells with Molecular Dynamics and
Non-Equilibrium Thermodynamics**

Der Fakultät für Maschinenbau
der Gottfried Wilhelm Leibniz Universität Hannover
zur Erlangung des akademischen Grades
Doktor-Ingenieurin/Doktor-Ingenieur
genehmigte Dissertation

von
Dipl.-Ing. Gerardo Valadez Huerta

2019

1. Referent: Prof. Dr.-Ing. Stephan Kabelac
 2. Referent: Prof. Dr.-Ing. Karsten Meier
- Tag der Promotion: 27.11.2018

Acknowledgments

The thesis presented here was carried out during my scientific work at the Institut für Thermodynamik of the Gottfried Wilhelm Leibniz Universität Hannover.

First, I am greatly thankful to my supervisor and chief of this institution, Prof. Dr.-Ing. Stephan Kabelac. Without his motivation, interest and faith in my ideas, the work presented here would not have been possible. I would also like to thank Prof. Dr.-Ing. Karsten Meier for being the second auditor of this work and Priv-Doz. Dr.-Ing. Gabriele Raabe for introducing me to the topic of molecular dynamics during my diploma thesis.

Especially, I would like to thank Dr.-Ing Michael Dragon, who helped me become familiar with the scientific work at the institute. I am also thankful to my colleagues Dr.-Ing Jan Eggers, Benjamin Markmann, Ebrahim Aeini, Anja-Elsa Polzin, Jannis Müller Ebhardt and Johann Ebeling, who began this great scientific journey with me. I also enjoyed the time spent with Taylan Tokan, Ruben Steinhoff, Maximilian Loth and Eckart Lange, who were part of this institute as students, but later became a part of the thermodynamic crew as colleagues. I would like to thank Dr.-Ing. Xing Luo, Cosima Fernkorn, Uwe Tenschert, Heinz Sorichta and Karsten Bocherding for their assistance in technical issues. Especially, I would like to mention Bettina Mietzke, who always assisted me in administrative issues. Thank you and all other colleagues for the profound scientific discussions and an unforgettable time.

As part of my work at the institute, several bachelor theses, research projects theses and master theses were carried out under my tutoring. Here, I would like to mention the theses of Benjamin Grüning, Conrad Zimmermann, Alexander Kasperek, David Storch, Andreas Goldmann, Janos Alfred, Petya Ivanova, Julia Rohrsen, Johannes Wert and Johanan Álvarez Jordán, who helped me to expand my thermodynamic knowledge as part of other projects and publications not coupled with the thesis presented here. I would like to thank my student co-workers Luis Deichmann and Sara Kershi for their recent assistance to my work.

Sincere thanks to my colleagues and friends Vincent Flasbart, Tobias Marquardt, Malte Siemen, Pablo Radici and Lucas Reus for their contributions to the papers presented here. I would also like to thank Sheridan Renzi for the English correction of this thesis and of all my publications.

I should like to express the warmest thanks to my friends Aydan Gedik, Hugo Cruz Champion, Anton Wenemoser, Ramon Gembus and, above all, to my mother Graciela Huerta Huerta and my brother José Ángel Valadez Huerta, because of their constant help, time and support. Finally, I want to dedicate this doctoral thesis to my father, Ángel Felipe Valadez Flores.

Abstract

The quantitative description of the transport mechanisms in solid oxide fuel cells (SOFCs) is relevant for cell development and the optimization of operating strategies. These mechanisms have an intrinsic multi-causality as given by Non-Equilibrium Thermodynamics (NET), which is not necessarily considered by empirical classical transport equations. If, e.g., additional heat is transported due to a potential gradient across the SOFC, this effect may have to be considered for the design of heating or cooling strategies.

The main focus of this thesis is the description of the transport mechanisms in the electrolyte of a SOFC. The electrolyte is an essential part of the cell and should be highly ionic conductive, gas-tight and an electronic insulator. The electrolyte materials analyzed are zirconium dioxide ZrO_2 co-doped with yttrium(III) oxide Y_2O_3 (YSZ) and ZrO_2 co-doped with 10 mol% scandium(III) oxide Sc_2O_3 and 1 mol% cerium dioxide CeO_2 (10Sc1CeSZ).

This work comprises three molecular dynamics (MD) studies, which provide data for the phenomenological coefficients based on NET for different YSZ compositions, as well as the ionic conductivity and different diffusion coefficients for 10Sc1CeSZ. The numerical data for the ionic conductivity of 10Sc1CeSZ agrees with experimental studies. Furthermore, the dependency of each transport mechanism on the Y_2O_3 concentration in YSZ is explained by linear response theory. A theoretical framework is proposed to give the electrostatic potential thermodynamic consistency and to relate it to the Coulomb contribution of other thermodynamic quantities.

Finally, simulations of a planar SOFC with an YSZ electrolyte are carried out using a validated one-dimensional(1D) NET model and the phenomenological coefficients from the MD simulations. If the coupled mechanisms are neglected, the temperature profile, the heat flux and the entropy production may not be correctly predicted.

The methodologies and results from this work can be used in future studies to describe more accurately the transport mechanisms in SOFCs with electrolytes based on ZrO_2 metal oxides or even other electrolyte technologies like proton conducting perovskites. Moreover, they can also be used to effectively predict the thermal behavior of SOFCs and, thus, they provide a contribution to the optimization of thermal strategies in SOFCs.

Keywords: SOFC; YSZ; 10Sc1CeSZ; Molecular Dynamics, Non-Equilibrium Thermodynamics

Kurzfassung

Titel: *Modellierung und Simulation der Transportmechanismen in Festoxid-Brennstoffzellen mittels Molekulardynamik und Thermodynamik irreversibler Prozesse*

Die quantitative Beschreibung der Transportmechanismen in Festoxidbrennstoffzellen (SOFCs) ist relevant zur Zellentwicklung und Optimierung von Betriebsstrategien. Laut der Thermodynamik irreversibler Prozesse (TiP) weisen diese Mechanismen eine intrinsische mehrfache Kausalität auf, die in aller Regel nicht durch klassische empirische Transportansätze berücksichtigt wird. Wenn, z. B., zusätzliche Wärme aufgrund eines elektrischen Potentialgradienten durch die SOFC transportiert wird, sollte dieser Effekt bei der Entwicklung von Aufheiz- und Kühlstrategien berücksichtigt werden.

Der Schwerpunkt dieser Arbeit ist die Beschreibung der Transportmechanismen im Elektrolyten einer SOFC. Der Elektrolyt ist ein wesentliches Element der Zelle und muss hoch ionenleitfähig, gasdicht und isolierend für Elektronen sein. Die analysierten Materialien sind mit Yttrium(III)oxid(Y_2O_3) stabilisiertes Zirconiumdioxid ZrO_2 (YSZ) und mit 10 mol% Scandium(III)oxid Sc_2O_3 und 1 mol% Ceriumdioxid CeO_2 stabilisiertes ZrO_2 (10Sc1CeSZ).

Die Arbeit umfasst drei Molekulardynamik(MD)-Studien, die numerische Werte für die auf dem TiP-Ansatz basierenden phänomenologischen Koeffizienten für unterschiedliche YSZ Zusammensetzungen sowie der ionischen Leitfähigkeit und unterschiedlicher Diffusionskoeffizienten für 10Sc1CeSZ liefern. Die berechneten Werte für die ionische Leitfähigkeit von 10Sc1CeSZ stimmen mit experimentellen Daten überein. Ferner wird die Abhängigkeit der Transportmechanismen von der Y_2O_3 -Konzentration in YSZ mittels der Linearen-Antwort-Theorie untersucht. Weiterhin wird eine Theorie aufgestellt, um dem elektrostatischen Potential thermodynamische Konsistenz zuzuweisen sowie den Coulomb-Anteil anderer thermodynamischer Größen aus dieser Größe abzuleiten.

Schließlich werden Simulationen einer planaren SOFC mit einem YSZ Elektrolyten mittels eines validierten eindimensionalen(1D) TiP-Modells und der phänomenologischen Koeffizienten aus den MD Simulationen durchgeführt. Die Vernachlässigung der gekoppelten Mechanismen kann in falschen Temperatur-, Wärmefluss- und Entropieproduktionsverläufen resultieren.

Die Methoden und Ergebnisse aus dieser Arbeit können in zukünftigen Studien verwendet werden, um die Transportmechanismen in SOFCs mit auf ZrO_2 basierten Elektrolytmaterialien oder sogar mit anderen Technologien, wie protonenleitenden Elektrolyten, besser zu beschreiben. Außerdem können sie auch verwendet werden, um das thermische Verhalten von SOFCs aussagekräftiger vorherzusagen und liefern somit einen Beitrag zur Optimierung thermischer Betriebsstrategien von SOFCs.

Stichwörter: SOFC; YSZ; 10Sc1CeSZ; Molekulardynamik, Thermodynamik irreversibler Prozesse

Table of Contents

Abstract.....	i
Kurzfassung	iii
Nomenclature and Abbreviations.....	vi
Publications list.....	xi
1. Introduction.....	1
2. Theoretical Background and Literature Survey	7
2.1 Thermodynamics of Galvanic Cells	7
2.1.1 Electrostatic Potential	9
2.1.2 Galvanic Cells Under Load.....	10
2.2 Non-Equilibrium Thermodynamics (NET).....	11
2.2.1 Phenomenological Coefficients and Linear Response Theory	12
2.3 Classical Molecular Dynamics	15
2.3.1 Ewald Sum	16
2.3.2 Molecular Simulation Studies on Transport Mechanisms.....	18
2.4 Fuel Cells	20
2.5 Solid Oxide Fuel Cells (SOFCs).....	22
2.5.1 Materials for SOFCs.....	24
2.5.2 Phase Diagrams, Structural Properties and Heat Capacities of YSZ and 10Sc1CeSZ	25
2.5.3 Transport Coefficients for YSZ and 10Sc1CeSZ.....	26
2.5.4 SOFC Modelling and Molecular Simulation for SOFCs.....	28
3. Simulation Methods	32
3.1 Molecular Dynamics Simulation	32
3.1.1 System, Interatomic Potential and Thermodynamic State for YSZ	32
3.1.2 Interatomic Potential for 10Sc1CeSZ.....	33
3.1.3 Computational Details.....	36
3.1.4 Calculation of the Electrostatic Potential	38
3.2 SOFC 1D NET Model	40
4. Summary and Interaction of Publications	43
4.1 Paper I.....	43
4.1.1 Author Contributions	43

4.1.2	Summary	43
4.1.3	Additional Discussion	45
4.2	Paper II.....	45
4.2.1	Author Contributions	45
4.2.2	Summary	46
4.2.3	Additional Discussion	47
4.3	Paper III	50
4.3.1	Author Contributions	50
4.3.2	Summary	50
4.4	Paper IV	51
4.4.1	Author Contributions	51
4.4.2	Summary	51
4.5	Interaction of the Publications	53
5.	Conclusions and Perspectives.....	55
	References.....	58
	Appendix	I

Nomenclature and Abbreviations

Symbols

A	Cell active area in m^2
A_{ij}	Buckingham FF parameter in eV
a	Lattice constant in \AA
a_i	Activity of species i
a_T	Thermal diffusivity in m^2/s
\mathbf{a}	Basis vector in m
C	Heat capacity in J/K
C_{ij}	Buckingham FF parameter in $\text{eV} \cdot \text{\AA}^6$
C_m	Molar heat capacity in $\text{J}/(\text{mol} \cdot \text{K})$
c	Specific heat capacity in $\text{J}/(\text{kg} \cdot \text{K})$
\check{c}_{ij}	Elastic constant in Pa
D	Diffusion coefficient in m^2/s
E	Voltage in V
E_0	Open circuit voltage V
f	General function (var. unit)
G_m	Molar Gibbs energy in J/mol
$\Delta^R G_m$	Molar Gibbs energy of reaction in J/mol
H_{0i}	The null hypothesis for case i
H_{1i}	The alternative hypothesis for case i
\mathcal{H}	Hamiltonian in J
I	Current in A
i	Imaginary unit
J_i	Thermodynamic flux (var. unit)
\mathbf{J}_i	Generalized thermodynamic flux vector (var. unit)
j	Current density in A/m^2
\mathbf{k}	Wave vector in reciprocal space in m^{-1}
L	Phenomenological coefficient (var. unit)
\mathcal{L}	Lagrangian in J
M	Number of periodic images; variable
m	Variable
N	Number of particles; variable
n	Amount of substance in mol; variable
Ox	Oxidized species
P	Power in W
p	Pressure in Pa
p_i	Partial pressure of species i in Pa
\mathbf{p}	Momentum vector in $\text{kg} \cdot \text{m}/\text{s}$
q	Charge in C
\mathbf{R}	Lattice vector in m
r	Distance in m
r_0	Nearest neighbor distance in m
\mathbf{r}	Position vector in m
Red	Reduced species

RF	Radiative forcing in W/m^2
S	Entropy in J/K
\check{S}_ϕ	Seebeck coefficient in V/K
T	Thermodynamic temperature in K
t	Time in s
U	Internal energy in J
U_c	Coulomb potential energy in J
U_c^*	Coulomb potential energy in m^{-1}
V	Volume in m^3
\mathbf{v}	Velocity vector in m/s
W_m	Work per mole in J/mol
X	Statistical variable (var. unit)
X_0	Estimate for statistical variable (var. unit)
X_i	Thermodynamic force (var. unit)
\mathbf{X}_i	Generalized Thermodynamic force vector (var. unit)
x	Mole fraction
y	Space coordinate perpendicular to cell area in m
Z	Thermodynamic property (var. unit)
z	Valence

Greek Symbols

α	Significance level
α_i	Deviation of a property i from equilibrium (var. unit)
α_L	Coefficient of thermal expansion (CTE) in K^{-1}
β	Type 2 error
β_c	Ewald parameter in m^{-1}
Δ	Difference
δ	Difference
η_{sys}	System efficiency
η^i	Activation overpotential
Φ	Electric contribution of the electrochemical potential in V
ϕ	Electric potential in V
φ	Electrostatic potential in V
φ^*	Electrostatic potential in reciprocal length units m^{-1}
γ	Proportion of the φ_o contribution
κ	Ionic conductivity in S/m
λ	Thermal conductivity in $W/(m \cdot K)$
μ_i	Chemical potential of species i in J/mol
$\tilde{\mu}_i$	Electrochemical potential of species i in J/mol
ν	Stoichiometric coefficient
Π	Probability
π	Peltier coefficient in V
ρ	Mass density in kg/m^3
ρ_{ij}	Buckingham FF parameter in \AA
ρ_q	Charge distribution density in C/m^3

$\dot{\sigma}$	Volumetric entropy production rate in W/(m ³ K)
σ^*	Entropy function in J/K
$\dot{\sigma}^*$	Entropy production rate in W/K
τ	Time variable in s
ϑ	Temperature in °C
ξ	Extent of reaction

Superscripts

\ddagger	Complex conjugate
\emptyset	Standard
K	Long-range contribution
MSD	Mean square displacement
n	Variable
R	Short-range contribution
S	Correction term
$VACF$	Velocity auto correlation function

Subscripts

0	Equilibrium
C	Coulomb
FC	Fuel Cell
i	Species i ; variable
j	Species j ; variable
k	Species k ; variable
m	Molar
max	Maximum
O	O ²⁻ -anions
op	Operational
p	Isobaric
V	Oxygen vacancies
Y	Y ³⁺ -cations
Y_2O_3	Y ₂ O ₃
Zr	Zr ⁴⁺ -cations
ZrO_2	ZrO ₂

Constants

e	Elementary charge (1.602176 · 10 ⁻¹⁹ C)
ϵ_0	Permittivity in vacuum (8.85419 · 10 ⁻¹² C ² /(J · m))
F	Faraday constant (96485.3 C/molK)
k_B	Boltzmann constant (1.38065 · 10 ⁻²³ J/(mol · K))
N_A	Avogadro constant (6.02214 · 10 ²³ mol ⁻¹)
R	Gas constant (8.3145 J/(mol · K))

Abbreviations

μ CHP	Micro Combined Heat and Power
μ VT	Grand Canonical
10Sc1CeSZ	$(\text{ScO}_3)_{0.11}(\text{CeO}_2)_{0.01}(\text{ZrO}_2)_{0.89}$
4T	Four Terminal
ACF	Auto Correlation Function
APU	Auxiliary Power Unit
BK	Brinkman
BMH	Born-Mayer-Huggins
CCF	Cross Correlation Function
CFD	Computer Fluid Dynamics
CL	Catalyst Layer
CTE	Coefficient of Thermal Expansion
D	Dimensional
DFT	Density Functional Theory
DLC	Dwivedi-Lewis-Comarck
DLR	German Aerospace Agency
DMFC	Direct Methanol Fuel Cell
EC	European Commission
EMD	Equilibrium Molecular Dynamics
EMF	Electromotive Force
FC	Fuel Cells
FDM	Finite Difference Method
FF	Force Field
GDL	Gas diffusion layer
GH	Greenhouse
GHG	Greenhouse Gas
GSM	Gotte-Schelling-Minervi
INDC	Intended Nationally Determined Contribution
LDM	Lau-Dunlap-Minervi
LJ	Lennard-Jones
LSM	$\text{La}_{1-x}\text{Sr}_x\text{MnO}_{3-\delta}$
MC	Monte Carlo
MCFC	Molten Carbonate Fuel Cell
MD	Molecular Dynamics
MS	Maxwell-Stefan
MSD	Mean Square Displacement
NEMD	Non-Equilibrium Molecular Dynamics
NET	Non-Equilibrium Thermodynamics
N_pT	Constant Pressure, Temperature and Particle Number
NSD	Nassi-Schniederma Diagram
NVE	Microcanonical
NVT	Canonical
OCV	Open Circuit Voltage
PAFC	Phosphoric Acid Fuel Cell

PCO	Pr_2CuO_4
PEMFC	Proton Exchange Membrane Fuel Cell
PIM	Partial Ionic Model
RDF	Radial Distribution Function
ReaxFF	Reactive Force Field
SI	Supporting Information
SOEC	Solid Oxide Electrolysis Cell
SOFC	Solid Oxide Fuel Cell
SP	Schelling-Phillpot
SPM	Schelling-Phillpot-Minervi
TEG	Thermoelectric Generator
VACF	Velocity Auto Correlation Function
VCCF	Velocity Cross Correlation Function
YSZ	$(\text{ZrO}_2)_{1-x}(\text{Y}_2\text{O}_3)_x$

Publications list

List of papers included in this thesis

- I. Valadez Huerta, G.; Kelle, A.; Kabelac, S. A phenomenological study of yttria-stabilized zirconia at 1300 K with the Green-Kubo formulation and equilibrium molecular dynamics. Reprinted with permission of *Chem. Phys.* **2017**, *485-486*, 108-117. DOI: 10.1016/j.chemphys.2017.01.011. Copyright 2017 Elsevier.
- II. Valadez Huerta, G.; Siemen M.; Kabelac S. Approach to the Coulomb Contribution of Thermodynamic Properties from the Mean Electrostatic Potential of the Ions in $(\text{ZrO}_2)_{1-x}(\text{Y}_2\text{O}_3)_x$. Reprinted with permission of *J. Phys. Chem. C* **2018**, *122*, 62-70. DOI: 10.1021/acs.jpcc.7b08710. Copyright 2018 American Chemical Society.
- III. Valadez Huerta, G.; Reus, L.; Kabelac, S. A Diffusivity Study of $(\text{Sc}_2\text{O}_3)_{0.1}(\text{CeO}_2)_{0.01}(\text{ZrO}_2)_{0.89}$ between 1100 and 1500 K at Zero Pressure with Molecular Dynamics. Reprinted with permission of *J. Chem. Eng. Data* **2018**, *63*, 1955-1960. DOI: 10.1021/acs.jced.7b01094. Copyright 2018 American Chemical Society.
- IV. Valadez Huerta, G.; Flasbart, V.; Marquardt, T.; Radici, P.; Kabelac, S. Impact of Multi-Causal Transport Mechanisms in an Electrolyte Supported Planar SOFC with $(\text{ZrO}_2)_{x-1}(\text{Y}_2\text{O}_3)_x$ Electrolyte. *Entropy*, **2018**, *20*, 469-1-19. DOI: 10.3390/e20060469.

List of papers not included in this thesis

- V. Siemer, M.; Marquardt, T.; Valadez Huerta, G.; Kabelac, S. Local Entropy Production Rates in a Polymer Electrolyte Membrane Fuel Cell. *J. Non-Equilib. Thermodyn.*, **2017**, *42*, 1-30. DOI: 10.1515/jnet-2016-0025
- VI. Valadez Huerta, G.; Álvarez Jordán, J., Dragon, M.; Leites, K.; Kabelac S. Exergy analysis of the diesel pre-reforming solid oxide fuel cell system with anode off-gas recycling in the SchIBZ project. Part I: Modeling and validation. *Int. J. Hydrogen Energy*, **2018**, *43*, 16684-16693. DOI: 10.1016/j.ijhydene.2018.04.216

1. Introduction

In Figure 1-1, (a) the carbon dioxide CO_2 concentration in the atmosphere measured on Hawaii and at the South Pole, (b) the ratio of atmospheric oxygen O_2 to nitrogen N_2 and (c) the ^{13}C isotope concentration in atmospheric CO_2 (c) are depicted over the time. Following the discussion of R. J. Salawitch et al. (2016), it can be concluded that the appreciable differences in the progression of the atmospheric CO_2 concentration between the northern hemisphere and the southern hemisphere can be attributed to human activity, since it occurs mostly in the northern hemisphere. Furthermore, the decreasing O_2 to N_2 ratio may be explained by the combustion of fossil fuels, where atmospheric O_2 is converted into CO_2 . This would not happen if CO_2 were a product of volcanic activity, because the combustion occurs with O_2 from the Earth's crust. Finally, volcanic activity produces heavier CO_2 , contrary to the depicted decreasing trend of the ^{13}C amount in atmospheric CO_2 . This also indicates that human activity is the main cause of the CO_2 emissions. Analogous discussions can be conducted for the greenhouse gases (GHGs) methane CH_4 and nitrous oxide N_2O .

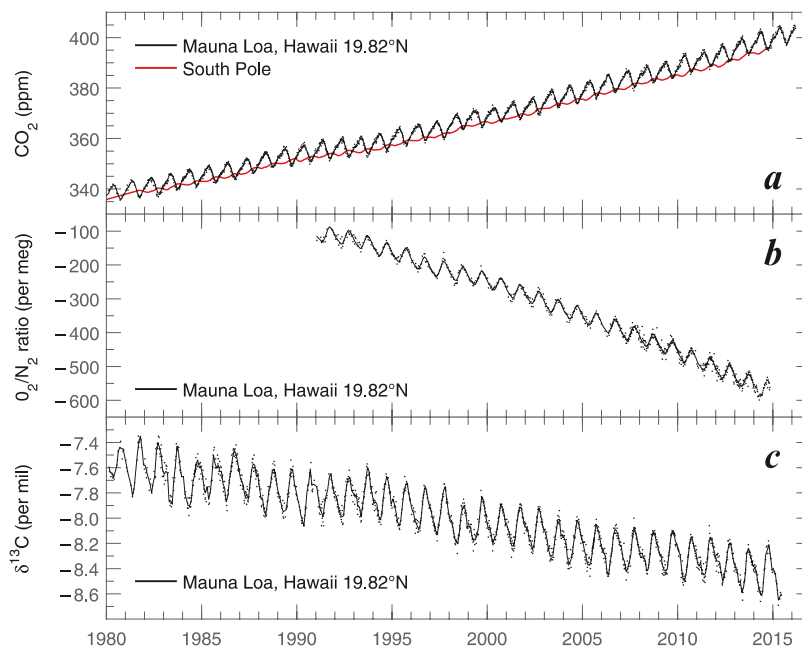


Figure 1-1. (a) atmospheric CO_2 concentration measured by the Mauna Loa Observatory on Hawaii and at the South Pole, (b) O_2 to N_2 ratio in the atmosphere measured in Hawaii and (c) amount of ^{13}C in atmospheric CO_2 measured on Hawaii relative to a standard. All quantities are depicted over time. The image was taken from R. J. Salawitch et al. (2016) (© by the Editors and authors; CC by 4.0).

The vibrational frequencies of GHGs correspond to the specific frequency of the infrared radiation coming from the earth's surface, meaning they can absorb this infrared radiation. After this absorption, the molecules may transfer the

energy to other molecules via collisions or emit infrared radiation in all directions (Bell, 2018). The change of the radiative forcing ΔRF describes the differences in the energy flow due to sunlight and infrared radiation at the tropopause relative to a start date, and it can be used to characterize the radiation sent back to the surface due to this GH effect (Salawitch, 2016). The change of the radiative forcing as a function of different factors is depicted in Figure 1-2, as well as a comparison to the global mean surface temperature difference, both relative to the year 1765. The influence of GHGs on the radiative forcing is evident from Figure 1-2, but, as stated by R. J. Salawitch et al. (2016), the correlation between the temperature increase and the increase of the ΔRF progression cannot be taken as evidence for causation. However, the authors show that a quantitative consistency exists between the temperature rise expected from the radiative forcing and the global temperature rise.

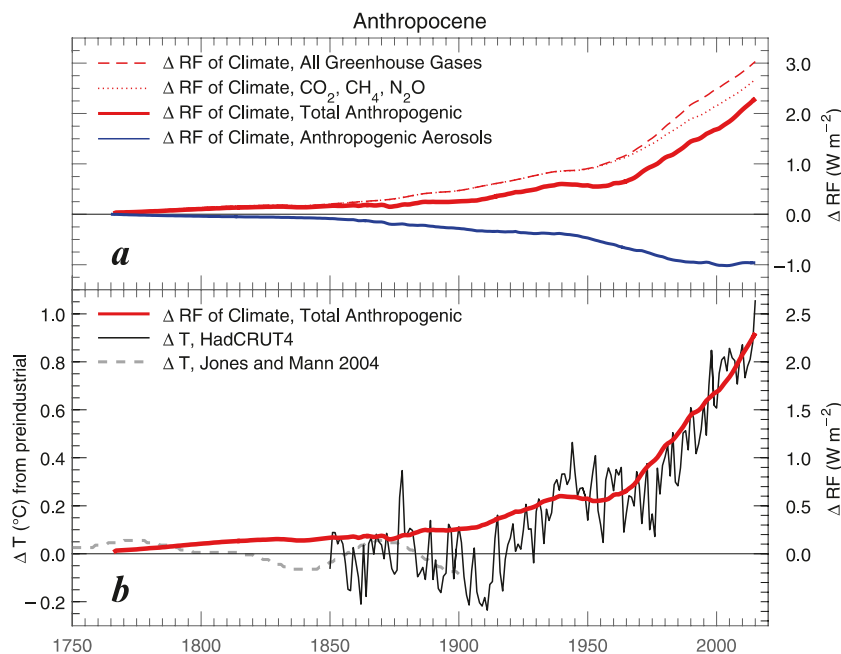


Figure 1-2. (a) Different contributions to the difference of the radiative forcing ΔRF and (b) temperature difference compared to the difference of the radiative forcing. All quantities are given over time and relative to the year 1765. The image was taken from R. J. Salawitch et al. (2016) (© by the Editors and authors; CC by 4.0).

Nevertheless, while the correlation between the population and the atmospheric GHGs N_2O , CH_4 and CO_2 is clear, the reconstruction of the mean temperature progression from the study of E. M. Mann et al. (1999), which resulted in the well-known Hockey Stick, remains controversial. The United States National Academy of Sciences (see (Salawitch, 2016)) argues that the study may be considered plausible, but that it is not possible to assure that the current period is the warmest one, due to the uncertainties in the temperature reconstruction. The existing scientific evidence, like that discussed above using the ΔRF , shows that the rising global temperature may be caused due to the

inherent GHGs from human activity. However, the study of E. M. Mann et al. (1999) needs a further revision.

Assuming the GHGs contribute significantly to the temperature rise and following the studies of H. D. Matthews and K. Caldeira (2008), as well as the work of R. Knutti and J. Rogelj (2016), all strategies to reduce global warming should focus on climate-neutrality, i.e., on the reduction of the CO₂ emissions, so that they become in net zero. In December 2015, the Paris Climate Agreement was adopted to limit the current global temperature increase to 2 °C above pre-industrial levels and to meet the requirements to expand this goal to 1.5 °C. The countries taking part in this agreement submit Intended Nationally Determined Contributions (INDCs), whose effect is well summarized by J. Rogelj et al. (2016). In this study, the authors point out that the INDCs do not cover policies to reduce global emissions due to aviation or maritime transport, despite the fact that these transport emissions contribute up to 23 % of the total emissions (Cruz-Champion, 2017). A possibility to cover this lack is the use of fuel cells (FCs) instead of common heat engines.

In a FC, the electrochemical reaction of hydrogen and oxygen into water results in electrical energy and heat. In comparison to a common heat engine, the conversion from chemical energy into electrical energy does not need any intermediate steps and is not limited by the Carnot efficiency. The most promising fuel cell technologies are the low temperature proton-exchange membrane fuel cell (PEMFC) and the high temperature solid oxide fuel cell (SOFC). In their recent work, H. Cruz-Champion and S. Kabelac (2017) present a detailed discussion of PEMFC systems to be used as an auxiliary power unit (APU) for civil aircrafts. The PEMFC advances in aviation made by the German Aerospace Center (DLR), like the aircraft HY4 for 4 passengers driven mainly by this technology (Flade, 2016), as well as the PEMFC system already implemented for propulsion of German navy submarines (Sharaf, 2014) are other examples of PEMFC applications in aviation or maritime transport. One disadvantage of PEMFCs is their low fuel flexibility, as the system's overall efficiency may be affected by the required hydrogen purification process (Weng, 2013). This drawback is significant, since, e.g., the sustainable energy security package of the European Commission (EC) from February 2016 (see (Aguilo-Rullan, 2017)) considers natural gas as an energy source up to the year 2030, when the EC aims for a transition to a low carbon energy system. However, even reformat of natural gas cannot be used directly to drive PEMFCs because it contains CO, which deactivates the anode catalytic sites. Further, 10 ppm CO are enough to strongly accelerate the cell aging parameters (Profatilova, 2018). On the contrary, SOFC systems can be used up to 2030 and beyond, since they can be driven by natural gas (Eisavi, 2018) or even gases from the reformation of common fuels (Leites, 2012). Additionally, they can be easily adapted to operate in a future hydrogen infrastructure. Therefore, SOFCs can be considered a key technology

during and after the energy transition period. Despite all these advantages and due to the weight and size of SOFC systems, this technology seems to be predestined for stationary decentralized energy supply, e.g., in households. As reported by the case study of L. Barelli et al. (2011), micro combined heat and power (μ CHP) plants based on SOFCs may have a 10 % higher efficiency (~ 40 %) than plants based on PEMFCs. The already completed project SOFT-PACT financed by the European Fuel Cell and Hydrogen Joint Undertaking Program for the demonstration of such plants based on SOFCs (Aquilorullan, 2017) and the national subsidies of the Japanese government to promote SOFC technologies for stationary energy supply (Horiuchi, 2013) are further examples to support the above statement. Nevertheless, SOFC systems can also be used for maritime applications, as is the aim of the ongoing SchIBZ project (see (Nehter, 2017) and publication VI not included in this thesis). The 50 kW on-land prototype SOFC system consists of two SOFC modules and is operated with anode off-gas recirculation and pre-reforming of road diesel fuel. To the date, this prototype operates successfully at partial load.

Through active involvement in the project and considering the discussion above, the candidate realizes the importance of SOFCs for the energy transition and that there are still open questions regarding basic FC and SOFC research beyond the topics of the project. The background behind these further questions is given by the theory of Non-Equilibrium Thermodynamics (NET). This theory introduces phenomenological equations based on an intrinsic multi-causality of the transport mechanisms, which is not explicitly given or is even neglected by classical transport equations. If all phenomenological coefficients L_{ij} (also known as conductivities due to their physical nature) are given, the phenomenological equations for a system can be solved and the entropy production can be directly calculated, providing the second law of thermodynamics a fundamental role in the prediction of the system's behavior. Despite the numerous numerical and experimental studies on SOFCs (see, e.g., (Ghorbani, 2018; Prokop, 2018; Tanveer, 2018; Yahya, 2018)), only few of them are directly based on this theoretical framework (see (Kjelstrup, 1997)).

The main objective of this doctoral thesis is to provide values for the phenomenological coefficients of different SOFC electrolyte materials and to develop a one-dimensional (1D) NET model using these coefficients to study the influence of the coupled transport mechanism for the prediction of SOFCs' behavior. For the estimation of the conductivities, the author chooses equilibrium molecular dynamics (MD) and the Green-Kubo approach. With these methods, the phenomenological coefficients can be directly calculated without any assumptions or transformations. The estimation of these coefficients is limited to the electrolyte, since the highest losses of an electrolyte-supported SOFC occur across this layer.

To fulfill the main objective, the following questions should be answered in this work:

- In the literature, some studies (see (Fèvre, 2005; Schelling, 2001)) give experimentally and numerically the effective transport coefficients of the state of the art electrolyte material zirconium dioxide ZrO_2 co-doped with yttrium(III)oxide Y_2O_3 (YSZ). However, there is no study providing data for the conductivities L_{ij} for this material. This work aims at providing values for the conductivities for different YSZ configurations at 1300 K, which is hot enough for the activation of anion diffusion. The Y_2O_3 concentration is chosen as variable because the ionic conductivity in YSZ experiences an experimental maximum for 8 mol% Y_2O_3 . This work should also provide an explanation of this peculiarity using linear response theory.
- The force driving the ionic conduction is the electrochemical potential. In NET, both the fluxes and the forces play an important role. In this work, the classical definition of the electrochemical potential will be discussed and, especially, the theory given by Guggenheim regarding electrostatics will be revisited. In this theory, classical electrostatics are not compatible with thermodynamics and, thus, the electrostatic potential may not describe a thermodynamically consistent quantity. This study intends to give this quantity in a thermodynamically consistent way.
- Analogous to the discussion of L. Xu et al. (2011), different diffusion coefficients in metal oxides may arise: the Brownian diffusion coefficient, the tracer diffusion coefficient, the Nernst-Planck diffusion coefficient and the Fick diffusion coefficient. The assumption of the ionic conductivity being proportional to the diffusion coefficient from the mean square displacement (MSD) of the ions in some studies (see, e.g., (Yamamura, 1999)) is not necessarily true, as can be seen from NET. Only the Nernst-Planck diffusion coefficient may be proportional to the ionic conductivity under certain conditions. This study provides an extensive diffusivity study of zirconium dioxide ZrO_2 co-doped with 10 mol% scandium(III)oxide Sc_2O_3 and 1 mol% cerium dioxide CeO_2 (10Sc1CeZ) between 1100 K and 1500 K. This material is chosen because no values for the different diffusion coefficients are available in the literature.
- It has been shown several times that it is necessary to explicitly or implicitly account for NET to describe the behavior of PEMFCs effectively (see (Bednarek, 2017) and publication V not included in this thesis). Is the NET approach also relevant for the description of SOFCs? To answer this last question, a 1D NET model of an electrolyte supported planar SOFC is developed using the MD-results from this study. With this SOFC model, simulations are carried out to compare the results of calculations accounting for multi-causal transport mechanisms with those neglecting them. The simulations' results may provide an answer to this last question.

In chapter 2 of this study, a short theoretical background is provided to complement the one provided in the four papers included in this thesis. A literature survey summarizing recent experimental and numerical studies about the electrolyte materials YSZ and 10Sc1CeSZ, as well as about numerical modelling on SOFCs, is also included in this chapter. Chapter 3 covers details of the simulation not mentioned in the papers. This comprises sample data, data to prove that the simulations for YSZ reached equilibrium, and a discussion of the capability of the proposed force field to describe other properties in 10Sc1CeSZ. A short discussion about the numerical algorithm behind the SOFC 1D model is also described in this chapter. Chapter 4 includes the summary of the papers and a further discussion of the results. In the last chapter, conclusions and perspectives are summarized.

2. Theoretical Background and Literature Survey

2.1 Thermodynamics of Galvanic Cells

This section is based on the work of P. Atkins and J. de Paula (Atkins, 2006). An electrochemical cell consists of two electrodes (an anode and a cathode) joined by an electrolyte. The electrolyte is an ionic conductor and electronic insulator. A galvanic cell is an electrochemical cell, which provides electricity due to the spontaneous redox reaction occurring in it. At the anode, the oxidation half reaction $\text{Red}_1 \rightarrow \text{Ox}_1 + \nu_e e^-$ occurs and the free electrons travel through an external circuit to the cathode, where the reduction half reaction $\text{Ox}_2 + \nu_e e^- \rightarrow \text{Red}_2$ takes place. Here, Ox is the oxidized species, Red the reduced species and $\nu_e > 0$ the stoichiometric number of the electrons. Electrodes of inert metals like platinum (Pt) or gold (Au) act as a source or a sink of electrons and as a catalyst for the electrochemical reactions, since they do not take part in them. While the oxidation reaction provides electrons, they are consumed in the reduction reaction. The electron transfer and the spatial separation of both half-reactions by the electrolyte result in an electrical field and in a lower electric potential at the anode compared to the cathode (Baehr, 2016). This electric potential difference is called the electromotive force (EMF) of the cell. A high EMF of 4.3 V is theoretically achievable by hybrid Li-air batteries, as reported by A. Manthiram and L. Li (2015), where the Li anode with a standard potential of -3.05 V works against a H_2/O_2 cathode with a standard potential of 1.23 V. Both potentials are defined relative to the standard hydrogen potential. The standard EMFs of other electrochemical cells, like H_2/O_2 fuel cells (1.23 V) or Li batteries (3.05 V) are lower than this EMF.

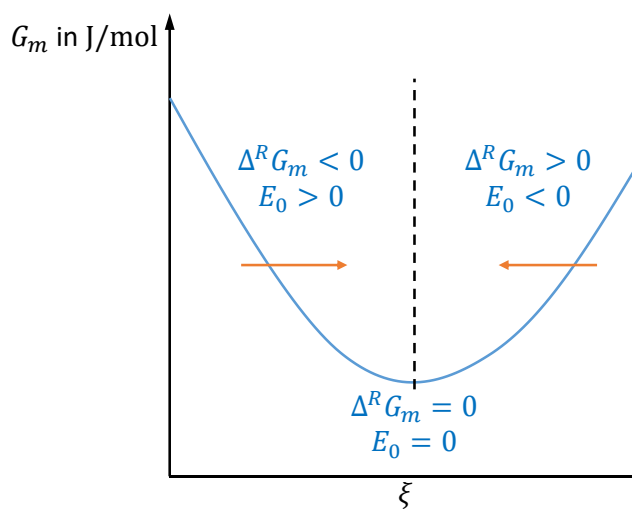


Figure 2-1. Progression of the molar Gibbs energy G_m near equilibrium as a function of the extent of reaction ξ and for different molar Gibbs energies of reaction $\Delta^R G_m$ and EMFs E_0 . This figure is a facsimile of figure 7.14 from P. Atkins and J. de Paula (2006) under permission of Wiley-VCH.

From an energy balance, the maximum work per mole aside from expansion work that can be provided by a system at constant pressure p and temperature T is given by the change in the molar Gibbs energy: $\delta W_{m,max} = dG_m$. If only one spontaneous reaction occurs within the system, we can write

$$dG_m = \Delta^R G_m(p, T, x_i) d\xi, \quad (2-1)$$

where $\Delta^R G_m(p, T, x_i)$ is the molar Gibbs energy of reaction, x_i the molar fraction of species i and ξ is the extent of reaction. Furthermore, the charge transported is given by the Faraday's law $-v_e e N_A d\xi = -v_e F d\xi$, where e is the elementary charge ($1.602176 \cdot 10^{-19}$ C), N_A the Avogadro constant ($6.02214 \cdot 10^{23}$ mol $^{-1}$) and F the Faraday constant (96485.3 C/mol). The product of the charge transported and the EMF E_0 results in the electrical work W_m , so that it follows from Eq. (2-1):

$$\Delta^R G_m = -v_e F E_0. \quad (2-2)$$

Physically, if an electrochemical cell is not in equilibrium, a spontaneous reaction may occur and a potential difference, i.e., the EMF E_0 , can be measured. This potential difference along with $\Delta^R G_m$ becomes zero if the electrochemical cell reaches equilibrium, as given by Eq. (2-1) (see Figure 2-1). We can use the so-called Nernst equation (Baehr, 2016; O'Hayre, 2016) for the calculation of the EMF E_0 :

$$E_0 = -\frac{\Delta^R G_m^\ominus(T)}{v_e F} - \frac{RT}{v_e F} \ln \left(\prod_{i=1}^N a_i^{v_i} \right), \quad (2-3)$$

where the superscript \ominus denotes standard conditions, R is the universal gas constant (8.31447 J/(molK)), a_i is the activity and v_i is the stoichiometric coefficient of the reactant i ($v_i > 0$ for products, $v_i < 0$ for educts). This potential difference E_0 describes the open circuit voltage (OCV) measured in a galvanic cell, where the consumed educts for the reaction are constantly compensated with new fresh educts. This OCV can also be defined separately for each half-cell reaction (see Paper IV). Moreover, the activity of the ions a_i acts as a corrected mole fraction to account for the real behavior relative to an ideal mixture. To calculate it, the electrochemical potential $\tilde{\mu}_i = \mu_i^\ominus + RT \ln a_i + z_i F \Phi$ (expressed with the symbol η in Paper I, II and III) is used instead of the chemical potential μ_i . The electrochemical potential also considers the charge of the ions and the resulting electric field with the term $z_i F \Phi$ (written as $z_i F \phi$ in Paper I, II and III), where z_i is the valence of the ions species i and Φ is assumed to be the local electrostatic potential.

2.1.1 Electrostatic Potential

Let us analyze a system with infinite point charges q_i in vacuum having the distance r_{ij} to each other. The potential energy U_C of the system is given by:

$$U_C = \frac{1}{2} \sum_{i=1}^{\infty} q_i \sum_{j \neq i}^{\infty} \frac{q_j}{4\pi\epsilon_0 r_{ij}} \quad (2-4)$$

in the unit J or by

$$U_C^* = U_C \cdot \frac{4\pi\epsilon_0}{e^2} = \frac{1}{2} \sum_{i=1}^{\infty} z_i \sum_{j \neq i}^{\infty} \frac{z_j}{r_{ij}} \quad (2-5)$$

in the unit m^{-1} (Patterson, 2010). Here, ϵ_0 denotes the vacuum permittivity ($8.85419 \cdot 10^{-12}$ F/m). The electrostatic potential φ_i of the point charge q_i is classically defined as

$$\varphi_i = \sum_{j \neq i}^{\infty} \frac{q_j}{4\pi\epsilon_0 r_{ij}} \quad (2-6)$$

in the unit V or as

$$\varphi_i^* = \varphi_i \cdot \frac{4\pi\epsilon_0}{e} = \sum_{j \neq i}^{\infty} \frac{z_j}{r_{ij}} \quad (2-7)$$

in the unit m^{-1} . It describes the influence of the Coulomb-forces on the point charge due to a conservative electric field. The definitions in Eq. (2-5) and in Eq. (2-7) will be used later.

For the potential energy, the following relationship can be written (see (Heyes, 1991)):

$$U_C = \frac{1}{2} \sum_{i=1}^{\infty} q_i \varphi_i \quad (2-8)$$

Only the half of the sum is considered because of the symmetry $q_i \varphi_j = q_j \varphi_i$. If the charges are not point charges but instead follow a charge distribution $\rho_{q,i}$, the electrostatic potential is given by Poisson's equation $\nabla^2 \varphi_i = -\rho_{q,i}/\epsilon_0$. In this work, the calculation of the Coulomb forces is limited to the classical assumption that ions in a crystal system can be seen as point charges. The so-defined electrostatic potential φ_i is a property specific for each charge point and, therefore, it should differ from the field property Φ , appearing in the definition of the electrochemical potential (see last section). One of the aims of this work is to analyze this discrepancy.

2.1.2 Galvanic Cells Under Load

If a galvanic cell is operated under load, i.e., for a given current $I > 0$, the measured potential difference E is lower than the OCV value E_0 and becomes a function of the current. This function is the voltage(E),current(I)-characteristic specific for each galvanic cell. In Figure 2-2, the typical progression of a E,I -characteristic is depicted. The electrical power P for a given operational point results from the product of the potential difference E and the current I .

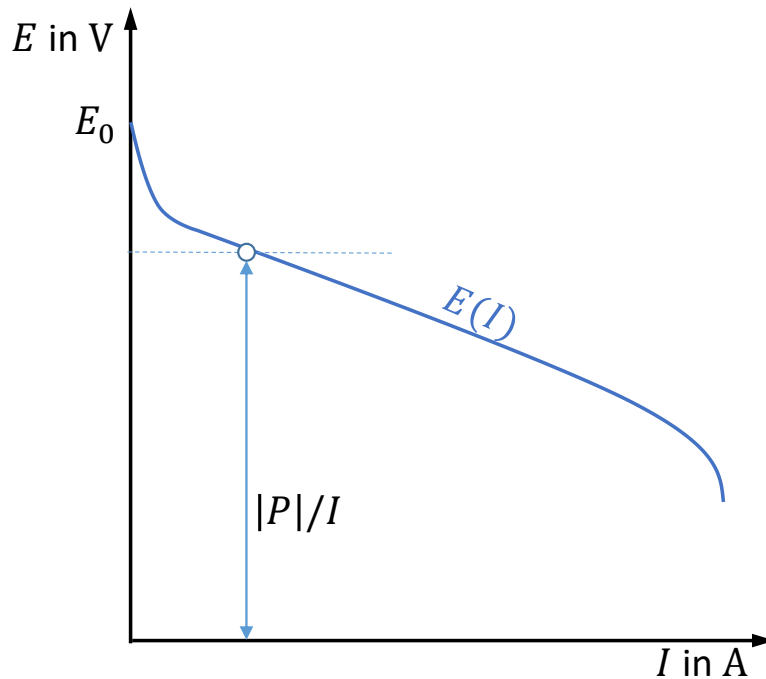


Figure 2-2. Typical progression of a voltage(E),current(I)-characteristic of a galvanic cell. E_0 describes the open circuit voltage (OCV) and P the electrical power.

The lower potential difference E under load results from the combination of different losses. These potential losses are primarily activation losses due to the reactions at the electrodes and losses due to the transport mechanisms in the bulk phases, like the ionic transport in the electrolyte or the electronic transport in the electrodes. As discussed in more detail in Paper IV, the activation losses can be described using the Butler-Volmer ansatz, which assumes these losses act as some kind of potential barrier for the rate of the reduction and oxidation half reactions at each electrode within an Arrhenius type formalism (Atkins, 2006). The losses due to the transport mechanisms in the bulk phases can be described using NET, as will be discussed in more detail in the next section.

2.2 Non-Equilibrium Thermodynamics (NET)

The core of NET is the relationship between the entropy production rate $\dot{\sigma}^*$ and the transport mechanisms, which is given in Eq. (2) of Paper I and IV (or in the Supporting Information (SI) of Paper III). It states that the entropy production rate $\dot{\sigma}$ per unit volume is the summation of the scalar products between the generalized fluxes \mathbf{J}_i of thermodynamic extensive properties with their corresponding generalized forces \mathbf{X}_i , i.e., gradients of thermodynamic intensive properties (Kjelstrup, 2017). Exemplarily in a galvanic cell, the corresponding force of, e.g., the ionic flux in the electrolyte is the gradient of the electrochemical potential expressed with the gradient of the electric potential.

We define the extensive variable $\sigma^* = S - S_0$ as the difference between the entropy of a system S and the entropy of this system in equilibrium S_0 . The entropy of a system depends on the thermodynamic properties Z_i , which can be expressed with the deviation $\alpha_i = Z_i - Z_{i,0}$ from equilibrium, so that we can write $\sigma^*(\alpha_1, \alpha_2 \dots)$. The so-defined entropy function σ^* is always negative or equal to zero, because in equilibrium the entropy is at its maximum. We can expand this function near equilibrium as follows:

$$\sigma^* \approx \frac{1}{2} \sum_{i=1}^N \sum_{j=1}^M \left(\frac{\partial^2 \sigma^*}{\partial \alpha_i \partial \alpha_j} \right)_0 \alpha_i \alpha_j. \quad (2-9)$$

Here, we neglect the derivatives of third or higher order, because only small changes near equilibrium are considered, i.e., we assume that the fundamental Gibbs equation of state

$$dG = -SdT + Vdp + \sum \mu_i dn_i \quad (2-10)$$

holds for these cases. Here, V is the volume of the system and n_i is the amount of substance of species i . Furthermore, not only σ_0^* and $\alpha_{i,0}$ are zero, but also the derivatives $(\partial \sigma^* / \partial \alpha_i)_0$, since σ^* has a maximum at equilibrium. Differentiating Eq. (2-9) with respect to time results in the following expression for the entropy production rate $\dot{\sigma}^*$:

$$\dot{\sigma}^* \approx \frac{1}{2} \sum_{i=1}^N \sum_{j=1}^M \left(\frac{\partial^2 \sigma^*}{\partial \alpha_i \partial \alpha_j} \right)_0 (\alpha_i \dot{\alpha}_j + \dot{\alpha}_i \alpha_j) = \sum_{i=1}^N \sum_{j=1}^M \left(\frac{\partial^2 \sigma^*}{\partial \alpha_i \partial \alpha_j} \right)_0 \alpha_i \dot{\alpha}_j. \quad (2-11)$$

X_i describes the thermodynamic forces driving the system to equilibrium and, thus, $X_i = \partial \sigma^* / \partial \alpha_i$ as a consequence of the fundamental equation of state (2-10). From a second Taylor expansion around equilibrium, but this time for the derivatives $\partial \sigma^* / \partial \alpha_i$ and neglecting all terms of second or higher order, we get:

$$X_i = \frac{\partial \sigma^*}{\partial \alpha_i} \approx \sum_{j=1}^M \left(\frac{\partial^2 \sigma^*}{\partial \alpha_i \partial \alpha_j} \right)_0 \alpha_j. \quad (2-12)$$

As a consequence of Eq. (2-12), only the entropy function σ^* is needed to calculate all forces in the system. If we choose the time derivatives of the deviations as the fluxes, i.e., $J_i = \dot{\alpha}_i$, another consequence of this equation is that the force X_i not only depends on its corresponding flux J_i , but also on all fluxes in the system and vice versa, i.e., $J_i = J_i(X_1, X_2, \dots)$. From a Taylor expansion and neglecting all terms of second or higher order, we finally get the phenomenological equations:

$$J_i = \dot{\alpha}_i \approx \sum_{j=1}^N \left(\frac{\partial J_i}{\partial X_j} \right)_0 X_j = \sum_{j=1}^N L_{ij} X_j, \quad (2-13)$$

with the conductivities L_{ij} . These phenomenological coefficients are the transport coefficients that describe the relaxation of a system from a non-equilibrium state to the equilibrium state.

If we consider an infinitesimally small volume element and define the entropy production rate per unit volume, i.e., $\dot{\sigma} = d\dot{\sigma}^*/dV$, the fluxes J_i are then expressed by their flux densities, i.e., the generalized fluxes \mathbf{J}_i , and the forces X_i by their spatial gradients ∇X_i , i.e., the generalized forces \mathbf{X}_i . With this transformation in the Euclidean vector space, one can write the phenomenological equations given in Eq. (1) of Paper I and IV. Here, it is assumed that the phenomenological coefficients are independent of the spatial coordinate; otherwise, the conductivities may be expressed with a rank-2 tensor (Mauri, 2013; Benfenati, 2018).

2.2.1 Phenomenological Coefficients and Linear Response Theory

If the auto correlation function (ACF) of the fluxes $\langle \mathbf{J}_i(0) \mathbf{J}_i(t) \rangle$ and the cross correlation function (CCF) between different fluxes $\langle \mathbf{J}_i(0) \mathbf{J}_j(t) \rangle$ are known, the phenomenological coefficients can be calculated. To demonstrate this, we can define the average of the CCF $\langle \alpha_k(0) \alpha_i(t) \rangle$ of the deviation $\alpha_i(0)$ at time $t = 0$ up to the deviation α_k at time $t > 0$ for a stationary process. This describes the progression of the information contained in the deviation α_i regarding the initial value of α_k over time.

Microscopic reversibility states that the equations of motion are invariant under time reversal. As a consequence, if the deviations of the variables α_i are only dependent on the momenta and positions of the particles, the conditional probability $\Pi(\alpha_i(t), t | \alpha_k(0), 0)$ that α_i assumes the value $\alpha_i(t)$ at time t provided that α_k assumes the value $\alpha_k(0)$ should be equal to the probability $\Pi(\alpha_i(-t), -t | \alpha_k(0), 0)$. Thus, it follows that $\langle \alpha_k(0) \alpha_i(t) \rangle = \langle \alpha_k(t) \alpha_i(0) \rangle$. The values $\alpha_i(0)$ and $\alpha_k(0)$ are constant over time and, therefore, we can write for the time derivatives $\langle \alpha_k(0) \dot{\alpha}_i(t) \rangle = \langle \dot{\alpha}_k(t) \alpha_i(0) \rangle$. With this last equation and the phenomenological equations (2-13), we get:

$$\sum_{j=1}^N L_{ij} \langle \alpha_k(0) X_j \rangle = \sum_{j=1}^N L_{kj} \langle \alpha_i(0) X_j \rangle. \quad (2-14)$$

It can be shown that $\langle \alpha_i(0) X_j(t) \rangle_{|t=0} = -\delta_{ij} k_B$ if the probability distribution function Π of the fluctuations is Boltzmann distributed with respect to σ , i.e., $\sigma = -k_B \ln \Pi$ (Mauri, 2013; Höpfner, 1977). With Eq. (2-14), this results in the Onsager reciprocity relations $L_{ij} = L_{ji}$.

Analogously, we can define the following averages:

$$\langle \alpha_k(0) \dot{\alpha}_i(t) \rangle_{|t=0} = \sum_{j=1}^N L_{ij} \langle \alpha_k(0) X_j \rangle_{|t=0} = -k_B L_{ik}. \quad (2-15)$$

The variable $\alpha_k(0)$ may result from the integration of its velocity $\dot{\alpha}_k(t)$ over time. If we choose the equilibrium state as the integration boundary, we get for long periods of time:

$$\alpha_{k,0} = 0 = \lim_{t \rightarrow \infty} \int_0^t \alpha_k(\tau) d\tau + \alpha_k(0) \rightarrow \alpha_k(0) = - \lim_{t \rightarrow \infty} \int_0^t \alpha_k(\tau) d\tau. \quad (2-16)$$

Integrating Eq. (2-16) in this way results in the Green-Kubo relations:

$$k_B L_{ik} = \lim_{t \rightarrow \infty} \int_0^t \langle \dot{\alpha}_i(0) \dot{\alpha}_k(\tau) \rangle d\tau = \lim_{t \rightarrow \infty} \int_0^t \langle J_i(0) J_k(\tau) \rangle d\tau, \quad (2-17)$$

where $\dot{\alpha}_i(0) = J_i(0)$ is defined at $t = 0$ because the condition $t = 0$ given in Eq. (2-15). Mathematically, the coefficients L_{ij} are proportional to the area under the curve of the CCFs. These equations can be also expressed with the flux densities \mathbf{J}_i (see Eq. (4) of Paper I) and can be derived in a more general framework from the perturbation of the Hamiltonian (Kubo, 1957; Zwanzig, 1965).

The progression of the auto correlation function (ACF) of a flux \mathbf{J}_i , i.e, Eq. (4) of Paper I with $j = i$, is given in Figure 2-3. For a gas, it simply decays from the initial value $\langle \mathbf{J}_i(0) \mathbf{J}_i(0) \rangle$ to the abscissa. Here, the particles do not stay in their initial position long and gradually lose the information about their initial value, resulting in the exponential decay. For a liquid, the particles may be trapped due to the higher particle density and bounce in this limited environment, resulting in a change of sign in the ACF. However, after a certain time the particles are able to leave their initial position and gradually lose the information about their initial value. The further maxima and minima in the progression correspond to new environments, where the particles may become trapped again. This trap effect is outstanding in the progression of the ACF for solids, since the particles do not necessarily leave their position in the crystal framework. This discussion can be extended for the description of CCFs.

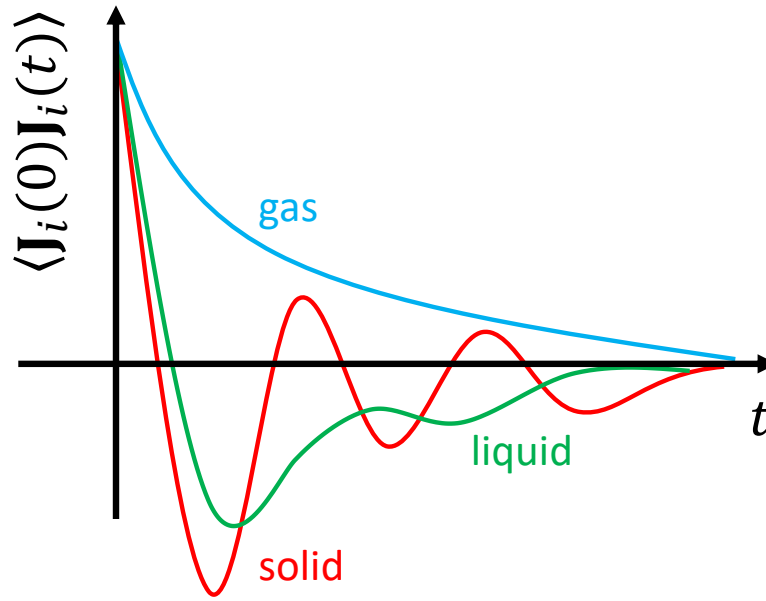


Figure 2-3. General behavior of the auto correlation function (ACF) for different systems. In blue, for a gas; in green, for a liquid; in red, for a solid.

At this point, particle diffusion should be discussed in more detail. Analogous to Eq. (14) of Paper I, the micro flux \mathbf{J}_k of the particles of species k in a mixture is given by:

$$\mathbf{J}_k = \frac{1}{V} \sum_{i=1}^{N_k} \mathbf{v}_i, \quad (2-18)$$

where \mathbf{v}_i is the velocity vector for a particle. We can write the following expression for the conductivity L_{kk} :

$$L_{kk} = \frac{1}{3k_B V} \lim_{t \rightarrow \infty} \left[\int_0^t \left\langle \sum_{i=1}^{N_k} \mathbf{v}_i(0) \mathbf{v}_i(\tau) \right\rangle d\tau + \int_0^t \left\langle \sum_{i=1}^{N_k} \mathbf{v}_i(0) \sum_{j \neq i}^{N_k} \mathbf{v}_j(\tau) \right\rangle d\tau \right], \quad (2-19)$$

which describes the diffusion of the particles of species k due solely to its (electro)chemical potential gradient. Here, the integral is divided into two terms: the first describes the sum of the velocity auto correlation functions (VACFs), and the second describes the sum of the velocity cross correlation functions (VCCFs). We can define the following diffusion coefficient using the term describing the VACFs and the conversion rule $D = L_{kk} k_B V / N$, analogous to Eq. (7) of Paper III:

$$D^{VACF} = \frac{1}{3} \lim_{t \rightarrow \infty} \frac{1}{N_k} \int_0^t \left\langle \sum_{i=1}^{N_k} \mathbf{v}_i(0) \mathbf{v}_i(\tau) \right\rangle d\tau. \quad (2-20)$$

In this equation, the sum is averaged with the number of particles N . In the linear domain, the average of the VACF is equal to the mean squared displacement (MSD) and we get

$$D^{VACF} = D^{MSD} = \frac{1}{3} \lim_{t \rightarrow \infty} \frac{\langle [r(t) - r(0)]^2 \rangle}{2t}, \quad (2-21)$$

resulting in the MSD diffusion coefficient D_{kk}^{MSD} . This diffusion coefficient only describes the Brownian motion of the particles, i.e., the equilibrium state. The coefficient L_{kk} in Eq. (2-19) describes the case of a gradient in the (electro)chemical potential, accounting for the influence of other particles of the same species in the system. A more detailed discussion of binary and ternary systems can be found in the work of X. Liu et al. (2011).

2.3 Classical Molecular Dynamics

Classical MD provides a way to calculate the electrostatic potential of the ions or the micro fluxes needed for the analysis of the transport phenomena in electrolytes in this work. This ansatz is based on the calculation of the system trajectory from the solution of the classical equations of motion at the molecular scale over time. From a given start configuration, other configurations can be generated. Under the assumption of the Quasi-Ergodic hypothesis that the time averages can be taken as the ensemble averages, each of the generated configurations describes a micro-state of a statistical ensemble (Leach, 2001).

The equations of motion are based on the Hamiltonian of the system

$$\mathcal{H}(\mathbf{r}, \mathbf{p}) = \sum_{k=1}^N \dot{\mathbf{r}}_k \cdot \mathbf{p}_k - \mathcal{L}(\mathbf{r}, \dot{\mathbf{r}}) = U, \quad (2-22)$$

which describes the internal energy U of the system and depends on the positions \mathbf{r} of all N particles and their momenta \mathbf{p} . This function is the Legendre transformed Lagrangian \mathcal{L} of the system and, thus, it contains the same information (Scheck, 2007). The Hamiltonian of a conservative system is equal to its total energy if the transformation does not depend explicitly on time (see (Goldstein, 2000; Lüdde 2008)). In this case, the potential energy given by the Hamiltonian becomes independent of time due to this transformation, meaning that only a time independent force field (FF), like the well-known Lennard-Jones(LJ)-FF, and the initial conditions are necessary to calculate the equations of motion of the system.

To solve the equations of motion, the force upon each particle is calculated using a start configuration and the interatomic FF. From the force, the acceleration for each particle can be calculated using Newton's second law. The new velocities and the positions of the atoms at time step $t + \delta t$ result from a discrete integration with a finite-difference method (FDM), like the Leapfrog or the Velocity-Verlet algorithm (Leach, 2001).

The solution of the equations of motion as described above would result in simulations in the micro canonical (NVE) ensemble, i.e., at constant energy, volume and particle number. Unfortunately, experimentation occurs at other boundary conditions such as constant temperature, pressure and particle number. To keep the temperature constant for simulations in the canonical (NVT) ensemble, methods like velocity scaling can be used (Allen, 2017). However, such velocity scaling can affect the dynamics of the system. A better method is applying thermostats, like using the Nosé-Hoover algorithm (Hoover, 1985). This algorithm is based on the coupling of the system to an external heat bath. However, this algorithm is not ergodic (Shinoda, 2004). G. J. Martyna et al. (1994) and M. E. Tuckerman et al. (2001) extended this algorithm to ensure that the dynamics of the system is correctly calculated. Analogously, this algorithm can be extended for simulations in the NpT ensemble using volume fluctuations to keep the average pressure constant.

Paper I includes a short description of the calculation procedure for the transport coefficients with non-equilibrium MD (NEMD). Paper I and III present in detail the methodologies for calculating transport coefficients using equilibrium MD (EMD). Therefore, the MD methods for the calculation of transport coefficients will be not repeated here. However, a short discussion about the calculation of the electrostatic potential using the Ewald Sum to complement the background of Paper II will be given in the next subsection.

2.3.1 Ewald Sum

This chapter is based on the works of L. V. Woodcock and K. Singer (1971), S. de Leeuw et al. (1980) and D. M. Heyes (1981). The Ewald sum is a method for the calculation of the Coulomb energy in Eq. (2-5) in systems with periodic boundary conditions. It guarantees the convergence of this equation (Frenkel, 2002). The basic idea is to calculate the Coulomb energy of the system as the sum of two contributions, i.e., $U_C^* = U_C^{R,*} + U_C^{K,*}$, where $U_C^{R,*}$ describes the short-range contribution and $U_C^{K,*}$ the long-range contribution. Using the complementary error function $\text{erfc}(x)$ as a window function, we can write:

$$U_C^{R,*} = U_C^* \cdot \text{erfc}(\beta_C \cdot r_{ij}) \quad (2-23)$$

and

$$\varphi_i^{R,*} = \sum_{j \neq i}^N \frac{z_j}{r_{ij}} \text{erfc}(\beta_C \cdot r_{ij}). \quad (2-24)$$

Eq. (2-23) means that the Coulomb energy is completely given by the short-range contribution $U_C^{R,*}$ for $r_{ij} = 0$. This contribution is damped as r_{ij} becomes higher, where the long-range contributions become the main contribution. Furthermore, the term $U_C^{K,*}$ becomes the only contribution for $r_{ij} \rightarrow \infty$, as given by:

$$U_C^{K,*} = U_C^* \cdot [1 - \operatorname{erfc}(\beta_C \cdot r_{ij})] = U_C^* \cdot \operatorname{erf}(\beta_C \cdot r_{ij}). \quad (2-25)$$

The Ewald parameter β_C is the damping factor for Eq. (2-23) and Eq. (2-25). A high Ewald parameter results in a fast decaying progression of the short-range contribution, while a small Ewald parameter leads to a slowly increasing progression of the long-range contribution. The short-range term and the long-range term contribute equally to the Coulomb energy at a distance $r_{ij} = 1/(2\beta_C)$.

In Eq. (2-25), U_C^* is defined as

$$U_C^* = \frac{1}{2} \sum_{i=1, j=1}^N \sum_{n=1}^M \frac{z_j}{r_{ij} + nL} \quad (2-26)$$

to account for the periodic M images of the system. $U_C^{K,*}$ can be Fourier transformed to:

$$\hat{U}_C^{K,*} = \frac{1}{2L^3} \sum_{k \neq 0}^K \frac{4\pi}{k^2} e^{-\frac{k^2}{4\beta_C^2}} \left| \sum_{i=1}^{\infty} z_i \cdot e^{-i\mathbf{k} \cdot \mathbf{r}_i} \right|, \quad (2-27)$$

where i is the imaginary unit and $k = |\mathbf{k}|$. The vector \mathbf{k} is the wave vector describing the lattice in reciprocal space. This vector describes waves that propagate in a lattice with the lattice vector $\mathbf{R} = n_1 \mathbf{a}_1 + n_2 \mathbf{a}_2 + n_3 \mathbf{a}_3$ given by the basis vectors \mathbf{a}_i and $n_i \in \mathbb{Z}$. These waves have a wavelength that corresponds to the lattice constant, so that all lattice points have the same wave phase, i.e.,

$$e^{i\mathbf{k} \cdot (\mathbf{r} + \mathbf{R})} = e^{i\mathbf{k} \cdot \mathbf{r}}, \quad (2-28)$$

where $\mathbf{k} \cdot \mathbf{R} = 2\pi m$ with $m \in \mathbb{Z}$. As a consequence, the \mathbf{k} -vector contains the same information as the lattice vector \mathbf{R} . The sum over different wave vectors in Eq. (2-27) results in an overlapping of the different waves and in peaks of the function at the atom positions and, thus, is convergent at the limits $N, M \rightarrow \infty$. This behavior mathematically resembles the behavior of the wave function in quantum mechanics, where the particle position cannot be determined if the particle momentum is given. After the overlapping of waves with different momenta, it is possible to determine the exact position of a particle at the expense of losing information about the momentum, resulting in Heisenberg's uncertainty principle.

The electrostatic potential in \mathbf{k} -space is given by

$$\hat{\phi}_k^{K,*} = \frac{4\pi}{k^2} \sum_{i=1}^N z_i \cdot e^{-\frac{k^2}{4\beta_C^2}} \cdot e^{-i\mathbf{k} \cdot \mathbf{r}_i} \quad (2-29)$$

and its reverse transformation, i.e., the electrostatic potential for the long-range contributions in real space is

$$\varphi^{K,*} = \sum_{k \neq 0}^K (\hat{\varphi}_k^{K,*})^\ddagger \cdot \hat{\varphi}_k^{K,*}, \quad (2-30)$$

where the \ddagger denotes the complex conjugate. In Eq. (2-29), the series considers all atoms including the point charge i . This is not in accordance with the definition of φ_i in Eq. (2-7). For this reason, a correction term $\varphi_i^{S,*}$ should be subtracted from Eq. (2-30) to calculate $\varphi_i^{K,*}$ as follows:

$$\varphi_i^{K,*} = \varphi^{K,*} - \varphi_i^{S,*} = \varphi^{K,*} - 2 \cdot z_i \cdot \frac{\beta_C}{\sqrt{\pi}} \quad (2-31)$$

Similarly, the correction term

$$U_C^{S,*} = \sum_{i=1}^N 2 \cdot z_i \cdot \frac{\beta_C}{\sqrt{\pi}} \quad (2-32)$$

should be subtracted from the Fourier reverse transformation of $\hat{U}_C^{K,*}$ to calculate $U_C^{K,*}$. Clearly, a correction for the dipole moments should also be considered. In this work, polarization and dipole effects are assumed to be negligible and, thus, such corrections are not implemented in the calculations, but the reader is referred to (Heyes, 1981) for a more detailed discussion.

2.3.2 Molecular Simulation Studies on Transport Mechanisms

This section is limited to recent molecular studies regarding advances on the calculation of transport coefficients. H. Dong et al. (2018) show in their recent study about MD calculations for the thermal conductivity that the EMD and NEMD methods should provide equivalent results, if they are correctly implemented and evaluated. This contradicts the frequently reported differences between the results from both methods (see, e.g., (He, 2012)). The discrepancies may lie in the linear extrapolation to “infinite” sizes needed when the thermal conductivity is calculated with the NEMD method, or result from incorrect implementation of the calculation of the micro heat fluxes, especially for many-body potentials (Fan, 2015). O.N. Bedoya-Martínez and J.-L. Barrat (2019) compare classical and quantum molecular methods for the calculation of the thermal conductivity, concluding that these methods may not be appropriate for the calculation of this transport coefficient for solids below the Debye temperature. Since the most accurate method using quantum perturbation theory is computationally inefficient, as stated by the authors of that study, the efficient and accurate calculation of the thermal conductivity below the Debye temperature is still a challenge.

The study of X. Liu et al. (2011) is an example of recent advances in computational methods for the calculation of diffusion coefficients in mixtures. In that study, the authors present a method to calculate the Fick diffusion coefficients from EMD. The thermodynamic factor is calculated using the radial

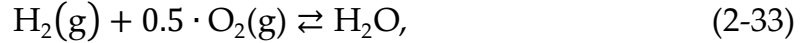
distribution function and the Kirkwood-Buff integrals (Schnell, 2011). The calculated Maxwell-Stefan (MS) diffusivities are then corrected to predict the Fick diffusivities. Here, the MS diffusivities are calculated using linear response theory, analogous to the phenomenological coefficients appearing in NET. Their results show a good agreement with experimental data and, thus, a NEMD calculation for the direct calculation of the Fick diffusion coefficients from an imposed concentration gradient or an extra grand-canonical Monte Carlo (μ VT-MC) simulation for the calculation of the thermodynamic factor can be avoided. Furthermore, the novel study of G. Pranami and M. H. Lamm (2015) discusses the statistics of the calculation of Brownian diffusivities from the MSD of the particles. From their conclusions, the error of calculated Brownian diffusion coefficients from a single simulation cannot be estimated, emphasizing that in this case multiple independent simulations are unavoidable in order to obtain reliable statistics. Since the diffusion coefficient of ions and the ionic conductivity are related, the above discussion applies also to the ionic conduction. Moreover, the electronic conduction can be calculated from *ab initio* calculations using the Kubo-Greenwood formula, where the ACF is defined by the electronic density function (Dufty, 2018).

Despite the many recent MD studies of the calculation of thermal diffusion coefficients (see (Lecce, 2018; Shimizu, 2017; Hafskjold, 2017)), the calculation of the Seebeck or Peltier coefficient using classical EMD or NEMD simulation is not common. This is because classical MD does not consider electrons or holes, which play an important role in describing thermoelectric generators (TEG) based on the thermoelectric effect. For that reason, most of the numerical studies investigating the Seebeck or the Peltier coefficient are based on *ab initio* calculations (Ahmad, 2018; Joshi, 2017). In those studies, the Seebeck coefficient is calculated with the well-known Mott formula, which is based on the Sommerfeld expansion and, thus, relates the Seebeck coefficient to the Fermi-Dirac distribution function (Jonson, 1980). Using this formula and *ab initio* calculations, M. Bilal et al. (2015) calculate the Seebeck coefficient of SnCCO_3 at room temperature with a deviation of 5.7 % from the experimental value, and they use their validated methods to predict Seebeck coefficients for further metallic antiperovskites.

Furthermore, dynamical NEMD is a new approach that provides the possibility of following the transient progression from the equilibrated system to the steady state in non-equilibrium (Hafskjold, 2017; Bonella, 2017). With this method, it is possible to gain some insight into the transport phenomena during transient changes, e.g., the time at which the temperature, mass density or concentration profile begins to relax into the steady state and the duration of this relaxation. In this way, it is possible to calculate the time scales for the dynamics of coupled transport mechanisms.

2.4 Fuel Cells

The bonding configuration of water molecules is energetically lower than that of hydrogen or oxygen. Therefore, the oxidation of hydrogen in an adiabatic combustion chamber, given by the overall reaction



results in heat (Baehr, 2016). Depending on the temperature, water can be liquid ($\Delta^f H_{m,\text{H}_2\text{O}(\text{l})}^\ominus(298 \text{ K}) = -285.83 \text{ kJ/mol}$) or gaseous ($\Delta^f H_{m,\text{H}_2\text{O}(\text{g})}^\ominus(298 \text{ K}) = -241.82 \text{ kJ/mol}$) (Atkins, 2006). A heat engine could partially convert the heat from this combustion reaction into mechanical energy. This mechanical energy can be used in a generator to supply electrical energy. This kind of process is thermodynamically limited by the Carnot-Factor and, due to this limitation and the many intermediate steps, it is not efficient (O'Hayre, 2016). On the contrary, the chemical energy can be converted directly into electrical energy in a FC. FCs are galvanic cells that usually operate with a continuous hydrogen flow. In this case, the reactants flow into different compartments and the combustion reaction is split into an oxidation half reaction and a reduction half reaction. If only O^{2-} ions are transported in the FC's electrolyte, the reduction reaction $0.5 \cdot \text{O}_2 + 2e^- \rightarrow \text{O}^{2-}$ occurs at the cathode while the oxidation reaction $\text{H}_2 + \text{O}^{2-} \rightarrow \text{H}_2\text{O} + 2e^-$ takes place at the anode. As discussed below, other fuels can also be used, depending on the FC type.

Following the discussion of J. Larminie and A. Dicks (2009), the most remarkable advantages of fuel cells are the high efficiency, lack of moving parts, low emissions, silence and scalability. The efficiency advantage can be argued following the discussion above, as the Carnot efficiency is not a limit anymore. The lack of moving parts results in systems with high reliability and long life regarding the components. If the fuel cells are driven with pure hydrogen produced, e.g., via electrolysis and renewable energy sources, the CO_2 emissions become zero. Nevertheless, even SOFCs operating with CH_4 or CO do not emit other environmentally harmful gases like NO_x and SO_x . The advantage of being a silent technology concerns the environmental noise, which is also a kind of pollution. Finally, FCs can be scaled without a considerable loss in performance in comparison to other power supply systems, like batteries (O'Hayre, 2016).

One disadvantage of FCs is the fuel itself, due to the currently unavailable hydrogen infrastructure and the CO_2 emissions inherent to the present hydrogen production processes (Larminie, 2009). Furthermore, the gravimetric power density of hydrogen (between 2 MJ/kg to 10 MJ/kg depending on the storage technology) is much lower than the one of, e.g., gasoline of $\sim 44 \text{ MJ/kg}$. Other disadvantages are the costs and some operational drawbacks, like their vulnerability to environmental poisoning and poor endurance under start-stop cycling, which are difficult to overcome. Due to technological efforts, the gravimetric power density of FCs, $\sim 500 \text{ W/kg}$, is closer to that of an internal

combustion engine, but further improvements are still needed in this area (O'Hayre,2016).

Table 2-1. Some features, including the operational temperature ϑ_{op} and the system efficiency η_{sys} , of the alkaline fuel cell (AFC), the direct methanol fuel cell (DMFC), the polymer electrolyte membrane fuel cell (PEMFC), the high temperature(HT)-PEMFC, the phosphoric acid fuel cell (PAFC), the molten carbonate fuel cell (MCFC) and the solid oxide fuel cell (SOFC). Data from (Baehr, 2016; O'Hayre, 2016; Larminie, 2009; Rechberger, 2018).

Parameter	AFC	DMFC	PEMFC	HT-PEMFC
ϑ_{op} in °C	60-80	80	60-85	120-200
Electrolyte	KOH(aq)	PEM	PEM	PEM
Fuel	H ₂	CH ₄ O	H ₂	H ₂
Charge carrier	OH ⁻	H ⁺	H ⁺	H ⁺
η_{sys}	~50	30-40	45-55	40-45
Application	Spacecraft	Portable energy supply Electronics Battery charger	Automotive Submarines Aircraft Rail transport Stationary power supply	APU Back-up power
Parameter	PAFC	MCFC	SOFC	
ϑ_{op} in °C	160-220	600-650	600-1000	
Electrolyte	H ₃ PO ₄ (aq)	Molten carbonate	Co-doped ZrO ₂	
Fuel	H ₂	H ₂ ,CH ₄	H ₂ ,CH ₄ ,CO	
Charge carrier	H ⁺	CO ₃ ²⁻	O ²⁻	
η_{sys}	40-45	40-45	45-60	
Application	Stationary power supply		APU Range extender Stationary power supply	

The most important FC technologies and some of their features are summarized in Table 2-1. These technologies are the alkaline fuel cell (AFC), the direct-methanol fuel cell (DMFC), the PEMFC, the high temperature PEMFC, the phosphoric acid fuel cell (PAFC), the molten carbonate fuel cell (MCFC) and the SOFC. Most of the fuel cells operate at temperatures below 230 °C and the ionic transport occurs in the aqueous phase, except in the MCFC and the SOFC, where the ionic transport occurs through a molten salt and co-doped ZrO₂, respectively. The crystal framework in co-doped ZrO₂ that allows for vacancy diffusion is described in Paper I and Paper III. The most promising systems are the DMFC, the PEMFC and the SOFC due to their present and possible wide application ranges. SOFC systems show the highest efficiency and fuel flexibility.

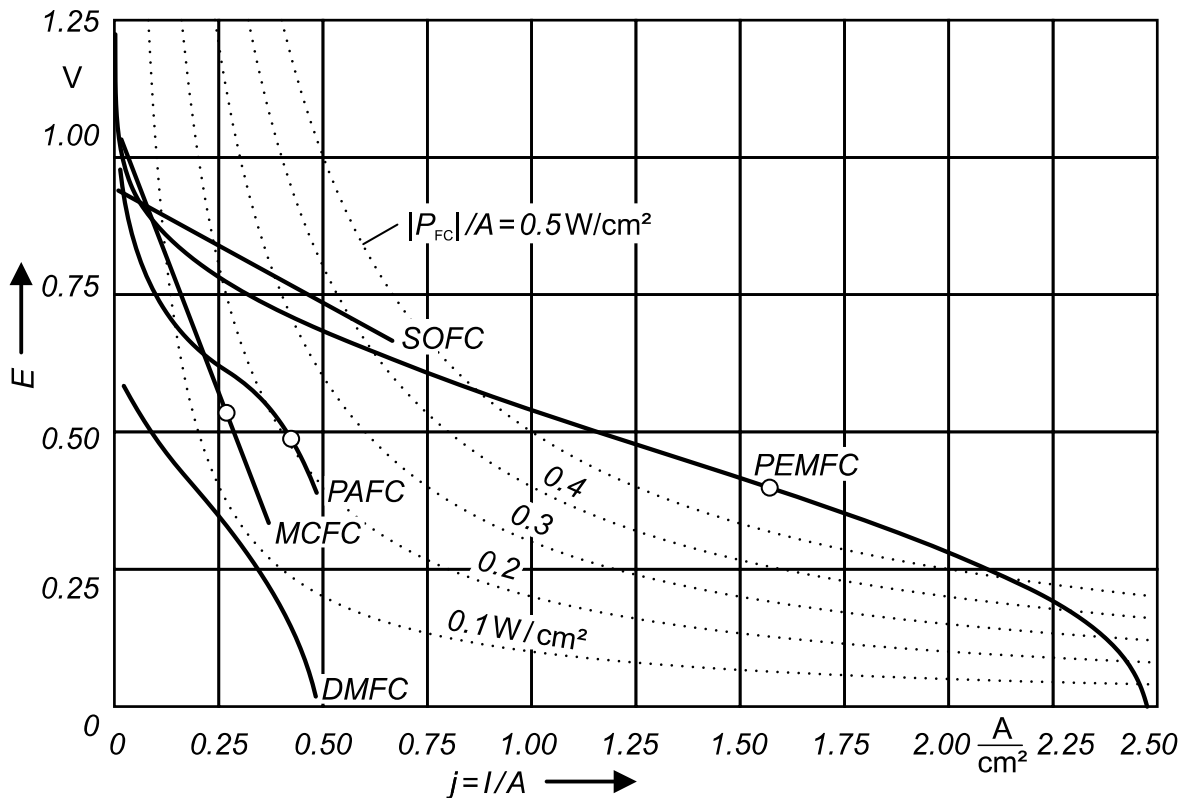


Figure 2-4. Typical progression of the voltage (E), current (I)-characteristic for different fuel cell technologies, as well as curves of constant power density $|P_{FC}|/A = E \cdot j$. A is the cell active area and j the current density. The circles denote operational points with maximum power density. The image is taken from (Baehr, 2016) under permission of Springer Vieweg and the authors. The nomenclature is adapted to the nomenclature of this work.

Finally, Figure 2-4 displays the E, j -characteristics for the different FC technologies, where j is the area specific current density I/A and A is the cell active area. The OCV is lowest for a DMFC followed by the OCV for a SOFC. However, the voltage E for a SOFC is the highest under load in comparison to the voltage for the other technologies. This results from the high temperature and may explain the high efficiency of SOFC systems. However, a comparison between FC technologies using solely the E, j -characteristics is not conclusive. Factors such as the performance at the desired operational point, costs and suitability for the chosen application should also be considered.

2.5 Solid Oxide Fuel Cells (SOFCs)

This work is limited to the study of single planar SOFCs. The representation of a SOFC design similar to the one used in the *Forschungszentrum Jülich* (Blum, 2011) is exemplarily depicted in Figure 2-5. For other cell designs, the reader is referred to the reviews of B. Timurkutluk et al. (2016) and M. Irshad et al. (2016).

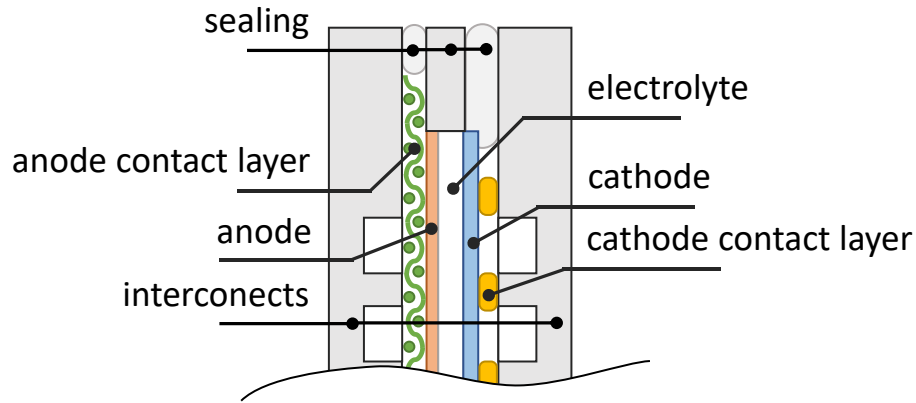
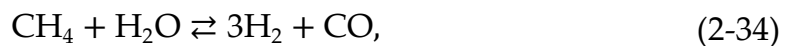


Figure 2-5. Exemplary representation of a planar SOFC based on the design used by the *Forschungszentrum Jülich*. (see (Blum, 2011)). For simplicity, the substrate that supports the cell is not depicted.

The basic layers of a SOFC are the porous anode layer, the porous cathode layer and the electrolyte. The anode and the cathode layers are porous gas diffusion layers (GDL), generally made of an inert metal or a metal-electrolyte mixture. Other combinations are possible, as discussed below. At the active sites of these layers, where the gas, the solid electrolyte and the metal phase meet at the well-known triple phase boundary, the anode and the cathode half reactions occur. The GDLs have the task of distributing the gases from the gas channels to these active sites. For mechanical stability, one of the two GDLs or the electrolyte is manufactured wider than the other layers (Droushiotis, 2014). The electrolyte not only provides the anionic transport from the cathode to the anode, but also hinders electron transport in order to avoid an electrical shortcut. Cells consisting of these basic layers are embedded between two interconnects, which contain gas channels. The gas channels ensure a homogenous gas distribution along the anode and cathode side. If the cell is driven with CH_4 or CO as part of the fuel gas mixture, the following reforming reaction, water-shift gas reaction and Boudouard reaction may take place at the anode side:



where the needed water vapor is available as part of the fuel mixture or as a product of the hydrogen oxidation. The carbon deposition given by the reaction (2-36) occurs only within a certain temperature range, which is determined by the gas composition (Sasaki, 2003).

2.5.1 Materials for SOFCs

SOFC materials for the anode GDL, the cathode GDL and the electrolyte have some common requirements (Mahato, 2015). Due to the high operational temperature, all materials should be thermally stable. Since the materials are interconnected, they should be chemically stable with the materials of the adjacent components and, additionally for the anode and the cathode materials, with the working gases (Jiang, 2004). Furthermore, the coefficient of thermal expansion (CTE) of the materials should be similar, as a different CTE may affect the interfaces during thermal expansion (Mahato, 2015). Mechanical strength is also an important requirement because of the stress resulting from the cell manufacturing or the cell operational conditions, like the pressure on a cell embedded in a stack or a thermal gradient (Laurencin, 2008). Additionally, anode and cathode materials require a high electronic conductivity (≥ 100 S/cm) to reduce the potential losses and a high catalytic activity to minimize activation losses. Furthermore, since oxygen diffusion is slow, cathode materials must provide enough porosity to allow the motion of the oxygen molecules. Electrolyte materials require a high ionic conductivity (~ 0.1 S/cm) and an electronic transference number lower than 10^{-3} (Mahato, 2015).

The state of the art material for the anode is the ceramic-metallic composite or cermet Ni-YSZ. This material fulfills almost all requirements mentioned above, and the nickel serves as catalyst for fuel reforming (Akdeniz, 2016). Nevertheless, this material is vulnerable to carbon deposition and sulfur poisoning (Mahato, 2015). F. Wang et al. (2014) and X. Song et al. (2016) proposed adding Al_2O_3 to Ni-YSZ cermets to improve the material's stability against carbon deposition and to enhance its electronic conductivity.

The state of the art material for the cathode GDL is the perovskite $\text{La}_{1-x}\text{Sr}_x\text{MnO}_{3-\delta}$ combined with YSZ (LSM/YSZ) (Yang, 2017). The current issues with this material are the reactivity of LSM with YSZ at high temperatures (higher than 1100°C) and the low catalytic activity for intermediate temperatures lower than 700°C (da Silva, 2017). Another commonly used perovskite for the cathode GDL is $\text{La}_{1-x}\text{Sr}_x\text{CoO}_{3-\delta}$ (Yang, 2017). $\text{La}_{2-x}\text{NiO}_{4\pm\delta}$ is a novel material with a low activation energy and, thus, can be used for temperatures lower than 700°C . However, this material reacts with YSZ at a lower temperature (900°C) than LSM (Ferkhi, 2016).

The state of the art electrolyte material is YSZ (see Paper I). The co-doping of Y_2O_3 in ZrO_2 not only results in a high ionic conductivity due to the crystal defects, but also stabilizes ZrO_2 in the cubic fluorite structure (see next section). Another relevant oxide is ScSZ (Xue, 2017). This material has a higher ionic conductivity than YSZ, but it lacks stability due to phase transitions at a temperature of $\sim 600^\circ\text{C}$ (Terner, 2014). Since CeO_2 is stable in the cubic phase from room temperature to $\sim 2400^\circ\text{C}$ (Mahato, 2015), the co-doping of CeO_2 in

ScSZ to form ScCeSZ, especially with the configuration 10Sc1CeSZ, has proven to be stable for a wide temperature range, while conserving the high ionic conduction properties.

Other materials like the perovskites $\text{Ln}_{2/3-x}\text{TiO}_{3-3x/2}$ for the anode (Lepe, 2005), Pr_2CuO_4 (PCO) for the cathode (Li, 2016) (both materials showing an enhanced electronic conductivity) or $\delta\text{-Bi}_2\text{O}_3$ based materials (Jiang, 1999), as well as perovskites based on LaMO_3 for the electrolyte (Hayashi, 1999) are a few examples of the many different SOFC materials discussed in the literature. The reader is referred to the reviews of F. S. da Silva and T. M. de Souza (2017), N. Mahato et al. (2015) and M. Irshad et al. (2016), the latter two reviews also providing information about materials for the interconnects.

2.5.2 Phase Diagrams, Structural Properties and Heat Capacities of YSZ and 10Sc1CeSZ

The phase diagram for YSZ is given in Figure 2-6. The data from X. Ren and W. Pan (2014), as well as the data from O. Fabrichnaya et al. (2005) are used. From the phase diagram, we can differentiate the following phases: a fluorite cubic phase (f, space group $Fm\bar{3}m$ (225)), a tetragonal phase (t, space group $P4_2/nmc$ (137)), a monoclinic phase (m, space group $P2_1/C$ (14)) (Viazzi, 2008), a cubic bixbyite phase (c, $Ia\bar{3}$ (206)) (Gajović, 2008) and a trigonal δ -phase corresponding to the intermediate compound $\text{Y}_4\text{Zr}_3\text{O}_{12}$ (space group $R\bar{3}$ (148)) (Gallardo-López, 2001).

Pure ZrO_2 presents a monoclinic phase at temperatures lower than 1478 K, a tetragonal phase for higher temperatures and a melting point of 2988 K. Moreover, the stabilization of the cubic fluorite structure due to the co-doping of Y_2O_3 is evident. For a mole fraction between ~ 20 mol% $\text{YO}_{1.5}$ and ~ 42 mol% $\text{YO}_{1.5}$, YSZ is cubic from room temperature up until the melting point. This range becomes wider for higher temperatures. For example, the cubic fluorite structure is fully stabilized for $0.15 \geq x_{\text{YO}_{1.5}} \geq 0.48$ at 1100 K to 1300 K. The melting point is ~ 3050 K for YSZ with 8 mol% $\text{YO}_{1.5}$ and ~ 2800 K for YSZ with 60 mol% $\text{YO}_{1.5}$. For higher Y_2O_3 concentrations, but for temperatures lower than ~ 1500 K, a δ -phase arises. Pure Y_2O_3 is stable in the cubic bixbyite phase, having a melting point at 2698 K. As discussed by A. Krogstad et al. (2011), metastable solid solutions are possible, like in systems at 1200 K with cubic f-phases and mole fractions lower than 15 mol% $\text{YO}_{1.5}$, which corresponds to YSZ08 (YSZ with 8 mol% Y_2O_3).

Several studies regarding thermodynamic properties and transport coefficients in YSZ are available in the literature. A. Krogstad et al. (2011) give the following correlation for the lattice constant a of the cubic fluorite phase in YSZ:

$$a = 5.11742 + 3.118 \cdot x_{\text{Y}_2\text{O}_3}. \quad (2-37)$$

That study and the study of C. Viazzi et al. (2008) include correlations for the measured lattice constants a and c of the tetragonal phase. H. Hayashi et al. (2005) report experimental values for the CTE for different YSZ compositions. Their measured values show a linear dependency on the Y_2O_3 composition ranging from $10.2 \cdot 10^{-6} K^{-1}$ for YSZ03 to $9 \cdot 10^{-6} K^{-1}$ for YSZ10. T. Tojo et al. (1999) give experimental data for the isobaric molar heat capacity $C_{p,m}$ for YSZ08 and YSZ10 for different temperatures. At room temperature (298.15 K), the resulting interpolated mean values are 60.198 J/(molK) for YSZ08 and 61.648 J/(molK) for YSZ10. This study also reports the Debye characteristics.

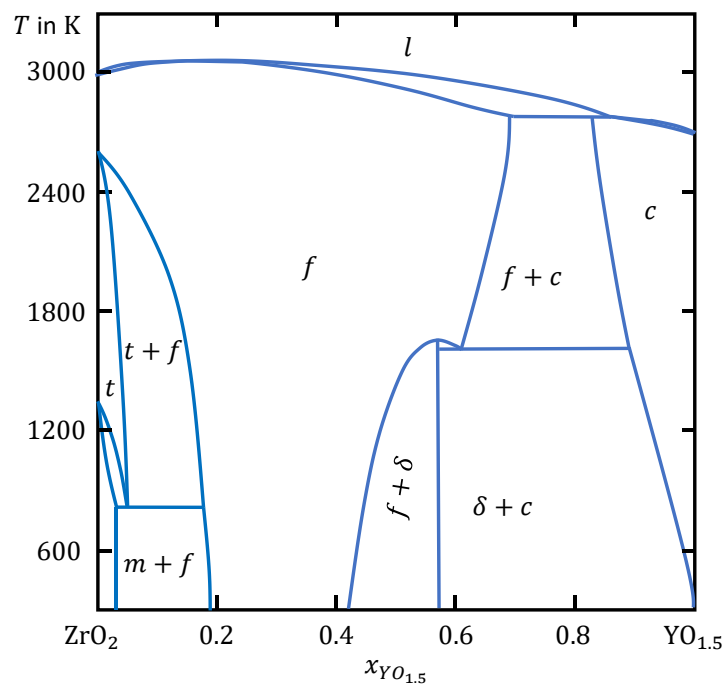


Figure 2-6. Phase diagram for YSZ. The data is taken from the studies of X. Ren and W. Pan. (2014), as well as O. Fabrichnaya et al. (2005). (f) fluorite phase (F3-3m), (t) tetragonal phase (P4₂/nmc), (m) monoclinic phase (P2₁/C), (c) bixbyite phase (Ia $\bar{3}$) and (δ) trigonal δ -phase (R3).

To the knowledge of the candidate, there is no phase diagram for ScCeSZ available in the literature. This is also true for the heat capacity of 10Sc1CeSZ. Experimental data from the literature for the lattice constant and the CTE is available in Paper III, along with a short, but informative review of the experimental studies for this material.

2.5.3 Transport Coefficients for YSZ and 10Sc1CeSZ

Since this thesis focuses on the transport coefficients of YSZ and 10Sc1CeSZ, a short description of the methods to measure empirical transport coefficients in metal oxides should be given here. As discussed in Paper I, III and IV, the empirical classical transport coefficients necessary to describe the kinetics in a

metal oxide are the ionic conductivity κ (expressed with the symbol σ in Paper II and III), the thermal conductivity λ and the Seebeck coefficient \check{S}_ϕ^1 (appearing respectively as κ and S in Paper I). From these classical transport coefficients, the conductivities L_{ij} given by NET (see Paper IV) can be estimated to some extent and vice versa (see Paper I and III). Different diffusion coefficients describing the O^{2-} -anion diffusion are also related to the ionic conductivity κ , i.e., to the corresponding conductivity L_{OO} .

The ionic conductivity κ of such oxides is measured with impedance spectroscopy or with the well-known four-terminal(4T)-sensing method. The samples usually have a cylindrical shape with a diameter between 8 and 20 mm and a height of 100 μm to 10 mm (Laguna-Becero, 2009). The electrical contact is done using platinum paste (Wang, 2005). The impedance is potentiostatically measured with a frequency ranging from 0.1 Hz to 1 MHz and amplitudes ranging from 10 mV to 100 mV (Liu, 2014; Grosso, 2013). In some studies, the frequency range is wider, with frequencies reaching more than 10 MHz (Kumar, 2016). In the impedance spectrum, two semicircles arise. For most cases, the semicircle at high frequencies corresponds to the bulk impedance, while the semicircle at low frequencies to the grain boundary impedance (Grosso, 2013). This differentiation is not possible with the 4T-sensing method, where only the total conductivity can be measured (Dasari, 2014).

The thermal conductivity λ is indirectly measured using the thermal diffusivity a_T and its definition $a_T := \lambda/(\rho c)$, where ρ is the mass density of the sample and c the specific heat capacity (Hongsong, 2015). The thermal diffusivity is measured using laser flash analysis, and the mass density with the Archimedes method (Jiang, 2017). If no experimental data for the heat capacity is available, it can be estimated using the Neuman-Kopp method (Leitner, 2010).

The method of measuring the Seebeck coefficient is well described in the works of S. Kjelstrup et al. (1991) and Z.-I. Takehara et al. (1989) for YSZ. Here, electrochemical cells with platinum electrodes and an YSZ electrolyte are measured in different gas atmospheres. One side of the cell is heated up, while the temperature at the other side is kept constant. The cell voltage E is then measured for various temperature differences. From the slope of the curve and the relationship:

$$F \left(\frac{dE}{dT} \right) = \frac{1}{4} \left[S_{O_2}(T) - RT \ln \left(\frac{p_{O_2}}{p} \right) \right] - S_{Pt}(T) - \frac{1}{2} S_{O^{2-}}(T), \quad (2-38)$$

the Peltier coefficient π can be calculated using the transported entropy of the ions $S_{O^{2-}}$ with $\check{S}_\phi = -0.5 \cdot S_{O^{2-}}(T)/F$. Here, S_i is the entropy of species i and

¹ The Seebeck \check{S}_ϕ coefficient and the Peltier coefficient π are related as follows $\pi = T\check{S}_\phi$ and, despite that they describe formally different effects, they are equivalent.

p_{O_2} the oxygen partial pressure in the gas atmosphere. This equation results from the NET approach.

Experimental values for the transport coefficient of YSZ along with the corresponding references are given in Table 6 of Paper I. To the best of the candidate's knowledge, no experimental data for the thermal conductivity or the Seebeck coefficient of 10Sc1CeSZ are available in the literature. Studies with experimental data for the ionic conductivity are mentioned in Paper III, and experimental values for the ionic conductivity from the literature for different temperatures are given also in this paper.

2.5.4 SOFC Modelling and Molecular Simulation for SOFCs

There are several numerical studies of SOFCs at different scales, ranging from the molecular level to the system level. First, studies regarding the SOFC and stack levels will be summarized, with the focus on the modelling methods and the assumptions for each SOFC layer. Second, literature studies at the molecular level concerning the SOFC materials YSZ and 10Sc1CeSZ will be reviewed.

Recent studies regarding stacks are given, e.g., by T. Parhizkar and S. Hafeznazami (2018), by R. T. Nishida et al. (2018) or by M. Peksen (2018), and regarding SOFC-systems, e.g., by A. Chitsaz et al. (2018), M. M. Whiston et al. (2017), and the publication VI not included in this thesis.

SOFC models are usually divided into the following domains: the fuel and air channels, the inert anode and cathode GDLs, the electrolyte, and two reactive catalyst layers (CLs) representing the reactive sites of the porous electrode layers (see (Hajimolana, 2011)). The division of the electrode porous layers into a reactive CL and non-reactive GDL is done for simplification purposes.

For the modelling of the fuel and air channels, the component balance, the energy balance and the momentum balance are solved (Menon, 2015). Usually, only convective mass transfer and a flux term coupling the gas channels with the GDLs are taken into account in the component balance, while diffusive mass transfer is neglected (Khazaei, 2017). The velocity needed to describe the convective term results from the momentum balance. The energy balances accounts for convective heat transfer, where the Nusselt number is calculated with empirical formulae (Ma, 2018). P. Pianko-Oprych et al. (2014) point out that radiative heat transfer has to be taken into account to describe the heat transfer between the SOFC components. This is especially true for reforming fuel mixtures including CO₂ and H₂O, because of their high absorption of infrared radiation and radiance at high temperatures (Nam, 2014). Other recent SOFC models considering the fuel gas channel and the air gas channel are the 3D models of J. Moreno-Blanco et al. (2018), M. Fardadi et al. (2016) and T. Choudhary and Sanjay (Choudhary, 2016). As it can be taken from the results of V. Menon et al. (2015), the calculation of the temperature profile along the fuel

channel may vary strongly if the cell is driven by internal reforming and, thus, a detailed modelling of the gas channels cannot be avoided. This is also true for SOFCs operated at high current densities, as can be seen from the simulation data resulting from calculations with the 3D model of J. M. Park et al. (2018).

For the description of the porous media, i.e., the anode and cathode GDLs, the component balance is described with a diffusion term and, if needed for the calculation of fuel reforming, with a reaction term (Menon, 2015). The diffusion may be described with the Fick or the Maxwell-Stefan ansatz and effective diffusion coefficients (Costamagna, 2004). Y. Fu et al. (2015) use the proportion of porosity to tortuosity of the porous medium to define new effective binary diffusion coefficients from the binary diffusion coefficients in the gas mixture. W. Kong et al. (2015) provide a novel ansatz to describe the tortuosity and the effective diffusion coefficient depending solely on the porosity. The Dusty Gas model (DGM) is a more sophisticated approach for the description of the mass transport mechanisms in porous media, which accounts for chemical and Knudsen diffusion, as well as for advection. A. Bertei and C. Nicolella (2015) revisited this sophisticated ansatz for SOFC modelling application, concluding that the assumption of uniform pressure may lead to Graham's law of effusion, which is not compatible with reaction stoichiometry and, thus, inconsistencies between the mole fractions and the component fluxes may arise. F. Yang et al. (2016) analyze the impact of neglecting Knudsen diffusion in the GDL modelling. The authors conclude that neglecting Knudsen diffusion would lead to misleading predictions if GDLs showing pore size smaller than 250 nm are studied. Finally, the viscous flux is described, e.g., by a pressure gradient assuming an empirical equation for the description of the permeability of the medium (Menon, 2015). Especially for SOFCs operating with internal reforming, L. van Biert et al. (2017) calculate the reaction rates with empirical equations of the Arrhenius type, while P. Costamagna et al. (2015) assume chemical equilibrium for the chemical reactions. In the energy balance, the heat transfer is described by heat conduction in the solid phase and a heat term accounting for the heat transported in the gas phase (Aydn, 2016). The effective thermal conductivity can be approximated as a superposition of the effective thermal conductivity of the gas and of the solid phase with the porosity as a weighting factor (Menon, 2015). Clearly, a term accounting for the electrical power is also considered in the energy balance of the GDLs.

The starting point for the description of the CLs is the OCV given by the Nernst equation for the overall cell reaction, which results from Eq. (2-3) (Beale, 2016). The activation losses are commonly described with the Butler-Volmer equation. Analytical approximations to solve the Butler-Volmer equation for the activation overpotential are given by P. Vijay et al. (2017). H. R. Amedi (2015) and P. Costamagna (2004) apply a concentration-dependent Arrhenius type relation for the description of the exchange current density. The research group

of K. Sasaki (Hosoi, 2015; Takino, 2017) provides more sophisticated approaches for the Arrhenius equation of the exchange current density in dependency of different step reaction mechanisms.

The energy balance of the electrolyte is calculated analogously to the energy balance of the GDLs (Menon, 2015). Here, the potential losses are usually considered using an effective ionic conductivity, which also follows an Arrhenius ansatz (Khazaee, 2017; Ma, 2018). The models based on these assumptions are able to reproduce the experimental E, I -characteristics of SOFCs (Costamagna, 2015). Another way to describe the transport mechanisms in the electrolyte is using the Nernst-Planck equation, which is implemented, e.g., in the models of S. Shen et al. (2018) and X. Jin et al. (2016). This approach is advantageous to analyze electronic leakage currents across the electrolyte.

Transient SOFC modelling (Ma, 2018; Bae, 2018), as well as modelling on degradation (Parhizkar, 2018; Chatzichristodoulou, 2016) are current research topics. S. A. Hajimolana et al. (2011) and C. Bao et al. (2018) present detailed reviews on SOFC modelling. SOFC NET models and numerical studies on the calculation of the entropy production rate in SOFCs available in the literature are summarized in Paper IV.

In the literature, there are many molecular dynamics studies and *ab initio* calculations concerning phenomena occurring in the anode, the cathode and the electrolyte of SOFCs. Exemplarily, H. Lu et al. (2018) investigate the adsorption mechanism of methane, methanol and ethanol in a Ni-anode using a reactive force field (ReaxFF). They conclude that first the methane molecules are chemisorbed in the Nickel surface, followed by the diffusion of the carbon atoms into the Ni-matrix. After the driving force for carbon diffusion, the chemical potential, is balanced, Ni-C bonds tend to break and form highly stable C-C clusters. Due to the formation of this new phase, a new driving force for carbon migration arises. S. Sugiura et al. (2016) investigate using *ab initio* MD methods the influence of vacancies on oxygen dissociation at the NiO cathode. They conclude that vacancies favor the oxygen dissociation, since Ni atoms near vacancies are more prone to donate their electrons than Ni atoms near oxygen atoms. The study of M. Razmkhah et al. (2016) presents numerical data for the CTE, the heat capacity and the ionic conductivity for different electrolyte materials based on zirconium dioxide to conduct a comparison between them. Another topic of recent research on SOFCs is the mechanisms and properties at the interfaces between the different layers. As an example, the research group of M. Koyama develops a ReaxFF to analyze a Ni/ZrO₂ interface (Saha, 2015). The simulations using the developed ReaxFF suggest that the interface Ni(220)/ZrO₂(220) has the highest stability in comparison to other crystal plane combinations.

For the numerical investigation of YSZ, several interatomic FFs are available in the literature. Parameterizations for the Born-Mayer-Huggins Coulomb

(BMHC) FF, also called the Buckingham FF, are given by P. K. Schelling and S. R. Phillpot (2001), as well as by H. W. Brinkman et al. (1995). The parameterization of such two-body potentials results from a fitting to the cohesive energy, elastic constants, and structural and electrical properties (Lewis, 1985). While simulations conducted with the FF developed by P. K. Schelling and S. R. Phillpot (2001) are available to quantitatively predict the transition from the cubic to the tetragonal phase, simulations with the FF parameterization of H. W. Brinkman et al. (1995) can effectively predict experimental data for the heat capacity of YSZ (Tojo, 1999). Due to their simple form, simulations with such FFs are computationally advantageous. However, they do not account for effects like covalence or polarization, which may be necessary for a more accurate prediction of, e.g., the phase transition. T. Arima et al. (2006) propose a BHMC-FF together with a partial ionic model (PIM). They show that simulations with this FF are able to predict the lattice constant, but they overestimate the thermal conductivity of YSZ. To mention a final example, A. C. van Duin et al. (2008) give the parameterization for a ReaxFF. The fitting methodology of a ReaxFF parameterization is based only on the ground equation of state for the different crystal phases from *ab initio* calculation and, as stated by the authors, simulations with such potentials may provide results with the accuracy of quantum chemical calculations. The simulation results for the Brownian diffusion coefficient in the study of A. C. van Duin et al. (2008) agree well with experimental data.

Simulation results on the transport coefficients of YSZ are well summarized in Table 6 of Paper I with their corresponding sources. *Ab initio* studies for the Coulomb energy of YSZ are mentioned and discussed in Paper II. To the knowledge of the candidate, there are no numerical studies on 10Sc1CeSZ, but numerical studies regarding ScSZ are mentioned in Paper III.

3. Simulation Methods

3.1 Molecular Dynamics Simulation

3.1.1 System, Interatomic Potential and Thermodynamic State for YSZ

The main goal of the study in Paper I is to analyze the transport mechanisms in YSZ using NET and linear response theory. One of the special features of this material is the maximum of the ionic conductivity at a certain Y_2O_3 concentration. Therefore, a single temperature is considered with different YSZ compositions. These YSZ compositions are marked in the relevant section of the phase diagram of YSZ in Figure 3-1. At first glance, one might think that the conversion rule between the mole fractions $x_{\text{Y}_2\text{O}_3}$ and $x_{\text{YO}_{1.5}}$ follows the equality $2x_{\text{Y}_2\text{O}_3} = x_{\text{YO}_{1.5}}$, since $\text{Y}_2\text{O}_3 \leftrightarrow 2 \cdot \text{YO}_{1.5}$. This is not true because for the definition of the mole fractions $x_{\text{Y}_2\text{O}_3}$ and $x_{\text{YO}_{1.5}}$, we have $N_{\text{Zr}} + N_{\text{Y}}/2$ and $N_{\text{Zr}} + N_{\text{Y}}$ as the total number of molecules, respectively. Both mole fractions reach the limit of 1, but with a different rate. This explains why the marked points are not equally distributed along the abscissa, and the corresponding conversions from $x_{\text{Y}_2\text{O}_3}$ to $x_{\text{YO}_{1.5}}$ are provided in Table 3-1 for the relevant cases in this work.

The LAMMPS (Plimpton, 1995) routine for the creation of the start configurations is given in the Appendix. Here, it is assumed that all configurations are in the cubic fluorite phase, despite the fact that YSZ04 ($x_{\text{YO}_{1.5}} = 0.08$) also has a tetragonal phase. The aim of doping ZrO_2 with Y_2O_3 is to stabilize the cubic phase and, therefore, it is favorable to analyze the dependency of YSZ's properties on the composition or the temperature in this particular phase. Furthermore, YSZ ceramics with metastable fluorite phases for $x_{\text{Y}_2\text{O}_3} < 0.08$ can be experimentally prepared, as mentioned in chapter 2.5.2.

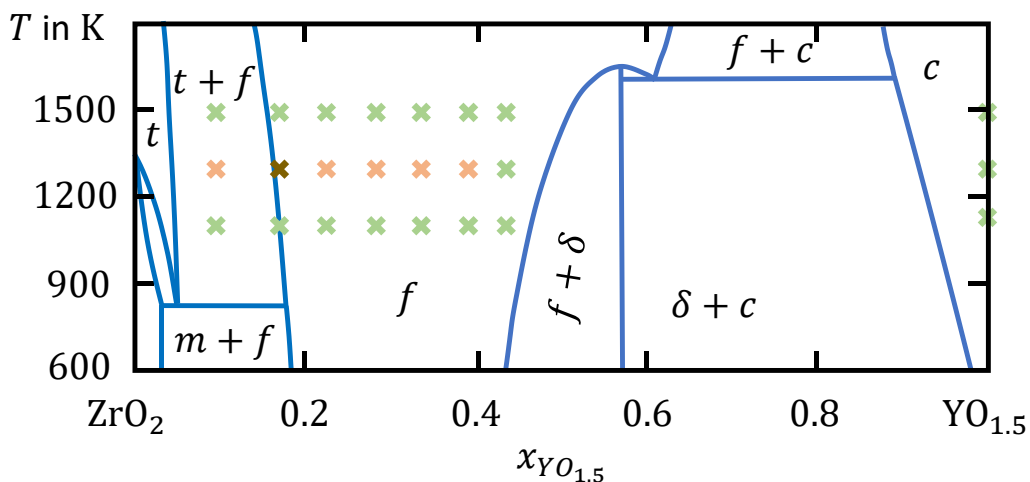


Figure 3-1. Section of the phase diagram of YSZ that is relevant for this study. The points mark the analyzed system compositions: The systems studied in Paper I are in orange, the systems studied in Paper IV are in dark orange and the systems studied in Paper II are in green, orange and dark orange.

The BMH-FF is chosen because simulations using this FF are computationally efficient due to its simplicity in comparison to complex FFs, like the ReaxFF reported by A. C. van Duin. et al (2008). Furthermore, following the discussion of V. V. Sizov et al. (2014), simulations with this FF parameterized with the parameters of P. K. Schelling and S. R. Phillpot (2001) (SP-FF) are able to qualitatively reproduce the behavior of the tracer diffusion in YSZ, showing a maximum of ca. $0.03 \cdot 10^{-5} \text{ cm}^2/\text{s}$ for YSZ05 at 1300 K. While the relative deviation of the simulated values for the tracer diffusion coefficient for YSZ10 is $\sim 11\%$ at temperatures between 1000 K and 1200 K with the SP-FF, the results of simulations for the same YSZ composition with the FF of H. W. Brinkman et al. (1995) (BK-FF) deviate $\sim 70\%$. Furthermore, the reported activation energy of the tracer diffusion coefficient for YSZ08 calculated with the SP-FF, 0.67 eV, deviates only 4.2 % from the experimental value of 0.7 eV. The simulations using the BK-FF result in a lower activation energy of 0.47 eV. Moreover, the qualitative behavior of the thermal conductivity is also given by the simulation results reported by P. K. Schelling and S. R. Phillpot (2001). For these reasons, the YSZ simulations are carried out using this FF parameterization.

Table 3-1. Conversion from $x_{Y_2O_3}$ into $x_{YO_{1.5}}$ for the YSZ compositions relevant in this study.

YSZ	YSZ04	YSZ08	YSZ12	YSZ16
$x_{Y_2O_3}$	0.04	0.08	0.12	0.16
$x_{YO_{1.5}}$	0.08	0.15	0.22	0.28
	YSZ20	YSZ24	YSZ28	Y ₂ O ₃
$x_{Y_2O_3}$	0.20	0.24	0.28	1.0
$x_{YO_{1.5}}$	0.33	0.39	0.44	1.0

The aim of the study in Paper II is to analyze the electrostatic potential of the cubic phase for the systems marked in Figure 3-1. For this aim, the FF must effectively reproduce the experimental lattice constant a , since it defines the positions of the atoms in the crystal framework and, thus, the electrostatic potential (see Eq. (2-6)). K. C. Lau and B. I. Dunlap (2011) report an agreement with experimental data for the calculated lattice constant of cubic ZrO₂ at 0 K using the SP-FF, with a relative deviation of 0.19 %. Further, W. Araki and Y. Arai (2010) also report agreement for the calculated lattice constant of YSZ08 at 2000 K using this FF with experimental data measured using high-temperature X-ray diffraction (see (Terblanche,1989)).

3.1.2 Interatomic Potential for 10Sc1CeSZ

The diffusivity study in Paper III concerns the material 10Sc1CeSZ. The system is well described in the paper and the LAMMPS (Plimpton, 1995) routine for the calculation of the 10Sc1CeSZ configuration is similar to the one for YSZ

given in the Appendix. However, the paper lacks justification for the chosen potential. This lack will be filled here. In Table 3-2, four parameterizations of the BMH-FF using values from the literature are presented. Only these parameterizations are included, since other combinations between them do not result in the required stabilized cubic 10Sc1CeSZ system.

Table 3-2. Different FFs' parameterizations for 10Sc1CeSZ. The values marked with (a) are from (Dwivedi, 1990), the values marked with (b) from (Lewis, 1985), the values marked with (c) from (Schelling, 2001), the values marked with (d) from (Minervi, 1999), the values marked with (e) from (Gotte, 2007) and the values marked with (f) from (Lau, 2011).

	DLC-FF (Paper III)			SPM-FF		
	A_{ij} in eV	ρ_{ij} in Å	C_{ij} in eVÅ ⁶	A_{ij} in eV	ρ_{ij} in Å	C_{ij} in eVÅ ⁶
Zr ⁴⁺ -O ²⁻	985.869 ^a	0.3760 ^a	0 ^a	1502.11 ^c	0.3450 ^c	5.1 ^c
Ce ⁴⁺ -O ²⁻	1013.60 ^b	0.3949 ^b	0 ^b	1809.68 ^d	0.3457 ^d	20.4 ^d
Sc ³⁺ -O ²⁻	1299.40 ^b	0.3312 ^b	0 ^b	1575.85 ^d	0.3211 ^d	0 ^d
O ²⁻ -O ²⁻	22764.30 ^a	0.1490 ^a	27.89 ^a	9547.96 ^c	0.2240 ^c	0 ^c
	GSM-FF			LDM-FF		
	A_{ij} in eV	ρ_{ij} in Å	C_{ij} in eVÅ ⁶	A_{ij} in eV	ρ_{ij} in Å	C_{ij} in eVÅ ⁶
Zr ⁴⁺ -O ²⁻	1502.11 ^c	0.3450 ^c	5.1 ^c	1292.85 ^f	0.3584 ^f	19.36 ^f
Ce ⁴⁺ -O ²⁻	755.1311 ^e	0.4290 ^e	0 ^e	1809.68 ^d	0.3547 ^d	20.40 ^d
Sc ³⁺ -O ²⁻	1575.85 ^d	0.3211 ^d	0 ^d	1575.85 ^d	0.3211 ^d	0 ^d
O ²⁻ -O ²⁻	9533.42 ^e	0.2340 ^e	224.88 ^e	13089.90 ^f	0.2197 ^f	49.30 ^f

A. Dwivedi and A. N. Comarck (1990) parameterized the BMH-FF for ZrO₂ using the structural parameters of the tetragonal phase and the dielectric constants. The parameterization of A. Dwivedi and A. N. Comarck (1990) can predict the lattice constant for cubic ZrO₂ with a relative deviation of 0.93 % and the dielectric constant with a relative deviation of 10 %. It reproduces the exact value for the oxygen parameter, i.e., the bond length between Zr and O. The features of the parameterization of P. K. Schelling and S. R. Phillpot (2001) for the description of ZrO₂ have already been described. The FF of K. C. Lau and B. I. Dunlap (2011) is parameterized using also structural properties, dielectric constants and phonon frequencies of cubic and tetragonal and ZrO₂, and Y₂O₃. Simulations using this FF produce results for the structural properties comparable to those from simulations with the SP-FF.

The parameterization for CeO₂ from G. V. Lewis and C. R. A. Catlow (1985) results from an extensive study of metal oxides, in which the parameters for this compound are derived from the extrapolation of property data of other metal oxides. Despite the relative antiquity of this parameterization, it is still used in recent MD studies, such as the one by X. Yang et al. (2018). One of the features of this study is that the parameterization for the O²⁻-O²⁻ interactions is the same for all the FFs provided by the authors and, thus, this parameterization can be used

for other potentials. Using this FF parameterization, the elastic constants are effectively described for CeO₂. The deviations from the experimental value for the elastic constants \check{c}_{11} , \check{c}_{12} and \check{c}_{44} are 16 %, 0.95 % and 7 % (see (Lewis, 1985; Minervi, 1999)). Moreover, the calculated cohesive energy of this compound deviate 1.2 % from the experimental value. The FF of L. Minervi et al. (1999) effectively describes the cohesive energy for CeO₂ with a relative deviation of 1.6%, but the elastic constants calculated with this FF have higher relative deviations than those obtained with the FF of G. V. Lewis and C. R. A. Catlow (1985). Unlike the study of G. V. Lewis and C. R. A. Catlow (1985), where the results for the structural properties of CeO₂ are in some way predictive, A. Gotte et al. (2007) use the cohesive energy, the elastic constants, the bulk modulus and the lattice constants of the perfect lattice to fit their parameterization. This procedure results in the best approach to describing these properties for CeO₂. However, the bulk modulus is yet overestimated with 236 GPa in comparison to the experimental value of 203.5 GPa.

In their extensive numerical study of metal oxides, G. V. Lewis and C. R. A. Catlow (1985) report a FF parameterization for ScO. The calculated cohesive energy for this compound deviates 0.1 % from the experimental value. Minervi et al. (1999) also give a parameterization for ScO. However, the authors do not report any results using it.

Preliminary simulations are conducted for 10Sc1CeSZ using the NpT-Nosé-Hoover thermostat at 1100 K, 1300 K and 1500 K with the FFs summarized in Table 3-3. The simulation and data evaluation methodologies are given in Paper III. Only one configuration is used, and one simulation is conducted for each FF. The results for the lattice constant are given in Table 3-3 alongside the extrapolated data from experiments taken from the SI of Paper III. The error bars are calculated with the well-known block average method (Allen, 2017).

Table 3-3. Calculated lattice constant a for 10Sc1CeSZ from a single MD simulation in the NpT ensemble using different FFs. The parameterizations for the FFs are given in Table 3-2.

T in K	DLC-FF a in Å	SPM-FF a in Å	GSM-FF a in Å	LDM-FF a in Å	Exp. a in Å
1100	5.115580(97)	5.12009(15)	4.818032(27)	5.108415(94)	5.1266
1300	5.124165(95)	5.127431(82)	4.82206(15)	5.115948(89)	5.1384
1500	5.13263(11)	5.13503(10)	4.826278(73)	5.123558(79)	5.1503

As can be seen in Table 3-3, the DLC-FF and the SPM-FF parameterizations give the best approach for the description of the absolute values of the lattice constant of 10Sc1CeSZ. Here, the maximum relative deviation from the experimental values for 1300 K is 0.34 % for the simulation values using the DLC-FF and 0.30 % using the SPM-FF. The best prediction using the DLC-FF

and with the SPM-FF is given for the values at 1100 K with a relative deviation of 0.21 % and 0.13 %, respectively. The CTE

$$\alpha_L = \frac{1}{a} \left(\frac{\partial a}{\partial T} \right)_p \quad (3-1)$$

is further calculated from a linear regression resulting in $8.32 \cdot 10^{-6} \text{ K}^{-1}$ for the DLC-FF simulation and $7.28 \cdot 10^{-6} \text{ K}^{-1}$ for the SPM-FF simulation. In both cases, the experimental value of $12.5 \cdot 10^{-6} \text{ K}^{-1}$ is underestimated, but the deviation resulting from the simulation value using the DLC-FF is smaller. For that reason, and due to the transferability character of the FF parameters taken from G. V. Lewis and C. R. A. Catlow (1985) discussed above, this FF is chosen for the calculations in Paper III.

Finally, the capability of the selected potential to reproduce caloric properties is analyzed. Following the methodology described below, an isobaric heat capacity of 26.423(98) J/(molK) is calculated for 10Sc1CeSZ from a linear regression of the average energy of the system in dependence on the studied temperatures. The values for the heat capacity at 298.15 K are 61.53 J/(molK) for CeO₂, 93.94 J/(molK) for Sc₂O₃ and 56.21 J/(molK) for ZrO₂, as is estimated by J. Leitner et al. (2002) using the Neumann-Kopp rule. Applying this rule, the heat capacity of 10Sc1CeSZ is estimated to be 60.036 J/(molK) at 298.15 K. This value is three times higher than the value calculated with the MD simulations, and it is expected that it will increase with higher temperatures. Since the heat capacity is related to the thermal conductivity, as discussed in chapter 2.5.3, there is a high probability that the transport coefficients related to this value will not be well described using this FF. For that reason, Paper III is limited to the calculation of the structural parameters, the anionic conductivity and the different anion diffusivities for 10Sc1CeSZ.

3.1.3 Computational Details

The computational details for the different MD simulations can be found in Paper I, II and III. The LAMMPS (Plimpton, 1995) routines for the NpT and NVT simulations, e.g., for the calculation of the phenomenological coefficients for YSZ, are provided in the Appendix. Unlike in these examples, the heat flux is not computed in the NVT simulations for 10Sc1CeSZ and, thus, no simulation *reruns* are conducted. In the NVT simulations for the electrostatic potential ϕ_i , neither simulation *reruns* nor fluxes are computed. It should be noted that for the NpT calculations to determine the lattice constant, an internal LAMMPS procedure is applied to couple the three diagonal components of the stress tensor during the computation of the pressure. In this way, a cubic simulation box is always ensured. The numerical methods used in this thesis are validated in Paper I.

Figure 3-2 shows the calculated internal energy U of a YSZ04 system configuration and a YSZ28 system configuration over the last 0.5 ns of the

equilibration time at 1300 K for NpT and NVT simulations. It also shows the calculated internal energy U of a YSZ16 system configuration at different temperatures for NpT and NVT simulations. The progression of the internal energy supports the assumption of equilibrium after 1 ns. These curves are representative of all independent simulations in Paper I and Paper II. An analysis of the 10Sc1CeSZ simulations is given in the SI of Paper III.

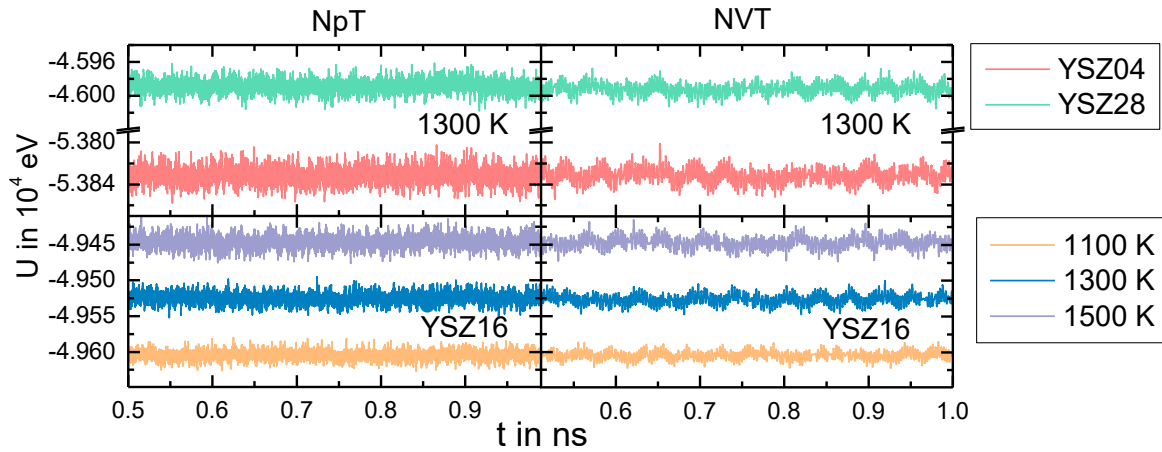


Figure 3-2. Calculated internal energy U of YSZ04, YSZ28 and YSZ16 system configurations over the last 0.5 ns of the equilibration time for NpT and NVT simulations, as well as for different temperatures for YSZ16.

In Table 3-4, some sample data is given for the lattice constant as well as for the phenomenological coefficients. The errors of the calculated values lie in the same order of magnitude, which confirms the repeatability of the simulations. The high errors for the values of the conductivities L_{00} and L_{0q} can be explained by the strong fluctuations of the ACF and the CCF, respectively. However, the error for L_{00} is similar to the error reported in the sample data of Paper III (see the corresponding SI). This means that the resulting fluctuations of the ACF for metal oxides with a fluorite type structure and oxygen vacancy may not depend on the system configuration, but further simulations with other metal oxides are needed to support this statement.

Table 3-4. Calculated values for the lattice constant a and the phenomenological coefficients L_{ij} for YSZ04 and YSZ20, and three of the 15 independent simulations.

YSZ	Sim.	a Å	L_{qq} 10^6 WK/m	L_{00} $10^{-6} \text{ mol}^2 \text{ K}(\text{Jsm})^{-1}$	L_{0q} $\text{molK}(\text{ms})^{-1}$
YSZ04	1	5.148878(76)	6.81(30)	0.85(47)	-0.04(21)
	2	5.148736(78)	7.33(25)	0.80(63)	-0.06(16)
	3	5.148756(76)	7.16(26)	0.72(52)	-0.18(21)
YSZ20	1	5.18731(15)	4.31(79)	0.20(51)	-0.05(38)
	2	5.18697(18)	4.87(52)	0.23(57)	-0.10(37)
	3	5.18728(17)	4.30(88)	0.15(58)	-0.04(26)

The calculated values for each independent simulation show high errors. However, this does not mean that a mean value cannot be built with reliable statistics. To demonstrate this, the two-sided null hypothesis, $H_{01}: X = X_0$ vs. $H_{11}: X \neq X_0$ at the significance level $\alpha = 0.05$ and type 2 error $\beta = 0.1$ for $X = a, L_{ij}$, is tested by calculating the sample size with the procedure described in the SI of Paper III. This results in a sample size larger than 9 independent simulations. Therefore, the hypothesis H_{01} cannot be rejected, and despite, e.g., the differences in the calculated values for L_{Oq} between the single simulations, one may regard the calculated means from 15 independent simulations for a and L_{ij} as estimates for the averages of these quantities.

3.1.4 Calculation of the Electrostatic Potential

As it is stated in Paper II, the MD open source package LAMMPS (Plimpton, 1995) calculates the Coulomb energy of the system avoiding the explicit calculation of the electrostatic potential for each ion with the Ewald sum because this would be computationally expensive. Therefore, the Fortran 95 algorithms given by M. P. Allen and D. J. Tildesley (Allen, 2017) are extended for the calculation of the electrostatic potential from the simulated system's trajectory. The resulting algorithms can be found in the Appendix. Since algorithms for the calculation of the Coulomb energy via the Ewald sum are standard, this discussion is limited to specific iterations describing the particularities regarding the calculation of $\varphi^{R,*}$ and $\varphi^{K,*}$.

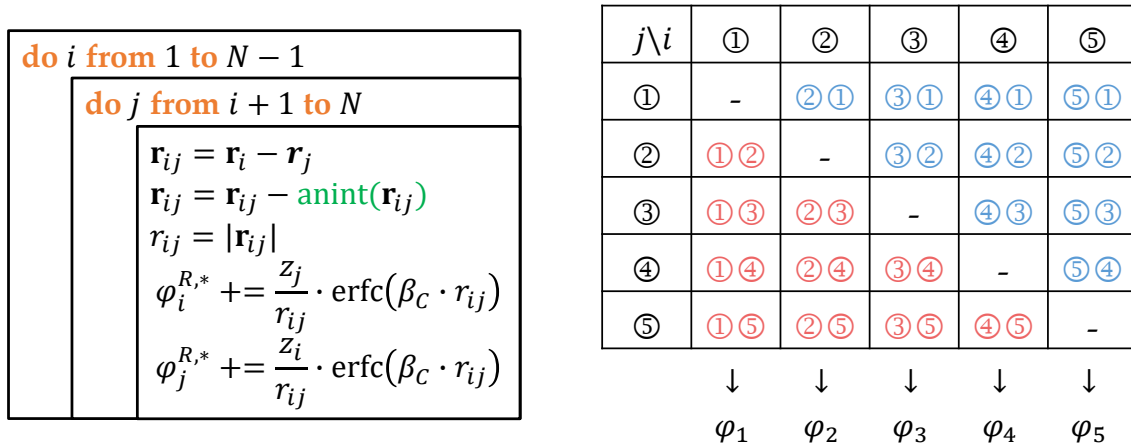


Figure 3-3. (left) Nassi-Schneidermann diagram (NSD) for the main do-loops in the calculation of the short-range contribution of the electrostatic potential $\varphi_i^{R,*}$ using the *phiR* subroutine (see Appendix). (right) Graphical representation of the calculation steps corresponding to the NSD.

The Fortran 95 subroutine *phiR* is used for the calculation of the short-range contribution of the electrostatic potential $\varphi^{R,*}$ (see Eq. (2-24)). In the subroutine, the positions of the point charges are normalized with the length of the

simulation box, resulting in a dimensionless position ranging from 0 to 1. Aside from the point charge position vector \mathbf{r} and the valence z , the Ewald parameter β_C is also necessary for the calculation. The main calculation of the short-range electrostatic potential comprises two do-loops given in the subroutine between line 32 and line 55 and in the Nassi-Schneiderman diagram (NSD) in Figure 3-3 (left). The first do-loop runs from point charge $i = 1$ up to point charge $N - 1$, while the second loop runs from point charge $j = i + 1$ up to point charge N . In the second loop, the distance vector \mathbf{r}_{ij} between the point charges i and j is calculated. The vector \mathbf{r}_{ij} is then corrected accounting for the minimum particle image convention using the Fortran 95 function *anint()*, which rounds a number to the next highest integer. Afterwards, the Euclidean length r_{ij} of the distance vector \mathbf{r}_{ij} is calculated. Finally, the sum in Eq. (2-24) is done for $\varphi_i^{R,*}$ and for $\varphi_j^{R,*}$. The graphical representation of the calculation using these two do-loops is given in Figure 3-3 (right) for the case of five point charges. In this way, the double calculation of the contributions is avoided and the calculation method is faster than a brute force alternative.

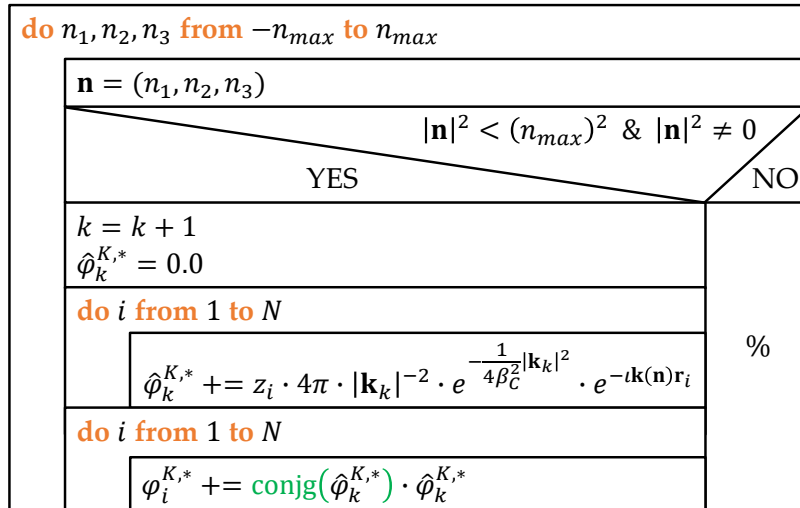


Figure 3-4. Nassi-Schneidermann diagram (NSD) for the calculation of the long-range contribution of the electrostatic potential $\varphi_i^{K,*}$.

In Figure 3-4, the NSD diagram for the calculation of Eq. (2-29) and Eq. (2-30) in the subroutine *phiK* (from line 81 to line 105) is depicted. Here, the necessary input parameters are the position and the valence of the point charges, as well as the Ewald parameter β_C and the maximum number of \mathbf{k} -vectors. The variables n_1 , n_2 and n_3 run along the three coordinates of the \mathbf{k} -vectors. Together with the variable k , they have the task of calculating the outer sum in Eq. (2-29). The assignment of the \mathbf{k} -vectors in a previous subroutine *kVector* explains the differentiation in these two variables: the terms depending on the pre-defined vectors run over the variable k and the terms first appearing in the subroutine *phiK* run over the variable n_i . The inner sum in Eq. (2-29) is calculated within the

second do-loop and the reverse Fourier transformation in Eq. (2-30) is calculated within the third do-loop.

The validation of the developed algorithms is given in Paper II. As discussed therein, the Ewald parameter β_C and the maximum number of \mathbf{k} -vectors are estimated for a given relative accuracy via a computational optimization procedure implemented in LAMMPS (see (Isele-Holder, 2012)). To be consistent with the simulation conducted using this package, the same values are used for the calculation of the electrostatic potential from the system trajectory.

Finally, Table 3-5 contains sample data from single simulations for the calculated electrostatic potential of the ions in YSZ04 and YSZ20 at different temperatures. These values are representative for all other calculated values. The similar order of magnitude of the errors proves the repeatability of the simulations. Here, the hypothesis $H_{02}: X = X_0$ vs $H_{12}: X \neq X_0$ is tested at the significance level $\alpha = 0.05$ and type 2 error $\beta = 0.1$ for $X = \varphi_i$, resulting in a sample size larger than six simulations. Therefore, our assumption that the mean electrostatic potential φ_i from ten independent simulations can be used as an estimate of φ_i cannot be rejected.

Table 3-5. Calculated electrostatic potential φ_i for O^{2-} , Zr^{4+} and Y^{3+} for three of the ten independent simulations for YSZ04 and YSZ20 at 1100 K and 1500 K.

i	Sim.	$T = 1100 \text{ K}$		$T = 1500 \text{ K}$	
		φ_i^{YSZ04} in eV	φ_i^{YSZ20} in eV	φ_i^{YSZ04} in eV	φ_i^{YSZ20} in eV
O^{2-}	1	23.2829(27)	23.3175(17)	23.3276(22)	23.3374(24)
	2	23.2775(24)	23.2866(22)	23.3252(26)	23.3279(30)
	3	23.2807(21)	23.3030(23)	23.3289(31)	23.3334(21)
Zr^{4+}	1	-42.4890(26)	-42.4241(18)	-42.3721(22)	-42.3050(25)
	2	-42.4930(22)	-42.4202(19)	-42.3716(28)	-42.2907(31)
	3	-42.4953(20)	-42.4183(35)	-42.3711(30)	-42.2939(25)
Y^{3+}	1	-32.0861(43)	-32.5254(24)	-31.9956(47)	-31.4106(57)
	2	-32.0992(47)	-31.5651(22)	-32.0078(42)	-31.4546(38)
	3	-32.0648(47)	-31.5478(24)	-31.9616(43)	-31.4311(25)

3.2 SOFC 1D NET Model

The equations and assumptions describing the SOFC NET model are given in detail in Paper IV. In this study, the SOFC is modelled only in the spatial dimension y , which is defined perpendicular to the active area of the SOFC from the anode to the cathode. The Matlab[®] routine along with all necessary functions can be found in the Appendix. Figure 3-5 contains its NSD. This routine does not include the calculation of the entropy production, which is calculated in a post-processing procedure using modified functions to recalculate and separately record the thermodynamic forces.

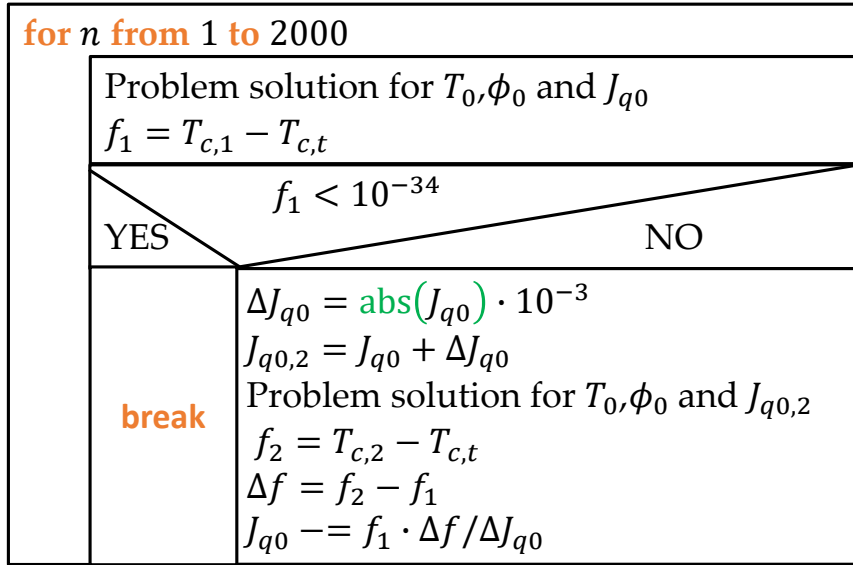


Figure 3-5. NSD diagram of the Matlab® model presented in Paper IV. The quantities labeled with the index 0 are defined at $y = 0$ and the quantities labeled with the index with c at $y_c = \Delta y_a + \Delta y_e + \Delta y_c$.

The algorithm centers on the implemented Newton-Raphson iteration. The main goal is to find the heat flux J_{q0} at $y = 0$ (see Figure 3-6) so that the temperature $T_c = T(y_c)$ at $y_c = \Delta y_a + \Delta y_e + \Delta y_c$ is equal to the target temperature $T_{c,t}$, i.e., to find the solution for equation $T_{c,t} = T_c(J_{q0})$.

Since the Newton-Raphson method solves for the root of a function, it is suitable to define the absolute deviation function as $f = T_c - T_{c,1} = f(J_{q0})$ and use the iteration method on this function. Solutions for this problem result from the well-known iteration given by

$$J_{q0}^{n+1} = J_{q0}^n - \frac{f(J_{q0}^n)}{f'(J_{q0}^n)} \quad (3-2)$$

until $f \approx 0$. While $f(J_{q,0}^n)$ can be calculated from the temperature T_0 , the potential ϕ_0 and an initial (random) value $J_{q,0}^n$ at $y = 0$, the value $f'(J_{q,0}^n)$ remains yet unknown. To solve this issue, the definition of the derivative

$$f'(J_{q0}) = \lim_{J_{q0,2}^n - J_{q0}^n} \frac{f(J_{q0,2}^n) - f(J_{q0}^n)}{J_{q0,2}^n - J_{q0}^n} \quad (3-3)$$

is used with a difference $\Delta J_{q,0}^n = J_{q,0,2}^n - J_{q,0}^n$ small enough to approximate the limit. Using this value, the solution of the problem for $J_{q,0,2}^n$, i.e., the value $f(J_{q0,2}^n)$, and with it the derivative in Eq. (3-3) can be estimated to calculate the value J_{q0}^{n+1} from Eq. (3-2) for the next Newton-Raphson iteration.

The results of the SOFC 1D NET model are given in detail in section 3 of Paper IV. The interaction of the papers and the overall picture of these contributions is shown and discussed in the next chapter.

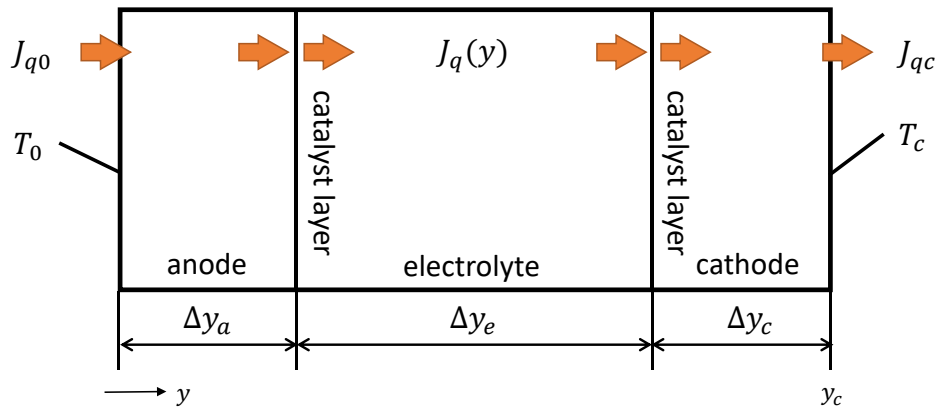


Figure 3-6. Simplified representation of the SOFC model. In this representation, the heat flux J_q as well as the initial and boundary conditions for the temperature $T_c = T(y_c)$ and $T_0 = T(y = 0)$ are included. A more detailed representation of the SOFC model can be found in Figure 2 of Paper IV.

4. Summary and Interaction of Publications

4.1 Paper I

Paper I is entitled *A phenomenological study of yttria-stabilized zirconia at 1300 K with the Green-Kubo formulation and equilibrium molecular dynamics*. Its main goal is the study of the heat and ionic transport in YSZ at 1300 K and zero pressure using NET and linear response theory. For this aim, the ACFs and CCFs of the fluxes are analyzed and phenomenological coefficients are calculated as a function of the Y_2O_3 concentration.

4.1.1 Author Contributions

The candidate conceived the idea and the theoretical background. He developed the LAMMPS (Plimpton,1995) routines and conducted the MD simulations and the validation. Two independent evaluations of the computational data were carried out: one using Fortran 95 and one using Matlab®. The candidate performed the Fortran 95 data evaluation and A. Kelle performed the Matlab® data evaluation under his supervision. The candidate wrote and revised the paper. He made the figures together with A. Kelle. Prof. S. Kabelac supervised the work and all authors approved the last version of the paper.

4.1.2 Summary

In metal oxides, only heat transport, ionic transport and electronic transport are present. Especially for YSZ, only anion diffusion occurs at 1300 K, so that only the descriptions of the heat flux and of the anion flux are of relevance when additional effects like polarization are neglected. Under these assumptions, only three independent phenomenological coefficients L_{qq} , L_{OO} and L_{qO} are needed to describe the kinetics of the system. While the time integration of the ACF of the micro heat flux \mathbf{J}_q and of the micro anion flux \mathbf{J}_O provides the values for the conductivities L_{qq} and L_{OO} , respectively, the integration over time of the CCF between both micro fluxes provides a value for the conductivity L_{qO} . The micro fluxes are calculated using the system trajectory from EMD simulations in the NVT ensemble with the density at zero pressure.

The integral of the total ACF for the estimation of L_{qq} is averaged in a time interval to assure reliable statistics. The average values of L_{qq} calculated with this method show a decreasing progression of this conductivity as the Y_2O_3 concentration increases. This behavior results from the longer relaxation time of the ACF for higher vacancy concentrations due to the larger range of motion of the anions. Furthermore, while the Coulomb contribution of the ACF of the heat flux is the highest, the kinetic contribution is negligibly small. The Coulomb and virial contributions each surpass the total ACF in size, but they flow in opposite

directions and, thus, the partial CCFs of both contributions result in the lower values for the total ACF.

The values for the conductivity L_{00} calculated with the method proposed above display a maximum between YSZ04 and YSZ08 if a negligible conductivity of ZrO_2 is assumed. This maximum results from the ACF progression, which adapts to an optimum of the positive area under the curve. A high number of vacancies result in a high mobility of the anions, but the collective motion is affected due to the decreased number of anions. Therefore, the activation energy necessary to avoid a back-jump to their initial position is not provided. The combination of both mechanisms results in this characteristic maximum of the conductivity L_{00} .

To calculate values for the conductivity L_{0q} , the time integral of the CCF of the micro heat flux and the micro anion flux is averaged with the method proposed above. The progression of the CCF mainly shows a Dufour-type behavior, but a Soret-type mechanism is also noticeable for lower Y_2O_3 concentrations. The calculated values for L_{0q} experience a minimum between YSZ08 and YSZ12. This minimum results from the combination of the heat transported with anions jumping back to their initial position and the heat transported with the anions diffusing to adjacent vacancies. The heat flux due to the Coulomb contribution is the highest and flows opposite to the micro anion flux, whereas the heat flux due to the virial contribution flows in the same direction. Due to this interplay between the heat flux and the anion flux, the minimum of L_{0q} does not arise at the same concentration as the maximum of L_{00} .

Empirical coefficients are estimated using the calculated phenomenological coefficients. The EMD results from this study overestimate the experimental thermal conductivity λ , but the discrepancies to NEMD results from literature studies with the same FF are lower than $0.35 \text{ mW}/(\text{mK})$. These latter discrepancies can be accounted for by the partial enthalpies of the anions, as these are not considered in the calculation of λ . Due to the application of a simple conversion rule, the diffusion coefficient from the EMD calculations cannot be compared with experimental data or with the MSD diffusion coefficient reported in the literature. Finally, the calculated values for the Seebeck-coefficient agree well with the experimental values reported in the literature for a mole fraction $x_{Y_2O_3}$ of up to 0.08.

To the knowledge of the candidate, this is the first work reporting such an extensive phenomenological study for different YSZ compositions and explaining the transport mechanisms for this compound using linear response theory.

4.1.3 Additional Discussion

In Paper I, the errors of the calculated lattice constant and phenomenological coefficients in YSZ are estimated with the corrected sample standard deviation. A better way to estimate the error is described in Paper III, where the errors are estimated assuming a one-sided Student's distribution given by a 95 % confidence interval. The results provided with the error from the new estimation are summarized in Table A1 of the Appendix. The errors calculated in this manner are lower than the errors calculated with the corrected sample standard deviation. With this new error estimation, it can be said with a 95 % confidence, e.g., that the coefficient L_{Oq} is negative for the studied YSZ compositions. Such a statement is not possible using the results reported in Paper I, because, e.g., for the YSZ16 and YSZ24, the estimated errors are higher than the mean values of L_{Oq} . Further, the Nernst-Planck diffusion coefficient can be calculated as described in the SI of Paper III. These further results for the Nernst-Planck diffusion coefficient are given in Table 4-1 for different YSZ compositions at 1300 K.

Table 4-1. Calculated Nernst-Planck diffusion coefficients for different YSZ compositions at 1300 K.

YSZ	YSZ04	YSZ08	YSZ12	YSZ16	YSZ20	YSZ24
D_o in $10^{-11} \text{ m}^2/\text{s}$	6.47(38)	5.56(39)	3.75(29)	2.66(19)	1.85(31)	1.38(21)

4.2 Paper II

Paper II has the title *Approach to the Coulomb Contribution of Thermodynamic Properties from the Mean Electrostatic Potential of the Ions in $(\text{ZrO}_2)_{1-x}(\text{Y}_2\text{O}_3)_x$* . Its aim is to provide a thermodynamic framework to the electrostatic potential by defining it using state variables of the electroneutral compounds in the mixture and relating it to the Coulomb contribution of other thermodynamic quantities.

4.2.1 Author Contributions

The candidate conceived the idea and the theoretical background. He developed the MD LAMMPS (Plimpton,1995) routines and conducted the MD simulations. The Fortran 95 algorithms for the electrostatic potential and the numerical validation were done with the kind help of M. Siemen under the supervision of the candidate. Again, two independent equivalent evaluations of the computational data were carried out: one using Fortran 95 and one using Matlab®. The candidate performed the Fortran 95 data evaluation and M. Siemen performed the Matlab® data evaluation. The candidate wrote the paper. He made all figures, except for figure 4, which was done together with M. Siemen. The

candidate revised the paper. Prof. S. Kabelac supervised the work and all authors approved its last version.

4.2.2 Summary

The electric contribution $z_i e \Phi$ appearing in the electrochemical potential is often assumed to be the electrostatic potential. However, electrostatics may not be compatible with classical thermodynamics. Therefore, a new quantity ψ_j is introduced and used instead of Φ to cover this lack.

The classical Coulomb energy U_C calculated from the electrostatic potential φ_i of the ions in a mixture can be seen as an extensive thermodynamic property, since it is a first order homogeneous function of other extensive properties and it is additive. However, systems consisting solely of ions of a single species are not thermodynamically stable. Therefore, the Coulomb energy in mixtures cannot be defined as a generalization of pure (instable) ionic systems without any thermodynamic inconsistency. The proposed quantity ψ_j is defined for electroneutral compounds in the mixture. Pure systems consisting of each of these electroneutral *molecules* may be stable. This so-defined quantity ψ_j should be equal to the *partial* molecular Coulomb Gibbs energy of the system, as can be derived from the fundamental equation of state. It is not necessarily equal to the electrostatic potential φ_j of the *molecules*, since this latter quantity is given by the partial molecular Coulomb internal energy. From a MC simulation in the μ VT-ensemble, the quantities ψ_j can be calculated and, applying a Maxwell relation, can be related to other thermodynamic Coulomb properties like the Coulomb entropy. In YSZ, the quantities $\psi_{Y_2O_3}$ and ψ_{ZrO_2} can be defined. Since these quantities cannot be easily calculated from EMD, the electrostatic potentials $\varphi_{Y_2O_3}$ and φ_{ZrO_2} , i.e., the partial molecular Coulomb energies, are calculated instead.

For this aim, the electrostatic potentials of the single ions φ_O , φ_{Zr} and φ_Y are calculated for different YSZ compositions at 1100 K, 1300 K and 1500 K. The calculated electrostatic potential of the anions has a maximum for YSZ12; the electrostatic potential of the cations increases with the Y_2O_3 concentration. This behavior results from the combined effect of the number of anions, their local density, the lattice constant, the number of Y^{3+} -cations and the temperature. The calculated Coulomb energy from an *ab initio* study from the literature agrees well with this study's extrapolated value for YSZ14, which corroborates that neglecting the polarization and multipole interactions in the calculation is valid.

The Coulomb internal energy per molecule shows a quantifiable excess part. This real behavior results from the high mobility of the ions in the system due to an increasing vacancy concentration. Therefore, it is possible to calculate the electrostatic potentials φ_{ZrO_2} and $\varphi_{Y_2O_3}$ from a tangent construction using the values of the Coulomb internal energy per molecule. Furthermore, mixing rules

for the calculation of these quantities from the potential of the single ions φ_O , φ_{Zr} and φ_Y are provided, which show equivalent results to the values calculated from the tangent construction. From a similar study, but for the quantities ψ_{ZrO_2} and $\psi_{Y_2O_3}$ estimated using MC calculations in the μ VT-ensemble, it may be possible to calculate other thermodynamic properties in YSZ, such as the Coulomb entropy S_C , directly from the electrostatic potential of the ions.

Using the electrostatic potential of the molecules, the anionic conduction in YSZ can be expressed with the molecular conductivities κ_{ZrO_2} and $\kappa_{Y_2O_3}$, which describe the anion distribution to form electroneutral molecules in the system. Since the quantities ψ_j are thermodynamically consistent, a direct approach to the thermodynamic factor and, thus, to the Fick conductivities is possible in this novel framework.

4.2.3 Additional Discussion

Analogous to the further discussion of the results of Paper I (see above), a new estimation for the error of the electrostatic potential of the ions φ_i is conducted using the methodology given in Paper III. The results provided with the errors from this new estimation are given in Table A2 in the Appendix.

In Paper II it is stated: "The values of φ_O for Y_2O_3 can even be considered as temperature-independent within the uncertainty range". To statistically prove that this assumption may not be rejected, the hypothesis $H_{03}: \bar{\varphi}_O|_{1100\text{ K}}^{1500\text{ K}} = \varphi_O(T)$ is tested against the hypothesis $H_{13}: \bar{\varphi}_O|_{1100\text{ K}}^{1500\text{ K}} \neq \varphi_O(T)$. The detailed test can be found in the Appendix, where it is concluded that the hypothesis H_{03} cannot be rejected.

Furthermore, Paper II lacks some physical background regarding the new mixing rules developed by the candidate in Eq. (24) and Eq. (25) of this paper. This chapter is dedicated to filling this gap. The starting point is the comparison of the Coulomb internal energy given in Paper II by Eq. (18) written as

$$2e^{-1} \cdot U_C = N_{Zr}z_{Zr}\varphi_{Zr} + N_Yz_Y\varphi_Y + N_Oz_O\varphi_O \quad (4-1)$$

and by Eq. (19) written as

$$2e^{-1} \cdot U_C = N_{Zr}(z\varphi)_{ZrO_2} + \frac{1}{2}N_Y(z\varphi)_{Y_2O_3} \quad (4-2)$$

with the equalities $N_{Y_2O_3} = N_Y/2$ and $N_{ZrO_2} = N_{Zr}$. The contributions of the electrostatic potential of the molecules $(z\varphi)_{ZrO_2}$ and $(z\varphi)_{Y_2O_3}$ to the Coulomb internal energy may be given by the superposition of the electrostatic potentials of their constituents

$$N_{Zr}(z\varphi)_{ZrO_2} = N_{Zr}z_{Zr}\varphi_{Zr} + \gamma N_Oz_O\varphi_O, \quad (4-3)$$

$$\frac{1}{2}N_Y(z\varphi)_{Y_2O_3} = N_Y z_Y \varphi_Y + (1 - \gamma)N_O z_O \varphi_O, \quad (4-4)$$

where $\gamma \in [0,1]$ describes the contribution of the electrostatic potential φ_O to the electrostatic potential $(z\varphi)_{ZrO_2}$. Clearly, the contribution of φ_O to $(z\varphi)_{Y_2O_3}$ should be equal to $1 - \gamma$. This definition also considers that the addition of Eq. (4-3) and Eq. (4-4) results in Eq. (4-1) and Eq. (4-2).

The proportion γ should be given by the probability of *finding an anion in an oxygen site in YSZ together with a ZrO₂ molecule in YSZ*, i.e., by the joint probability $\gamma = \Pi(O \cap ZrO_2)$. This probability is given as the product of the conditional probability $\Pi(O|ZrO_2)$ of *finding an oxygen anion in an oxygen site in YSZ under the condition of previously finding a ZrO₂ molecule in YSZ* and the probability $\Pi(O)$ of *finding an oxygen anion in an oxygen site in YSZ*:

$$\Pi(O \cap ZrO_2) = \Pi(O|ZrO_2) \cdot \Pi(O). \quad (4-5)$$

The probability $\Pi(O)$ is given by

$$\Pi(O) = \frac{N_O}{N_O + N_V}, \quad (4-6)$$

where the maximum number of possible oxygen sites in the YSZ crystal framework is given by the number of oxygen atoms N_O and the number of vacancies N_V . This sum is constant and equal to the number of anions in pure ZrO₂, i.e., $N_O + N_V = N_O(ZrO_2)$. Moreover, the probability $\Pi(ZrO_2)$ of *finding a ZrO₂ molecule in YSZ* is given by

$$\Pi(ZrO_2) = \frac{N_{Zr}}{N_{Zr} + N_Y/2} = \frac{N_{Zr}}{N_{YSZ}}, \quad (4-7)$$

where the definition for N_{YSZ} given in Paper II is used. Applying the Gibb's phase rule to the YSZ system results in four degrees of freedom. The values in Eq. (4-3) and Eq. (4-4) are defined for a constant pressure and a constant temperature, so that only two degrees of freedom remain. This means that the number of Zr⁴⁺ cations N_{Zr} and the number of O²⁻ anions N_O are theoretically independent of each other. The probability $\Pi(ZrO_2)$ is defined with N_{Zr} in Eq. (4-7). Therefore, the conditional probability $\Pi(O|ZrO_2)$ should be equal to the probability $\Pi(ZrO_2)$ (see, e.g., (Hartung,2005)). It follows for the proportion γ :

$$\gamma = \Pi(O \cap ZrO_2) = \Pi(ZrO_2)\Pi(O) = \frac{N_{Zr}}{N_{YSZ}} \cdot \frac{N_O}{N_O(ZrO_2)}. \quad (4-8)$$

If this proportion is combined with Eq. (4-3) and Eq. (4-4), it results in Eq. (24) and Eq. (25) of Paper II, respectively. The term $1 - \gamma = 1 - \Pi(O \cap ZrO_2)$ may be expressed with the probability $\Pi(O \cap Y_2O_3)$ of *finding an oxygen anion in YSZ together with an Y₂O₃ molecule*:

$$\Pi(\text{O} \cap \text{Y}_2\text{O}_3) = \frac{1}{2} \frac{N_Y}{N_{YSZ}} \cdot \frac{N_O}{N_O(\text{ZrO}_2)}. \quad (4-9)$$

To show that such an expression is possible, the element balance $N_{YSZ} = N_{Zr} + N_Y/2$ is implemented in Eq. (4-8) to calculate $1 - \gamma$:

$$1 - \gamma = 1 - \left(1 - \frac{1}{2} \frac{N_Y}{N_{YSZ}}\right) \cdot \Pi(\text{O}) = 1 - \Pi(\text{O}) + \Pi(\text{Y}_2\text{O}_3)\Pi(\text{O}), \quad (4-10)$$

where $\Pi(\text{Y}_2\text{O}_3) = N_Y/(2N_{YSZ})$, analogous to the definition of $\Pi(\text{ZrO}_2)$. Following the discussion above, the number of Y^{3+} -cations and O^{2-} -anions are independent of each other and, thus, the joint probability $\Pi(\text{O} \cap \text{Y}_2\text{O}_3)$ should be equal to $\Pi(\text{Y}_2\text{O}_3)\Pi(\text{O})$. Moreover, the probability of *finding an oxygen vacancy in an oxygen site in YSZ* is given by $\Pi(\text{V}_\text{O})$ and should be equal to $1 - \Pi(\text{O})$. It follows:

$$1 - \gamma = \Pi(\text{V}_\text{O}) + \Pi(\text{O} \cap \text{Y}_2\text{O}_3). \quad (4-11)$$

What does the sum of these probabilities mean? To give Eq. (4-11) a more physical background, we can define the probability $\Pi(\text{V}_\text{O} \cup (\text{O} \cap \text{Y}_2\text{O}_3))$ of *finding a vacancy in YSZ or of finding an oxygen anion together with a Y_2O_3 molecule in YSZ* as follows:

$$\Pi(\text{V}_\text{O} \cup (\text{O} \cap \text{Y}_2\text{O}_3)) = \Pi(\text{V}_\text{O}) + \Pi(\text{O} \cap \text{Y}_2\text{O}_3) - \Pi(\text{V}_\text{O} \cap (\text{O} \cap \text{Y}_2\text{O}_3)). \quad (4-12)$$

This probability is equal to the sum in Eq. (4-11), because the joint probability $\Pi(\text{V}_\text{O} \cap (\text{O} \cap \text{Y}_2\text{O}_3))$ is zero due to the mutual exclusion of $\Pi(\text{O})$ and $\Pi(\text{V}_\text{O})$. Therefore, it follows:

$$1 - \gamma = \Pi(\text{V}_\text{O} \cup (\text{O} \cap \text{Y}_2\text{O}_3)) = \frac{N_V}{N_O(\text{ZrO}_2)} + \frac{1}{2} \frac{N_Y}{N_{YSZ}} \frac{N_O}{N_O(\text{ZrO}_2)}. \quad (4-13)$$

The probability $\Pi(\text{V}_\text{O} \cup (\text{O} \cap \text{Y}_2\text{O}_3))$ is 1 for pure Y_2O_3 , meaning that in this system only vacancies or oxygen atoms belonging to Y_2O_3 molecules can be found. For lower Y_2O_3 concentrations, the oxygen anions corresponding to ZrO_2 reduce this probability. For completeness, the mixing rules given in Eq. (24) and in Eq. (25) of Paper II are written here again using the defined probabilities:

$$(z\varphi)_{\text{ZrO}_2} = z_{\text{Zr}}\varphi_{\text{Zr}} + \Pi(\text{O} \cap \text{ZrO}_2) \frac{N_O}{N_{\text{Zr}}} z_{\text{O}}\varphi_{\text{O}}, \quad (4-14)$$

$$(z\varphi)_{\text{Y}_2\text{O}_3} = 2 \left[z_{\text{Zr}}\varphi_{\text{Zr}} + \Pi(\text{V}_\text{O} \cup (\text{O} \cap \text{Y}_2\text{O}_3)) \frac{N_O}{N_Y} z_{\text{O}}\varphi_{\text{O}} \right], \quad (4-15)$$

with $1 = \Pi(\text{O} \cap \text{ZrO}_2) + \Pi(\text{V}_\text{O} \cup (\text{O} \cap \text{Y}_2\text{O}_3))$. This latter condition has the character of a Gibbs-Duhem equation because it couples the probabilities $\Pi(\text{ZrO}_2)$ and $\Pi(\text{Y}_2\text{O}_3)$, thereby reducing the degrees of freedom of the system. While the contribution of φ_{O} to $(z\varphi)_{\text{ZrO}_2}$ is solely given by the probability $\Pi(\text{O} \cap \text{ZrO}_2)$, the contribution φ_{O} in $(z\varphi)_{\text{Y}_2\text{O}_3}$ is not only given by $\Pi(\text{O} \cap$

Y_2O_3), but also by the probability $\Pi(\text{V}_\text{O})$ of finding a vacancy in an oxygen site in YSZ.

4.3 Paper III

Paper III has the title *A Diffusivity Study of $(\text{Sc}_2\text{O}_3)_{0.1}(\text{CeO}_2)_{0.01}(\text{ZrO}_2)_{0.89}$ between 1100 and 1500 K at Zero Pressure with Molecular Dynamics*. Its goal is to provide, to the best of the candidate's knowledge, for the first time numerical data for structural properties and different ionic conduction transport coefficients for the relevant SOFC electrolyte compound 10Sc1CeSZ.

4.3.1 Author Contributions

The candidate conceived the idea and the theoretical background. He developed the MD LAMMPS (Plimpton,1995) routines and conducted the MD simulations. Two independent evaluations of the computational data were carried out too: one using Fortran 95 and one using Matlab®. The candidate performed the Fortran 95 data evaluation and L. Reus performed the Matlab® data evaluation under his supervision. The candidate wrote the paper, revised it and made the figures. Prof. S. Kabelac supervised the work and all authors approved the last version of the paper.

4.3.2 Summary

Experimental data regarding the structural, electrical and mechanical properties of the material 10Sc1CeSZ and its aging behavior can be found in the literature. However, to the knowledge of the candidate, no computational studies of this compound are available.

In this study, the lattice constant is calculated for this material at different temperatures using EMD. The results agree well with data obtained from experiments, despite the relative deviation of the CTE at 1100 K. The radial distribution functions (RDFs) for the ion pairs Ce-O, Sc-O, Zr-O and O-O are calculated. From the results, the doping of cerium is seen to create a shifting of the oxygen anions from their tetrahedral site. Moreover, the coordination number for Ce-O is the largest in comparison to the coordination numbers of Zr-O and Sc-O, due to the larger ionic radius of Ce. Despite the different progressions of the RDFs for Sc-O and Zr-O, the coordination numbers are similar. Moreover, all coordination numbers decrease for higher temperatures.

The Brownian diffusion coefficient D_O^{MSD} is calculated from the MSD of the anions. These calculated values are transformed to determine the Brownian diffusion coefficient of the vacancies D_V^{MSD} . The tracer diffusion coefficient D_O^* is also calculated from these values and the geometrical correlation factor. The resulting activation energy is equal for all MSD diffusivities. To the best of the candidate's knowledge, no experimental data for these diffusivities is available in the literature.

The average of the integral of the ACF of the micro anion flux using the method reported in Paper I provides values for the ionic conductivity, as well as values for the Nernst-Planck diffusivities for different temperatures. The simulated activation energies for both quantities are almost equal and agree well with the experimental value for the activation energy of the bulk ionic conductivity from the literature. The calculated values of the ionic conductivity are higher than the experimental data reported in the literature. However, the relative deviation between the different experimental values is similar to the relative deviation between them and the calculated values, so that the approach may be considered as effective as the experimental measurement. Since the MSD of the anions is proportional to their VACF and the VACF is part of the micro anion flux (see section 2.2.1), there is a high probability that the MSD diffusivities calculated in this study predict the ionic transport as effectively as the ionic conductivities do.

4.4 Paper IV

Paper IV has the title *Impact of Multi-Causal Transport Mechanisms in an Electrolyte Supported Planar SOFC with $(\text{ZrO}_2)_{x-1}(\text{Y}_2\text{O}_3)_x$ Electrolyte*. Its aim is to show the relevance of considered multi-causal transport mechanisms in the electrolyte for the prediction of the temperature and the electric potential profile, as well as the heat flux and the entropy production across an SOFC.

4.4.1 Author Contributions

The author contributions are well described in the paper itself. Here, to be more precise, a clarification has to be made. The candidate did the calculation of the activation energy and the pre-exponential factor from the Arrhenius plot of the experimental data for the exchange current density and for the specific electrolyte resistance. Aside from this, the experimental work was done by T. Marquardt and P. Radici. Therefore, this experimental work may not be considered to be part of this thesis and, thus, more details or discussion about the experiments or their background beyond what is described in Paper IV will not be provided here.

4.4.2 Summary

The transport mechanisms across an electrolyte supported planar SOFC are simulated with a 1D NET model. This model is divided into five domains: three bulk layers (an inert anode GDL, an inert cathode GDL and the electrolyte) and two interfaces (the anode and cathode CLs). The spatial coordinate for the 1D calculation is defined perpendicular to the cell active area from the anode GDL to the cathode GDL. The transport mechanisms in the GDLs are calculated accounting for thermal conduction, a Peltier mechanism and gas diffusion. The CLs are threatened as a separate layer from the GDL for each electrode. They are

calculated isothermally with the Nernst equation and the Butler-Volmer approach. The Arrhenius equation for the exchange current density is parameterized with this study's experimental data. The transport in the electrolyte is calculated using the phenomenological coefficients from Paper I, and the SOFC is modelled on the basis of the phenomenological equations as given by NET, which is one of the novelties of this study.

The model is successfully validated with experimental data for the E, j -characteristic, meaning that the parameterization of the Butler-Volmer kinetics used for the description of the CLs is well implemented in the model. Despite the relative deviation of $\sim 10\%$ between the resistance calculated from the conductivity L_{00} and the value calculated using the experimental Arrhenius equation, the model predicts the voltage with a relative deviation of $\sim 1\%$ from the value determined from the curve based on experimental data at 8000 A/m^3 .

The calculated temperature decreases across the GDLs and increases across the electrolyte, experiencing a minimum at the anode and a maximum at the cathode. If the coupled mechanism between anion diffusion and thermal conduction is neglected, the absolute values of the temperature and of the temperature gradients decrease. Furthermore, the temperature gradient is positive across the anode GDL, and the temperature progression shows a maximum across the electrolyte, e.g., for YSZ20. The pronounced temperature gradients for the case where all mechanisms are considered can be explained with a Seebeck contribution, which counters the Ohmic contribution to assure a constant ionic flux.

The electric potentials at the electrodes are given by the equilibrium potential jumps and the activation losses. While the potential gradient across the GDLs is mainly given by the coupled mechanisms, this is not the case for the electrolyte. Since the potential differences across the GDLs are negligibly small, the potential profile is, on the whole, not substantially influenced by the coupled mechanisms.

In agreement with the behavior reported in the literature, the heat flux has a negative jump at the anode CL due to the endothermic reaction and a positive jump at the cathode CL due to the exothermic reaction. For electrolytes with a Y_2O_3 mole fraction higher than $8 \text{ mol}\%$, the heat flows across the electrolyte from a lower to a higher temperature in a non-Fourier conduction behavior. This behavior results from the Seebeck-contribution and is not seen if the coupled mechanisms within the NET approach are neglected. In this latter case, the direction of the net heat flux may not be correctly predicted.

The heat flux contribution of the entropy production $\dot{\sigma}_Q$ across the bulk phases is higher for higher Y_2O_3 concentrations and higher current densities, being the highest for the GDLs. It is negative across the electrolyte for YSZ08 due to the Peltier effect. While simulations neglecting the coupled mechanisms predict a reduction of $\dot{\sigma}_Q$ across the electrolyte to 30% of the initial value at the anode CL, an increase to 150% of this initial value is predicted if the coupled

mechanisms are taken into account. The potential contribution of the entropy production $\dot{\sigma}_\phi$ in the bulk phases becomes higher for higher current densities and higher vacancy concentrations in the electrolyte. While neglecting the coupled mechanisms results in smaller values for $\dot{\sigma}_\phi$ across the GDLs, this is not relevant for the values of $\dot{\sigma}_\phi$ across the electrolyte. Finally, the diffusion contribution $\dot{\sigma}_c$ only depends on the current density and not on the electrolyte composition. For this quantity, there are no appreciable differences between the values from the calculations considering or neglecting the coupled mechanisms.

Finally, the calculated jumps in the entropy production rate only depend on the current density. Accounting for all losses, it is determined that 3 % of the losses in an electrolyte supported SOFC may originate in the GDLs, 73 % in the electrolyte and 24 % in the CLs.

This study is, to the knowledge of the candidate, the first providing a discussion about the relevance and consequences of simulating SOFCs bulk phases, especially the electrolyte, using the NET approach.

4.5 *Interaction of the Publications*

Finally, the interactions of the papers and their contributions to this thesis are to be discussed at this point. In Figure 4-1, a representation of these interactions is depicted. This study has different levels and modelling scales. While the modelling and simulation of the MD studies in Paper I, Paper II and Paper III occur at the nanoscale with systems of ~ 1500 atoms, the SOFC layers are modelled at the microscale in Paper IV. Moreover, YSZ as a material or an electrolyte is analyzed in Paper I, Paper II and Paper IV; 10Sc1CeSZ is only analyzed in Paper III. The MD methodology of Paper I is used for the MD calculation in Paper II and Paper III. Furthermore, for the calculation of the molecular conductivities κ_{ZrO_2} and $\kappa_{Y_2O_3}$ in Paper II, the phenomenological coefficients from Paper I are used.

Moreover and as stated in Paper I, it is difficult to compare the diffusion coefficients for YSZ calculated from the conductivities L_{00} with other values from the literature, due to the conversion rule applied. However, from this phenomenological coefficient, the ionic conductivity can be directly calculated. The results are given in Paper II and a successful validation of the calculated conductivity is done in Paper IV with experimental data for YSZ08.

The connection between Paper I and Paper IV is clear, since the transport mechanisms in the YSZ electrolyte are calculated in the SOFC-model of Paper IV using the phenomenological coefficients from the MD study in Paper I. Moreover, the information given in Paper II and Paper III is used to build the theoretical background of this model. Here, the phenomenological equations in Eq. (40) and Eq. (41) needed to describe the kinetics in the YSZ electrolyte are derived from a more general framework in Eq. (34) to Eq. (36) of Paper IV, respectively. The core of the derivation is based on the assumptions of neglecting

cation diffusion and polarization effects. While the assumption of neglecting cation diffusion can be supported by results reported in the literature, as is mentioned in Paper I, this is not the case for neglecting polarization effects. However, the comparison given in Paper II of the results with density functional theory (DFT) calculations supports this latter assumption. Furthermore, Eq. (14) of the Arrhenius type in Paper IV is not typical at the first glance. The derivation given in Paper III for the ionic conductivity for 10Sc1CeSZ under the point of view of NET provides the theoretical background for this equation. Finally, part of the additional discussion of the results given above concerns the statistical methods appearing in Paper III, but applied in the results of Paper I and Paper II.

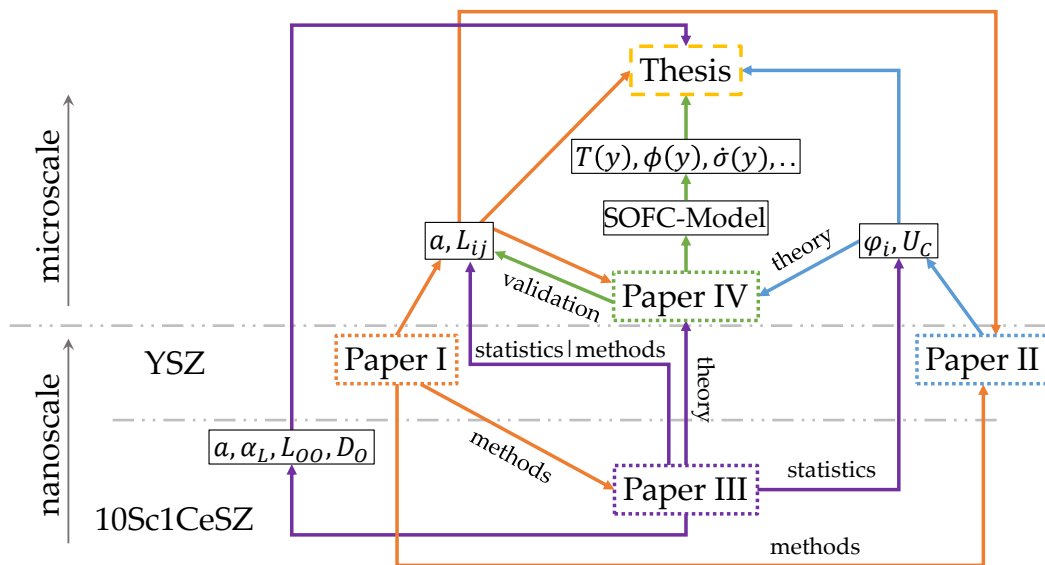


Figure 4-1. Representation of the interaction of the papers and the thesis. The given scale considers only the modelling and simulation of each paper. The direction of the arrows represents the direction of the information flux. E.g., Paper I provides the results for the lattice constant a and the phenomenological coefficients L_{ij} in cubic YSZ, but a new uncertainty analysis of the results is first provided in this thesis using the statistical methods given in Paper III, and so on.

The results in Paper I, II, III and IV as well as the detailed discussion in each paper and the additional discussions above are the main content of this doctoral thesis.

5. Conclusions and Perspectives

The aim of this doctoral thesis is to present a detailed analysis of the transport mechanisms in two electrolyte materials, YSZ and 10Sc1CeSZ, using the general NET approach in order to show the relevance of this ansatz for the modelling of SOFCs.

In the first part of this thesis, MD data for the phenomenological coefficients L_{ij} is provided for different YSZ compositions at 1300 K. The experimental maximum of the ionic conductivity given by the coefficient L_{00} is qualitatively predicted, as is a minimum in the coefficient L_{0q} , which describes the coupled mechanism between the anion flux and the heat flux. The maximum of L_{00} is explained by the combined effect of the high mobility of the anions and the reduced collective motion, both due to a higher vacancy concentration. The minimum of L_{0q} results from the heat transported along with anions jumping back to their initial lattice site and with anions hopping to adjacent oxygen sites. Both mechanisms are explained in this work using linear response theory.

The thermodynamic framework provided in the second study gives thermodynamic consistency to the electric contribution of the electrochemical potential in ionic systems, which is not given if this quantity is assumed to be an electrostatic potential. This framework is based on the definition of electroneutral compounds in ionic systems, and the resulting quantities can be calculated from MC calculations in the μVT -ensemble. A mixing rule, which relates the electrostatic potential of the ions to these new quantities, is developed and tested.

The third study in this thesis also provides calculated values for the ionic conductivity in 10Sc1CeSZ that agree well with experimental data. For the first time, MD data for the Nernst-Planck diffusion coefficient, the tracer diffusion coefficient and the Brownian diffusion coefficient of the anions in this material are reported. A validation of this numerical data is not possible because no experimental data is available. The reliability of the results may be similar to the one reported for the calculated ionic conductivity.

As can be interpreted from the simulation results using the SOFC 1D NET model presented in the last study of this thesis, the temperature, the heat flux and the entropy production may not be well predicted if the coupled mechanisms are neglected. Interestingly, the potential profile, i.e., the $E-j$ -characteristic, is not substantially affected by these coupled transport mechanisms. One can therefore argue that accounting for coupled transport mechanisms is not necessary at all. However, since the thermal processes are strongly influenced by such transport mechanisms, a validation of a SOFC numerical model using solely the $E-j$ -characteristic, as is usually done in the literature, may be risky and insufficient. To assume that simulation results using such standard SOFC models are reliable enough may lead to wrong decisions when planning heating or cooling strategies of SOFCs.

Despite the questions answered in this thesis, some issues are still open regarding each of the studies presented in this work. The study in Paper I could be repeated in simulations with a more accurate FF like the ReaxFF developed by A. C. van Duin et al (2008). Further DFT studies to analyze the electronic transport using the Kubo-Greenwood approach and the coupled mechanism between the electronic and the ionic transport in YSZ could be also conducted. Furthermore, a method for the calculation of the electronic transport in this compound using classical MD and polarizable FFs may be also possible. The methodologies proposed can also be used in the bulk phases of other electrochemical systems, e.g., for the calculation of the transport mechanisms in other solid electrolytes, such as proton conducting perovskites. Such an extensive phenomenological study can be applied to the analysis of the transport mechanisms in electrochemical interfaces, which are part of current research due to the difficulty of examining them experimentally in high detail. Here, not only the coupled mechanisms between heat and ionic transport but also the coupled mechanisms between different electrochemical reactions and reaction steps can be clarified using linear response theory. Dynamical NEMD simulations are also an option to analyze the time at which each transport mechanism begins to relax into the non-equilibrium steady state.

The developed thermodynamic framework given in Paper II can be tested on other binary or ternary metal oxides. Furthermore, MC calculations in the μ VT-ensemble can be done to calculate the electronic contributions of the electrochemical potential and, e.g., the partial molecular Coulomb entropies. Under the assumption that the mixing rules provided have a general character, it is possible to determine different quantities beyond Coulomb contributions. For example, the partial molecular entropies can be calculated for a binary metal oxide by performing a thermodynamic integration. From the coefficient L_{qO} , the transported entropy of the anions could be calculated. With this knowledge and by applying the mixing rules, the entropy of the cations can be determined. Other possibilities are also open. This framework can also be tested for the description of other electrochemical systems like ionic liquids.

Since Paper III contains, to the best of the candidate's knowledge, the first numerical study of $10\text{Sc}1\text{CeSZ}$, more numerical studies for this material can be done to answer the questions that are still open. In this case, a more accurate potential for the description of the properties in this compound, like a ReaxFF or a polarizable potential, is still desirable. Furthermore, if such a potential were available, a more extensive phenomenological study could be done. Here, the calculation of the Fick-diffusion coefficient of the anions can be calculated in addition to the diffusivities presented in Paper III. In this case, the chemical potential of the oxygen anions could be calculated, e.g., using the thermodynamic framework described in Paper II. Since experimental data is only available in the literature for the ionic conductivity and the lattice constant,

future numerical studies may provide valuable estimates for other transport coefficients or other thermodynamic properties.

The model presented in Paper IV can be extended with new experimental or numerical data for the transport mechanisms in each layer. Here, thermodiffusion in the GDLs or coupled reaction mechanisms in the CLs are examples of effects not considered in the model presented in this study, which should be considered in future SOFC models. Furthermore, the dimensionality of the model can be also extended. Here, a computer fluid dynamics (CFD) SOFC model based on NET for the simultaneous description of the gas flow in the gas channels and the transport mechanisms across the cell is a novel possibility. Furthermore, a NET SOFC stack can also be modelled to account for a more realistic temperature field and the resulting thermomechanical stress of the interconnects. While simple NET models could be used for an exergy analysis of SOFC or solid oxide electrolysis cell (SOEC) systems, dynamical NET SOFC models may be used for the calculation of the heating and cooling procedures of SOFCs or SOECs.

References

- Aguilo-Rullan, A.; Atanasiu, M.; Biebuyck, B.; Lymperopoulos, N.; Marengo, C.; Tsimis, D. The Status of SOFC and SOEC R&D in the European Fuel Cell and Hydrogen Joint Undertaking Program. *ECS Trans.* **2017**, *78*, 41-61. DOI: 10.1149/07801.0041ecst
- Ahmad, S.; Ahmad, R.; Bilal, M.; Rehman, N. U. J. DFT studies of thermoelectric properties of R-Au intermetallics at 300 K. *J. Rare Earths* **2018**, *36*, 197-202. DOI: 10.1016/j.jre.2017.08.004
- Akdeniz, Y.; Timurkutluk, B.; Timurkutluk, C. Development of anodes for direct oxidation of methane fuel in solid oxide fuel cells. *Int. J. Hydrogen Energy* **2016**, *41*, 10021-10029.
- Allen, M. P.; Tildesley, D. J. *Computer Simulation of Liquids*. Oxford University Press: Oxford, United Kingdom, **2017**. ISBN: 978-0-19-880319-5
- Amedi, H. R. Control of anode supported SOFCs (solid oxide fuel cells): Part I. mathematical modeling and state estimation within one cell. *Energy* **2015**, *90*, 605-621. DOI: 10.1016/j.energy.2015.07.095
- Araki, W.; Arai, Y. Molecular dynamics study on oxygen diffusion in yttria-stabilized zirconia subjected to uniaxial stress in terms of yttria concentration and stress direction. *Solid State Ionics* **2010**, *181*, 1534-1541. DOI: 10.1016/j.ssi.2010.08.023
- Arima, T.; Yamasaki, S.; Yamahira, K.; Idemitsu, K.; Inagaki, Y.; Degueldre, C. Evaluation of thermal conductivity of zirconia-based inert matrix fuel by molecular dynamics simulation. *J. Nucl. Mater.* **2006**, *352*, 309-317. DOI: 10.1016/j.jnucmat.2006.02.066.
- Atkins, P.; de Paula, J. *Physical Chemistry*; Wiley-VCH: Oxford, United Kingdom, **2006**. ISBN: 0-7167-8759-8
- Aydın, Ö.; Nakajima, H.; Kitahara, T. Reliability of the numerical SOFC models for estimating the spatial current and temperature variations. *Int. J. Hydrogen Energy* **2016**, *41*, 15311-15324. DOI: 10.1016/j.ijhydene.2016.06.194
- Bae, Y.; Lee, S.; Yoon, K. J.; Lee, J.-H.; Hong, J. Three-dimensional dynamic modeling and transport analysis of solid oxide fuel cells under electrical load change. *Energy Convers. Manage.* **2018**, *165*, 405-418. DOI: 10.1016/j.enconman.2018.03.064
- Baehr, H. D.; Kabelac, S. *Thermodynamik. Grundlagen und technischen Anwendungen*; Springer Vieweg: Berlin, Germany, **2016**. ISBN: 978-3-662-49568-1
- Bao, C.; Wang, Y.; Feng, D.; Jiang, Z.; Zhang, X. Macroscopic modeling of solid oxide fuel cell (SOFC) and model-based control of SOFC and gas turbine hybrid system. *Prog. Energy. Convers. Sci.* **2018**, *66*, 83-140. DOI: 10.1016/j.pecs.2017.12.002.

- Barelli, L.; Bidini, G.; Gallorini, F.; Ottaviano, A. An energetic-exergetic comparison between PEMFC and SOFC-based micro-CHP systems. *Int. J. Hydrogen Energy* **2011**, *36*, 3206-3214. DOI: 10.1016/j.ijhydene.2010.11.079
- Beale, S. B.; Choi, H.-W.; Pharoah, J. G.; Roth, H. K.; Jasak, H.; Jeon, D. H. Open-source computational model of a solid oxide fuel cell. *Comput. Phys. Commun.* **2016**, *200*, 15-26. DOI: 10.1016/j.cpc.2015.10.007
- Bednarek, T.; Tsotridis, G. Issues associated with modelling of proton exchange membrane fuel cell by computational fluid dynamics. *J. Power Sources* **2017**, *343*, 550-563. DOI: 10.1016/j.jpowsour.2017.01.059
- Bedoya-Martínez, O. N.; Barrat, J.-L., Rodney, D.; Computation of the thermal conductivity using methods based on classical and quantum molecular dynamics. *Phys. Rev. B.* **2014**, *89*, 014303-1-7. DOI: 10.1103/PhysRevB.89.014303.
- Bell, D. A.; Marcum, J. C. Adapting Three Classic Demonstrations To Teach Radiant Energy Trapping and Transfer As Related to the Greenhouse Effect. *J. Chem. Educ.* **2018**, *95*, 611-614. DOI: 10.1021/acs.jchemed.7b00626.
- Benfenati, F.; Beretta, P. Ergodicity, Maximum Entropy Production, and Steepest Entropy Ascent in the Proofs of Onsager's Reciprocal Relations. *J. Non-Equilib. Thermodyn.* **2018**, *43*, 101-110. DOI: 10.1515/jnet-2017-0054.
- Bertei, A.; Nicoletta C. Common inconsistencies in modeling gas transport in porous electrodes: The dusty-gas model and the Fick law. *J. Power Sources* **2015**, *279*, 133-137. DOI: j.jpowsour.2015.01.007
- Bertei, A; Nicoletta, C. Dusty-Gas Model with Uniform Pressure: A Numerical Study on the Impact of a Frequent Inconsistent Assumption in SOFC Electrode Modeling. *ECS Trans.* **2015**, *68*, 2887-2895. DOI: 10.1149/06801.2887ecst
- Bilal, M.; Ahmad, I.; Asadabadi, S. J.; Ahmad, R.; Maqbool, M. Thermoelectric Properties of Metallic Antiperovskites AXD_3 (A=Ge, Sn, Pb, Al, Zn, Ga; X=N, C; D=Ca, Fe, Co) *Electron. Mater. Lett.* **2015**, *11*, 466-480. DOI: 10.1007/s13391-015-4425-2
- Blum, L.; Groß, S. M.; Malzbender, J.; Pabst, U.; Peksen, M.; Peters, R.; Vinke, I. C. Investigation of solid oxide fuel cell sealing behavior under stack relevant conditions at Forschungszentrum Jülich. *J. Power Sources* **2011**, *196*, 7175-7181. DOI: 10.1016/j.jpowsour.2010.09.041
- Bonella, S.; Ferrario, M.; Civvotti, G. Thermal Diffusion in Binary Mixtures: Transient Behavior and Transport Coefficients from Equilibrium and Nonequilibrium Molecular Dynamics. *Langmuir*, **2017**, *33*, 11281-11290. DOI: 10.1021/acs.langmuir.7b02565
- Brinkman, H. W.; Briels, W. J.; Verweij, H. Molecular dynamics simulations of yttria-stabilized zirconia. *Chem. Phys. Lett.* **1995**, *247*, 386-390. DOI: 10.1016/S0009-2614(95)01231-1
- Chatzichristodoulou, C.; Chen, M.; Hendriksen, P. V.; Jacobsen, T.; Mogensen, M. B. Understanding degradation of solid oxide electrolysis cells through modeling of

- electrochemical potential profiles. *Electrochim. Acta* **2016**, *189*, 265-282. DOI: 10.1016/j.enconman.2018.03.064
- Chitsaz, A.; Sadeghi, M.; Sadeghi, M.; Ghanbarloo, E. Exergoenvironmental comparison of internal reforming against external reforming in a cogeneration system based on solid oxide fuel cell using an evolutionary algorithm. *Energy* **2018**, *144*, 420-431. DOI: 10.1016/j.energy.2017.12.008
- Choudhary, T.; Sanjay Computational analysis of IR-SOFC: Thermodynamic, electrochemical process and flow configuration dependency. *Int. J. Hydrogen Energy* **2016**, *41*, 1259-1271. DOI: 10.1016/j.ijhydene.2015.10.098.
- Costamagna, P.; Grosso, S.; Travis, R.; Magistri, L. Integrated Planar Solid Oxide Fuel Cell: Steady-State Model of Bundle and Validation through Single Tube Experimental Data. *Energies* **2015**, *8*, 13231-13254. DOI: 10.3390/en81112364
- Costamagna, P.; Selimovic, A.; Del Borghi, M.; Agnew, G. Electrochemical model of the integrated planar solid oxide fuel cell (IP-SOFC). *Chem. Eng. J.* **2004**, *102*, 61-69. DOI: 10.1016/j.cej.2004.02.005
- Cruz-Champion, H.; Kabelac, S. Multifunctional fuel cell system for civil aircraft: Study of the cathode exhaust gas dehumidification. *Int. J. Hydrogen Energy* **2017**, *42*, 29518-29531.
- da Silva, F. S.; de Souza, T. M. Novel materials for solid oxide fuel cell technologies: A literature review. *Int. J. Hydrogen Energy* **2017**, *42*, 26020-26036. DOI: 10.1016/j.ijhydene.2017.08.105
- Das, S. The Madelung constant of the sodium chloride crystal lattice. *Reson.* **2003**, *8*, 76-84. DOI: 10.1007/BF02840710
- Dasari, H.; Ahn, J.; Ahn, K.; Park, S.-Y.; Hong, J.; Kim, H.; Yoon, K.; Son, J.-W. ; Lee, H.-W. and Lee, J.-H. Synthesis, sintering and conductivity behavior of ceria-doped Scandia-stabilized zirconia. *Solid State Ionics*, **2014**, *263*, 103-109. DOI: 10.1016/j.ssi.2014.05.013
- de Leeuw, S.; Perram, J.; Smith, E. Simulation of electrostatic systems in periodic boundary conditions. I. Lattice sums and dielectric constants. *Proc. R. Soc. London A* **1980**, *3743*, 27-56. DOI: DOI: 10.1098/rspa.1980.0135.
- Devanathan, R.; Weber, W. J.; Shinghal, S. C.; Gale, J. D. Computer simulation of defects and oxygen transport in yttria-stabilized zirconia. *Solid States Ionics* **2006**, *117*, 125-1258. DOI: 10.1016/j.ssi.2006.06.030
- Dong, H.; Fan, Z.; Shi, L.; Harju, S.; Ala-Nissila, T. Equivalence of the equilibrium and the nonequilibrium molecular dynamics methods for thermal conductivity calculations: From bulk to nanowire silicon. *Phys. Rev. B.* **2018**, *97*, 094305-1-8. DOI: 10.1103/PhysRevB.97.094305
- Dreizler, R. M.; Lüdde, C. S. *Theoretische Physik 1. Theoretische Mechanik*; Springer-Verlag: Berlin, Heidelberg, Germany, **2008**. ISBN: 978-3-540-70558-4

- Droushiotis, N.; Dal Grande, F.; Dzarfan Orthman, M. H.; Kanawka, K.; Dorawami, U.; Metcalfe, I. S.; Li, K.; Kelsall, G. Comparison Between Anode-Supported and Electrolyte-Supported Ni-CGO-LSCF Micro-tubular Solid Oxide Fuel Cells. *Fuel Cells* **2014**, *14*, 200-211. DOI: 10.1002/fuce.201300024
- Dufty, J.; Wrighton, J.; Luo, K.; Trickey, S.-B. On the Kubo-Greenwood model for electron conductivity. *Contrib. Plasma. Phys.* **2018**, *58*, 150-154. DOI: 10.1002/ctpp.201700102
- Dwivedi, A.; Comarck, A. N. A computer simulation study of the defect structure of calcia-stabilized zirconia. *Philos. Mag. A* **1990**, *60*, 1-22. DOI: 10.1080/01418619008235554
- Eisavi, B.; Chitsaz, A.; Hosseinpour, J.; Ranjbar, F. Thermo-environmental and economic comparison of three different arrangements of solid oxide fuel cell-gas turbine (SOFC-GT) hybrid systems. *Energy Convers. Manage.* **2018**, *168*, 343-356. DOI: 10.1016/j.enconman.2018.04.088
- Fabrichnaya, O.; Wang, Ch.; Zinkevich, M.; Aldinger, F.; Levi, C. G. Phase equilibria and thermodynamic properties of the $\text{ZrO}_2\text{-GdO}_{1.5}\text{-YO}_{1.5}$ system. *J. Phase. Equilib. Diffus.* **2005**, *26*, 591-604. DOI: 10.1007/s11669-005-0004-9.
- Fan, Z.; Pereira, L. F. C.; Wang, H.-Q.; Zheng, J.-C.; Donadio, D.; Harju, A. Force and heat current formulas for many-body potentials in molecular dynamics simulations with applications to thermal conductivity calculations. *Phys. Rev. B.* **2015**, *92*, 094301-1-12. DOI: 10.1103/PhysRevB.92.094301
- Fardadi, M.; McLarty, D. F.; Jabbari, F. Investigation of thermal control for different SOFC flow geometries. *Appl. Energy* **2016**, *178*, 43-55. DOI: 10.1016/j.apenergy.2016.06.015.
- Ferkhi, M.; Yahia, H. A. Electrochemical and morphological characterizations of $\text{La}_{2-x}\text{NiO}_{4\pm\delta}$ ($x=0.01, 0.02, 0.03$ and 0.05) as new cathodes materials for IT-SOFC. *Mater. Res. Bull.* **2016**, *83*, 268-274. DOI: 10.1016/j.materresbull.2016.06.009
- Fèvre, M.; Finel, A.; Caudron, R.; Mévrel, R. Local order and thermal conductivity in yttria-stabilized zirconia. II. Numerical and experimental investigations of thermal conductivity. *Phys. Rev. B* **2005**, *72*, 104118-1-7. DOI: 10.1103/PhysRevB.72.104118.
- Findenegg, G. H.; Hellweg, T. *Statistische Thermodynamik*, Springer-Verlag: Heidelberg, Germany, **2015**. ISBN: 978-3-642-37871-3
- Flade, S.; Stephan, T.; Thalau, O.; Burberg, T.; Schirmer, J.; Kallo, J. Air breathing PEM Fuel Cells in Aviation. *ECS. Trans.* **2016**, *75*, 471-477. DOI: 10.1149/07514.0471ecst
- Frenkel, D.; Smit, B. *Understanding Molecular Simulation*; Academic Press: San Diego, United States, **2002**. ISBN: 0-12-167351-4
- Fu, Y.; Jiang, Y.; Poizeau, S.; Dutta, A.; Mohanram, A.; Pietras, J. D.; Bazant, M. Z. Multicomponent Gas Diffusion in Porous Electrodes. *J. Electrochem. Soc.* **2015**, *162*, F613-F621. DOI: 10.1149/2.0911506jes.

- Gajović, A.; Tomašić, N.; Djerdj, I.; Su, D. S.; Furić, K. Influence of mechanochemical processing to luminescence properties in Y_2O_3 powder. *J. Alloys Compd.* **2008**, *456*, 313-319. DOI: 10.1016/j.jallcom.2007.02.083.
- Gallardo-López, A.; Martínez-Fernández, J.; Domínguez-Rodríguez, A.; Ernst, F. Origin of diffuse electron scattering in yttria-cubicstabilized zirconia single crystals with 24-32 mol% yttria. *Philos. Mag.* **2001**, *81*, 1675-1689. DOI: 10.1080/01418610010019053.
- Ghorbani, B.; Vijayaraghavan, K. 3D and simplified pseudo-2D modeling of single cell of a high temperature solid oxide fuel cell to be used for online control strategies. *Int. J. Hydrogen Energy* **2018**, *43*, 9733-9748. DOI: 10.1016/j.ijhydene.2018.03.211
- Goldstein, H.; Poole, C.; Safko, J. *Classical Mechanics. Third Edition*; Addison Wesley: San Francisco, United States, **2000**. ISBN: 978-0-201-65702-9
- Gotte, A.; Spangberg, D.; Hermansson, K.; Baudin, M. Molecular dynamics study of oxygen self-diffusion in reduced CeO_2 . *Solid State Ionics* **2007**, *178*, 1421-1427. DOI: 10.1016/j.ssi.2007.08.003
- Grosso, R.; Bertolete, M.; Machado, I.; Muccillo, R. und Muccillo, E. Ionic conductivity and phase stability of spark plasma sintered scandia and ceria-stabilized zirconia. *Solid State Ionics*, **2013**, *230*, 48-51. DOI: 10.1016/j.ssi.2012.08.006
- Hafskjold, B. Non-equilibrium molecular dynamics simulations of the transient Ludwig-Soret effect in binary Lennard-Jones/spline mixture. *Eur. Phys. J. E* **2017**, *40*, 4-1-9, DOI: 10.1140/epje/i2017-11492-9
- Hajimolana, S. A.; Hussain, M. A.; Ashri Wan Daud, W. M.; Soroush, M.; Shamiri, A. Mathematical modeling of solid oxide fuel cell: A review. *Renewable Sustainable Energy Rev.* **2011**, *15*, 1893-1917. DOI: 10.1016/j.rser.2010.12.011
- Hartung, J. *Statistik: Lehr- und Handbuch der angewandten Statistik*. Oldenbourg Wissenschaftsverlag GmbH: München, Germany, **2005**. ISBN 3-486-57890-1
- Hayashi, H.; Inaba, H.; Matsuyama, M.; Lan, N. G.; Dokiya, M.; Tagawa, H. Structural consideration on the ionic conductivity of perovskite-type oxides. *Solid State Ionics* **1999**, *122*, 1-15. DOI: 10.1016/S0167-2738(99)00066-1
- Hayashi, H.; Saitou, T.; Maruyama, N.; Inaba, H.; Kawamura, K.; Mori, M. Thermal expansion coefficient of yttria stabilized zirconia for various yttria contents. *Solid State Ionics* **2005**, *176*, 613-619. DOI: 10.1016/j.ssi.2004.08.021
- He, Y.; Savić, I.; Donadio, D.; Galli, G. Lattice thermal conductivity of semiconducting bulk materials: atomistic simulations. *Phys. Chem. Chem. Phys.* **2012**, *14*, 16209-16222. DOI: 10.1039/C2CP42394D
- Heyes, D. M. Electrostatic potentials and fields in infinite point charge lattices. *J. Chem. Phys.* **1981**, *74*, 1924-1929. DOI: 10.1063/1.441285

- Hongsong, Z.; Lei, S.; Yongde, Z.; Gang, L.; Zhenjun, L. Thermal Conductivities and Thermal Expansion Coefficients of $(\text{Sm}_{0.5}\text{Gd}_{0.5})_2(\text{Ce}_{1-x}\text{Zr}_x)_2\text{O}_7$ Ceramics. *J. Mater. Eng. Perform.* **2015**, *24*, 3394-3399. DOI: 10.1007/s11665-015-1621-z
- Hoover, W. G. Canonical dynamics: Equilibrium phase-space distributions. *Phys. Rev. A* **1985**, *31*, 1695-1697. DOI: 10.1103/PhysRevA.31.1695
- Höpfner, A. *Irreversible Thermodynamik für Chemiker*; Walter de Gruyter: Berlin, Germany. **1977**, ISBN: 3-11-003520-0
- Horiuchi, K. Current Status of National SOFC Projects in Japan. *ECS Trans.* **2013**, *57*, 3-10. DOI: 10.1149/05701.0003ecst
- Hosoi, T.; Yonekura, T.; Sunada, K.; Sasaki, K. Exchange Current Density of SOFC Electrodes: Theoretical Relations and Partial Pressure Dependencies Rate-Determined by Electrochemical Reactions. *J. Electrochem. Soc.* **2015**, *162*, F136-F152. DOI: 10.1149/2.0561501jes.
- Irshad, M.; Siraj, M.; Raza, R.; Ali, A.; Tiwari, P.; Zhu, B.; Rafique, A.; Ali, A.; Ullah, M. K.; Usman, A. A Brief Description of High Temperature Solid Oxide Fuel Cell's Operation, Materials, Design, Fabrication Technologies and Performance. *Appl. Sci.* **2016**, *6*, 75. DOI: 10.3390/app6030075
- Isele-Holder, R. E.; Mitchell, W.; Ismail, A. E. Development and application of a particle-particle particle-mesh Ewald method for dispersion interactions. *J. Chem. Phys.* **2012**, *137*, 174107-1-13. DOI: 10.1063/1.4764089
- Jiang, K.; Liu, S.; Wang, X. Phase stability and thermal conductivity of nanostructured tetragonal yttria-stabilized zirconia thermal barrier coatings deposited by air-plasma spraying. *Ceram. Int.* **2017**, *43*, 12633-12640. DOI: 10.1016/j.ceramint.2017.06.142
- Jiang, N.; Wachsman, E. D. Structural Stability and Conductivity of Phase-Stabilized Cubic Bismuth Oxides. *J. Am. Ceram. Soc.* **1999**, *82*, 3057-3064. DOI: 10.1111/j.1151-2916.1999.tb02202.x
- Jiang, S. P.; Chan, S. H. A review of anode materials development in solid oxide fuel cells. *J. Mater. Sci.* **2004**, *39*, 4405-4439
- Jin, X.; White, R. E.; Huang, K. Simulating Charge Transport in Solid Oxide Mixed Ionic and Electronic Conductors: Nernst-Planck Theory vs Modified Fick's Law. *J. Electrochem. Soc.* **2016**, *163*, A2702-A2719. DOI: 10.1149/2.0941613jes
- Jonson, M.; Mahan, G. D. Mott's formula for the thermopower and the Wiedemann-Fianz law. *Phys. Rev. B* **1980**, *21*, 4223-4229. DOI: 10.1103/PhysRevB.21.4223.
- Joshi, H.; Rai, D. P.; Verma, K. D.; Bharmu, K. C.; Thapa, R. K. Thermoelectric properties of tetragonal half-Heusler compounds, TixSb (X=Ge,Si): A probe from Density Functional Theory (DFT). *J. Alloys Compd.* **2017**, *726*, 1155-1160. DOI: 10.1016/j.jallcom.2017.08.065

- Khazaei, I.; Rava, A. Numerical simulation of the performance of solid oxide fuel cell with different flow channel geometries. *Energy* **2017**, *119*, 235-244. DOI: 10.1016/j.energy.2016.12.074.
- Kjelstrup, S., Seip Førland K. The Transported Entropy of Oxygen Ion in Yttria-Stabilized Zirconia. *J. Electrochem. Soc.* **1991**, *138*, 2374-2376. DOI: 10.1149/1.2085979
- Kjelstrup, S.; Bedeaux, D. Jumps in electric potential and in temperature at the electrode surfaces of the solid oxide fuel cell. *Physica A* **1997**, *244*, 213-226. DOI: 10.1016/S0378-4371(97)00296-3
- Kjelstrup, S.; Bedeaux, D. *Non-Equilibrium Thermodynamics of Heterogeneous Systems*; World Scientific: Singapore, Singapore, **2017**, ISBN: 13 978-981-277-913-7
- Knutti, R.; Rogelj, J. The legacy of our CO₂ emissions: a clash of scientific facts, politics and ethics. *Clim. Change* **2015**, *133*, 361-373. DOI: 10.1007/s0584-015-1340-3
- Kong, W.; Zhang, Q.; Xu, X.; Chen, D. A Simple Expression for the Tortuosity of Gas Transport Paths in Solid Oxide Fuel Cells' Porous Electrodes. *Energies* **2015**, *8*, 13953-13959. DOI: 10.3390/en81212406
- Krogstad, J. A.; Lepple, M.; Gao, Y.; Lipkin, D. M.; Levi, C. G. Effect of Yttria Content on the Zirconia Unit Cell Parameters. *J. Am. Ceram. Soc.* **2011**, *91*, 4548-4555. DOI: 10.1111/j.1551-2916.2011.04862.x.
- Kubo, R. Statistical-Mechanical Theory of Irreversible Processes I. General Theory and Simple Applications to Magnetic and Conduction Problems. *J. Phys. Soc. Jpn.* **1957**, *12*, 570-586.
- Kumar, A.; Jaiswal, A.; Sanbui, M.; Omar, S. Scandia stabilized zirconia-ceria solid electrolyte ($x\text{Sc}_1\text{Ce}_x\text{SZ}$, $5 < x < 11$) for IT-SOFCs: Structure and conductivity studies *Scr. Mater.* **2016**, *121*, 10-13. DOI: 10.1016/j.scriptamat.2016.04.023
- Laguna-Bercero, M. A.; Skinner, S. J.; Killner, J. A. Performance of solid oxide electrolysis cells based on Scandia stabilized zirconia. *J. Power Sources* **2009**, *192*, 126-131. DOI: 10.1016/j.jpowsour.2008.12.139
- Larmine J. Dicks, A. *Fuel Cell Systems Explained*; John Wiley & Sons: Chichester, England, **2009**. ISBN: 978-0-470-84857-9
- Lau, K. C.; Dunlap, B. I. Molecular dynamics of yttria-stabilized (YSZ) crystalline and amorphous solids. *J. Phys. Condens. Matter* **2011**, *23*, 035401-1-16. DOI: 10.1088/0953-8984/23/3/035401
- Laurencin, J.; Delette, G.; Lefebvre-Joud, F.; Dupeux, M. A numerical tool to estimate SOFC mechanical degradation: Case of the planar cell configuration. *J. Eur. Ceram. Soc.* **2008**, *28*, 1857-1869. DOI: 10.1016/j.jeurceramsoc.2007.12.025.
- Leach, A. R. *Molecular Modelling. Principles and Applications*. Pearson Education Limited: Dorchester, Dorset, United Kingdom, **2001**. ISBN: 978-0-582-38210-7

- Lecce, S. D.; Bresme, F.; Soret coefficients and thermal conductivities of alkali halide aqueous solutions via non-equilibrium molecular dynamics simulations. *Mol. Sim.* **2018** (in press) DOI: 10.1080/08927022.2018.1481960.
- Leites, K.; Bauschulte, A.; Dragon, M.; Kummrich, S.; Nehter, P. SchIBZ-Design of Different Diesel Based Fuel Cell Systems for Seagoing Vessels and Their Evaluation. *ECS Trans.* **2012**, *42*, 49-58. DOI: 10.1149/1.4705479
- Leitner, J.; Chuchvalec, P.; Sedmidubský D.; Strejcek, A.; Abrman, P. Estimation of heat capacities of solid mixed oxides. *Thermochim. Acta* **2002**, *395*, 27-46. DOI: 10.1016/S0040-6031(02)00177-6
- Leitner, J.; Voňka, P.; Sedmidubsky, D.; Svoboda, P. Application of Neuman-Kopp rule for the estimation of heat capacities of mixed oxides. *Thermochim. Acta* **2010**, *497*, 7-13. DOI: 10.1016/j.tca.2009.08.002
- Lepe, F. J.; Fernández-Urbán, J.; Mestres, L.; Martínez-Sarrión, M. L. Synthesis and electrical properties of new rare-earth titanium perovskites for SOFC anode applications. *J. Power Sources*, **2005**, *151*, 74-78. DOI: 10.1016/j.jpowsour.2005.02.087
- Lewis, G. V.; Catlow, C. R. A. Potential models for ionic oxides. *J. Phys. C: Solid State Phys.* **1985**, *18*, 1149-1161. DOI: 10.1088/0022-3719/18/6/010
- Li, H.; Cai, Z.; Li, Q.; Sun, C.; Zhao, H. Electrochemical investigation of Pr₂CuO₄-based composite cathode for intermediate temperature solid oxide fuel cells. *J. Alloys Compd.* **2016**, *688*, 972-977. DOI: 10.1016/j.jallcom.2016.05.350
- Liu, M.; He, C.; Wang, W. and Wang, J. Synthesis and characterization of 10Sc1CeSZ powders prepared by a solid-liquid method for electrolyte-supported solid oxide fuel cells. *Ceram. Int.*, **2014**, *40*, 5441-5446. DOI: j.ceramint.2013.10.129.
- Liu, X.; Schnell, S. K.; Simon, J.-M.; Bedeaux, D.; Kjelstrup, S.; Bardow, A.; Vlugt, T. J. H. Fick Diffusion Coefficients of Liquid Mixtures Directly Obtained From Equilibrium Molecular Dynamics. *J. Phys. Chem. B* **2011**, *115*, 44, 12921-12929. DOI: 10.1021/jp208360s
- Lu, H.; Hua, D.; Isqabl, T.; Zhang, X.; Li, G.; Zhang, D. Molecular dynamics simulations of the coke formation progress on the nickel-based anode of solid oxide fuel cells. *Int. Comm. Heat Mass Transfer* **2018**, *91*, 40-47 DOI: 10.1016/j.icheatmasstransfer.2017.11.009
- Ma, R.; Gao, F.; Breaz, E.; Huangfu, Y.; Brioris, P. Multidimensional Reversible Solid Oxide Fuel Cell Modeling for Embedded Applications. *IEEE Trans. Energy Convers.* **2018**, *33*, 692-701. DOI: 10.1109/TEC.2017.2762962
- Mahato, N.; Banerjee, A.; Gupta, A.; Omar, S.; Kantesh, B. Progress in material selection for solid oxide fuel cell technology: A review. *Prog. Mater. Sci.* **2015**, *72*, 141-337. DOI: 10.1016/j.pmatsci.2015.01.001
- Mann, E. M.; Bradley, R. S. Northern Hemisphere Temperatures During the Past Millennium: Inferences, Uncertainties and Limitations. *Geophys. Res. Lett.* **1999**, *26*, 759-762. DOI: 10.1029/1999GL900070

- Manthiram, A.; Li, L. Hybrid and Aqueous Lithium-Air Batteries. *Adv. Energy Mater.* **2015**, *5*, 1401302-1-17. DOI: 10.1002/aenm.201401302
- Martyna, G.; Douglas, J.; Klein, M. Constant pressure molecular dynamics algorithms. *J. Chem. Phys.* **1994**, *101*, 4177-4189. DOI: 10.1063/1.467468
- Matthews, H. D.; Caldeira, K. Stabilizing climate requires near-zero emissions. *Geophys. Res. Lett.* **2008**, *35*, L04705-1-5. DOI: 10.1029/2007GL032388
- Mauri, R. *Non-Equilibrium Thermodynamics in Multiphase Flows*; Springer Science+Business Media: Dodrecht, Nethelands, **2013**, ISBN: 978-94-007-5461-4
- Menon, V.; Banerjee, A.; Dailly, J., Deutschmann, O. Numerical analysis of mass and heat transport in proton-conducting SOFC with direct internal reforming. *Appl. Energy* **2015**, *149*, 161-175. DOI: 10.1016/j.apenergy.2015.03.037
- Minervini, L; Zacate, M. O.; Grimes, R. W. Defect cluster formation in M_2O_3 -doped CeO_2 . *Solid State Ionics* **1999**, *116*, 339-349. DOI: 10.1016/S0167-2738(98)00359-2
- Moreno-Blanco, J.; Elizalde-Blancas, F.; Riesco-Avila, J. M.; Belman-Flores, J. M.; Gallegos-Muñoz, A. On the effect of gas channels-electrode interface area on SOFCs performance. *Int. J. Hydrogen Energy* **2018** (in press). DOI: 10.1016/j.ijhydene.2018.02.108
- Nam, H. J.; Kwon, O. J. Infrared radiation modeling of NO, OH, CO, H₂O and CO₂ for emissivity/radiance prediction at high temperature. *Infrared Phys. Technol.* **2014**, *67*, 293-291. DOI: 10.1016/j.infrared.2014.08.003
- Nehter, P.; Wildrath, B.; Bauschulte, A.; Leites, K. Diesel Based SOFC Demonstrator for Maritime Applications. *ECS Trans.* **2017**, *78*, 171-180. DOI: 10.1149/07801.0171ecst
- Nishida, R. T.; Beale, S. B.; Pharoah, J. G.; de Haart, L. G. J.; Blum, J. Three-dimensional computational fluid dynamics modelling and experimental validation of the Jülich Mark-F solid oxide fuel cell stack. *J. Power Sources* **2018**, *373*, 203-210. DOI: 10.1016/j.jpowsour.2017.10.030.
- O'Hayre, R.; Cha, S.-W.; Colella W.-G., Prinz, F. B. *Fuel Cell Fundamentals*; John Wiley & Sons: New Jersey, United States of America, **2016**. ISBN: 978-1-119-11420-8.
- Parhizkar, T.; Hafeznezami, S. Degradation based operational optimization model to improve the productivity of energy systems, case stud: Solid oxide fuel cell stacks. *Energy Convers. Manage.* **2018**, *158*, 81-91. DOI: 10.1016/j.enconman.2017.12.045
- Park, J. M.; Kim, D. Y.; Baek, J. D.; Yoon, Y.-J.; Su, P.-C.; Lee, S.-H. Effect of Electrolyte Thickness on Electrochemical Reactions and Thermo-Fluidic Characteristics inside a SOFC Unit cell. *Energies*, **2018**, *11*,473-1-15. DOI: 10.3390/en11030473
- Patterson, J.; Bailey, B. *Solid-State Physics. Introduction to the Theory*; Springer-Verlag: Heidelberg, Germany, **2010**. ISBN: 978-3-642-02589-1

- Peksen, M. Safe heating-up of a full scale SOFC system using 3D multiphysics modelling optimization. *Int. J. Hydrogen Energy* **2018**, *43*, 354-362. DOI: 10.1016/j.ijhydene.2017.11.026
- Pianko-Oprych, P.; Kasilova, E.; Jaworski, Z. Quantification of the Radiative and Convective Heat Transfer Processes and their Effect on mSOFC by CFD Modelling. *Pol. J. Chem. Technol.* **2014**, *16*, 51-55. DOI: 10.2478/pjct-2014-0029.
- Plimpton, S. Fast Parallel Algorithmus for Short-Range Molecular Dynamics. *J. Comput. Phys.* **1995**, *117*, 1-19. DOI: 10.1006/jcph.1995.1039
- Pranami, G.; Lamm, M. H. Estimating Error in Diffusion Coefficients Derived from Molecular Dynamics Simulations. *J. Chem. Theory Comput.* **2015**, *11*, 4586-4592. DOI: 10.1021/acs.jctc.5b00574
- Profatilova, I.; Jacques, P.-A.; Escribano, S. Evaluation of Parameters Accelerating the Aging of PEMFCs Operating under Reformate Containing Carbon Monoxide. *J. Electrochem. Soc.* **2018**, *165*, F3251-F3260.
- Prokop, T. A.; Berent, K.; Iwai, H.; Szmyd, J. S.; Brus, G. A three-dimensional heterogeneity analysis of electrochemical energy conversion in SOFC anodes using electron nanotomography and mathematical modeling. *Int. J. Hydrogen Energy* **2018**, *43*, 10016-10030. DOI: 10.1016/j.ijhydene.2018.04.023
- Razmehhah, M.; Mosavian, M. T. H.; Moosavi, F. Transport thermodynamic, and structural properties of rare earth zirconia-based electrolytes by molecular dynamics simulation. *Int. J. Energy. Res.* **2016**, *40*, 1712-1723. DOI: 10.1002/er.3559
- Rechberger, J. Grundlagen der Brennstoffzellentechnologie. In *Grundlagen Verbrennungsmotoren. Funktionsweise und alternative Antriebssysteme, Messtechnik und Simulation*; Merker, G. P.; Teichmann, R., Ed.; Springer Vieweg: Berlin, Germany, **2018**. ISBN: 978-3-658-19212-9
- Ren, X.; Pan, W. Mechanical properties of high-temperature-degraded yttria stabilized zirconia. *Acta Mater.* **2014**, *69*, 397-406. DOI: 10.1016/j.actamat.2014.01.017
- Rogelj, J.; den Elzern, M.; Höhne, N.; Fransen, T.; Fekete, H.; Winkler, H.; Schaeffer, R.; Sha, F.; Riahi, K.; Meinshausen M. Paris Agreement climate proposals need a boost to keep warming well below 2 °C. *Nature* **2016**, *534*, 631-639. DOI: 10.1038/nature18307
- Saha, L. C.; Iskandarov, A.; Nakao, K.; Ishimoto, T.; Umeno, Y.; Koyama, M. Reactive Force-Field Development for Metal/Ceramic SOFC Anode Modeling. *ECS Trans.* **2015**, *68*, 2943-2949. DOI: 10.1149/06801.2943ecst
- Salawitch, R. J.; Bennet, B. F.; Hope, A. P.; Tribett, W. R.; Canty, T. P. Earth's Climate System. In *Paris Climate Agreement: Beacon of Hope*; Salawitch, R. J.; Canty, T. P.; Hope, A. P.; Tribett W. R.; Bennet, B. F., Eds.; Springer: Berlin, Heidelberg, **2016**. ISBN: 978-3-319-46939-3
- Sasaki, K.; Teraoka, Y. Equilibria in Fuel Cell Gases II. The C-H-O Ternary Diagrams. *J. Electrochem. Soc.* **2003**, *150*, A885-A888. DOI: 10.1149/1.1577338

- Scheck, F. *Theoretische Physik 1: Mechanik*, Springer-Verlag: Heidelberg, Germany, 2007. ISBN: 978-3-540-71377-7
- Schelling, P. K., Phillpot, S. R. Mechanism of Thermal Transport in Zirconia and Yttria-Stabilized Zirconia by Molecular-Dynamics Simulation. *J. Am. Ceram. Soc.* **2001**, *84*, 2997-3007. DOI: 10.1111/j.1151-2916.2001.tb01127.x
- Schnell, S. K.; Liu, X.; Simon, J.-M.; Bardow, A.; Bedeaux, D.; Vlucht, T. J. H.; Kjelstrup, S. Calculating Thermodynamic Properties from Fluctuations at Small Scales. *J. Phys. Chem. B*, **2011**, *115*, 10911–10918. DOI: 10.1021/jp204347p
- Sharaf, O. Z.; Orhan, M. F. An overview of fuel cell technology: Fundamentals and applications. *Renewable Sustainable Energy Rev.* **2014**, *32*, 810-853.
- Shen, S.; Kuang, Y.; Zheng, K.; Gao, Q. A 2D model for solid oxide fuel cell with a mixed ionic and electronic conducting electrolyte. *Solid State Ionics* **2018**, *315*, 44-51. DOI: 10.1016/j.ssi.2017.11.028
- Shimizu, M.; Kato, H.; Nishi, M.; Hanakawa, D.; Nagashima, K.; Visbal, H.; Itasaja, H.; Sakakura, M.; Shimotsuma, Y.; Miura, K.; Hirao, K.; Molecular dynamics simulation of the Soret effect in a CaSiO₃ glass melt. *J. Ceram. Soc. Jpn.* **2017**, *125*, 180-184. DOI: 10.2109/jcersj2.16187
- Shinoda, W.; Shiga, M.; Mikami, M. Rapid estimation of elastic constants by molecular dynamics simulation under constant stress. *Phys. Rev. B* **2004**, *69*, 134103-1-8. DOI: 10.1103/PhysRevB.69.134103
- Sizov, V. V.; Lampinen, M. J.; Laaksonen, A. Molecular dynamics simulation of oxygen diffusion in cubic yttria-stabilized zirconia: Effects of temperature and composition. *Solid State Ionics* **2014**, *266*, 29-35. DOI: 10.1016/j.ssi.2014.08.003
- Song, X.; Dong, X.; Li, M.; Wang, H. Effects of adding alumina to the nickel-zirconia anode materials for solid oxide fuel cells and a two-step sintering method for half cells. *J. Power Sources*, **2016**, *308*, 58-64. DOI: 10.1016/j.jpowsour.2016.01.070
- Sugiura, S.; Shibuta, Y.; Shimamura, K.; Misawa, M.; Fuyuki, S.; Yamaguchi, S. Role of oxygen vacancy in dissociation of oxygen molecule on SOFC cathode: Ab initio molecular dynamics simulation. *Solid State Ionics* **2016**, *285*, 209-214. DOI: 10.1016/j.ssi.2015.06.008
- Takehara, Z.-I.; Kanamura, K.; Yoshioka, S. Therman Energy Generated by Entropy Change in Solid Oxide Fuel Cell. *J. Electrochem. Soc.* **1989**, *136*, 2506-2511.
- Takino, A.; Tachikawa, Y.; Shiratori, Y.; Taniguchi, S.; Sasaki, K. Effect of Exchange Current Density on Current Distribution at Planar-Type SOFC Anodes *ECS Trans.* **2017**, *78*, 1523-1531. DOI: 10.1149/07801.1523ecst
- Tanveer, W. H.; Iwai, H.; Yu, W.; Pandiyan, A.; Ji, S.; Lee, Y. H.; Lee, Y.; Yaqoob, K.; Cho, G. Y.; Cha, S. W. Experimentation and modelling of nanostructured nickel cermet anodes for submicron SOFCs fueled indirectly by industrial waste carbon. *J. Mater. Chem. A* **2018**, *6*, 11169-11179. DOI: 10.1039/C7TA10273A

- Terblanche, S. P. Thermal-expansion coefficients of yttria-stabilized cubic zirconias. *J. Appl. Cryst.* **1989**, *22*, 283-284. DOI: 10.1107/S0021889888013937
- Terner, M. R. On the conductivity degradation and phase stability of solid oxide fuel cell (SOFC) zirconia electrolytes analyzed via XRD. *Solid State Ionics* **2014**, *263*, 180-189. DOI: 10.1016/j.ssi.2014.06.006
- Timurkutluk, B.; Timurkutluk, C.; Mat, M. D.; Kaplan, Y. A review on cell/stack designs for high performance solid oxide fuel cells. *Renewable Sustainable Energy Rev.* **2016**, *56*, 1101-1121. DOI: 10.1016/j.rser.2015.12.034
- Tojo, T.; Atake, T.; Mori, T.; Yamamura, H. Excess Heat Capacity in Yttria Stabilized Zirconia. *J. Therm. Anal. Calorim.* **1999**, *57*, 447-458. DOI: 10.1023/A:1010159807127
- Tojo, T.; Atake, T.; Mori, T.; Yamamura, H. Heat capacity and thermodynamic functions of zirconia and yttria-stabilized zirconia. *J. Chem. Thermodyn.* **1999**, *31*, 831-845. DOI: 10.1006/jcht.1998.0481.
- Tojo, T.; Kawaji, H.; Atake, T. Molecular dynamics study on lattice vibration and heat capacity of yttria-stabilized zirconia. *Solid State Ionics* **1999**, *118*, 349-353. DOI: 10.1016/S0167-2738(98)00424-X
- Tuckerman, M. E.; Liu, Y.; Ciccoli, G.; Martyna, G. J. Non Hamiltonian molecular dynamics: Generalizing Hamiltonian phase space principles to non-Hamiltonian systems. *J. Chem. Phys.* **2001**, *115*, 1678-1702. DOI: 10.1063/1.1378321
- van Biert, L.; Thallam Thattai, A.; Aravind, P. V. Predicting MSR Rates in SOFCs Using Experimental Data and CFD Methods. *ECS Trans.* **2017**, *78*, 2823-2834. DOI: 10.1149/07801.2823ecst
- van Duin, A. C.; Merinov, B. V.; Jang, S. S.; Goddard III, W. A. ReaxFF Reactive Force Field for Solid Oxide Fuel Cell Systems with Application to Oxygen Ion Transport in Yttria-Stabilized Zirconia. *J. Phys. Chem. A*, **2008**, *112*, 3133-3140. DOI: 10.1021/jp076775
- Viazzi, C.; Bonino, J.-P.; Ansart, F.; Barnabé, A. Structural study of metastable tetragonal YSZ powders produced via a sol-gel route. *J. Alloys Compd.* **2008**, *452*, 337-383. DOI: 10.1016/j.jallcom.2006.10.155.
- Vijay, P.; Tadé, M. O. Improved approximation for the Butler-Volmer equation in fuel cell modelling. *Comput. Chem. Eng.* **2017**, *102*, 2-10. DOI: 10.1016/j.compchemeng.2016.10.018.
- Wang, F.; Wang, W.; Ran, R.; Tade, M. O.; Shao, Z. Aluminum oxide as a dual-functional modifier of Ni-based anodes of solid oxide fuel cells for operation on simulated biogas. *J. Power Sources*, **2014**, *268*, 787-793. DOI: 10.1016/j.jpowsour.2014.06.087
- Wang, Z.; Cheng, M.; Bi, Z.; Dong, Y.; Zhang, H.; Zhang, J.; Feng, Z. and Li, C. Structure and impedance of ZrO₂ doped with Sc₂O₃ and CeO₂. *Mater. Lett.*, **2005**, *59*, 2579-2582. DOI: 10.1016/j.matlet.2004.07.065

- Weng, F.; Cheng, C.-K.; Chen, K.-C. Hydrogen production of two-stage temperature steam reformer integrated with PBI membrane fuel cells to optimize thermal management. *Int. J. Hydrogen Energy* **2013**, *38*, 6059-6064. DOI: j.ijhydene.2013.01.090. DOI: 10.1016/j.rser.2014.01.012
- Whiston, M. M.; Collinge, W. O.; Bilec, M. M.; Schaefer, L. A. Exergy and economic comparison between kW-scale hybrid and stand-alone solid oxide fuel cell systems. *J. Power Sources* **2017**, *353*, 152-166. DOI: 10.1016/j.jpowsour.2017.03.113
- Woodcock, L. V.; Singer, K. Thermodynamic and structural properties of liquid ionic salts obtained by Monte Carlo computation. Part 1. –Potassium chloride. *Trans. Faraday Soc.* **1971**, *67*, 12-30. DOI: 10.1039/TF9716700012
- Xue, Q.; Huang, X.; Wang, L.; Dong, J.; Xu, H.; Zhang, J. Effects of Sc doping on phase stability of $Zr_{1-x}Sc_xO_2$ and phase transition mechanism: First principles calculations and Rietveld refinement. *Mater. Des.* **2017**, *114*, 297-302. DOI: 10.1016/j.matdes.2016.11.020
- Yahya, A.; Ferrero, D.; Dhahri, H.; Leone, P.; Slimi, K.; Santarelli, M. Electrochemical performance of solid oxide fuel cell: Experimental study and calibrated model. *Energy* **2018**, *142*, 932-943. DOI: 10.1016/j.energy.2017.10.088
- Yamamura, Y.; Kawasaki, S.; Sakai, H. Molecular dynamics analysis of ionic conduction mechanism in yttria-stabilized zirconia. *Solid State Ionics* **1999**, *126*, 181-189. DOI: 10.1016/S0167-2738(99)00227-1
- Yang, F.; Gu, J.; Ye, L.; Zhang, Z.; Rao, G.; Liang, Y.; Wen, K.; Zhao, J.; Goodenough, J. B.; He, W. Justifying the significance of Knudsen diffusion in solid oxide fuel cells. *Energy* **2016**, *95*, 242-246. DOI: 10.1016/j.energy.2015.12.022
- Yang, Z.; Guo, M.; Wang, N.; Ma, C.; Wang, J.; Han, M. A short review of cathode poisoning and corrosion in solid oxide fuel cell. *Int. J. Hydrogen Energy*, **2017**, 24948-24959. DOI: 10.1016/j.ijhydene.2017.08.057
- Yang, X.; Fernández-Carrión, A. J.; Wang, J.; Porcher, F.; Fayon, F.; Allix, M.; Kuang, X. Cooperative mechanisms of oxygen vacancy stabilization and migration in the isolated tetrahedral anion Scheelite structure. *Nat. Commun.* **2018**, *9*, 4484-1-11. DOI: 10.1038/s41467-018-06911-w
- Zwanzig, R. Time-Correlation Functions and Transport Coefficients in Statistical Mechanics. *Annu. Rev. Phys. Chem.* **1965**, *16*, 67-102. DOI: 10.1146/annurev.pc.16.100165.000435

Appendix

To Chapter 3.1.1 *System, Force Field and Thermodynamic State*

Routine A1. LAMMPS routine for the generation of YSZ configurations

```

1 # LAMMPS input script to create YSZ configurations
2 # Definition of the variables
3
4 variable          setupNo index 01 02 03 04 05 06 07 08 09 10 11 12 13 14 15
5 label             loop_s
6 clear
7
8 variable          T equal 70
9 variable          dt equal 4.0
10 variable         x_Y2O3_soll equal 0.8
11 variable         PrztY2O3 string 08
12 variable         Nlx equal 5
13 variable         Nly equal 5
14 variable         Nlz equal 5
15
16 # Setup problem and periodic boundary conditions
17
18 units             metal
19 dimension         3
20 boundary          p p p
21
22 # Zirconium dioxide lattice setup
23
24 lattice           custom 5.0 a1 1.0 0.0 0.0 a2 0.0 1.0 0.0 a3 0.0 0.0 1.0 basis 0.0 0.0 0.0 &
                    basis 0.5 0.5 0.0 basis 0.5 0.0 0.5 basis 0.0 0.5 0.5 basis 0.25 0.25 0.25 &
                    basis 0.25 0.75 0.25 basis 0.75 0.25 0.25 basis 0.75 0.75 0.25 &
                    basis 0.25 0.25 0.75 basis 0.25 0.75 0.75 basis 0.75 0.25 0.75 basis 0.75 0.75 0.75
25 region           box block 0 ${Nlx} 0 ${Nly} 0 ${Nlz}
26 create_box       3 box
27 create_atoms     2 region box basis 1 1 basis 2 1 basis 3 1 basis 4 1 basis 5 2 basis 6 2 &
                    basis 7 2 basis 8 2 basis 9 2 basis 10 2 basis 11 2 basis 12 2
28 group           zrc type 1
29 group           oxy type 2
30
31 # Loop for the random substitution of zirconium by yttrium
32
33 label            loop_y
34 variable         index loop 200000
35 variable         ytt_id equal round(random(1,count(all),8${setupNo}034002))
36 group           ytr_all id ${ytt_id}
37 group           ytr intersect ytr_all zrc
38 group           zrc delete
39 group           zrc type 1
40 variable         NZr equal count(zrc)
41 variable         NY equal count(ytr)
42 variable         x_Y2O3 equal (${NY}/2)/(${NY}/2+${NZr})

```

```

43 set                group ytr type 3
44 if                 "${x_Y2O3} >= ${x_Y2O3_soll}" then "jump in.YSZ_setup break_y"
45 next              index
46 jump              in.YSZ_setup loop_y
47 label             break_y
48 variable          x_Y2O3_soll delete
49 variable          index delete
50
51 # Loop for the random creation of vacancies
52
53 label             loop_v
54 variable          index loop 2000
55 variable          vac_id equal round(random(1,count(all),1437${setupNo}435))
56 group            vacancy_all id ${vac_id}
57 group            vacancy intersect vacancy_all oxy
58 variable          Nv equal count(vacancy)
59 variable          Nv_hilfe equal ${NY}/2
60 if                 "${Nv} >= ${Nv_hilfe}" then "jump in.YSZ_setup break_v"
61 next              index
62 jump              in.YSZ_setup loop_v
63 label             break_v
64 delete_atoms     group vacancy
65 variable          vac_id delete
66 variable          Nv_hilfe delete
67 variable          Nv delete
68 variable          index delete
69
70 group            ytr delete
71 group            zrc delete
72 group            oxy delete
73 variable          NY delete
74 variable          NZr delete
75
76 # Calculating resulting Y2O3 concentration
77
78 group            zrc type 1
79 group            oxy type 2
80 group            ytr type 3
81
82 variable          NZr equal count(zrc)
83 variable          NOx equal count(oxy)
84 variable          NY equal count(ytr)
85 variable          neut equal 4*${NZr}+3*${NY}-2*${NOx}
86 variable          x_Y2O3 equal (${NY}/2)/(${NY}/2+${NZr})
87
88 print            "${x_Y2O3}"
89 print            "${neut}" append log.proof
90
91 # Potential parameterization for a random simulation of one single step
92
93 mass              1 1.0
94 mass              2 1.0

```

```

95 mass                3 1.0
96 pair_style          lj/cut 13.0
97 pair_coeff          ** 0.0 0.0
98 timestep            ${dt}
99
100 # Saving start configuration at t=0 with a random simulation of one single step
101
102 velocity            all create $T 102486 mom yes rot yes dist gaussian
103 fix                 NVT all nvt temp $T $T 10 drag 0.2
104 dump                myDump all atom 100 &
                        dump.YSZ${PrztY2O3}_setup${setupNo}
105 run                 1
106 next                setupNo
107 jump                in.YSZ_setup loop_s

```

To Chapter 3.1.2 *Computational Details*

Routine A2. LAMMPS routine for the NpT simulations for YSZ

```

1 # LAMMPS input script for the calculation of the lattice constant in YSZ (NpT ensemble)
2 # Units and declaration of the variables
3
4 units                metal
5
6 variable             T equal 1300
7 variable             PrztY2O3 string 08
8 variable             setupNo index 01 02 03 04 05 06 07 08 09 10 13 14 15
9
10 variable            Nlx index 5
11 variable            Nly index 5
12 variable            Nlz index 5
13 variable            aLat equal 5.136*(1+10^-5*($T-300)) # from Sizov et al.
14 variable            aBox_x equal ${Nlx}*${aLat}
15 variable            aBox_y equal ${Nly}*${aLat}
16 variable            aBox_z equal ${Nlz}*${aLat}
17 variable            ax equal lx/${Nlx}
18 variable            ay equal ly/${Nly}
19 variable            az equal lz/${Nlz}
20
21 variable            dt equal 0.5e-3
22
23 variable            tequil equal 2000000
24 variable            tdump equal 200
25 variable            tdump_run equal 1
26 variable            dthermo_eq equal 10
27
28 variable            trun equal 1000000
29 variable            dthermo_run equal 1
30
31 # Setup problem and periodic boundary conditions
32
33 dimension            3

```

```

34 boundary          p p p
35
36 kspace_style      ewald 1.0e-4
37 atom_style        charge
38 atom_modify       map array sort 0 0.0
39 region            box block 0 ${Nlx} 0 ${Nly} 0  ${Nlz}
40 create_box        3 box
41 label             loop
42 read_dump         ../YSZ_setup/dump.YSZ${PrztY2O3}_setup${setupNo} 0 x y z &
                    box yes add yes
43 change_box        all x final 0.0 ${aBox_x} y final 0.0 ${aBox_y} &
                    z final 0.0 ${aBox_z} remap units lattice
44 timestep          ${dt}
45 thermo            ${dthermo_eq}
46
47 # Charge assignation
48
49 group zrc          type 1
50 group oxy          type 2
51 group ytr          type 3
52 set               group zrc charge 4
53 set               group oxy charge -2
54 set               group ytr charge 3
55
56 # Parameterization of the Force Field (Schelling, 2001)
57
58 mass              1 91.224
59 mass              2 15.999
60 mass              3 88.9058
61
62 pair_style         buck/coul/long 10.0
63
64 pair_coeff         1 2 1502.11 0.345 5.1
65 pair_coeff         2 3 1366.35 0.348 19.6
66 pair_coeff         2 2 9547.96 0.224 32.0
67
68 pair_coeff         1 1 0.0 1.0 0.0
69 pair_coeff         3 3 0.0 1.0 0.0
70 pair_coeff         1 3 0.0 1.0 0.0
71
72 # Equilibration and Thermalization
73
74 log               log.YSZ_equil${setupNo}
75 reset_timestep 0
76 dump              myDump all atom ${tdump} dump.YSZ${PrztY2O3}_setup${setupNo}
77 velocity          all create $T 856${setupNo}44 mom yes rot yes dist gaussian
78 fix               NPT all npt temp $T $T 0.1 iso 0.0 0.0 1
79 thermo_style      custom step time temp press etotal v_ax
80 run               ${tequil}
81 undump            myDump
82 write_restart     restart.equil${setupNo}
83

```

```

84 # Production run
85
86 log                log.YSZ_run${setupNo}
87 dump              myDump all custom ${tdump_r} dump.YSZ${PrztY2O3}_run &
                    id type x y z vx vy vz
88 thermo           ${dthermo_run}
89 run               ${trun}
90 undump            myDump
91 unfix             NPT
92 write_restart     restart.run${setupNo}
93 delete_atoms      group all
94 next              setupNo
95 jump              in.YSZ loop

```

Routine A3. LAMMPS routine for the NVT simulations for YSZ

```

1 # LAMMPS input script for the simulation of the phenomenological coefficients in YSZ
2 # Declaration of the variables
3
4 variable           T equal 1300
5 variable           PrztY2O3 string 08
6 variable           setupNo index 01 02 03 04 05 06 07 08 09 10 13 14 15
7
8 variable           dt equal 0.5e-3
9 variable           tequil equal 2000000
10 variable          trun equal 1000000
11 variable          dthermo_equil equal 10
12 variable          dthermo_run equal 1
13 variable          tdump equal 500
14 variable          tdumpr equal 1
15
16 # Physical constants
17
18 variable          NA equal 6.022140857e23
19 variable          e equal 1.60217662e-19
20
21 # Lattice constant from the NpT simulations
22
23 variable          Nlx index 5
24 variable          Nly index 5
25 variable          Nlz index 5
26 variable          aLat index 5.14888 5.14874 5.14868 5.14881 5.14876 5.14881 5.14880 &
                    5.14883 5.14886 5.14885 5.14890 5.14900 5.14876 5.14873 5.14889
27
28 # Units and setup problem
29
30 label             loop
31 clear
32
33 units             metal
34 variable          aBox_x equal ${Nlx}*${aLat}
35 variable          aBox_y equal ${Nly}*${aLat}
36 variable          aBox_z equal ${Nlz}*${aLat}

```

```

37 variable          V equal ${aBox_x}*${aBox_y}*${aBox_z}*1e-30
38
39 dimension         3
40 boundary         p p p
41
42 kspace_style      ewald 1.0e-4
43 atom_style        charge
44
45 read_restart      aLat/restart.run${setupNo}
46 group            zrc type 1
47 group            oxy type 2
48 group            ytr type 3
49 change_box        all x final 0.0 ${aBox_x} y final 0.0 ${aBox_y} z final 0.0 &
                    ${aBox_z} remap units lattice
50
51 timestep          ${dt}
52
53 # Equilibration and thermalization
54
55 log               log.YSZ_equil${setupNo}
56 thermo           ${dthermo_equil}
57 reset_timestep    0
58 dump             myDump all atom ${tdump}
                    & dump.YSZ${PrztY2O3}equil_setup${setupNo}
59 fix              NVT all nvt temp $T $T 0.5
60 thermo_style      custom step time temp press etotal
61 run              ${tequil}
62 undump           myDump
63 write_restart    restart.equil${setupNo}
64 reset_timestep    0
65
66 # Production run and calculation of the micro fluxes
67
68 log              log.YSZ_run${setupNo}
69 thermo           ${dthermo_run}
70 dump             myDump all custom ${tdumpr} &
                    dump.YSZ${PrztY2O3}run_setup${setupNo} &
                    id type x y z vx vy vz
71
72 # Calculation of the micro molar flux of the anions
73
74 compute          w all property/atom vx vy vz
75 compute          wSum oxy reduce sum c_w[1] c_w[2] c_w[3]
76 variable         wSumX equal c_wSum[1]*100/($V*${NA})
77 variable         wSumY equal c_wSum[2]*100/($V*${NA})
78 variable         wSumZ equal c_wSum[3]*100/($V*${NA})
79
80 # Calculation of the micro heat flux
81
82 compute          ekin all ke/atom
83 compute          epot all pe/atom
84 compute          eB all pe/atom bond

```

```

85 compute          stress all stress/atom NULL virial
86 compute          Jq all heat/flux ekin epot stress
87 compute          JqK all heat/flux ekin eB stress
88 variable         JqX equal c_Jq[1]*100*$e/$V
89 variable         JqY equal c_Jq[2]*100*$e/$V
90 variable         JqZ equal c_Jq[3]*100*$e/$V
91 variable         JqKX equal c_JqK[4]*100*$e/$V
92 variable         JqKY equal c_JqK[5]*100*$e/$V
93 variable         JqKZ equal c_JqK[6]*100*$e/$V
94 variable         JqPX equal (c_Jq[1]-c_JqK[4])*100*$e/$V
95 variable         JqPY equal (c_Jq[2]-c_JqK[4])*100*$e/$V
96 variable         JqPZ equal (c_Jq[3]-c_JqK[4])*100*$e/$V
97 print            "$V"
98
99 # Production run
100
101 thermo_style     custom step temp press etotal pe ke v_wSumX v_wSumY &
                   v_wSumZ v_JqX v_JqY v_JqZ v_JqKX v_JqKY &
                   v_JqKZ v_JqPX v_JqPY v_JqPZ
102 run             ${trun}
103 undump          myDump
104 unfix           NVT
105 write_restart   restart.run${setupNo}
106
107 # Setup problem for rerun
108
109 clear
110 log              log.YSZ_rerun${setupNo}
111
112 clear
113
114 units            metal
115 variable         aBox_x equal ${Nlx}*$aLat}
116 variable         aBox_y equal ${Nly}*$aLat}
117 variable         aBox_z equal ${Nlz}*$aLat}
118 variable         V equal ${aBox_x}*${aBox_y}*${aBox_z}*1e-30
119
120 dimension        3
121 boundary         p p p
122
123 kspace_style     ewald 1.0e-4
124 atom_style       charge
125
126 read_restart     aLat/restart.run${setupNo}
127 group           zrc type 1
128 group           oxy type 2
129 group           ytr type 3
130 change_box       all x final 0.0 ${aBox_x} y final 0.0 ${aBox_y} z final 0.0 ${aBox_z} &
                   remap units lattice
131
132 set              atom * charge 0.0
133

```

```

134 timestep          ${dt}
135
136 # Recalculation of the micro heat flux
137
138 compute            ekin all ke/atom
139 compute            epot all pe/atom
140 compute            eB all pe/atom bond
141 compute            stress all stress/atom NULL virial
142 compute            Jq all heat/flux ekin epot stress
143 compute            JqK all heat/flux ekin eB stress
144 print              "$V"
145
146 # Production run
147
148 thermo             ${dthermo_run}
149 thermo_style       custom step temp press etotal pe ke v_JqX v_JqY v_JqZ v_JqKX &
                    v_JqKY v_JqKZ v_JqPX v_JqPY v_JqPZ
150 rerun              dump.YSZ${PrztY2O3}run_setup${setupNo} dump x y z vx vy vz
151 next                setupNo
152 next                aLat
153 jump                in.YSZ loop

```

To Chapter 3.1.4 *Calculation of the Electrostatic Potential*

The following Fortran 95 subroutines are based on the algorithms of M. P. Allen and D. J. Tidesley (2017), but modified for the calculation of φ_i .

Subroutine A1. Fortran 95 subroutine for the calculation of $\varphi_i^{R,*}$ with Eq. (2-24).

```

1 subroutine phiR ( phi, beta, ri, N )
2
3 ! Fortran 95 subroutine for the calculation of the short-range contribution phiR
4 ! ri is a N x 4 matrix that the position vectors (rxi, ryi, rzi) and the valences zi
5 ! Declaration of the variables
6
7 integer, intent(in):: N
8 integer index1, index2
9
10 double precision, intent(in) :: beta
11 double precision rxi, ryi, rzi
12 double precision rxij, ryij, rzij
13 double precision rij, krij
14 double precision erfc
15 double precision, dimension(N) :: phi
16 double precision, dimension(N,4) :: ri
17
18 ! Initialization of the variables
19
20 rxi = 0.0
21 ryi = 0.0
22 rzi = 0.0

```

```

23  rxij = 0.0
24  ryij = 0.0
25  rzij = 0.0
26  rij  = 0.0
27  krij = 0.0
28  phi  = 0.0
29
30 ! Loop for the calculation of phiR
31
32  do index1 = 1, N - 1
33
34      rxi = ri(index1,1)
35      ryi = ri(index1,2)
36      rzi = ri(index1,3)
37
38      do index2 = index1 + 1, N
39
40          rxij = rxi - ri(index2,1)
41          ryij = ryi - ri(index2,2)
42          rzij = rzi - ri(index2,3)
43
44          rxij = rxij - anint ( rxij )
45          ryij = ryij - anint ( ryij )
46          rzij = rzij - anint ( rzij )
47
48          rij = rxij**2.0 + ryij**2.0 + rzij**2.0
49          rij  = sqrt ( rij )
50          krij = beta * rij
51
52          phi(index1) = ri(index2,4) * erfc ( krij ) / rij + phi(index1)
53          phi(index2) = ri(index1,4) * erfc ( krij ) / rij + phi(index2)
54      end do
55  end do
56
57 end subroutine phiR

```

Subroutine A2. Fortran 95 subroutine for the initialization of the **k**-vectors

```

1  subroutine kVec (k , beta, maxk, kmax)
2
3  ! Fortran 95 subroutine for the definition of the k-vector
4  ! Declaration of the variables
5
6  implicit none
7
8  integer, intent(in) :: maxk, kmax
9  integer totk
10 integer ksqmax, ksq
11 integer kx, ky, kz
12
13 double precision, intent(in) :: beta
14 double precision rkx, rky, rkz, rksq
15 double precision pi, b

```

```

16  double precision, dimension(maxk) :: k
17
18  ! Initialization and definition of the variables
19
20  ksqmax = kmax**2 + 2
21  pi = 3.1415926
22  b = 1.0/(4.0*beta**2.0)
23
24  kx = 0
25  ky = 0
26  kz = 0
27  rkx = 0.0
28  rky = 0.0
29  rkz = 0.0
30  rksq = 0.0
31
32  totk = 0
33
34  ! Loop for the definition of the k-vector
35
36  do kx = 0, kmax
37      rkx = 2.0 * pi * kx
38      do ky = -kmax, kmax
39          rky = 2.0 * pi * ky
40          do kz = -kmax, kmax
41              rkz = 2.0 * pi * kz
42              ksq = kx * kx + ky * ky + kz * kz
43              if ( ( ksq < ksqmax ) .and. ( ksq /= 0 ) ) then
44                  totk = totk + 1
45                  if ( totk > maxk ) stop 'KVEC IS TOO SMALL'
46                  rksq = rkx**2.0 + rky**2.0 + rkz**2.0
47                  k(totk) = 2.0*pi * exp ( -b * rksq ) / rksq
48              end if
49          end do
50      end do
51  end do
52
53 end subroutine kVec

```

Subroutine A3. Fortran 95 subroutine for the calculation of $\varphi^{K,*}$ in Eq. (2-30).

```

1  subroutine phiK (phi, kvec, beta, ri, N, Nk, kmax )
2
3  ! Fortran 95 subroutine for the calculation of phiK with the Ewald sum
4  ! ri is a N x 4 matrix that includes the position vectors (rx_i, ry_i, rz_i) and the valences z_i
5  ! Declaration of the variables
6
7  implicit none
8
9  integer, intent(in) :: N, Nk
10 integer kmax, ksqmax
11 integer kx, ky, kz, ksq
12 integer totk

```

```

13  integer index
14  integer factor
15
16  double precision, dimension(Nk), intent(in) :: kvec
17  double precision, dimension(N,4), intent(in) :: ri
18  double precision, intent(in) :: beta
19  double precision, dimension(N) :: phi
20  double precision pi, rsqpi
21
22  complex, dimension(Nk) :: phiD
23  complex, dimension(N) :: eikr
24  complex, dimension(1:N,0:kmax) :: eikx
25  complex, dimension(1:N,-kmax:kmax) :: eiky
26  complex, dimension(1:N,-kmax:kmax) :: eikz
27
28 ! Initialization and definition of the variables
29
30  pi = 3.1415926
31  factor = 0
32  kx = 0
33  ky = 0
34  kz = 0
35  phi = 0.0
36  rsqpi = 1 / pi**0.5
37  ksqmax = kmax**2 + 2
38
39
40 ! Calculation of e^(ikri)
41
42  do index = 1, N
43
44      eikx(index, 0) = (1.0, 0.0)
45      eiky(index, 0) = (1.0, 0.0)
46      eikz(index, 0) = (1.0, 0.0)
47
48      eikx(index, 1) = cmplx ( cos( 2.0*pi*ri(index,1) ), sin( 2.0*pi*ri(index,1) ) )
49      eiky(index, 1) = cmplx ( cos( 2.0*pi*ri(index,2) ), sin( 2.0*pi*ri(index,2) ) )
50      eikz(index, 1) = cmplx ( cos( 2.0*pi*ri(index,3) ), sin( 2.0*pi*ri(index,3) ) )
51
52      eiky(index, -1) = conjg ( eiky(index, 1) )
53      eikz(index, -1) = conjg ( eikz(index, 1) )
54
55  end do
56
57  do kx = 2, kmax
58      do index = 1, N
59          eikx(index, kx) = eikx(index, kx-1) * eikx(index, 1)
60      end do
61  end do
62
63  do ky = 2, kmax
64      do index = 1, N

```

```

65     eiky(index, ky) = eiky(index, ky-1) * eiky(index, 1)
66     eiky(index, -ky) = conjg ( eiky(index, ky) )
67     end do
68 end do
69
70 do kz = 2, kmax
71     do index = 1, N
72         eikz(index, kz) = eikz(index, kz-1) * eikz(index, 1)
73         eikz(index, -kz) = conjg ( eikz(index, kz) )
74     end do
75 end do
76
77 ! Main loop for the calculation of phiK
78
79 totk = 0
80
81 do kx = 0, kmax
82     if ( kx == 0 ) then
83         factor = 1.0
84     else
85         factor = 2.0
86     end if
87
88     do ky = -kmax, kmax
89         do kz = -kmax, kmax
90             ksq = kx**2 + ky**2 + kz**2
91             if ( ( ksq < ksqmax ) .and. ( ksq /= 0 ) ) then
92                 totk = totk + 1
93                 phiD(:) = (0.0, 0.0)
94                 do index = 1, N
95                     eikr(index) = eikx(index,kx) * eiky(index,ky) * eikz(index,kz)
96                     phiD(totk) = ri(index,4) * factor * kvec(totk) * eikr(index) + phiD(totk)
97                 end do
98
99                 do index = 1, N
100                     phi(index) = conjg(phiD(totk)) * phiD(totk) + phi(index)
101                 end do
102             end if
103         end do
104     end do
105 end do
106
107 end subroutine phiK

```

Subroutine A4. Fortran 95 subroutine for the calculation $\varphi_i^{S,*}$ in Eq. (2-32).

```

1 subroutine phiS(phi, beta, q, N)
2
3 ! Fortran 95 Subroutine for the calculation of phiS
4 ! Declaration of the variables
5

```

```

6  implicit none
7
8  integer, intent(in) :: N
9  integer index
10
11 double precision, intent(in) :: beta
12 double precision pi, rsqpi
13 double precision, dimension(N), intent (in) :: q
14 double precision, dimension (N) :: phi
15
16 ! Definition and initialization of the variables
17
18 pi = 3.1415926
19 rsqpi = 1 / pi**0.5
20 phi = 0.0
21
22 ! Loop for the calculation of phiS
23
24 do index = 1, N
25     phi(index) = 2* q(index) * beta * rsqpi
26 end do
27
28 end subroutine phiS

```

To Chapter 3.2 *SOFC 1D NET Model*

Routine A4. MATLAB® SOFC 1D NET model

```

1 % MATLAB script for the calculation of a planar SOFC based on NET
2
3 clc;
4 close all;
5
6 % Physical constants
7
8 global F R NA
9
10 F = 96485.3329;           % Faraday constant in C/mol
11 R = 8.31446;             % gas constant in J/molK
12 NA = 6.022e23;          % Avogadro constant in 1/mol
13
14 % Initial and boundary conditions
15
16 x0 = 0;
17 p0 = 1e5;                % Druck in Pa
18 T0 = 1300;              % Temperatur at x=0 in K
19 phi0 = 0;               % Potential at x=0 in V
20 Jq0 = 8000;             % Initial value in W/m² for Newton iteration
21 j = 8000;               % Current density in A/m²
22
23 %% Parameters for the anode GDL
24

```

25	$x_a = 40e-6;$	% Thickness in m
26	$\lambda_{a_a} = 2;$	% Thermal conductivity in W/mK
27	$pelt_a = -5.4e-4*T0;$	% Peltier coefficient in J/C
28	$r0a = 1/95e6;$	% electr. Resistance in Ohm*m
29	$EA_ra = 1150*R;$	% Activ. Energy in J/mol
30	$D_a = 2.1e-5;$	% Diffusion coeff. in m^2/s
31		
32	% Parameters for the electrolyte	
33		
34	$YSZ = 8;$	
35		
36	$z = -2;$	
37	$Jo = j/z/F;$	% Anion flux density in mol/m^2s
38		
39	$x_e = 160e-6;$	% Thickness in m
40		
41	$Lqq_vec = [7.21;6.21;5.37;4.85;4.54;4.17]*1e6;$	
42	$Lqo_vec = [-0.70;-0.81;-0.77;-0.55;-0.48;-0.34]/R;$	
43	$Loo_vec = [4.47;3.75;2.47;1.72;1.17;0.86]*1e17/NA;$	
44		
45	$Lqq = Lqq_vec(YSZ/4);$	% Conductivity Lqq in WK/m
46	$Lqo = Lqo_vec(YSZ/4);$	% Conductivity Lqo in molK/ms
47	$Loq = Lqo;$	% Conductivity Loq in molK/ms
48	$Loo = Loo_vec(YSZ/4);$	% Conductivity Loo in mol^2K/Jms
49		
50	% Parameters for the cathode GDL	
51		
52	$x_c = 40e-6;$	% Thickness in m
53	$Tend = T0;$	% Temperature in K at $y=ya+ye+yc$
54	$\lambda_{c_c} = \lambda_{a_a};$	% Thermal conductivity in W/mK
55	$pelt_c = -6.2e-4*T0;$	% Peltier coefficient in J/C
56	$r0c = 1/42e6;$	% electr. Resistance in Ohm*m
57	$EA_rc = 1200*R;$	% Aktiv. energy in J/mol
59	$D_c = 5.4e-6;$	% Diffusion coeff. in m^2/s
59		
60	% Parameters for the anode CL	
61		
62	$\alpha_a = 0.5;$	% Symmetriefaktor Anode
63		
64	$\gamma_a = 24208247.87;$	% exp. Faktor in A/m^2
65	$EA_a = 72751.3496;$	% Aktivierungsenergie in J/mol
66		
67	$m_{H2} = 0.41;$	% Exponent
68	$m_{H2O} = 0.4;$	% Exponent
69		
70	% Parameters for the cathode GDL	
71		
72	$\alpha_c = 0.3;$	% Charge transfer coefficient
73		
74	$\gamma_c = 181733792067.07;$	% exp. factor in A/m^2
75	$EA_c = 156398.2586;$	% Act. energy in J/mol
76		

77	$m_{O_2} = 0.3;$	% Exponent
78		
79	% Molar enthalpy of reaction & Gibbs energies	
80		
81	$nu_{H_2} = -1;$	
82	$nu_{O_2} = -0.5;$	
83	$nu_{H_2O} = 1;$	
84	$nu_{O_Ion} = 1;$	% Relative to the cathode half reaction
85	$nu_{El} = -2;$	% Relative to the cathode half reaction
86		
87	$Cp_{O_2} = kabl('Cp','T',T0,'p',p0,'O_2');$	
88	$Cp_{H_2} = kabl('Cp','T',T0,'p',p0,'H_2');$	
89	$Cp_{H_2O} = kabl('Cp','T',T0,'p',p0,'H_2O');$	
90		
91	$H_{O_2} = kabl('H','T',T0,'p',p0,'O_2');$	
92	$H_{H_2} = kabl('H','T',T0,'p',p0,'H_2');$	
93	$H_{H_2O} = kabl('H','T',T0,'p',p0,'H_2O');$	
94		
95	$G_{O_2} = kabl('G','T',T0,'p',p0,'O_2');$	
96	$G_{H_2} = kabl('G','T',T0,'p',p0,'H_2');$	
97	$G_{H_2O} = kabl('G','T',T0,'p',p0,'H_2O');$	
98		
99	$S_{O_2} = kabl('S','T',T0,'p',p0,'O_2');$	
100	$S_{H_2} = kabl('S','T',T0,'p',p0,'H_2');$	
101	$S_{H_2O} = kabl('S','T',T0,'p',p0,'H_2O');$	
102	$S_{O_Ion} = 42;$	% Entropy of O ²⁻ ions in J/molK
103	$S_{El} = -1;$	% Entropy of the electrons in J/molK
104		
105	$DrH_{Cath} = 40.25e3;$	% Enthalpy of reaction at the cathode in J/mol
106	$G_{O_Ion} = DrH_{Cath} + 0.5 * H_{O_2} - T0 * S_{O_Ion};$	
107	$G_{O_Ion} = 0.0;$	
108		
109	$DrS = nu_{H_2O} * S_{H_2O} + nu_{H_2} * S_{H_2} + nu_{O_2} * S_{O_2};$	
110	$DrS_{Cath} = nu_{O_Ion} * S_{O_Ion} + nu_{O_2} * S_{O_2} + nu_{El} * S_{El};$	
111	$DrS_{An} = nu_{H_2O} * S_{H_2O} - nu_{El} * S_{El} + nu_{H_2} * S_{H_2} - nu_{O_Ion} * S_{O_Ion};$	
112		
113	% Nernst equation	
114		
115	$x_{H_2O} = 0.5;$	% Mole fraction H ₂ O
116	$x_{H_2} = 0.5;$	% Mole fraction H ₂
117	$x_{O_2} = 0.21;$	% Mole fraction O ₂
118		
119	$c_{H_2_0} = x_{H_2} * p0 / R / T0;$	% Concentration H ₂
120	$c_{H_2O_0} = x_{H_2O} * p0 / R / T0;$	% Concentration H ₂ O
121	$c_{O_2_0} = x_{O_2} * p0 / R / T0;$	% Concentration O ₂
122		
123	$DrG = nu_{H_2O} * G_{H_2O} + nu_{H_2} * G_{H_2} + nu_{O_2} * G_{O_2};$	
124	$Q = (x_{H_2O})^{nu_{H_2O}} * (x_{H_2})^{nu_{H_2}} * (x_{O_2})^{nu_{O_2}};$	
125		
126	$dphi0 = -1 / (2 * F) * (DrG + R * T0 * \log(Q));$	
127	$dphi0A = -1 / 2 * F * (-nu_{H_2O} * G_{H_2O} - nu_{H_2} * G_{H_2} + \dots$ $\quad nu_{O_Ion} * G_{O_Ion}) + R * T0 / 2 * F * \log(x_{H_2O} / x_{H_2});$	

```

128 dphi0C = -1/2/F*(nu_O2*G_O2+nu_O_Ion*G_O_Ion)+R*T0/2/F*log(x_O2^0.5);
129
130 diff = dphi0-(dphi0C-dphi0A);           % As proof
131
132 % Initial conditions and parameters for differential equations
133
134 xspan_a = [x0 ; xa];
135 xspan_e = [xa ; xa+xe];
136 xspan_c = [xa+xe ; xa+xe+xc];
137
138 % Solution for temperature y(1), potential y(2) and heat flux y(3)
139
140 for n=1:1:1000
141
142 % Anode GDL
143
144 y0a = [T0, phi0, Jq0];                 % Initial conditions
145
146 [x1,y] = ode45(@TphiJBulkAnArtikel,...
                xspan_a,y0a,[],j,lambda_a,pelt_a,r0a,EA_ra,Cp_H2,Cp_H2O);
147
148 Tma = y(end,1);
149 phima = y(end,2);
150 Jqma = y(end,3);
151
152 % Anode CL
153
154 Tsa = Tma;
155 Tea = Tsa;
156
157 etha_ap = -R*Tsa/2/F*log((1-j*xa/(c_H2_0*2*2*F*D_a))/(1+j*xa/(c_H2O_0*2*2*F*D_a)));
158 etha_aa = ButVol(j,alpha_a,gamma_a,EA_a,2,Tsa,x_H2,x_H2O,m_H2,m_H2O);
159
160 Sigma_sa = etha_aa*j/Tsa;
161
162 Jqea = Jqma-Tsa*DrS_An*j/2/F+sigma_sa*Tsa;
163
164 % Electrolyte
165
166 phi0e = phima-etha_aa-etha_ap-dphi0A;
167
168 y0e = [Tea, phi0e, Jqea];
169
170 [x2,y2] = ode45(@TphiJElektrolyt,xspan_e,y0e,[],z,Jo,Lqq,Lqo,Loq,Loo);
171
172 Tec = y2(end,1);
173 phiec = y2(end,2);
174 Jqec = y2(end,3);
175
176 % Cathode CL
177
178 Tsc = Tec;

```

```

179 Tmc = Tsc;
180
181 etha_cp = R*Tsc/2/2/F*log(1-j*xc/c_O2_0/2/2/F/D_c);
182 etha_ca = -ButVol(j,alpha_c,gamma_c,EA_c,2,Tsc,x_O2,1,m_O2,1);
183
184 sigma_sc = -etha_ca*j/Tsc;
185
186 Jqmc = Jqec-Tsc*DrS_Cath*j/4/F+sigma_sc*Tsc;
187
188 % Cathode GDL
189
190 phi0c = phiec+etha_ca+etha_cp+dphi0C;
191
192 y0c = [Tmc, phi0c, Jqmc];
193
194 [x3,y4] = ode45(@TphiJBulkCathArtikel,xspan_c,y0c,[],j,lambda_c,pelt_c,r0c,EA_rc,Cp_O2);
195
196 Tc = y4(end,1);
197 phic = y4(end,2);
198 Jqc = y4(end,3);
199
200 % Newton iteration
201
202 f1 = Tend-Tc;
203
204 if abs(f1) < 1e-34; break;
205 end
206
207 % 2nd iteration
208
209 % Anode GDL
210
211 dJq0 = abs(Jq0)*0.0001;
212 Jq02 = Jq0 + dJq0;
213
214 y0a = [T0, phi0, Jq02];
215
216 [x1,y1] = ode45(@TphiJBulkAnArtikel,...
                xspan_a,y0a,[],j,lambda_a,pelt_a,r0a,EA_ra,Cp_H2,Cp_H2O);
217
218 Tma = y1(end,1);
219 phima = y1(end,2);
220 Jqma = y1(end,3);
221
222 %% Anode CL
223
224 Tsa = Tma;
225 Tea = Tsa;
226
227 etha_ap = -R*Tsa/2/F*log(((1-j*xa/(c_H2_0*2*2*F*D_a))/(1+j*xa/(c_H2O_0*2*2*F*D_a))));
228 etha_aa = ButVol(j,alpha_a,gamma_a,EA_a,2,Tsa,x_H2,x_H2O,m_H2,m_H2O);
229

```

```

230 sigma_sa = etha_aa*j/Tsa;
231
232 Jqea = Jqma-Tsa*DrS_An*j/2/F+sigma_sa*Tsa;
233
234 % Elektrolyte
235
236 phi0e = phima-etha_aa-etha_ap-dphi0A;
237
238 y0e = [Tea, phi0e, Jqea];
239
240 [x2,y3] = ode45(@TphiJElektrolyt,xspan_e,y0e,[],z,Jo,Lqq,Lqo,Loq,Loe);
241
242 Tec = y3(end,1);
243 phiec = y3(end,2);
244 Jqec = y3(end,3);
245
246 % Cathode CL
247
248 Tsc = Tec;
249 Tmc = Tsc;
250
251 etha_cp = R*Tsc/2/2/F*log(1-j*xc/c_O2_0/2/2/F/D_c);
252 etha_ca = -ButVol(j,alpha_c,gamma_c,EA_c,2,Tsc,x_O2,1,m_O2,1);
253
254 sigma_sc = -etha_ca*j/Tsc;
255
256 Jqmc = Jqec-Tsc*DrS_Cath*j/4/F+sigma_sc*Tsc;
257
258 % Cathode GDL
259
260 phi0c = phiec+etha_ca+etha_cp+dphi0C;
261
262 y0c = [Tmc, phi0c, Jqmc];
263
264 [x3,y5] = ode45(@TphiJBulkCathArtikel,xspan_c,y0c,[],j,lambda_c,pelt_c,r0c,EA_rc,Cp_O2);
265
266 Tc = y5(end,1);
267 phic = y5(end,2);
268 Jqc = y5(end,3);
269
270 f2 = Tend - Tc;
271 df = f2 - f1;
272 dfdJq0 = df/dJq0;
273 Jq0 = Jq0 - f1/dfdJq0;
274
275 end

```

Function A1. MATLAB® function for the calculation of the anode GDL

```

1 function [dydx] = TphiJBulkAnArtikel(x,y,j,lambda,pelt,r0,EA,Cp1,Cp2)
2
3 % Matlab® function for the calculation of the anode GDL
4 % y(1)=T, y(2)=phi, y(3)=Jq

```

```

5
6 global R F
7
8 % Transport equations
9
10 dydx(1,1) = (pelt*j-y(3))/lambda;
11 r = r0*exp(EA/R/y(1));
12 dydx(2,1) = -pelt/y(1)*dydx(1,1)-r*j;
13
14 % Energy balance
15
16 dydx(3,1) = -j*(dydx(2,1)+1/2/F*(Cp1+Cp2)*dydx(1,1));
17
18 end

```

Function A2. MATLAB® function for the calculation of the cathode GDL

```

1 function [dydx] = TphiJBulkCathArtikel(x,y,j,lambda,pelt,r0,EA,Cp1)
2
3 % Matlab® function for the calculation of the cathode GDL
4 % y(1)=T, y(2)=phi, y(3)=Jq
5
6 global R F
7
8 % Transport equations
9
10 dydx(1,1) = (pelt*j-y(3))/lambda;
11 r = r0*exp(EA/R/y(1));
12 dydx(2,1) = -pelt/y(1)*dydx(1,1)-r*j;
13
14 % Energy balance
15
16 dydx(3,1) = -j*(dydx(2,1)-1/4/F*Cp1*dydx(1,1));
17
18 end

```

Function A3. MATLAB® function for the calculation of the electrolyte

```

1 function [dydx] = TphiJElektrolyt(~,y,z,Jo,Lqq,Lqo,Loq,Loo)
2
3 % Matlab® function for the calculation of the electrolyte
4 % y(1)=T, y(2)=phi, y(3)=Jq
5
6 global F
7
8 % Transport equations
9
10 dydx(1,1) = (y(3)-Lqo/Loo*Jo)/(-Lqq+Lqo*Loq/Loo)*(y(1)^2);
11 dydx(2,1) = (Jo+Loq/(y(1)^2)*dydx(1,1))/(-Loo*z*F/y(1));
12
13 % Energy balance
14
15 dydx(3,1) = -dydx(2,1)*Jo*z*F;

```

16
17 **end**

Function A4. MATLAB® function for the calculation of the CLs

```

1 function [etha] = ButVol(i, alpha, gamma, EA, z, T, x1, x2, m1, m2)
2
3 % Matlab® function for the calculation of the CLs
4
5 global R F
6
7 % Calculation of Butler-Volmer Kinetics for different overpotentials (-1 to 1) and interpolation
8
9 i0 =x1^m1*x2^m2*gamma*exp(-EA/R/T);
10 ethaall = (-1:0.0001:1);
11 iall = i0*(exp((1-alpha).*ethaall.*z*F/R/T)-exp(-alpha.*ethaall.*z*F/R/T));
12 etha = interp1(iall,ethaall,i);
13
14 end

```

To Chapter 4.5. *Interaction of the Publications*

In Table A1, the calculated values for the lattice constant a and the phenomenological coefficients L_{00} of the ions are summarized for different YSZ compositions at 1300 K. The mean values are taken from the data presented in Paper I, but the error is estimated using the methodology reported in Paper III.

Table A1. Calculated lattice constant a and phenomenological coefficients L_{qq} , L_{00} and L_{0q} from Paper I, but with a new error estimation following the methodology given in Paper III.

YSZ	a Å	L_{qq} WK/μm	$N_A L_{00}$ mol · K(J · cm · fs) ⁻¹	RL_{0q} W/m
YSZ04	5.148820(44)	7.21(24)	4.47(26)	-0.70(35)
YSZ08	5.160489(81)	6.21(14)	3.75(26)	-0.81(38)
YSZ12	5.17073(15)	5.37(27)	2.47(19)	-0.77(42)
YSZ16	5.17935(15)	4.85(34)	1.72(12)	-0.55(31)
YSZ20	5.18714(24)	4.54(16)	1.17(18)	-0.48(20)
YSZ24	5.19494(34)	4.17(17)	0.86(13)	-0.34(22)

In Table A2, the calculated values for the electrostatic potential φ_i of the ions are summarized for different YSZ compositions at 1100 K, 1300 K and 1500 K. The mean values are taken from the data presented in Paper II, but the error is estimated using the methodology reported in Paper III.

For the test of the hypothesis $H_{03}: \bar{\varphi}_O|_{1100\text{ K}}^{1500\text{ K}} = \varphi_O(T)$ against $H_{03}: \bar{\varphi}_O|_{1100\text{ K}}^{1500\text{ K}} \neq \varphi_O(T)$, the value

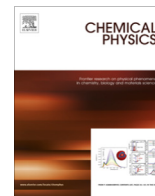
$$z_X = \frac{\bar{X} - X(T)}{\sigma_X} \sqrt{n_X} \quad (\text{A-1})$$

is calculated following the methodology given in the SI of Paper III, where σ_X is the corrected standard deviation, n_X the number of samples and $X = \varphi_O(\text{Y}_2\text{O}_3)$. We reject the hypothesis H_{03} if $|z_X| > u_{0.975} = 1.96$. The calculated values for $|z_{\varphi_O(\text{Y}_2\text{O}_3)}|$ of 1.30 at 1100 K, 0.67 at 1300 K and 1.96 at 1500 K do not meet the mentioned condition and, thus, the hypothesis cannot be rejected within the studied temperature range.

Table A2. Calculated electrostatic potential φ_i of the ions in YSZ at 1100 K, 1300 K and 1500 K and for different Y_2O_3 concentrations. While the average values are taken from Paper II, the error estimation is done using the methodology reported in Paper III.

φ_O in eV	YSZ04	YSZ08	YSZ12	YSZ16
1100 K	23.2790(13)	23.3047(18)	23.3194(31)	23.3163(36)
1300 K	23.30310(95)	23.3347(12)	23.3349(20)	23.3315(21)
1500 K	23.32750(92)	23.3441(12)	23.3532(13)	23.3458(21)
φ_O in eV	YSZ20	YSZ24	YSZ28	Y_2O_3
1100 K	23.3057(66)	23.2851(46)	23.2595(31)	22.3869(36)
1300 K	23.3180(41)	23.2972(61)	23.2706(54)	22.3880(43)
1500 K	23.3307(45)	23.3085(31)	23.27980(92)	22.3927(37)
φ_{Zr} in eV	YSZ04	YSZ08	YSZ12	YSZ16
1100 K	-42.4934(17)	-42.4527(35)	-42.4279(45)	-42.4095(70)
1300 K	-42.4330(16)	-42.3904(31)	-42.3676(39)	-42.3487(69)
1500 K	-42.3714(11)	-42.3283(32)	-42.3048(32)	-42.2867(57)
φ_{Zr} in eV	YSZ20	YSZ24	YSZ28	Y_2O_3
1100 K	-42.406(12)	-42.4151(74)	-42.4209(96)	-
1300 K	-42.3453(93)	-42.3533(98)	-42.361(11)	-
1500 K	-42.282(10)	-42.291(10)	-42.3009(83)	-
φ_Y in eV	YSZ04	YSZ08	YSZ12	YSZ16
1100 K	-32.085(16)	-31.885(17)	-31.737(14)	-31.6476(91)
1300 K	-32.041(18)	-31.838(19)	-31.683(12)	-31.594(12)
1500 K	-31.993(18)	-31.787(19)	-31.632(13)	-31.541(10)
φ_Y in eV	YSZ20	YSZ24	YSZ28	Y_2O_3
1100 K	-31.569(19)	-31.489(11)	-31.4381(80)	-31.3133(35)
1300 K	-31.512(17)	-31.434(14)	-31.381(10)	-31.2569(38)
1500 K	-31.456(19)	-31.382(12)	-31.3263(77)	-31.2001(39)

I



A phenomenological study of yttria-stabilized zirconia at 1300 K with the Green-Kubo formulation and equilibrium molecular dynamics



G. Valadez Huerta*, A. Kelle, S. Kabelac

Institut für Thermodynamik, Gottfried-Wilhelm Leibniz Universität Hannover, Callinstr. 36, D-30167 Hannover, Germany

ARTICLE INFO

Article history:

Received 17 October 2016

In final form 25 January 2017

Available online 1 February 2017

ABSTRACT

In this study, we analyze the transport mechanisms in different yttria-stabilized zirconia compositions as an example for an ionic solid at 1300 K and zero pressure with EMD and the Green-Kubo formulation. As it can be interpreted from the partial and the total correlation functions of the micro fluxes, a certain amount of anions should be given to activate the diffusion of other anions. An incomplete vacancy diffusion favors the coupled effect of heat and diffusion. The heat conduction decreases for higher concentration of vacancies and the optimum of the diffusion is reproducible with this method. We predict a minimum of the thermo-diffusion conductivity at 10 mol% Y_2O_3 . The understanding of the heat and electrical conduction of ionic solids and of the couple effect is essential in systems, where the gradients of different kind of forces are present.

© 2017 Elsevier B.V. All rights reserved.

1. Introduction

There are many approaches to describe the transport mechanisms in gases, liquids and solids. Usually, these are depicted by empirical equations and empirical kinetic coefficients, such as Fourier's law for thermal conduction, Fick's law and the Maxwell-Stefan diffusion models (see [1,2]). These types of empirical equations are part of current research, e.g., in the case of rarefied gases [3] and nanofluids [4]. This is because of their measurability and easy handling describing the kinetics of simple or, to a limited extent, complex systems.

A more general approach is given by the non-equilibrium thermodynamics. This theory was developed in the works of Onsager [5,6] and the later works of Prigogine [7,8]. In this theory the flux of an extensive thermodynamic state quantity is correlated to all the thermodynamic forces in the system and not only to a single force. With \mathbf{J}_i as a generalized flux and \mathbf{X}_j as a generalized force, the set of phenomenological equations in a system of K forces is given by

$$\mathbf{J}_i = \sum_{j=1}^K L_{ij} \mathbf{X}_j. \quad (1)$$

L_{ij} are the phenomenological coefficients. Every flux \mathbf{J}_i has a conjugate force \mathbf{X}_i . With the conjugate forces and fluxes it is possible to calculate the entropy production rate of the system as follows

$$\dot{\sigma} = \sum_{i=1}^K \mathbf{J}_i \mathbf{X}_i. \quad (2)$$

Thus, the second law of thermodynamics becomes quantifiable for the analyzed system. A system of K fluxes and K forces produces a matrix of phenomenological equations with K^2 components that has to be determined. Due to the Onsager relations

$$L_{ij} = L_{ji}, \quad (3)$$

the number of independent coefficients reduces to the upper or the lower triangular matrix elements including the diagonal components. It is difficult to determine experimentally the influence of a single force on the different fluxes, especially when the influence is small. Nevertheless, these calculations can be done using methods such as non-equilibrium molecular dynamics (NEMD).

Several works have already described the kinetics of non-ionic fluids, ionic fluids and solids with NEMD (see, e.g., [9–11]). The works of Reith et al. [12] and MacGowan et al. [13] concerning Lennard-Jones fluids provide examples for the calculation of these coefficients for non-ionic binary systems. The main idea is to set a temperature gradient on the system and calculate the heat and concentration gradient. Due to Eq. (1) and Eq. (3), all four coefficients can be calculated with the knowledge of these two gradients and the heat flux, since in a stationary state there is no net mass flux for a closed system.

By applying this approach in ionic systems, the influence of the Coulomb interactions in the transport coefficients cannot be clarified or analyzed in detail. However, a better method is to calculate the coefficients via the Green-Kubo (GK) formula and equilibrium

* Corresponding author.

E-mail address: valadez@ift.uni-hannover.de (G. Valadez Huerta).

molecular dynamics (EMD). In this case the contributions of each kind of force can be analyzed independently (see, e.g., [14]). Further, the phenomenological coefficients can be calculated with the correlation function of the fluxes as follows

$$L_{ij} = \frac{V}{3k_B} \int_0^\infty \langle \mathbf{J}_i(0) \mathbf{J}_j(t) \rangle dt \quad (4)$$

where V is the volume of the system and k_B is the Boltzmann constant. The symmetrical character of the coefficients, due to the Onsager-Relations, is automatically given in this approach. The works of Arima et al. [15,16] are examples of implementing this method in ionic solids to calculate the thermal conductivity and other empirical coefficients based on the phenomenological coefficients.

In comparison to these works, we calculate the set of phenomenological coefficients using non-equilibrium thermodynamics in order to obtain a better understanding of the kinetics of the well-known ceramic yttria stabilized zirconia (YSZ). This material is chosen because of its significance in electrochemical applications (see [17,18]). We analyze different configurations at a temperature of 1300 K, since at this temperature the oxygen anion diffusion is already activated.

2. Theory

The embedding of yttrium(III) oxide Y_2O_3 into zirconium dioxide ZrO_2 to form YSZ results in oxygen vacancies. If we consider ion diffusion of the ion species O^{2-} , Zr^{4+} and Y^{3+} , we can write the following general relation for the entropy production rate:

$$\frac{\dot{\sigma}}{k_B} = \mathbf{J}_q \nabla \beta + \sum_{k=1}^3 \mathbf{J}_k \nabla (-\beta \eta_k). \quad (5)$$

The heat flux \mathbf{J}_q is the conjugate flux to the reciprocal of the thermodynamic temperature $\beta = 1/(k_B T)$. This correspondence is also the case for the molar ion flux \mathbf{J}_k and the force $\nabla(\beta \eta_k)$. Here, η_k denotes the electrochemical potential of the ion species k given by the expression:

$$\eta_k = \mu_k + z_k F \phi, \quad (6)$$

where μ_k is the chemical potential of the species k , z_k its valency, F the Faraday constant and ϕ the local electrical potential in the YSZ bulk crystal.

At high temperatures (e.g., 1000 °C, see [19]) the oxygen anions O^{2-} diffuse along the vacancies. The diffusion of the zirconium and yttrium cations takes place at temperatures higher than 2000 K [20] and therefore can be neglected. Based on these assumptions the system can be described by two fluxes (the heat flux \mathbf{J}_q and the anion molar flux \mathbf{J}_O) and their conjugate forces ($\nabla \beta$ and $\nabla(-\beta \eta_O)$ respectively).

The phenomenological equations from Eq. (1) can then be written as

$$\frac{\mathbf{J}_q}{k_B} = L_{qq} \nabla \beta + L_{qO} \nabla (-\beta \eta_O), \quad (7)$$

$$\frac{\mathbf{J}_O}{k_B} = L_{Oq} \nabla \beta + L_{OO} \nabla (-\beta \eta_O), \quad (8)$$

with the Onsager relation

$$L_{qO} = L_{Oq}. \quad (9)$$

Finally, the GK formulae can be applied for the calculation of the phenomenological coefficients:

$$L_{qq} = \frac{V}{3k_B} \int_0^\infty \langle \mathbf{J}_q(0) \mathbf{J}_q(t) \rangle dt, \quad (10)$$

$$L_{OO} = \frac{V}{3k_B} \int_0^\infty \langle \mathbf{J}_O(0) \mathbf{J}_O(t) \rangle dt, \quad (11)$$

$$L_{Oq} = \frac{V}{3k_B} \int_0^\infty \langle \mathbf{J}_O(0) \mathbf{J}_q(t) \rangle dt. \quad (12)$$

In this work we use classical EMD to calculate the microscopic fluxes. The heat flux can be described by a given interatomic potential $u(r_{ij})$ as follows

$$\mathbf{J}_q = \frac{1}{V} \left[\frac{1}{2} \sum_{i=1}^N (m_i v_i^2 + \sum_{j \neq i}^N u(r_{ij})) \mathbf{v}_i + \sum_{i=1}^N \sum_{j \neq i}^N \mathbf{r}_{ij} (\mathbf{f}_{ij} \cdot \mathbf{v}_i) \right]. \quad (13)$$

The first summation includes the contributions of the kinetic and potential energy to the heat flux. The second summation is done over the stress tensor. If the Coulomb contributions are integrated, e.g., with the Ewald formulation, the stress tensor may be calculated as suggested by Heyes [21].

The calculation of the molar oxygen anion flux can be described with the approach of Vogelsang et al. [22]:

$$\mathbf{J}_O = \frac{1}{N_A V} \sum_{i=1}^{N_O} \mathbf{v}_i, \quad (14)$$

where N_A is the Avogadro constant.

However, some remarks have to be made at this point. Firstly, another choice of forces and conjugate fluxes to describe the entropy production rate is possible (see, e.g., [23]). Secondly, all the fluxes are defined as per area fluxes. Thirdly, it is known from other works (see, e.g., [24]) that the partial molar enthalpies of the components should be subtracted in Eq. (13) to calculate the heat flux. This is only true, however, if the thermodynamic force of the electrochemical potential is defined at constant temperature, i.e., $\nabla_T(-\beta \eta_O)$. Finally, in comparison to Vogelsang et al. [22], we calculate a molar flux in Eq. (14), not a mass flux.

3. System, interatomic potential and state

Zirconium dioxide ZrO_2 has a cubic fluorite structure [25]. This structure is stabilized with yttrium(III) oxide Y_2O_3 to form YSZ. As a result of the combination, oxygen vacancies arise [26] (see Fig. 1).

To build the start configuration for our MD simulations, we use the method presented, e.g., by Sizov et al. [27]. The starting point is

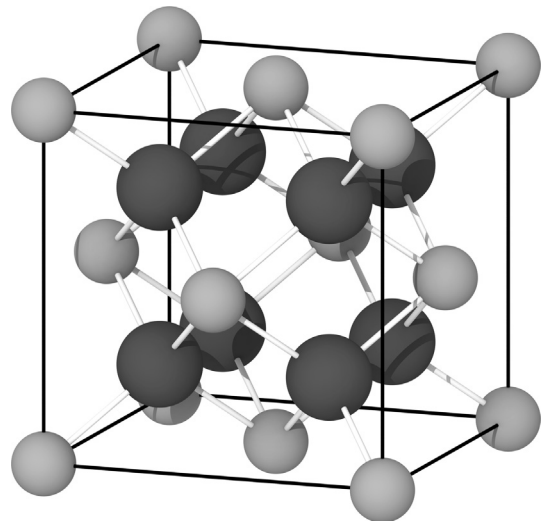


Fig. 1. YSZ cubic structure. In light grey, Zr or Y atoms. In dark grey, O atoms or vacancies v_O . The figure was rendered using the visualization tool OVITO of Stukowsky [29].

Table 1
YSZ configurations.

YSZ	$x_{Y_2O_3} \cdot 10^2$	N_{Zr}	N_O	N_Y
YSZ04	3,95	462	981	38
YSZ08	7,99	426	963	74
YSZ10	9,89	410	955	90
YSZ12	12,08	392	946	108
YSZ16	15,97	362	931	138
YSZ20	19,90	334	917	166
YSZ24	24,00	306	903	194

Table 2
Potential parameters.

	A_{ij} (eV)	ρ_{ij} (Å)	C_{ij} (eVÅ ⁶)
Zr ⁴⁺ -O ²⁻	1502,11	0,345	5,1
Y ³⁺ -O ²⁻	1366,35	0,348	19,6
O ²⁺ -O ²⁻	9547,96	0,224	32,0

given through the cubic fluorite structure of zirconium dioxide. We choose a $5 \times 5 \times 5$ lattice simulation box. Sizov et al. [27] and Devanathan et al. [28] analyze the finite size effects on the MD simulation results for YSZ systems concluding this simulation box size to be appropriate. Primarily, this simulation box consists of 1000 oxygen anions O²⁻ and 500 zirconium cations Zr⁴⁺. Randomly, a zirconium cation is chosen and substituted with a yttrium cation Y³⁺, whereby, for every two substitutions, one oxygen anion is removed until the desired mole fraction $x_{Y_2O_3}$ of Y₂O₃ is achieved. The electro neutrality of the configurations built in this manner is always checked.

The lattice constant a for each start configuration is considered to be temperature dependent only with the following relation given by Li et al. [30]:

$$a = 5.136 \text{ \AA} \cdot (1 + 10^{-5} (T/K - 300)). \quad (15)$$

In this work, we analyze systems with different mole fractions of Y₂O₃, namely YZ04 (i.e., 4 mol% Y₂O₃), YSZ08, YSZ12, YSZ16, YSZ20 and YSZ24. For validation of our model, we use a YSZ10 composition. The mole fraction and the number of ions in each configuration are summarized in Table 1.

The interatomic interactions are described with the Buckingham-Potential and a Coulomb term:

$$u(r_{ij}) = A_{ij} e^{-\frac{r_{ij}}{\rho_{ij}}} - \frac{C_{ij}}{r_{ij}^6} + \frac{q_i q_j}{4\pi\epsilon_0 r_{ij}}. \quad (16)$$

We choose the parameter set of Schelling and Phillpot [31] given in Table 2.

We analyze a thermodynamic state at a temperature of 1300 K. The simulations are done in the canonical ensemble with the volume at zero pressure.

4. Computational details

The calculations are performed using the LAMMPS¹ algorithm [32]. The MD approach in this study is strictly classical. In all simulations periodic boundary conditions apply and the cutoff radius is set to 10 Å for all interatomic interactions. The equations of motion are integrated with the standard Verlet algorithm. The long-range Coulomb interactions are calculated with the Ewald formulation. The accuracy of the RMS force error in the real space calculation is set to 10^{-4} of the force of a single pair interaction, estimated as done by Petersen [33].

The integration time step is set to 0.5 fs. In all simulations we assign a Gaussian velocity distribution to all atoms of the start configuration and the system is equilibrated for 1 ns. After this equilibration, a production run of 0.5 ns takes place. Velocities and positions of the atoms are recorded at each time step.

All our calculations are done in the Nosé-Hoover NpT and the Nosé-Hoover canonical ensemble. For the calculations in the NpT ensemble the damping parameter for the temperature is set to

0.1 ps and the damping parameter for the pressure to 1.0 ps. For the calculations in the canonical ensemble the damping parameter of the temperature is the same as in the NpT ensemble.

The simulations are done for fifteen independent start configurations for each mole fraction (see section III) of Y₂O₃ at 1300 K and ten extra configurations of YSZ10 at 1125 K for validation.

For each start configuration we calculate the mean lattice constant at zero pressure with the data of the production run of a simulation in the NpT ensemble. Thereafter, the system is simulated in the canonical ensemble. Here, the volume of the simulation box is scaled, so that the lattice constant a matches the calculated mean lattice constant. The production run in the canonical ensemble is used to calculate the radial distribution functions (RDFs) of YSZ10 and the phenomenological coefficients of the other YSZ compositions.

In the latter case, we recalculate the interatomic forces with the protocol of the production run, but assuming non charged atoms. Hence, the Coulomb contributions are the difference of the potential forces with and without charges.

The RDFs and the correlation functions of the microscopic fluxes are calculated with self-developed algorithms. For the calculation of the RDFs, the configurations at each 5 fs are used with a cutoff radius of 6 Å discretized into 100 bins. We average the correlation functions over the whole production time, but the correlation time for their integration is different in all cases.

To check the repeatability of our simulations, the error was calculated with the standard block averaging method as reported by Friedberg et al. [34] for properties such as the lattice constant and with the correlation time as suggested, e.g., by Zwanzig et al. [35] for the correlation functions. In the case of the phenomenological coefficients, we determine the mean value of the fifteen calculated values for each mole fraction of YSZ and estimate the error with the corrected sample standard deviation. We do not proceed with further calculations to estimate an error of the RDFs, because they are only used for validation.

5. Results and discussion

5.1. Model validation

In Fig. 2 the RDFs of the oxygen anions to the other anions and to the cations are shown. The results agree very well with the simulation data reported earlier [28]. Therefore, our assumptions for the calculation process seem to be appropriate.

5.2. Conductivity L_{qq}

We calculate the conductivity L_{qq} by integrating the autocorrelation function (ACF) of the microscopic heat flux $\langle \mathbf{J}_q(0) \mathbf{J}_q(t) \rangle$ (see Eq. (10)). In Fig. 3 the calculated mean ACF of the microscopic heat flux is shown for various YSZ compositions normalized with $\langle \mathbf{J}_q(0) \mathbf{J}_q(0) \rangle_{\text{YSZ24}}$. The transported heat flux is proportional to the value $\langle \mathbf{J}_q(0) \mathbf{J}_q(0) \rangle$. Since this value is larger for higher concentrations of Y₂O₃, the heat flux increases for higher vacancy concentrations. In all cases, the ACF progresses in an oscillatory behavior typical for solids. Due to the dense state, the ions may be trapped in a local region and they are forced to bounce in this restricted

¹ <http://lammps.sandia.gov>.

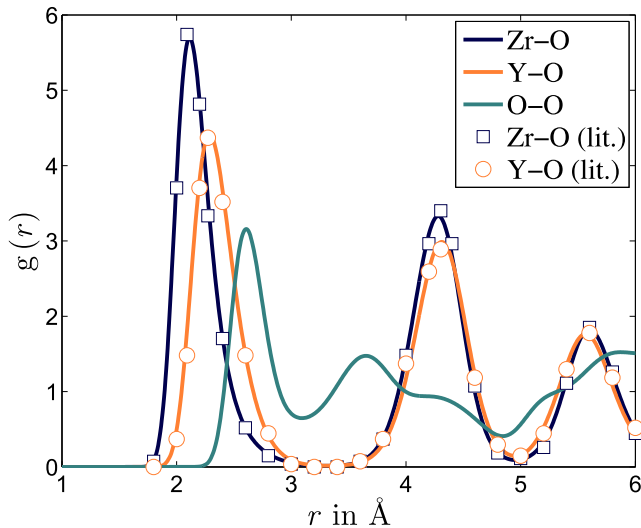


Fig. 2. Calculated RDF of Zr-O (dark blue line), Y-O (orange line) and O-O (green line) for YSZ10 at 1125 K in comparison to literature data [28] for Zr-O (squares) and Y-O (circles) (For interpretation of the references to color in this figure legend, the reader is referred to the web version of this article.)

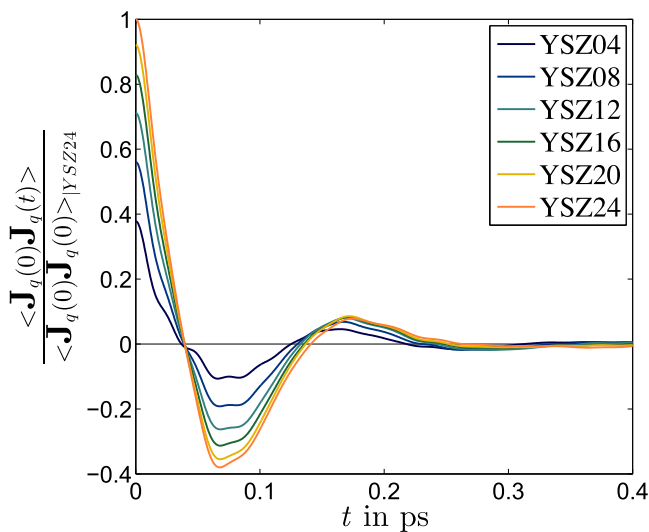


Fig. 3. Calculated mean partial ACF of the heat flux for various YSZ compositions at 1300 K normalized with the value $\langle \mathbf{J}_q(0)\mathbf{J}_q(0) \rangle_{\text{YSZ24}}$

environment. In this case, the ACF becomes negative. For higher vacancy concentrations, the ions have a larger range of motion. This results in a longer relaxation time.

To analyze this in more detail, we calculate the partial ACFs of the heat flux of the Coulomb (ϕ), the virial (V) and the kinetic (K) terms. In Fig. 4 these partial ACFs and the total ACF of the heat flux are plotted normalized with the value $\langle \mathbf{J}_q(0)\mathbf{J}_q(0) \rangle$ representative for the configuration YSZ12. The kinetic contribution is small enough to be neglected. The biggest contribution to the ACF of the heat flux is made by the Coulomb forces. The duration of the negative part of the curve is longer for the Coulomb partial ACF than for the virial partial ACF. The virial interatomic interactions are only cation-anion and anion-anion interactions, as determined by the chosen interatomic potential. In addition to these interactions, Coulomb forces also include cation-cation interactions, which result in the longer relaxation time.

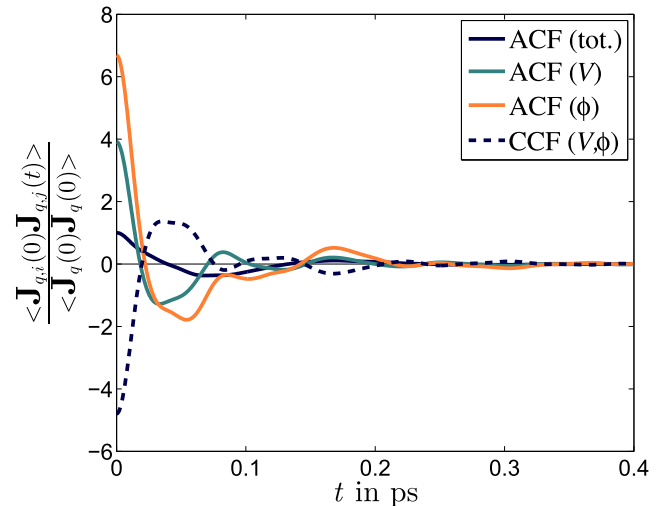


Fig. 4. Calculated mean partial ACFs of the Coulomb (ϕ) term (solid orange line), the virial (V) term (solid green line) of the heat flux, partial CCF of both terms (dashed dark blue line) and total ACF (solid dark blue line) of the heat flux for YSZ12 at 1300 K normalized with the value $\langle \mathbf{J}_q(0)\mathbf{J}_q(0) \rangle$ (For interpretation of the references to color in this figure legend, the reader is referred to the web version of this article.)

As the Coulomb partial ACF and the virial partial ACF surpass the total ACF in size, the heat fluxes of the Coulomb and the virial terms may flow in opposite directions. That means the contribution to the total ACF of the mixed term of the Coulomb and the virial heat fluxes cannot be neglected. Therefore, we plot the cross correlation function (CCF) $\langle \mathbf{J}_{q,v}(0)\mathbf{J}_{q,\phi}(t) \rangle$ in Fig. 4. As expected, the CCF has a different sign than the ACFs. So, the net transported heat flux decreases.

In Fig. 5 and in Fig. 6 the Coulomb partial ACF and the virial partial ACF are plotted for various YSZ compositions, respectively. The initial value $\langle \mathbf{J}_{q,v}(0)\mathbf{J}_{q,v}(0) \rangle$, which is proportional to the heat flux due to the virial contributions, seems not to be affected by the Y_2O_3 concentration. However, for the Coulomb part a higher concentration of Y_2O_3 leads to a bigger partial heat flux, which agrees with the total heat flux.

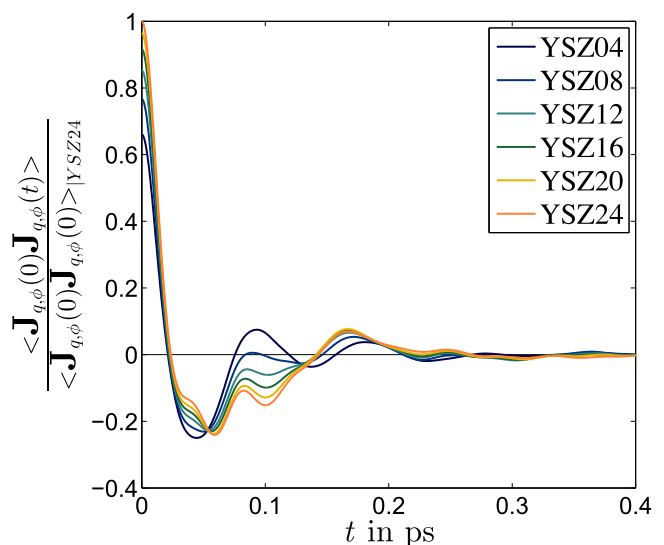


Fig. 5. Calculated mean partial ACF of the Coulomb term (ϕ) of the heat flux for various YSZ compositions at 1300 K normalized with the value $\langle \mathbf{J}_{q,\phi}(0)\mathbf{J}_{q,\phi}(0) \rangle_{\text{YSZ24}}$.

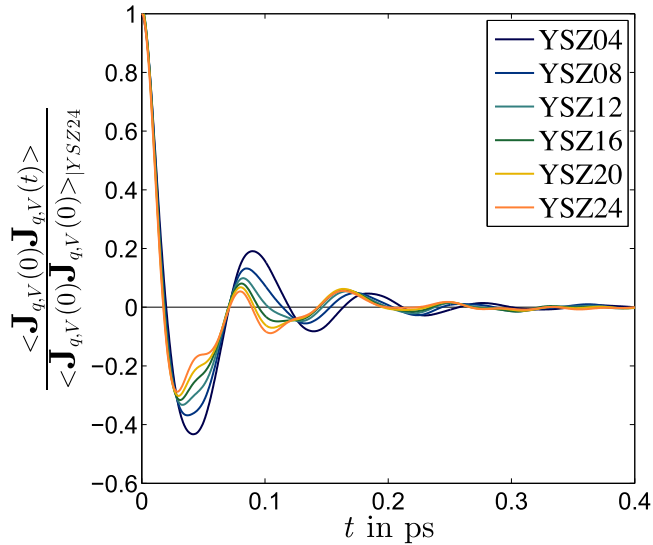


Fig. 6. Calculated mean ACF of the virial (V) term of the heat flux for various YSZ compositions at 1300 K normalized with the value $\langle \mathbf{J}_{q,V}(0)\mathbf{J}_{q,V}(0) \rangle_{\text{YSZ24}}$.

Fig. 5 shows that the second maximum of the Coulomb partial ACF decreases as the Y_2O_3 concentration increases and becomes negative for the concentrations above YSZ08. The long relaxation time is characteristic for a liquid behavior with a wider range of motion of the molecules. However, the local fluctuations indicate a higher probability of collisions, as is typical in solids.

As shown in Fig. 6, the virial partial ACF is vertically compressed after the first x-intercept as the vacancy concentration increases. At higher vacancy concentrations there is a smaller probability of collisions. Additionally, the cation-cation interactions are not taken into account. Both factors result in less heat being transferred.

In order to calculate the conductivity L_{qq} , an arbitrary correlation time should be determined from the mean total ACF. As seen in Fig. 3 the curve seems to be decayed to zero at around 0.3 ps for all configurations. However, due to the relatively strong fluctuations after the decay, it is difficult to determine a specific correlation time. Therefore, it is suitable to take the mean value of a certain interval after 0.3 ps. In addition, the initial value of the averaging should not lay too close to the decay point of the curve and it should not be stretched to the last values of the correlation function, because the last values are averaged over too few time origins.

The results of the conductivity L_{qq} and its error are summarized in Table 3 for two different averaging intervals, i.e., 1–1.5 ps and 1–2 ps. The calculated mean value does not seem to be affected by the time interval we choose. However, in most cases the error of the results increases slightly for the longer interval. Hence, we use the mean value $[\bar{L}_{qq}]_{1\text{ps}}^{1.5\text{ps}}$ for further discussion.

The calculated values of the conductivity L_{qq} of YSZ are shown in Fig. 7. A higher conductivity can be seen for smaller Y_2O_3

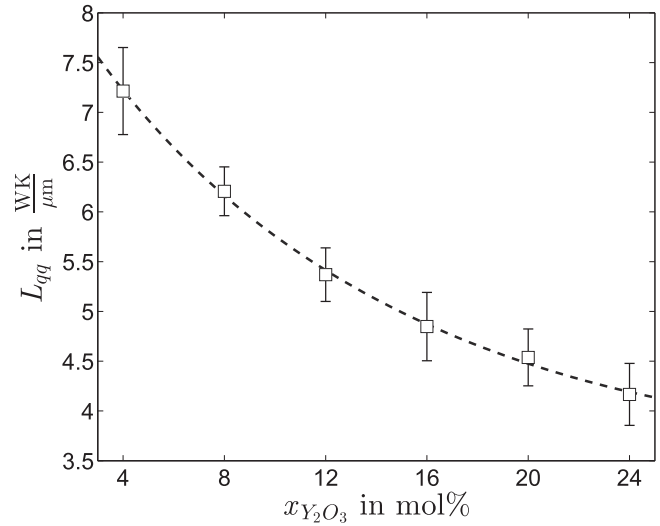


Fig. 7. Calculated conductivities L_{qq} for various YSZ compositions (squares) at 1300 K and trend curve (dashed blue line).

concentrations. Despite, the bigger heat flux for higher vacancy concentrations, i. e., a bigger positive area under the total ACF, the negative area under the curve is big enough to compensate the positive area.

5.3. Conductivity L_{00}

To calculate the conductivity L_{00} the time integral of the ACF of the anion molar flux given in Eq. (11) has to be determined. The mean ACF normalized with the value $\langle \mathbf{J}_0(0)\mathbf{J}_0(0) \rangle_{\text{YSZ04}}$ is shown for various YSZ compositions in Fig. 8. The initial value $\langle \mathbf{J}_0(0)\mathbf{J}_0(0) \rangle$ of the ACF decreases slightly for higher concentrations of Y_2O_3 . Since the flux is a per area flux and the excess volume of the mixture of ZrO_2 and Y_2O_3 is positive, the volume increases with the number of vacancies. As the anion molar flux is calculated in mol/m^2 , the volume appears in the denominator of its definition in Eq. (14).

The second positive area of the ACF of the molar anion flux decreases for higher vacancy concentrations, similar to the partial

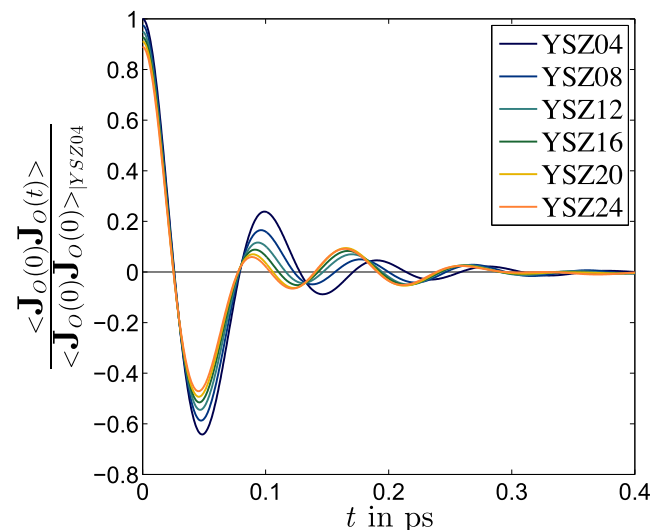


Fig. 8. Calculated mean ACF of the anion molar flux for various YSZ compositions at 1300 K normalized with the value $\langle \mathbf{J}_q(0)\mathbf{J}_q(0) \rangle_{\text{YSZ04}}$.

Table 3

Calculated conductivities L_{qq} for YSZ at 1300 K and two different averaging time intervals.

YSZ	$[\bar{L}_{qq}]_{1\text{ps}}^{1.5\text{ps}}$ (WK/ μm)	$[\bar{L}_{qq}]_{1\text{ps}}^{2\text{ps}}$ (WK/ μm)
YSZ04	7.21 ± 0.44	7.22 ± 0.47
YSZ08	6.21 ± 0.25	6.24 ± 0.29
YSZ12	5.37 ± 0.27	5.35 ± 0.28
YSZ16	4.85 ± 0.34	4.85 ± 0.38
YSZ20	4.54 ± 0.29	4.56 ± 0.36
YSZ24	4.17 ± 0.31	4.18 ± 0.30

Table 4
Calculated conductivities L_{OO} for YSZ at 1300 K.

YSZ	$N_A L_{OO} \left(\frac{1}{\text{cm fs}} \right) \left(\frac{\text{J}}{\text{molK}} \right)^{-1}$
YSZ04	4.47 ± 0.47
YSZ08	3.75 ± 0.47
YSZ12	2.47 ± 0.35
YSZ16	1.72 ± 0.22
YSZ20	1.17 ± 0.35
YSZ24	0.86 ± 0.24

ACFs of the heat flux in Figs. 5 and 6. This implicates a better diffusion for the anions. After that, the oscillations become stronger in a solid like behavior. Additionally, the curve is compressed horizontally starting from the first x-intercept. That means, the anion diffusion has a shorter life time for higher vacancy concentration.

We calculate the conductivities L_{OO} with the same method we used for the conductivities L_{qq} . Additionally, we check the correctness of our results by averaging the conductivities at different time intervals. The results for an averaging time interval of 1–2 ps are summarized in Table 4. Assuming a negligible conductivity L_{OO} for pure ZrO_2 , a maximum between the conductivities for YSZ04 and YSZ08 should be present, since the progression of the ACF adapts to an optimum of the positive area under the curve.

Despite the increasing number of vacancies for higher Y_2O_3 concentrations, the oxygen anions jump back into their start position instead of hopping completely from their lattice site to an adjacent vacancy. In this case, the higher vacancy concentrations result in an increased mobility of the oxygen anions. However, the corresponding decrease in anion concentration reduces the collective motions which provide the necessary activation energy for the vacancy diffusion and prevent anions from returning to their original lattice site. Due to this cooperative mechanism, i. e., high mobility and a sufficient amount of anions for the collective motions, there is an optimal configuration with a maximal conductivity L_{OO} . This maximum has been observed experimentally and discussed extensively for YSZ where the optimal electrical conductivity occurs at 8 mol% of Y_2O_3 [18]. The data obtained using EMD simulation and the GK formulation supports this statement, however, our maximum lies at 5 mol% Y_2O_3 .

The simulated data of the conductivity L_{OO} is shown in Fig. 9 with a trend curve assuming a negligible conductivity L_{OO} for ZrO_2 , as stated before.

5.4. Conductivity L_{Oq}

To calculate the conductivity L_{Oq} Eq. (12) has to be solved and the CCF of the heat flux and the molar anion flux $\langle \mathbf{J}_O(0) \mathbf{J}_q(t) \rangle$ has to be integrated over the time. The CCF describes a combination of the transport mechanism of the molar anion flux due to a temperature gradient in a Soret-type behavior and the transport mechanism of the heat flux due to a concentration gradient in a Dufour-type behavior. Fig. 10 shows the mean CCF for various YSZ compositions normalized with the absolute value $|\langle \mathbf{J}_O(0) \mathbf{J}_q(0) \rangle|_{\text{YSZ24}}$. The initial value $\langle \mathbf{J}_O(0) \mathbf{J}_q(0) \rangle$ is negative in all cases. Therefore, the heat flux and the anion molar flux are transported in opposite directions.

The duration of the first positive part of the CCF is short for small vacancy concentrations, whereas the following negative part decays slowly. For higher vacancy concentrations, the positive part stretches horizontally. In this case the CCF resembles the heat flux ACF but with the opposite sign (see Fig. 3). Therefore, the transport mechanism is similar to a heat transfer and thus has a Dufour-type behavior. For smaller Y_2O_3 concentrations, the Soret-type behavior is noticeable in the overlying oscillations which correspond to the anion molar flux ACF (see Fig. 8).

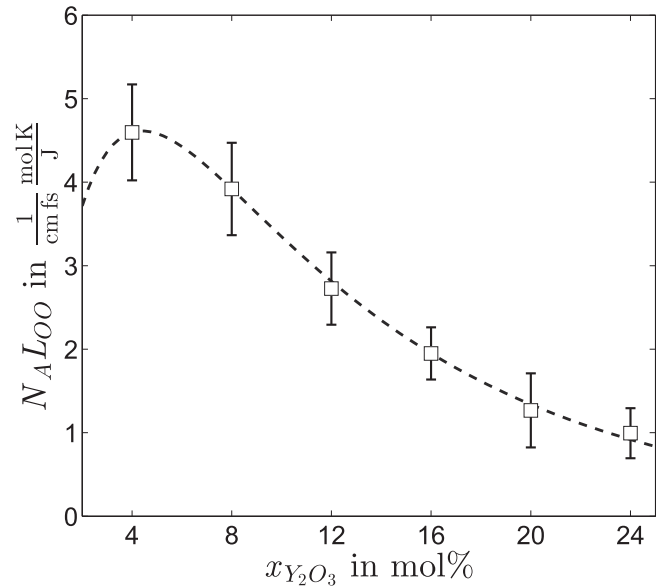


Fig. 9. Calculated conductivities L_{OO} for various YSZ compositions (squares) and trend curve (dashed blue line).

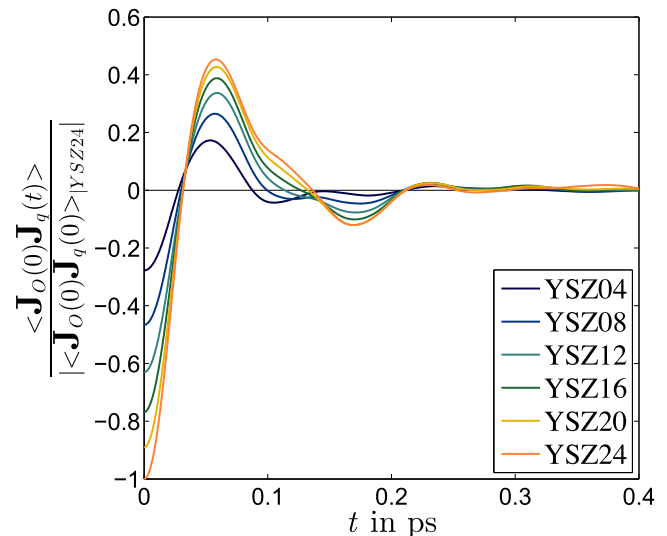


Fig. 10. Calculated mean CCF of the heat flux and the anion molar flux for various YSZ compositions at 1300 K normalized with the absolute value $|\langle \mathbf{J}_O(0) \mathbf{J}_q(0) \rangle|_{\text{YSZ24}}$.

In Fig. 11, we plot the total CCF ($O, \text{tot.}$), the Coulomb partial CCF (O, ϕ) and the virial partial CCF (O, V) normalized with the absolute value $|\langle \mathbf{J}_O(0) \mathbf{J}_q(0) \rangle|$ for YSZ12. The kinetic contribution is too small to have any mentionable influence and therefore is not taken into account.

The initial value of the Coulomb partial CCF is negative, whereas that of the virial partial CCF is positive. The Coulomb heat flux flows in the opposite direction of the virial heat and the anion molar flux. Both partial CCFs oscillate relatively strongly around the x-axis. Their superposition results in a weak oscillating total CCF. For the most part, this total CCF has the same sign of the Coulomb partial CCF indicating that the Coulomb contribution to the total CCF is the most significant.

In Fig. 12, the Coulomb partial CCF is shown normalized with the value $|\langle \mathbf{J}_O(0) \mathbf{J}_{q,\phi}(0) \rangle|_{\text{YSZ24}}$ for various YSZ compositions. For

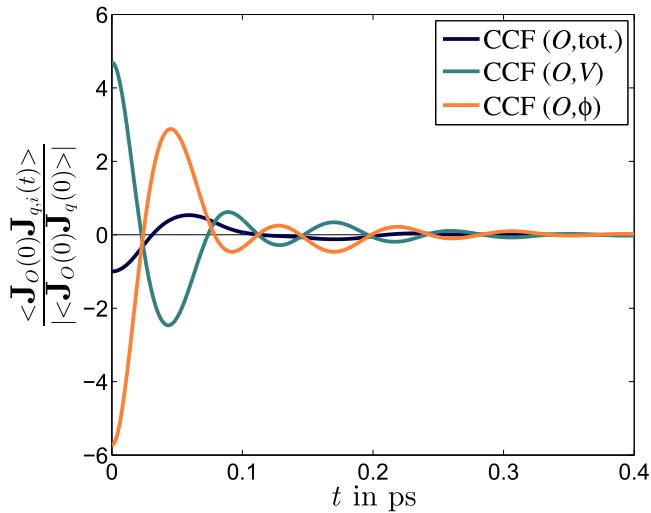


Fig. 11. Calculated mean partial CCFs of the Coulomb (ϕ) term (orange line), the virial (V) term (green line) and the total CCF (dark blue line) of the heat flux and the anion flux for YSZ12 at 1300 K normalized with the absolute value $|\langle \mathbf{J}_O(0) \mathbf{J}_q(0) \rangle|$. (For interpretation of the references to color in this figure legend, the reader is referred to the web version of this article.)

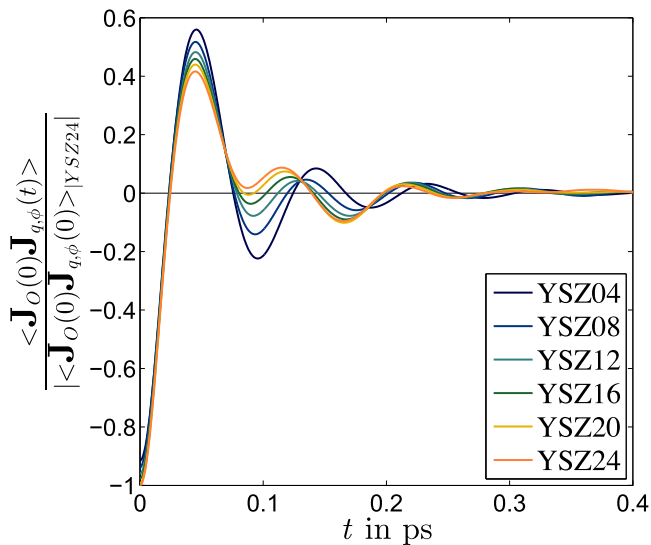


Fig. 12. Calculated mean partial CCF of the Coulomb term (ϕ) of the heat flux and the anion molar flux for various YSZ compositions at 1300 K normalized with the absolute value $|\langle \mathbf{J}_O(0) \mathbf{J}_{q,\phi}(0) \rangle|_{\text{YSZ24}}$.

small vacancy concentrations, the thermo-diffusion through the Coulomb interactions has a Soret-type behavior. Furthermore, the progression of the CCF for YSZ04 corresponds to the ACF of the molar anion flux (see Fig. 8) but with a different sign. However, the second minimum becomes positive for higher Y_2O_3 concentrations. This is related to a longer relaxation time of the heat flux in a Dufour-type effect.

In Fig. 13, we plot the partial virial CCF for different YSZ compositions normalized with the value $\langle \mathbf{J}_O(0) \mathbf{J}_{q,V}(0) \rangle_{\text{YSZ04}}$. Its progression is almost equal to the progression of the ACF of the molar anion flux. Hence, the virial thermo-diffusion has only Soret-type behavior. This is because the chosen interatomic potential does not consider cation-cation interactions.

We calculate the mean conductivity L_{Oq} for different averaging time intervals of the time integral of the total CCF. The values of

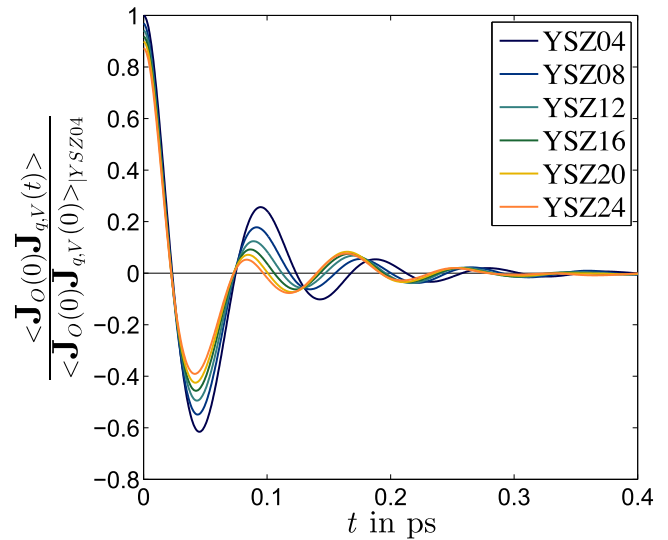


Fig. 13. Calculated mean partial CCF of the virial term (V) of the heat flux and the anion molar flux for various YSZ compositions at 1300 K normalized with the value $\langle \mathbf{J}_O(0) \mathbf{J}_{q,V}(0) \rangle_{\text{YSZ04}}$.

the calculated conductivities have an error two to three times larger than the mean value for all YSZ compositions. This is caused by the strong statistical fluctuations of the mean CCF after its decay.

To improve the quality of our results, we use the method of Vogelsang et al. [36] and calculate an artificial CCF. This is done by subtracting the individual ACFs of the heat flux and the molar anion flux from the ACF of the sum of the heat and the molar anion flux as follows:

$$\langle \mathbf{J}_O(0) \mathbf{J}_q(t) \rangle = \frac{1}{2} [\langle \mathbf{J}_{O+q}(0) \mathbf{J}_{O+q}(t) \rangle - \langle \mathbf{J}_O(0) \mathbf{J}_O(t) \rangle - \langle \mathbf{J}_q(0) \mathbf{J}_q(t) \rangle], \quad (17)$$

where $\mathbf{J}_{O+q}(t)$ is $\mathbf{J}_O(t) + \mathbf{J}_q(t)$. The mean artificial CCF is shown in comparison to the directly calculated mean CCF for YSZ08 in Fig. 14. Since generally the statistical fluctuations of ACFs are smaller than of directly calculated CCFs, the artificial CCF progresses smoother. The results of the conductivity L_{Oq} calculated with the mean artificial CCF and an averaging time interval of 1–1.5 ps are given in Table 5.

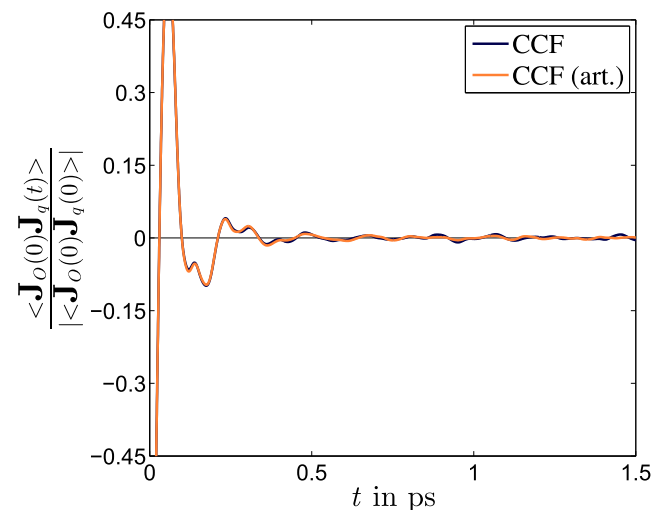


Fig. 14. Calculated artificial CCF in comparison with the mean CCF of the heat flux and the molar anion flux for YSZ08 at 1300 K normalized with the absolute value $|\langle \mathbf{J}_O(0) \mathbf{J}_q(0) \rangle|$.

Table 5
Calculated conductivity L_{Oq} for YSZ at 1300 K.

YSZ	RL_{Oq}
W/m	
YSZ04	-0.70 ± 0.64
YSZ08	-0.81 ± 0.69
YSZ12	-0.77 ± 0.75
YSZ16	-0.55 ± 0.56
YSZ20	-0.48 ± 0.36
YSZ24	-0.34 ± 0.41

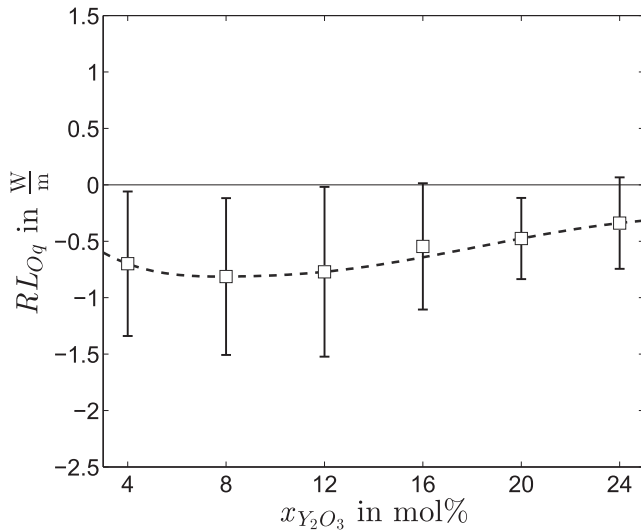


Fig. 15. Calculated conductivities L_{Oq} for various YSZ compositions (squares) and trend curve (dashed blue line).

Since the calculated conductivity L_{Oq} is negative, YSZ is a p-type semiconductor (Fig. 15). Further, the progression has a minimum for a concentration of around 10 mol% Y_2O_3 . Because the conductivity L_{Oq} describes the amount of heat transported through anion diffusion, it can be explained as follows: For very small Y_2O_3

concentrations, the anions do not diffuse at all and the absolute value of the conductivity L_{Oq} decreases. Since the heat flux and the anion molar flux flow in opposite directions, a long diffusion process is not the most effective method of heat transportation. Therefore, the minimum of the conductivity L_{Oq} does not correspond with the maximum of the conductivity L_{OO} around 5 mol% Y_2O_3 . In our proposed microscopic mechanism, the collective motions of the anions are necessary for the diffusion to adjacent free lattice sites. If there are insufficient collective motions, the anions hop back to their start position resulting in an incomplete vacancy diffusion process. By jumping back, the heat flows with the anions in the opposite direction of the net anion molar flux. At around 10 mol% Y_2O_3 , the number of anions transporting heat while hopping back and the number of anions diffusing into adjacent lattice sites result in a minimal conductivity L_{Oq} . For higher vacancy concentrations, the fewer collective motions result in fewer anions diffusing and a decrease of the absolute value of the conductivity L_{Oq} . Finally, we plot the calculated conductivity for different YSZ compositions with a trend curve in Fig. 14.

5.5. Comparison with other data

We calculate various empirical coefficients with our results and compare them with other simulation and experimental data (see Table 6). We only consider MD calculations with the same interatomic potential. The conversion equations we used for each coefficient can be found in the Appendix A. Our results overestimate the value of the heat conductivity in comparison with the experimental data of Fèvre et al. [37]. Further, they are in all cases smaller than the NEMD values of Schelling and Phillpot [31]. The relatively small discrepancies between our EMD results and the NEMD results may be related to the partial enthalpies of the ions, which we are not taking into account. Despite these discrepancies, our EMD results can still be considered equivalent to the NEMD results.

Our simulation values for the diffusion coefficient are slightly larger in comparison with the EMD values of Sizov et al. [27], which are calculated with the mean square displacement (MSD). This difference is the largest for YSZ12. We use a simple conversion rule given in Eq. (19). However, a better conversion rule should be applied, as stated by Allnatt et al. [38,39]. In this case, a more extensive study is necessary. In addition, our calculated values

Table 6

Comparison of the calculated data (EMD-GK) for the heat conductivity κ , the diffusion coefficient D and the Seebeck coefficient S with other calculated (NEMD, EMD-MSD, [27,31]) and experimental data [23,37,40,41] for various YSZ compositions and 1300 K (≈ 1000 °C).

YSZ	Method	κ (W/mK)	D (10^{-7} cm ² /s)	S (mV/K)	Ref.
YSZ04	EMD-GK	4.26 ± 0.26	2.82 ± 0.30	0.45 ± 0.42	This work
YSZ04	EMD-MSD		2.50		[27]
YSZ05	Exp.		2.10		[40,41]
YSZ05	Exp.			0.487	[23]
YSZ08	EMD-GK	3.66 ± 0.15	2.38 ± 0.30	0.63 ± 0.54	This work
YSZ08	NEMD	3.92			[31]
YSZ08	EMD-MSD		2.21		[27]
YSZ08	Exp.	2.00			[37]
YSZ08	Exp.			0.495	[23]
YSZ09	Exp.		4.5		[40,41]
YSZ12	EMD-GK	3.16 ± 0.16	1.58 ± 0.22	0.90 ± 0.89	This work
YSZ12	EMD-MSD		1.00		[27]
YSZ12	Exp.			0.478	[23]
YSZ15	Exp.		1.05		[40,41]
YSZ16	EMD-GK	2.86 ± 0.20	1.10 ± 0.14	0.92 ± 0.95	This work
YSZ20	EMD-GK	2.68 ± 0.17	0.76 ± 0.21	1.17 ± 0.95	This work
YSZ20	NEMD	3.00			[31]
YSZ20	Exp.	1.82			[37]

overestimate the diffusion coefficient in comparison with the experimental data of Strickler et al. [40,41] for all YSZ compositions except YSZ08, where the experimental value is larger than our calculated diffusion coefficient.

Finally, we do not have any knowledge of MD results for the Seebeck coefficient S , neither for various YSZ compositions, nor with the same interatomic potential. However, we can compare our results with the experimental data of Kjelstrup et al. [20]. Unfortunately, their experiment did not examine mole fractions larger than 12 mol% Y_2O_3 . Due to the division with the conductivity L_{00} , the predicted minimum of the conductivity L_{0q} cannot be found in the calculated Seebeck coefficient. Nevertheless, our calculated values agree well with the experimental values up to a mole fraction of 8 mol% Y_2O_3 . For YSZ12 the calculated value overestimates the Seebeck coefficient. In a future work we will experimentally determine the Seebeck coefficient for higher YSZ compositions to prove the increasing trend of our simulated results.

6. Summary and conclusions

The objective of this contribution is a phenomenological study of YSZ calculating the conductivities L_{ij} as given by non-equilibrium thermodynamics for various compositions at 1300 K using classical EMD and the GK formulation. We choose the EMD method, because the different contributions on the conductivities can be analyzed separately. The calculations are done in the canonical ensemble for systems of around 1500 ions at zero pressure. We use the potential as given by Schelling and Phillpot [31]. We calculate the mean correlation functions for fifteen independent start configurations with different YSZ compositions and evaluate them by averaging the time integrals for a given correlation time interval.

From these calculations we conclude that the number of vacancies is crucial for the shape of the correlation functions and for the magnitude of the conductivities for each YSZ composition. The ACF of the heat flux decays slower for higher vacancy concentrations due to the larger range of motion of the ions. The biggest contribution to the total ACF of the heat flux is made by the Coulomb forces. For higher Y_2O_3 concentrations, the partial Coulomb ACF of the heat flux shows a liquid-like behavior with local oscillations and the negative area under the curve increases. This results in a smaller conductivity L_{qq} .

The ACF of the anion molar flux oscillates around the x-axis for all YSZ compositions, as is expected for solids. For higher vacancy concentrations it tends to behave similarly to the ACF of a liquid for the first picoseconds, but afterwards it oscillates stronger. Thus, a cooperative mechanism between high mobility and collective anion motions results in a maximum positive area under the ACF, i. e., an optimum for the conductivity L_{00} at a concentration of around 5 mol% Y_2O_3 .

The combination of the Soret and the Dufour transport mechanisms can be seen in the progression of the CCF of the heat flux and the anion molar flux. Further, the Coulomb and the virial partial CCFs progress mainly in a Soret-type behavior. Nevertheless, for higher vacancy concentrations the shape of the Coulomb partial CCF is influenced by the heat flux transport from a Dufour-type effect. The largest contribution to the total CCF is made by the Coulomb interactions. Therefore, the calculated conductivity L_{0q} is negative, indicating that YSZ is a p-type semiconductor for the analyzed compositions. Since the heat and the molar anion flux flow in opposite directions, high anion diffusivity is not an effective way to transport heat. A more effective way to transport heat is through diffusive processes moving in the same direction of the heat flux, as is the case

for back-hopping anions. At around 10 mol% Y_2O_3 the amount of heat transported due to back-hopping anions and anions diffusing to adjacent vacancies is maximal. This results in a minimum for the conductivity L_{0q} which does not correspond with the maximum of the conductivity L_{00} .

Finally, the values calculated with the GK formulation can be regarded as consistent with NEMD and EMD results from other studies using the same interatomic potential. Our results overestimate the heat conductivities and the diffusion coefficient in comparison to experimental data. However, for YSZ08, the calculated value of the diffusion coefficient is two times smaller than the experimental one. We do not know any MD data of the Seebeck coefficient for YSZ with the same interatomic potential, but our calculated mean values agree well with the experimental data of Kjelstrup et al. [23] for YSZ04 and YSZ08. The discrepancy lies at 12 mol% Y_2O_3 , where our calculated value overestimates the Seebeck coefficient. Further experimental studies are necessary to prove that the Seebeck coefficient increases for higher concentrations of Y_2O_3 as predicted from our MD calculations.

Acknowledgments

We would like to thank our co-workers Tobias Marquardt, Hugo Cruz-Champion, Malte Siemen and Sheridan Renzi for the discussions, corrections and friendly advice when developing this work.

Appendix A

The simulated lattice constant to calculate the volume for different YSZ compositions at zero pressure and 1300 K can be found in Table 7.

If we assume steady state, i. e., no net molar anion flux ($\mathbf{J}_0 = 0$), we can write the following relation for the heat conductivity κ with Eqs. (7)–(9) and the Fourier's law:

$$\kappa = (k_B\beta)^2 \left(L_{qq} - \frac{L_{0q}^2}{L_{00}} \right). \quad (18)$$

The anion flux is equal to the vacancy flux, but with different sign, i. e., $\mathbf{J}_0 = -\mathbf{J}_v$. Assuming an ideal mixture and no gradients in the temperature, i. e., $\nabla\beta = 0$, the Maxwell-Stefan diffusion coefficient is equal to the diffusion coefficient of the Fick's law. We can directly write for the diffusion coefficient:

$$D = R \frac{c_0 c_v}{c^2} \left(\frac{1}{c_v} + \frac{1}{c_0} \right) L_{00}, \quad (19)$$

where c_0 denotes the anion concentration, c_v the vacancy concentration and c the concentration of all ions plus the vacancies in YSZ.

Finally, we can calculate the Seebeck coefficient S with following relation from Eq. (7) and Eq. (8) for a given constant temperature:

$$S = k_B\beta \left(\frac{\mathbf{J}_q}{-2F\mathbf{J}_0} \right) = -\frac{k_B\beta}{2F} \frac{L_{0q}}{L_{00}}. \quad (20)$$

Table 7

Calculated lattice constant for various YSZ compositions at 1300 K and zero pressure.

YSZ	a (Å)
YSZ04	$5.1488 \pm 8 \cdot 10^{-5}$
YSZ08	$5.1605 \pm 1 \cdot 10^{-4}$
YSZ12	$5.1707 \pm 3 \cdot 10^{-4}$
YSZ16	$5.1794 \pm 3 \cdot 10^{-4}$
YSZ20	$5.1871 \pm 4 \cdot 10^{-4}$
YSZ24	$5.1949 \pm 6 \cdot 10^{-4}$

References

- [1] G. Lebon, *J. Non-Equilib. Thermodyn.* 39 (2014) 35.
[2] K.S. Ghandi, *AIChE J.* 58 (2012) 3601.
[3] W.D. Zhou, B. Liu, S.K. Yu, W. Hua, *Phys. Rev. E* 81 (2010) 011204.
[4] D.H. Kumar et al., *Phys. Rev. Lett.* 93 (2004) 144301.
[5] L. Onsager, *Phys. Rev.* 37 (1931) 405.
[6] L. Onsager, *Phys. Rev.* 38 (1931) 2265.
[7] P. Glansdorff, I. Prigogine, *Physica* 30 (1964) 351.
[8] P. Glansdorff, I. Prigogine, *Physica* 31 (1965) 1242.
[9] N. Jackson, J.M. Rubi, F. Bresme, *Mol. Simul.* 42 (2016) 1214.
[10] O. Borodin, G.D. Smith, H. Kim, *J. Phys. Chem. B* 113 (2009) 4771.
[11] J.O. Nilsson et al., *Phys. Rev. B* 93 (2016) 024102.
[12] D. Reith, F. Müller-Plathe, *J. Chem. Phys.* 112 (2000) 2436.
[13] D. MacGowan, D.J. Evans, *Phys. Rev. A* 34 (1986) 2133.
[14] K. Meier, A. Laesecke, S. Kabelac, *J. Chem. Phys.* 121 (2004) 3671.
[15] T. Arima et al., *J. Nucl. Mater.* 352 (2006) 309.
[16] T. Arima, S. Yamasaki, Y. Inagaki, K. Idemitsu, *J. Alloys Compd.* 400 (2005) 43.
[17] B.S. Prakash, S.S. Kumar, S.T. Aruna, *Renewable Sustainable Energy Rev.* 36 (2014) 149.
[18] N. Mahato, A. Banerjee, A. Gupta, S. Omar, K. Balani, *Prog. Mater. Sci.* 72 (2015) 141.
[19] C. León, M.L. Lucía, J. Santamaría, *Phys. Rev. B* 55 (1997) 882.
[20] M. Kilo et al., *Solid State Ionics* 175 (2004) 823.
[21] D.M. Heyes, *Phys. Rev. B* 49 (1994) 755.
[22] R. Vogelsang, C. Hoheisel, *Phys. Rev. A* 36 (1987) 3964.
[23] S. Kjelstrup Ratkje, K. Seip Forland, *J. Electrochem. Soc.* 138 (1991) 2374.
[24] R. Vogelsang, C. Hoheisel, *Phys. Rev. A* 35 (1987) 3487.
[25] S.-M. Ho, *J. Mater. Sci. Eng.* 54 (1982) 23.
[26] V. Vonk, N. Khorshidi, A. Stierle, H. Dosch, *Surf. Sci.* 612 (2013) 69.
[27] V.V. Sizov, M.J. Lampinen, A. Laaksonen, *Solid State Ionics* 266 (2014) 29.
[28] R. Devanathan, W.J. Weber, S.C. Singhal, J.D. Gale, *Solid State Ionics* 177 (2006) 1251.
[29] A. Stukowsky, *Modell. Simul. Mater. Sci. Eng.* 18 (2010) 015012.
[30] X. Li, B. Hafkjold, *J. Phys. Condens. Matter.* 7 (1995) 1255.
[31] P.K. Schelling, S.R. Phillpot, *J. Am. Ceram. Soc.* 84 (2001) 2997.
[32] S. Plimpton, *J. Comput. Phys.* 117 (1995) 1.
[33] H.G. Petersen, *J. Chem. Phys.* 103 (1995) 3668.
[34] R. Friedberg, J.E. Cameron, *J. Chem. Phys.* 52 (1970) 6049.
[35] R. Zwanzig, N.K. Ailawadi, *Phys. Rev.* 182 (1969) 280.
[36] R. Vogelsang, C. Hoheisel, *Phys. Rev. A* 38 (1988) 6296.
[37] M. Fèvre, A. Finel, R. Caudron, R. Mèvrel, *Phys. Rev. B* 72 (2005) 104118.
[38] A.R. Allnatt, *J. Phys. Chem.* 43 (1965) 1855.
[39] A.R. Allnatt, L.S. Rowley, *J. Phys. Chem.* 53 (1970) 3217.
[40] D.W. Strickler, W.G. Carlson, *J. Am. Ceram. Soc.* 47 (1964) 122.
[41] R. Krishnamurthy, Y.-G. Yoon, D.J. Srolovitz, R. Car, *J. Am. Ceram. Soc.* 87 (2004) 1821.

II

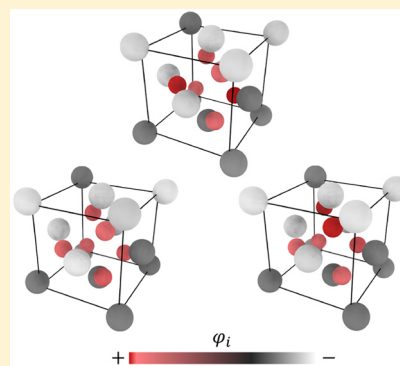
Approach to the Coulomb Contribution of Thermodynamic Properties from the Mean Electrostatic Potential of the Ions in $(\text{ZrO}_2)_{1-x}(\text{Y}_2\text{O}_3)_x$

Gerardo Valadez Huerta,¹ Malte Siemen, and Stephan Kabelac*

Institut für Thermodynamik, Gottfried Wilhelm Leibniz Universität Hannover, Callinstraße 36, D-30167 Hannover, Germany

Supporting Information

ABSTRACT: Metal oxides with oxygen vacancies are widely used in electrochemical processes at high temperature due to their ionic conductivity. These processes are strongly influenced by the electrostatic potential of the ions because it is closely related to the electrochemical potential. We calculate the partial molecular Coulomb internal energy for different compositions of yttria-stabilized zirconia (YSZ) with molecular dynamics (MD) at different temperatures and zero pressure. On the basis of thermodynamic considerations, we assume that these quantities correspond to the electrostatic potential of ZrO_2 and Y_2O_3 . We also calculate the mean electrostatic potential of the ions and develop a mixing rule between this potential and the electrostatic potential of the molecules. With this mixing rule and following the thermodynamic framework proposed in this study, one can calculate the Coulomb contribution of other thermodynamic properties like the entropy or the Nernst–Planck diffusivities for YSZ-like metal oxides. Furthermore, the methods proposed here can be extended for other electrolyte mixtures.



1. INTRODUCTION

Because of their ionic conductivity at high temperatures, crystalline oxides are important for electrochemical processes.¹ These oxides are ionic compounds, which consist of a metal and an oxygen sublattice. The ion diffusion may occur through vacancies or interstitials.² Compounds based on zirconia ZrO_2 , like $(\text{ZrO}_2)_{1-x}(\text{Y}_2\text{O}_3)_x$ (YSZ) and $(\text{ZrO}_2)_{1-x}(\text{Sc}_2\text{O}_3)_x$ (ScSZ), or based on ceria CeO_2 , like $(\text{CeO}_2)_{1-x}(\text{Sm}_2\text{O}_3)_x$ (SDC) and $(\text{CeO}_2)_{1-x}(\text{Gd}_2\text{O}_3)_x$ (GDC), are examples of oxygen ion conductors. The codoping of many other metal oxides is a topic of active research.^{3,4}

The electrochemical potential is the driving force for ion diffusion and is closely related to the electrostatic potential of the ions. Therefore, it is important to determine the electrostatic potential in this kind of compounds. For electrolyte systems, a quantity ϕ , assumed to be the electrostatic potential, appears in the common definition of the electrochemical potential η_i of the ions of species i ⁵

$$\eta_i = \mu_i + z_i e \cdot \phi \quad (1)$$

Here, z_i is the valency, μ_i is the chemical potential, and e is the elementary charge. E. A. Guggenheim⁶ declared electrostatics to be “a mathematical theory of an imaginary fluid electricity, whose equilibrium or motion is determined entirely by the electric field”. He also determined the equilibrium of ions and electrons to be of a completely different nature than this hypothetical fluid electricity because this equilibrium is a thermodynamic and not an electrostatic one. However, if we assume the quantity ϕ to be of thermodynamic nature, then it

should be possible to give it a physical significance. In this case and because of eq 1, ϕ should be an ion-specific thermodynamic property instead of a global quantity.

In this work, we define a quantity ψ_j for each molecular species instead of ϕ . To give the quantity ψ_j a thermodynamic significance, we derive it from the fundamental equation of state for the Coulomb internal energy and relate it to other thermodynamic properties and to the electrostatic potential ϕ_i of the ions, which should also be different to the quantity ϕ appearing in eq 1. Because of the constraints in the derivatives, it is not easy to calculate the quantity ψ_j with classical MD simulations. However, we check the reliability of our method calculating a thermodynamically consistent electrostatic potential $(z\phi)_j$ for the molecules ZrO_2 and Y_2O_3 in different YSZ compositions from the partial molecular Coulomb internal energy. Furthermore, we determined a mixing rule to calculate $(z\phi)_j$ with the electrostatic potential ϕ_i of the ions in YSZ. This mixing rule and calculations in the appropriate ensemble should allow access to other Coulomb thermodynamic properties in this kind of metal oxides.

2. THEORETICAL METHODS

2.1. Coulomb Internal Energy as a Thermodynamic Property.

The first step in our considerations is to split the internal energy of an electrolyte system into a non-Coulomb

Received: September 1, 2017

Revised: November 14, 2017

Published: December 6, 2017

internal energy U_{KW} (containing the kinetic (K) and the van der Waals (W) contributions) and a Coulomb internal energy U_C

$$U = U_K + U_W + U_C = U_{KW} + U_C \quad (2)$$

The Coulomb internal energy is a function of the temperature T , pressure p , and the number of atoms N_i for each constituent i

$$U_C = U_C(N_1, \dots, N_k, T, p) \quad (3)$$

It is an extensive thermodynamic property and should thus be a homogeneous function of first order. That means for a given temperature or pressure it should follow

$$\lambda U_C(N_1, \dots, N_k) = U_C(\lambda N_1, \dots, \lambda N_k) \quad (4)$$

with λ as an arbitrary factor. The relation 4 is true for a system with K ions, if the ions are seen as point charges, because U_C is calculable from the sum of the electrostatic potentials

$$U_C = \frac{1}{2} \sum_{i=1}^K N_i e(z\varphi)_i \quad (5)$$

However, a system of only ions of the same type cannot exist in thermodynamic equilibrium. That means the superposition in eq 5 works mathematically but is not thermodynamically consistent.

Nevertheless, we can consider the same system as a mixture of electroneutral compounds M , which together build a new

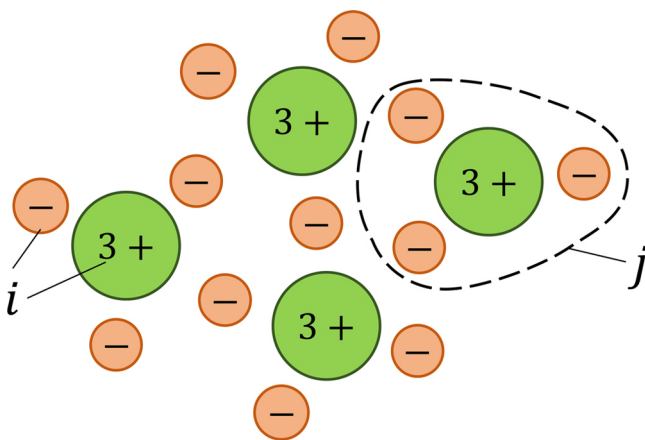


Figure 1. Electrolyte system seen as a mixture of ions i and as a mixture of electroneutral compounds j .

electroneutral electrolyte mixture (see Figure 1), and see them as point charges. In this case, we can rewrite eq 5 as follows

$$U_C = \frac{1}{2} \sum_{j=1}^M N_j e(z\varphi)_j \quad (6)$$

An example of this kind of mixtures are metal oxides like YSZ, which is conformed of the electroneutral compounds ZrO_2 and Y_2O_3 . This definition is crucial for our further discussion and can be extended to other kind of electrolyte systems because the hereafter-called molecules M can just be electroneutral subsystems. Now, if we consider the Coulomb internal energy per molecule \bar{U}_C of an electrolyte mixture, we can calculate it from the sum of the Coulomb internal energies per molecule $\bar{U}_{C,0j}$ of the mixture components M and an excess term $\Delta^E \bar{U}_C$

$$\bar{U}_C = \sum_{j=1}^M \bar{U}_{C,0j} + \Delta^E \bar{U}_C \quad (7)$$

Finally, we can express eq 3 in terms of partial molecular internal energies

$$U_C = \sum_{j=1}^M N_j \left(\frac{\partial U_C}{\partial N_j} \right)_{T,p,N_{k \neq j}} \quad (8)$$

because of eq 4. With eq 6 a relation between the partial molecular internal energies and the electrostatic potential φ_j arises

$$\left(\frac{\partial U_C}{\partial N_j} \right)_{T,p,N_{k \neq j}} = \frac{1}{2} e(z\varphi)_j \quad (9)$$

2.2. Quantity ψ_j . Let us consider the fundamental equation of state for the system described before

$$dU = TdS - pdV + \sum_{j=1}^M \eta_j dN_j \quad (10)$$

where S is the entropy and V is the volume of the system. In this case, the definition of the electrochemical potential η_j is as follows

$$\eta_j = \left(\frac{\partial U}{\partial N_j} \right)_{S,V,N_{k \neq j}} \quad (11)$$

If we set eq 2 into eq 11 we get

$$\eta_j = \left(\frac{\partial U_{KW}}{\partial N_j} \right)_{S,V,N_{k \neq j}} + \left(\frac{\partial U_C}{\partial N_j} \right)_{S,V,N_{k \neq j}} \quad (12)$$

If we define η_j as

$$\eta_j = \mu_j + e(z\psi)_j \quad (13)$$

assigning a different ψ_j to each molecule sort, it follows from eq 12 and eq 13

$$\left(\frac{\partial U_{KW}}{\partial N_j} \right)_{S,V,N_{k \neq j}} = \mu_j \quad (14)$$

and

$$\left(\frac{\partial U_C}{\partial N_j} \right)_{S,V,N_{k \neq j}} = e(z\psi)_j \quad (15)$$

Likewise, we get for the relations with the free Coulomb enthalpy G_C

$$\left(\frac{\partial G_C}{\partial N_j} \right)_{T,p,N_{k \neq j}} = e(z\psi)_j \quad (16)$$

That shows the so-defined ψ_j is not necessarily equal to the electrostatic potential φ_j of the molecules in the system, calculated by classical Coulomb integration, because in eqs 9 and 15 the derivatives have different constraints. Moreover, we can calculate the Coulomb contribution of other thermody-

dynamic properties from ψ_j like the Coulomb entropy, for example, applying the appropriate Maxwell relation

$$e \left(\frac{\partial(z\psi)_j}{\partial T} \right)_{p, N_k} = - \left(\frac{\partial S_C}{\partial N_j} \right)_{T, p, N_{k \neq j}} \quad (17)$$

This is not directly possible with the electrostatic potential. To calculate the property $(z\psi)_j$ of the molecules, we may conduct Monte Carlo (MC) simulations in the grand canonical ensemble, calculate the resulting Coulomb energy per molecule in the system for different concentrations, and assume it to be equal to G_C . Despite the required electroneutrality of the system, MC methods are possible.^{7,8} Furthermore, if one only exchanges electroneutral molecules with the reservoir to keep the chemical potential constant, then the electroneutrality of the system is not violated. For electrolyte systems like YSZ, this information is enough to calculate $(z\psi)_j$.

2.3. Electrostatic Potential of ZrO_2 and Y_2O_3 in YSZ.

We do not conduct MC calculations in this work, but we use the framework presented beforehand to calculate a thermodynamically consistent electrostatic potential of ZrO_2 and Y_2O_3 in YSZ. This electrolyte system consists of the ions Zr^{4+} , O^{2-} , and Y^{3+} . In this case, and assuming no electron transport, we can write for the Coulomb internal energy with eq 5

$$U_C = \frac{1}{2} e(N_{Zr}(z\varphi)_{Zr} + N_O(z\varphi)_O + N_Y(z\varphi)_Y) \quad (18)$$

and $z_{Zr} = 4$, $z_O = -2$, and $z_Y = 3$. The same Coulomb energy may be expressed with the electrostatic potential of the molecules and eq 6

$$U_C = \frac{1}{2} e(N_{ZrO_2}(z\varphi)_{ZrO_2} + N_{Y_2O_3}(z\varphi)_{Y_2O_3}) \quad (19)$$

or with the partial molecular Coulomb energies

$$U_C = N_{ZrO_2} \left(\frac{\partial U_C}{\partial N_{ZrO_2}} \right) + N_{Y_2O_3} \left(\frac{\partial U_C}{\partial N_{Y_2O_3}} \right) \quad (20)$$

To calculate $(z\varphi)_{ZrO_2}$ and $(z\varphi)_{Y_2O_3}$, we have to calculate the molecular internal Coulomb energy $\bar{U}_C = U_C/(N_{Zr} + N_Y/2)$ for different mole fractions $x_{Y_2O_3}$. The electrostatic potentials of the molecules follow directly from the partial molecular internal Coulomb energies

$$\frac{1}{2} e(z\varphi)_{ZrO_2} = \left(\frac{\partial U_C}{\partial N_{ZrO_2}} \right)_{p, T} \quad (21)$$

and

$$\frac{1}{2} e(z\varphi)_{Y_2O_3} = \left(\frac{\partial U_C}{\partial N_{Y_2O_3}} \right)_{p, T} \quad (22)$$

which are the intercepts of the tangent of the curve U_C for a given mole fraction $x_{Y_2O_3}$ with the lines $x_{Y_2O_3} = 0$ and $x_{Y_2O_3} = 1$ (see Figure 2).

2.4. Molecular Dynamics Simulations. The description of the system, the parameters for the interatomic potential, and the simulation details are reported in our previous work.⁹ Using the MD package LAMMPS (<http://lammps.sandia.gov>),¹⁰ we analyze here the same YSZ compositions in thermodynamic states of 1100, 1300, and 1500 K, each at zero pressure and in

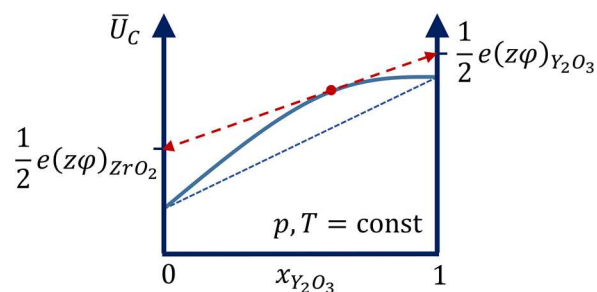


Figure 2. Tangent construction for calculation of the electrostatic potentials φ_{ZrO_2} and $\varphi_{Y_2O_3}$ from the molecular Coulomb internal energy in YSZ at constant pressure and temperature.

the canonical ensemble. Unlike our previous study, we use only 10 independent simulations for our calculations and simulate additionally YSZ28, that is, 28 mol % Y_2O_3 , and pure Y_2O_3 . The number of ions for each configuration is given in Table 1. The calculated lattice constants can be found in the Supporting Information.

Table 1. YSZ Compositions Analyzed in This Work

system	$x_{Y_2O_3} \times 10^2$	N_{Zr}	N_O	N_Y
YSZ04	3.95	462	981	38
YSZ08	7.99	426	963	74
YSZ12	12.08	492	946	108
YSZ16	15.97	362	931	138
YSZ20	19.90	334	917	166
YSZ24	24.00	306	903	194
YSZ28	28.21	280	890	220
Y_2O_3	100.0	0	750	500

Because it is only possible to calculate the Coulomb energy with LAMMPS, we develop our own algorithm for the calculation of the electrostatic potential with the Ewald summation based on standard works from the literature.^{11–13} In this case, we use a relative precision of 10^{-4} and set half of the simulation box length as the cutoff radius. The resulting Ewald parameter is $\sim 30\%$ of the simulation box length for all calculations, and we evaluate the electrostatic potential at each atom position. We only use the configurations at each 5 fs of the total 0.5 ns production run. Furthermore, we calculate the Coulomb energy at each 0.5 fs of the total production run using LAMMPS. In both cases, we check the repeatability of our simulations with the error calculated using the well-known block averaging method.¹⁴ The results presented in this work are the values averaged over all mean values of the 10 independent simulations for each YSZ composition. We use the corrected sample standard deviation to estimate the error of the resulting values.

To check the correct implementation of the Ewald summation, we calculate the electrostatic potential of Na^+ and Cl^- in the perfect $NaCl$ lattice. We use a lattice constant of $a_{NaCl} = 5.64$ Å resulting in $\varphi_{Na} = -4.4618$ eV and $\varphi_{Cl} = 4.4618$ eV, respectively, which agrees very well with the values calculated with the Madelung constant given in the literature.¹⁵

Finally, we approximate the slope m of the tangent of the \bar{U}_C curve for a certain mole fraction $x_{Y_2O_3}$ with the slope of a secant line as follows

$$m = \frac{\bar{U}_C(x_{Y_2O_3} + \Delta x_{Y_2O_3}) - \bar{U}_C(x_{Y_2O_3} - \Delta x_{Y_2O_3})}{2 \cdot \Delta x_{Y_2O_3}} \quad (23)$$

For YSZ04, we use the values of the Coulomb internal energy of ZrO_2 and YSZ08. For YSZ08, we use the values of YSZ04 and YSZ12 and so on. We calculate intermediate values, too. In this case, we estimate the values of the slope for YSZ02, with the values for ZrO_2 and YSZ04, and so on. With this information, the calculation of the partial molecular Coulomb energy for different YSZ compositions with the method discussed before is straightforward. Because we do not calculate \bar{U}_C for ZrO_2 , we extrapolate it from the values of YSZ08 and YSZ04.

3. RESULTS AND DISCUSSION

3.1. Electrostatic Potential of Single Ions. In Figure 3, the simulated values for the electrostatic potential φ_i of Zr^{4+} ,

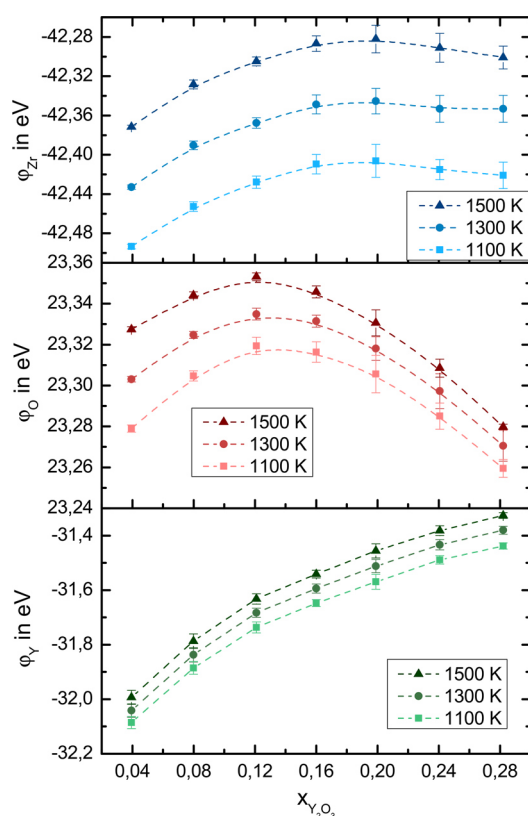


Figure 3. Calculated electrostatic potential of the ions Zr^{4+} (blue symbols), O^{2-} (red symbols), and Y^{3+} (green symbols) and trend curves (dashed lines) for different YSZ composition and different temperatures.

O^{2-} , and Y^{3+} are plotted for different YSZ compositions and different temperatures. The respective values for Y_2O_3 are given in Table 2. As expected, the electrostatic potential of the anions is positive and the electrostatic potential of the cations is negative. The progress of the calculated values for the

electrostatic potential φ_{Zr} for concentrations between 20 and 28 mol % Y_2O_3 should be the beginning of an inflection point, because in the limit of the infinite dilution the value $\varphi_{Zr}^\infty = \lim_{x_{Y_2O_3} \rightarrow 1} \varphi_{Zr}$ should be approximately as high as

$\varphi_Y(Y_2O_3)$ for pure yttria due to the Coulomb integration. The electrostatic potential φ_O should only have a maximum at 12 mol %, because for pure Y_2O_3 the calculated value $\varphi_O(Y_2O_3)$ is the lowest for all temperatures. Furthermore, the calculated electrostatic potential φ_Y of the Y^{3+} cations should only increase for higher Y_2O_3 concentrations because of $\varphi_Y(Y_2O_3)$.

The following parameters have an impact on the evolution of the electrostatic potential in all cases: the number of vacancies in the system, the volume of the system, the number of Y^{3+} cations, the local density of the anions, and the temperature.

For a higher Y_2O_3 concentration and constant temperature, the number of anions decreases. Therefore, the contribution of the negative charges gets smaller. Furthermore, the nearest-neighbor ions have a higher contribution in the Coulomb force. In sum, for fewer anions the electrostatic potential of the cations and of the remaining anions increases. Nevertheless, an increasing number of Y^{3+} cations has the opposite effect. Despite the electroneutrality of the system, the lower charge number in Y^{3+} as compared with Zr^{4+} and the nearest-neighbor contributions lead to the decrease in φ_O and φ_{Zr} .

Moreover, the simulated lattice constant increases with the number of vacancies (see the Supporting Information). In this case, the distance between the ions gets smaller and the electrostatic potential decreases for the anions and increases for the cations. This difference may explain the maximum in φ_O and the inflection point in φ_{Zr} over the Y_2O_3 concentration.

We plot the local density of the oxygen ions in their tetrahedral site for YSZ04, YSZ12, and YSZ24 at 1300 K in Figure 4. To build the density plot, we averaged the trajectory of the production run for all anions in the system in a single tetrahedral site, such that only 10 000 positions are displayed. We also color the local density with the average electrostatic potential of the anions at each position. For smaller vacancies concentrations, the O^{2-} ions are equally distributed in the tetrahedral site. For higher vacancies concentrations, they show a higher mobility in the direction of adjacent free lattice positions and the distribution becomes wider. This high mobility does not mean higher vacancy diffusion,⁹ but the probability of finding an anion between two oxygen sites is higher. In this position, the distance between anions and cations is the smallest. The electrostatic potential increases. However, because of the discussed effect of the number of anions and the influence of the Y^{3+} concentration, for higher Y_2O_3 concentrations the electrostatic potential in the core of the distribution gets smaller. The width in the local density, as in the distribution of the electrostatic potential, may explain the higher error for higher concentrations.

Finally, the electrostatic potential of each ion increases with the temperature independently from the composition. One would expect a decrease in the electrostatic potential of the anions because the lattice constant increases with the

Table 2. Calculated Electrostatic Potential of Ions O^{2-} and Y^{3+} for Y_2O_3 at 1100, 1300, and 1500 K

T (K)	1100	1300	1500
$\varphi_O(Y_2O_3)$ in eV	$22.387 \pm 5.0 \times 10^{-3}$	$22.388 \pm 6.1 \times 10^{-3}$	$22.393 \pm 5.7 \times 10^{-3}$
$\varphi_Y(Y_2O_3)$ in eV	$-31.313 \pm 4.8 \times 10^{-3}$	$-31.256 \pm 5.3 \times 10^{-3}$	$-31.200 \pm 5.5 \times 10^{-3}$

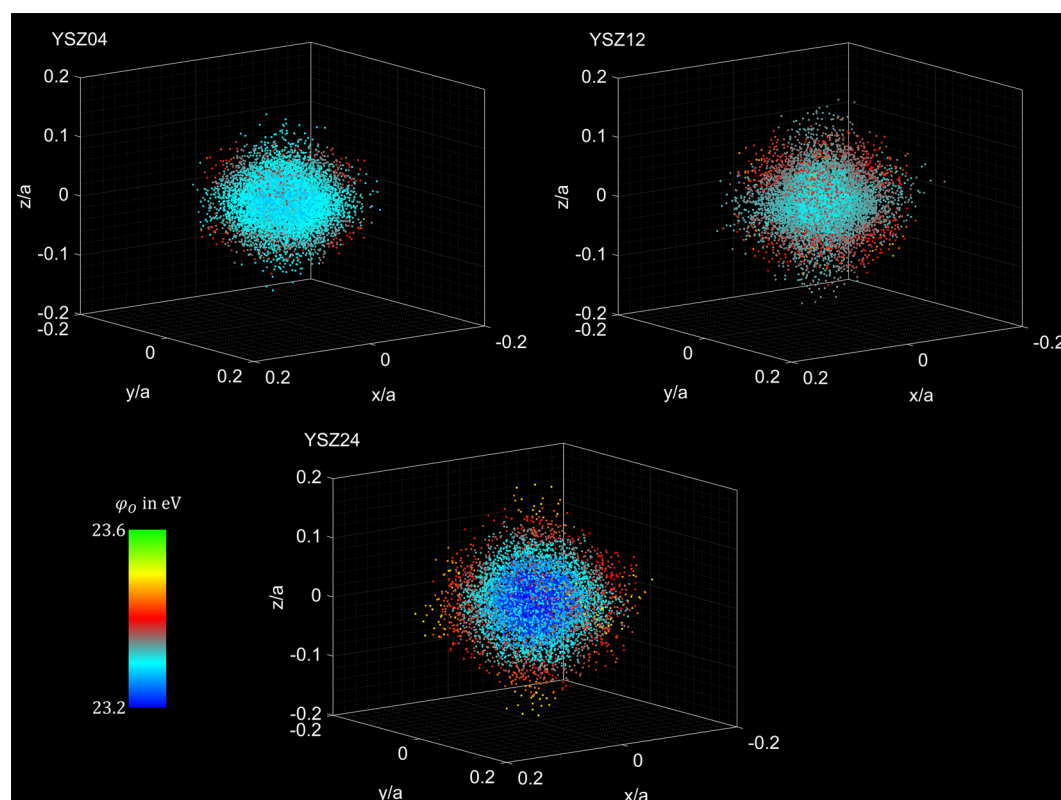


Figure 4. Calculated positions of the O^{2-} ions in the oxygen tetrahedral site for YSZ04, YSZ12, and YSZ24 at 1300 K. The 10 000 positions in each plot represent the average position of the ions for all 10 independent simulations for each YSZ composition. The positions are in reduced units with a as the lattice constant. The distribution of the electrostatic potential φ_O is also plotted, and the colors represent the mean value for each ion position in the tetrahedral site.

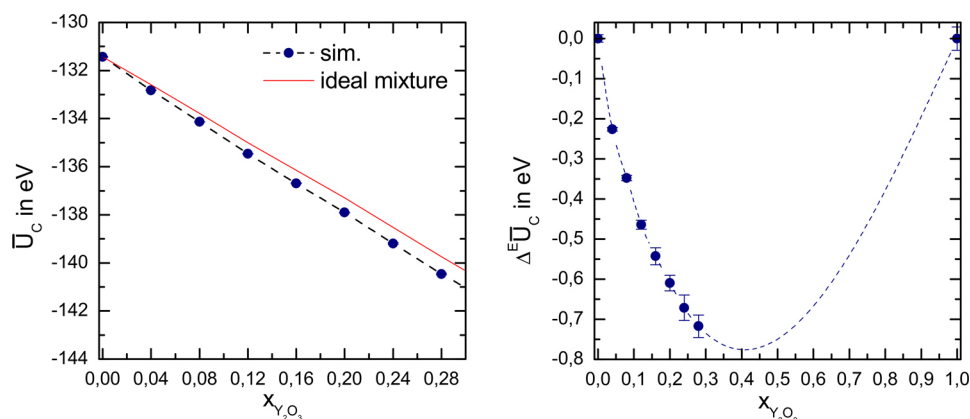


Figure 5. Left: Calculated Coulomb energy per molecule \bar{U}_C for various YSZ compositions (circles), trend curve (dashed blue line), and Coulomb energy per molecule for the ideal mixture (red solid line). Right: Calculated excess Coulomb energy per molecule $\Delta^E \bar{U}_C$ for various YSZ compositions (circles) and trend curve (dashed blue line). All plotted values correspond to a simulation temperature of 1300 K.

temperature, as has been previously discussed. Nevertheless, the opposite effect may occur due to the high velocity of the anions. In this case, the local density distribution of the anions expands and the electrostatic potential φ_O increases. Moreover, for the cations the dependency on the temperature is similar for all concentrations, but the temperature dependence of φ_O decreases for higher Y_2O_3 concentrations. The values of φ_O for Y_2O_3 can even be considered as temperature-independent within the uncertainty range (see Table 2). That means that the extra increment for the electrostatic potential φ_O due to the high velocities is not given for a high number of vacancies because the anions already have a broad local density and their

distribution in space may not be substantially affected by the temperature. However, this effect is not noticeable in the electrostatic potential of the cations because they are embedded in the metal sublattice and their distribution in space may not be considerably influenced by the vacancies.

To our knowledge, there are no ab initio, MD, or experimental studies that explicitly provide values for the electrostatic potential of the ions in YSZ. Nevertheless, we can expect quantitative differences with values calculated within density functional theory (DFT). Bogicevic and Wolverton¹⁶ compare in their study the results of the electronic (unrelaxed) part of the energy in YSZ calculated with a full quantum-

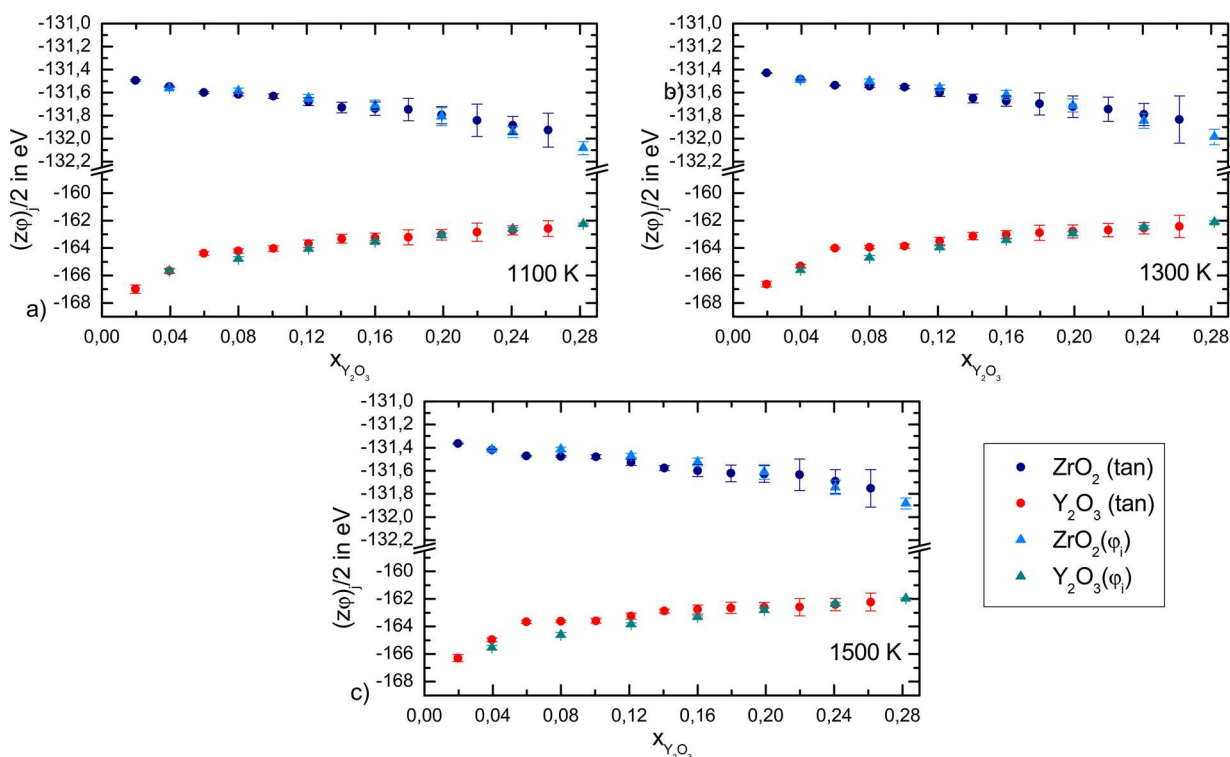


Figure 6. Calculated electrostatic potential of the molecules $j = ZrO_2$ and $j = Y_2O_3$ for different YSZ compositions estimated with the tangent construction (ZrO_2 : dark blue circles, Y_2O_3 : red circles) and directly calculated with the electrostatic potential of the ions ϕ_i (ZrO_2 : blue triangles, Y_2O_3 : dark cyan triangles) at different temperatures: (a) 1100, (b) 1300, and (c) 1500 K.

mechanical approach with the results from classical electrostatics computed with the Ewald summation. They conclude that the main contribution to the electronic part of the energy in YSZ is due to electrostatics and that the effect of ionic polarization, multipole interactions, and so on is negligible. Stapper et al.¹⁷ calculate the Coulomb energy per atom at 0 K and zero pressure with ab initio methods for different unrelaxed structures of YSZ14. For this purpose, they assign the yttrium ions a charge of $-1e$ and the vacancies a charge of $+2e$. The mean value of their calculations is (-42.167 ± 0.043) eV, which is in the same magnitude as the interpolated value (-41.476 ± 0.003) eV for YSZ14, for example, at 1300 K in this study. This means our approach seems to be consistent with ab initio calculations.

3.2. Electrostatic Potential of ZrO_2 and Y_2O_3 in YSZ.

We show in Figure 5 the calculated Coulomb energy per molecule \bar{U}_C (left diagram) and the calculated excess Coulomb energy per molecule $\Delta^E \bar{U}_C$ (right diagram) exemplary for 1300 K and for different YSZ compositions, respectively. The Coulomb energy shows a real part. Despite the relatively small difference between the real part and the ideal mixture, this difference is smaller than the calculated error for all YSZ compositions. Therefore, in this case the real part is quantifiable. This also leads to a quantifiable excess Coulomb energy, whose error bars are smaller in comparison with the absolute values. Because the Coulomb energy and the excess Coulomb energy are negative, the Coulomb interactions in the mixture are higher than in the ideal case, despite the higher volume and the lower number of ions in the system. That means that the determining effect for a real behavior of the Coulomb energy is the mobility of the ions in the system.

Given this, it is possible to calculate partial molecular Coulomb energies, that is, the electrostatic potential of the

molecules ZrO_2 and Y_2O_3 with the geometrical method proposed in this work. We plot the results in Figure 6 for different temperatures. As expected, the electrostatic potential of ZrO_2 decreases and the electrostatic potential of Y_2O_3 increases for higher Y_2O_3 concentrations in all cases. The error of the calculated values increases according to the discussion of the error of the calculated electrostatic potential of the single ions. Furthermore, the electrostatic potential of the molecules does not show any substantial dependency on the temperature, as is the case for the electrostatic potential of the single ions.

We found the following relationships between the electrostatic potential of the molecules and the electrostatic potential of the ions

$$(z\phi)_{ZrO_2} = z_{Zr}\phi_{Zr} + \frac{N_O^2}{N_O(ZrO_2)N_{YSZ}}z_O\phi_O \quad (24)$$

$$(z\phi)_{Y_2O_3} = 2 \left(\left(1 - \frac{N_O N_{Zr}}{N_O(ZrO_2)N_{YSZ}} \right) \frac{N_O}{N_Y} z_O \phi_O + z_Y \phi_Y \right) \quad (25)$$

with

$$N_{YSZ} = (N_{Zr} + N_Y/2)$$

We also plot in Figure 6 the values calculated using this mixing rule and the values of the electrostatic potential for the single ions. Despite some discrepancies in the calculated values for $(z\phi)_{Y_2O_3}$ at small Y_2O_3 concentrations, most of the values are equivalent within the statistical accuracy of the results. The discrepancy may be given by the odd approximation of the tangents with secants. Nevertheless, the superposition of the

electrostatic potential of the ions leads to a thermodynamically plausible advance of the electrostatic potential of the molecules. That means it is possible to express the electrostatic potential of the molecules with the electrostatic potential of the ions for this kind of binary metal oxide mixtures. It may also be possible to determine similar mixing rules for mixtures of higher order.

If such mixing rules are known, then a single computation is needed to calculate the partial molecular Coulomb energies of the system at a given thermodynamic state. With this information, the following procedure can be used to calculate, for example, the Coulomb entropy S_C for a binary metal oxide:

- Calculation of the electrostatic potential of the ions in the system in the Grand canonical ensemble, for example, with Monte Carlo methods, at different temperatures and the same pressure.
- Calculation of the quantities $(z\psi)_j$, that is, of the partial molecular Coulomb free enthalpies, with the mixing rules proposed here.
- Evaluation of the Maxwell relation in eq 17 to calculate the partial molecular entropies
- The addition of these values multiplied with the mole fraction of the respective molecule results into the molecular Coulomb entropy \bar{S}_C , which can be easily transformed in a per ion quantity if desired.

3.3. Nernst–Planck Equations for YSZ. With the new quantities $(z\psi)_j$ defined in this study, we can write the following set of Nernst–Planck equations to describe the ionic transport in the system

$$\mathbf{J}_{ZrO_2} = D_{ZrO_2} \nabla(-c_{ZrO_2}) + \frac{\sigma_{ZrO_2}}{e} \nabla(-(z\psi)_{ZrO_2}) \quad (26)$$

$$\mathbf{J}_{Y_2O_3} = D_{Y_2O_3} \nabla(-c_{Y_2O_3}) + \frac{\sigma_{Y_2O_3}}{e} \nabla(-(z\psi)_{Y_2O_3}) \quad (27)$$

It can be shown that the conductivities σ_{ZrO_2} and $\sigma_{Y_2O_3}$ are related to the anion conductivity σ_O as follows (see the Supporting Information)

$$\sigma_{ZrO_2} = \frac{x_{ZrO_2}}{2x_{ZrO_2} + 3x_{Y_2O_3}} \frac{N_O(ZrO_2)N_{YSZ}}{N_O^2} \sigma_O \quad (28)$$

$$\sigma_{Y_2O_3} = \frac{x_{Y_2O_3}}{2x_{ZrO_2} + 3x_{Y_2O_3}} \left(1 - \frac{N_O N_{Zr}}{N_O(ZrO_2)N_{YSZ}}\right)^{-1} \frac{N_Y}{N_O} \sigma_O \quad (29)$$

We use the simulated phenomenological coefficients L_{OO} from our previous work⁹ to calculate the conductivities σ_O , σ_{ZrO_2} and $\sigma_{Y_2O_3}$ for different YSZ compositions at 1300 K and plot them in Figure 7. The molecular conductivities σ_{ZrO_2} and $\sigma_{Y_2O_3}$ are lower than the ionic conductivity σ_O , with $\sigma_{Y_2O_3}$ being the lowest in all cases. This is reasonable because the single contribution from the molecules should not surpass the net ionic conductivity. However, the conductivities are not additive. Because the cations do not diffuse at all, the molecular conductivities may describe the distribution of the anions to form electroneutral molecules in the system, and this distribution is not necessarily in accordance with the net anionic flux. Furthermore, the zirconia conductivity is almost equal to the oxygen conductivity for YSZ04, but the gap between the zirconia and the oxygen conductivity increases for higher Y_2O_3 concentrations, resulting in a smaller gap between the molecular conductivities. The low

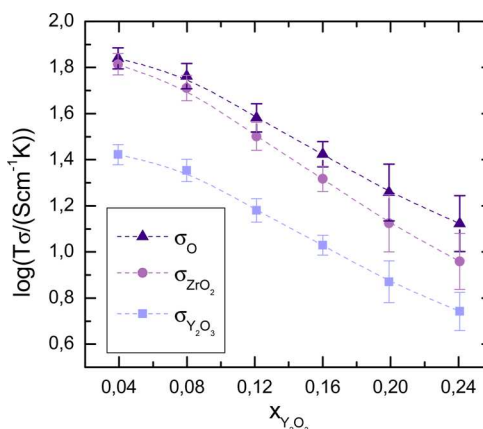


Figure 7. Ionic conductivity σ_O and molecular conductivities σ_{ZrO_2} and $\sigma_{Y_2O_3}$ for different YSZ compositions at 1300 K and zero pressure.

Y_2O_3 conductivity means a higher resistance so that the ions prefer to flow through the ZrO_2 molecules rather than through the Y_2O_3 molecules. A higher concentration of Y_2O_3 affects the ZrO_2 conductivity, too, due to the increased probability of finding Zr – Y ion pairs. This may explain the progression of the curves. These findings are also in accordance with the study of Kilo et al.,¹⁸ in which the authors show the yttrium cations to have a blocking effect on the vacancy diffusion.

Mathematically, we did a coordinate transformation defining two different conductivities instead of a solely one. Despite the plausibility of the results, it may not appear to have any practical use at first glance. However, the Fick diffusion coefficients D_j can be calculated with the conductivities σ_j and with the thermodynamic factor Γ_j (see the Supporting Information)

$$D_{ZrO_2} = \frac{\sigma_{ZrO_2}}{\beta e^2 c_{ZrO_2}} \Gamma_{ZrO_2} = \frac{\sigma_{ZrO_2}}{e^2 c_{ZrO_2}} \left(\frac{\partial \mu_{ZrO_2}}{\partial \ln x_{ZrO_2}} \right) \quad (30)$$

$$D_{Y_2O_3} = \frac{\sigma_{Y_2O_3}}{\beta e^2 c_{Y_2O_3}} \Gamma_{Y_2O_3} = \frac{\sigma_{Y_2O_3}}{e^2 c_{Y_2O_3}} \left(\frac{\partial \mu_{Y_2O_3}}{\partial \ln x_{Y_2O_3}} \right) \quad (31)$$

with c_j as the molecular concentration. The thermodynamic factor is well-defined in our thermodynamically consistent framework: If the electrochemical potential of the molecules is known, for example, from thermodynamic integration, and the quantities $(z\psi)_j$ are given, for example, from MC simulation, then the chemical potential of the molecules μ_j can be calculated from eq 13 for different compositions and, as a direct consequence, so can the thermodynamic factor. With the Fick diffusion coefficient and the molecular conductivities, the Nernst–Planck eqs 26 and 27 can be then used to describe the transport mechanism in metal oxide systems in a thermodynamically consistent manner.

4. CONCLUSIONS

We calculate a thermodynamically consistent electrostatic potential of ZrO_2 and Y_2O_3 in YSZ with classical MD simulations. If we consider the internal Coulomb energy as a thermodynamic property, it follows from electrostatics that the internal partial Coulomb energy of a mixture is proportional to the electrostatic potential of the molecules in an electrolyte mixture. In this framework, we understand as an electrolyte mixture a mixture of electroneutral components, which

together build a new electroneutral system. If we analyze the internal Coulomb energy from the point of view of the fundamental equation of state, then a quantity ψ_j arises, which is related to the electrochemical potential of the molecules in the system. Such a quantity may be calculated with, for example, MC methods. For a metal oxide like YSZ, the electrostatic potential of the molecules can be estimated from the Coulomb internal energy and a tangent construction. To calculate the Coulomb internal energy in YSZ for different compositions at different temperatures, that is, 1100, 1300 and 1500 K, and zero pressure, we conduct MD simulations with LAMMPS and the methodology reported in our previous work.⁹ Furthermore, we calculate the electrostatic potential of the ions with algorithms we developed.

The calculated electrostatic potential of oxygen anions has a maximum at 12 mol % Y_2O_3 , the calculated electrostatic potential of the zirconium cations has an inflection point at ~ 24 mol % Y_2O_3 , and the electrostatic potential of the yttrium cations increases for higher Y_2O_3 . The electrostatic potential for all ion species increases for higher temperatures due to the increment in the anion velocities, which influences the local anion density. This temperature dependency is not noticeable for φ_O (Y_2O_3) because of the broad local density of the anions due to the high number of free lattice sites in the oxygen sublattice. For a higher Y_2O_3 concentration in YSZ, that is, a higher number of vacancies, and a given temperature, the electrostatic potential of all ion species increases due to the decreasing number of anions and nearest-neighbor contributions. The opposite effect results from a high number of Y^{3+} and a large volume. From the local density of the anions and the local distribution of the electrostatic potential, we notice that a high mobility of the anions results in a higher value for φ_O and a smaller value for φ_{Zr} and φ_Y .

The relatively strong temperature dependency of the electrostatic potentials of the ions and the particular progression of their curves over the Y_2O_3 concentration are not present in the progression of the electrostatic potential of the molecules. In contrast, the electrostatic potential of ZrO_2 decreases and that of Y_2O_3 increases, as is expected of partial molecular Coulomb energies in binary mixtures. The partial molecular Coulomb internal energies for YSZ-like metal oxides can be estimated with the mixing rule proposed in this work, which only considers the electrostatic potential of the ions and the composition of the system. With this knowledge, one can estimate the Coulomb contribution for other thermodynamic properties if the simulations are done in the appropriate ensemble.

Finally, we calculate the molecular conductivities σ_{ZrO_2} and $\sigma_{Y_2O_3}$ using the mixing rules and the values for the phenomenological coefficient L_{OO} from our previous work.⁹ We do this to give Nernst–Planck kinetics consistent with the suggested thermodynamic framework. The results for the molecular conductivities are reasonable because they reproduce the blocking effect of the yttrium cations on the anions during vacancy diffusion reported in the literature.¹⁷ Moreover, a direct approach to the Fick diffusivities may be possible with the knowledge of the quantities $(z\psi)_j$, the electrochemical potential η_j , and the molecular conductivities calculated in this study.

■ ASSOCIATED CONTENT

📄 Supporting Information

The Supporting Information is available free of charge on the ACS Publications website at DOI: 10.1021/acs.jpcc.7b08710.

Table 1. Calculated lattice constants for different YSZ compositions at different temperatures and zero pressure. Nernst–Planck diffusivities. (PDF)

■ AUTHOR INFORMATION

Corresponding Author

*E-mail: kabelac@ift.uni-hannover.de.

ORCID

Gerardo Valadez Huerta: 0000-0002-4858-5314

Notes

The authors declare no competing financial interest.

■ ACKNOWLEDGMENTS

We thank our colleague Sheridan Renzi for the English language corrections in this paper.

■ REFERENCES

- (1) Mahato, N.; Banerjee, A.; Gupta, A.; Omar, S.; Balani, K. Progress in Material Selection for Solid Oxide Fuel Cell Technology: A Review. *Prog. Mater. Sci.* **2015**, *72*, 141–337.
- (2) Chroneos, A.; Yildiz, B.; Tarancón, A.; Parfitt, D.; Kilner, J. A. Oxygen Diffusion in Solid Oxide Fuel Cell Cathode and Electrolyte Materials: Mechanistic Insights from Atomistic Simulations. *Energy Environ. Sci.* **2011**, *4*, 2774–2789.
- (3) Amarsingh Bhabu, K.; Theerthagiri, J.; Madhavan, J.; Balu, T.; Rajasekaran, T. R. Superior Oxide Ion Conductivity of Novel Acceptor Doped Cerium Oxide Electrolytes for Intermediate-Temperature Solid Oxide Fuel Cell Applications. *J. Phys. Chem. C* **2016**, *120*, 18452–18461.
- (4) Tao, Z.; Ding, H.; Chen, X.; Hou, G.; Zhang, Q.; Tang, M.; Gu, W. The Co-Doping Effect of Sm and In on Ceria for Electrolyte Application in IT-SOFC. *J. Alloys Compd.* **2016**, *663*, 750–754.
- (5) Zhu, H.; Kee, R. J. Membrane polarization in mixed conducting ceramic fuel cells and electrolyzers. *Int. J. Hydrogen Energy* **2016**, *41*, 2931–2943.
- (6) Guggenheim, E. A. The Conceptions of Electrical Potential Difference between Two Phases and The Individual Activities of Ions. *J. Phys. Chem.* **1928**, *33*, 842–849.
- (7) Sloth, P. On the Calculation of Single Ion Activity Coefficients in Homogeneous Ionic Systems by Application of the Grand Canonical Ensemble. *J. Chem. Phys.* **1993**, *98*, 7319–7323.
- (8) Sloth, P.; Sorensen, T. S. Monte Carlo Simulations of Single Ion Chemical Potentials. Results for the Unrestricted Primitive Model. *Chem. Phys. Lett.* **1988**, *146*, 452–455.
- (9) Valadez Huerta, G.; Kelle, A.; Kabelac, S. A Phenomenological Study of Yttria-Stabilized Zirconia at 1300 K with the Green–Kubo Formulation and Equilibrium Molecular Dynamics. *Chem. Phys.* **2017**, *485*, 108–117.
- (10) Plimpton, S. Fast Parallel Algorithmus for Short-Range Molecular Dynamics. *J. Comput. Phys.* **1995**, *117*, 1–19.
- (11) Woodcock, L.; Singer, K. Thermodynamic and Structural Properties of Liquid Ionic Salts Obtained by Monte Carlo Computation. Part 1.-Potassium Chloride. *Trans. Faraday Soc.* **1971**, *67*, 12–30.
- (12) De Leeuw, S. W.; Perram, J. W.; Smith, E. R. Simulation of electrostatic systems in periodic boundary conditions. I. Lattice sums and dielectric constants. *Proc. R. Soc. London, Ser. A* **1980**, *373*, 27–56.
- (13) Heyes, D. M. Electrostatic Potentials and Fields in Infinite Point Charge Lattices. *J. Chem. Phys.* **1981**, *74*, 1924–1929.

(14) Friedberg, R.; Cameron, J. E. Test of Monte Carlo Method: Fast Simulation of a Small Ising Lattice. *J. Chem. Phys.* **1970**, *52*, 6049–6058.

(15) Benson, G. C. A Simple Formula for Evaluating the Madelung Constant of a NaCl-Type Crystal. *Can. J. Phys.* **1956**, *34*, 888–890.

(16) Bogicevic, A.; Wolverton, C. Nature and strength of defect interactions in cubic stabilized zirconia. *Phys. Rev. B: Condens. Matter Mater. Phys.* **2003**, *67*, 0241061–02410613.

(17) Stapper, G.; Bernasconi, M.; Nicoloso, N.; Parrinello, M. Ab initio study of structural and electronic properties of yttria-stabilized cubic zirconia. *Phys. Rev. B: Condens. Matter Mater. Phys.* **1999**, *59*, 797–810.

(18) Kilo, M.; Argirusis, C.; Borchardt, G.; Jackson, R. A. Oxygen diffusion in yttria stabilized zirconia – experimental results and molecular dynamics calculations. *Phys. Chem. Chem. Phys.* **2003**, *5*, 2219–2224.

An Approach to the Coulomb Contribution of Thermodynamic Properties from the Mean Electrostatic Potential of the Ions in $(\text{ZrO}_2)_{1-x}(\text{Y}_2\text{O}_3)_x$

Gerardo Valadez Huerta, Malte Siemen, Stephan Kabelac.

SUPPORTING INFORMATION

2.4 Molecular Dynamics Simulations. The calculated lattice constants are given in Table 1.

Table 1. Calculated lattice constants for different YSZ compositions at different temperatures and zero pressure.

System	$a(1100 \text{ K})$ in Å	$a(1300 \text{ K})$ in Å	$a(1500 \text{ K})$ in Å
YSZ04	$5,1410 \pm 1 \cdot 10^{-4}$	$5.14880 \pm 6 \cdot 10^{-5}$	$5.15662 \pm 6 \cdot 10^{-5}$
YSZ08	$5.1528 \pm 2 \cdot 10^{-4}$	$5.1605 \pm 2 \cdot 10^{-4}$	$5.1681 \pm 2 \cdot 10^{-4}$
YSZ12	$5.1633 \pm 4 \cdot 10^{-4}$	$5.1707 \pm 3 \cdot 10^{-4}$	$5.1783 \pm 3 \cdot 10^{-4}$
YSZ16	$5.1719 \pm 4 \cdot 10^{-4}$	$5.1792 \pm 2 \cdot 10^{-4}$	$5.1868 \pm 2 \cdot 10^{-4}$
YSZ20	$5.1796 \pm 4 \cdot 10^{-4}$	$5.1872 \pm 3 \cdot 10^{-4}$	$5.1945 \pm 4 \cdot 10^{-4}$
YSZ24	$5.1879 \pm 7 \cdot 10^{-4}$	$5.1951 \pm 6 \cdot 10^{-4}$	$5.2024 \pm 4 \cdot 10^{-4}$
YSZ28	$5.1945 \pm 6 \cdot 10^{-4}$	$5.2019 \pm 7 \cdot 10^{-4}$	$5.2091 \pm 6 \cdot 10^{-4}$
Y_2O_3	$5.233 \pm 1 \cdot 10^{-3}$	$5.241 \pm 1 \cdot 10^{-3}$	$5.2478 \pm 6 \cdot 10^{-4}$

3.3 *Nernst-Planck Diffusivities* Analogous to the Nernst-Planck equations (26) and (27) for the molecular fluxes \mathbf{J}_j , we can write for the anion flux \mathbf{J}_O :

$$\mathbf{J}_O = D_{O,c} \nabla(-c_O) + \frac{\sigma_O}{e} \nabla(-(z\psi)_O). \quad (\text{S1})$$

On one hand, the fluxes are related due to stoichiometry:

$$\mathbf{J}_{ZrO_2} = \frac{x_{ZrO_2}}{2x_{ZrO_2} + 3x_{Y_2O_3}} \mathbf{J}_O = C \mathbf{J}_O, \quad (\text{S2})$$

$$\mathbf{J}_{Y_2O_3} = \frac{2x_{Y_2O_3}}{2x_{ZrO_2} + 3x_{Y_2O_3}} \mathbf{J}_O = D \mathbf{J}_O. \quad (\text{S3})$$

On the other hand, the forces may follow a mixing rule such as the one given in this work (see Eq. (24) and (25)). We can write exemplarily for the electrostatic forces:

$$\nabla(-z\psi_{ZrO_2}) = A \nabla(-z_O\psi_O) + \nabla(-z_{Zr}\psi_{Zr}), \quad (\text{S4})$$

$$\nabla(-z\psi_{Y_2O_3}) = 2(B \nabla(-z_O\psi_O) + \nabla(-z_Y\psi_Y)). \quad (\text{S5})$$

with

$$A = \frac{N_O^2}{N_O(ZrO_2)N_{YSZ}}, \quad (\text{S6})$$

$$B = \left(1 - \frac{N_ON_{Zr}}{N_O(ZrO_2)N_{YSZ}}\right) \frac{N_O}{N_Y}. \quad (\text{S7})$$

If we neglect the gradient of the electrostatic potential of the cations, i. e., $\nabla(-z_{Zr}\psi_{Zr}) = \nabla(-z_Y\psi_Y) = 0$, we can relate the electrical conductivities from Eq. (26), Eq. (27) and Eq. (S1) with Eq. (S4), Eq. (S5) and some mathematical manipulation:

$$\sigma_{ZrO_2} = \frac{C}{A}\sigma_O, \quad (S8)$$

$$\sigma_{Y_2O_3} = \frac{D}{2B}\sigma_O. \quad (S9)$$

Moreover, we can write for the molecular fluxes according to non-equilibrium thermodynamics the following phenomenological equations:

$$\mathbf{J}_{ZrO_2} = L_{ZrO_2}^* \nabla(-\beta\eta_{ZrO_2}), \quad (S10)$$

$$\mathbf{J}_{Y_2O_3} = L_{Y_2O_3}^* \nabla(-\beta\eta_{Y_2O_3}), \quad (S11)$$

$$\mathbf{J}_O = L_{OO} \nabla(-\beta\eta_O). \quad (S12)$$

Here, L_j^* and L_{OO} are the phenomenological coefficients and $\beta = (k_B T)^{-1}$ the reciprocal of the thermodynamic temperature with k_B as the Boltzmann constant. In Eq. (S10) and Eq. (S11), we neglect diffusion due to a temperature gradient, assume local equilibrium and use the Gibbs-Duhem equation to reduce the number of phenomenological coefficients with new defined coefficients:

$$L_{ZrO_2}^* = L_{ZrO_2} - \frac{x_{Y_2O_3}}{x_{ZrO_2}} L_{ZrO_2}^{Y_2O_3}, \quad (S13)$$

$$L_{Y_2O_3}^* = L_{Y_2O_3} - \frac{x_{ZrO_2}}{x_{Y_2O_3}} L_{Y_2O_3}^{ZrO_2}. \quad (S14)$$

Furthermore, we neglect cation diffusion in Eq. (S12). We can expand these phenomenological equations using Eq. (13) and assuming constant temperature as follows:

$$\mathbf{J}_{ZrO_2} = \beta L_{ZrO_2}^* \nabla(-\mu_{ZrO_2}) + \beta L_{ZrO_2}^* \nabla(-e(z\psi)_{ZrO_2}), \quad (\text{S15})$$

$$\mathbf{J}_{Y_2O_3} = \beta L_{Y_2O_3}^* \nabla(-\mu_{Y_2O_3}) + \beta L_{Y_2O_3}^* \nabla(-e(z\psi)_{Y_2O_3}), \quad (\text{S16})$$

$$\mathbf{J}_O = \beta L_{OO} \nabla(-\mu_{OO}) + \beta L_{OO} \nabla(-e(z\psi)_O). \quad (\text{S17})$$

From a comparison of Eq. (S15), Eq. (S16) and Eq. (S17) with Eq. (26), Eq. (27) and Eq. (S1) using Eq. (S8) and Eq. (S9) we get:

$$\sigma_{ZrO_2} = e^2 \beta L_{ZrO_2}^* = e^2 \beta \frac{C}{A} L_{OO}, \quad (\text{S20})$$

$$\sigma_{Y_2O_3} = e^2 \beta L_{Y_2O_3}^* = e^2 \beta \frac{D}{2B} L_{OO}, \quad (\text{S11})$$

The Fick diffusion coefficients D_j of the molecules are related to the phenomenological coefficients L_j^* and therefore also to the molecular conductivities σ_{ZrO_2} and $\sigma_{Y_2O_3}$:

$$D_{ZrO_2} = \frac{L_{ZrO_2}^*}{c_{ZrO_2}} \Gamma_{ZrO_2} = \frac{\sigma_{ZrO_2}}{\beta e^2 c_{ZrO_2}} \Gamma_{ZrO_2}, \quad (\text{S12})$$

$$D_{Y_2O_3} = \frac{L_{Y_2O_3}^*}{c_{Y_2O_3}} \Gamma_{Y_2O_3} = \frac{\sigma_{Y_2O_3}}{\beta e^2 c_{Y_2O_3}} \Gamma_{Y_2O_3}, \quad (\text{S13})$$

with the molecular concentration c_j and the thermodynamic factor:

$$\Gamma_j = \beta \left(\frac{\partial \mu_j}{\partial \ln x_j} \right). \quad (\text{S14})$$

III

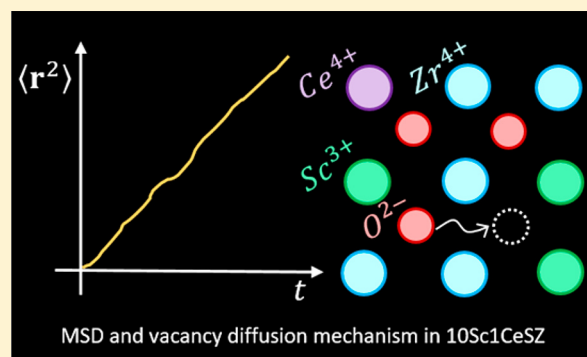
A Diffusivity Study of $(\text{Sc}_2\text{O}_3)_{0.1}(\text{CeO}_2)_{0.01}(\text{ZrO}_2)_{0.89}$ between 1100 and 1500 K at Zero Pressure with Molecular Dynamics

Gerardo Valadez Huerta,¹ Lucas Reus,[†] and Stephan Kabelac*

Institut für Thermodynamik, Gottfried Wilhelm Leibniz Universität Hannover, Callinstr. 36, D-30167 Hannover, Germany

Supporting Information

ABSTRACT: Zirconium dioxide (ZrO_2) codoped with 10 mol % scandium(III) oxide Sc_2O_3 and 1 mol % cerium dioxide CeO_2 (10Sc1CeSZ) is a relevant electrolyte material for high temperature fuel or electrolysis cells, due to its high ionic conductivity and its stability in the cubic phase in comparison to other metal oxides. Despite the many experimental studies for 10Sc1CeSZ, there are to our knowledge no computational studies of this material. In this paper, we calculate the diffusivities and ionic conductivity of 10Sc1CeSZ using classical molecular dynamics for different temperatures and the density at zero pressure in the canonical ensemble. Our results for the ionic conductivity are comparable with experimental data for temperatures equal to or above 1200 K. This may hopefully also be the case for the Brownian diffusion coefficient and the tracer diffusion coefficient calculated in this work, for which no literature values are available. The values given in this paper can be used in future studies describing transport phenomena in fuel or electrolysis cells with 10Sc1CeSZ electrolytes.



1. INTRODUCTION

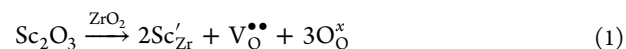
In a fuel cell, hydrogen and oxygen react electrochemically, producing water, electrical power, and heat. In a solid oxide fuel cell (SOFC), oxygen anions are transported through the electrolyte from the cathode to the anode.¹ The electrolyte is a metal oxide with crystal defects in the oxygen sublattice, so that the anion transport occurs through vacancy diffusion.²

The standard material for SOFC electrolytes is yttrium(III) oxide-stabilized zirconium dioxide with 8 mol % Y_2O_3 (YSZ08). This concentration is used because it results in the maximum conductivity of this material.³ Nevertheless, stabilized zirconia with a concentration of 10 mol % scandium(III) oxide Sc_2O_3 and 1 mol % cerium dioxide CeO_2 (10Sc1CeSZ) has an even higher ionic conductivity.⁴ For this reason, there are several experimental studies of 10Sc1CeSZ in the literature. In these experimental studies, only the structural,^{5–8} electrical,^{9–11} and mechanical^{12–14} properties of 10Sc1CeSZ, as well as the aging behavior,^{15–17} are analyzed, usually in dependence on the sintering process. Despite the already conducted computational studies on ScSZ,^{18–20} to our knowledge, there are no computational studies for 10Sc1CeSZ.

The purpose of this study is an extensive diffusivity analysis of this material with classical molecular dynamics (MD) calculations. For our investigation, we use the Buckingham potential with Coulomb interactions and a parametrization based on the works of Dwivedi and Comarck²¹ and Lewis and Catlow.²² Finally, the computational results for conductivity are compared to experimental data from the literature.

2. METHODS

2.1. Theory. As the result of doping of Sc_2O_3 into ZrO_2 in 10Sc1CeSZ, oxygen vacancies $V_{\text{O}}^{\bullet\bullet}$ form in the oxygen sublattice according to the following defect reaction in Kröger–Vink notation:



From reaction 1, it is clear that the electroneutrality condition is given by $[\text{Sc}'_{\text{Zr}}] = 2[V_{\text{O}}^{\bullet\bullet}]$. To describe the vacancy diffusion, we have to differentiate between Brownian diffusion and diffusion due to a potential gradient. On one hand, the Brownian diffusion coefficient $D_{\text{O}}^{\text{MSD}}$ is given by the mean square displacement (MSD) of the anions $r^2(t)$

$$\langle r^2(t) \rangle = 2nD_{\text{O}}^{\text{MSD}}t \quad (2)$$

where n is the number of spatial dimensions. This diffusion coefficient is closely related to the tracer diffusion coefficient D_{O}^* given by²³

$$D_{\text{O}}^* = f_{\text{O}}D_{\text{V}}^{\text{MSD}}x_{\text{V}} \quad (3)$$

Here, f_{O} is the geometrical correlation factor and $D_{\text{V}}^{\text{MSD}}$ is the diffusion coefficient of the vacancies. In this case, we use the jump balance $D_{\text{O}}x_{\text{O}} = D_{\text{V}}x_{\text{V}}$, where x_{O} is the mole fraction of the oxygen anions and x_{V} is the mole fraction of the vacancies.

Received: December 18, 2017

Accepted: May 16, 2018

Published: May 25, 2018

For simple cubic sublattices, such as the oxygen sublattice in 10Sc1CeSZ, the correlation factor can be calculated as follows²⁴

$$f_O \approx 1 - \frac{2}{Z_O} \quad (4)$$

where Z_O is the first coordination number, which can be determined from the radial distribution function (RDF) of the anions.

On the other hand, the vacancy diffusion of the anions due to a potential gradient can be described using the non-equilibrium thermodynamics approach:²⁵

$$J_O/k_B = -L_{OO}\nabla(\beta\eta_O) = -\beta L_{OO}\nabla(\mu_O + z_OF\phi) \quad (5)$$

This equation gives the flux density J_O of the anions in mol/(m² s). Here, L_{OO} is the phenomenological coefficient describing the anion diffusion, F the Faraday constant, ϕ the electrostatic potential, k_B the Boltzmann constant, and $\beta = (k_B T)^{-1}$ the reciprocal of the thermodynamic temperature. Additionally, η_O is the electrochemical potential, μ_O the chemical potential, and z_O the valency of the oxygen anions. In this case, we assume that there are no temperature gradients and no cation diffusion; otherwise, additional terms have to be added in eq 5. We can also describe the kinetics with the Nernst–Planck equation:

$$J_O = \frac{c_O D_O}{RT} \nabla(-\mu_O) + \frac{\sigma_O}{F} \nabla(-z_O \phi) \quad (6)$$

Here R is the ideal gas constant and $c_O = [O_O^x]$ is the concentration of the oxygen anions. The ionic conductivity σ_O and the diffusion coefficient D_O are then given by

$$\frac{c_O D_O}{R} = \frac{T \sigma_O}{F^2} = L_{OO} \quad (7)$$

The phenomenological coefficient L_{OO} can be calculated from the anion microflux using the Green–Kubo relation, as was done in our previous work.²⁶

2.2. System, Force Field, and Thermodynamic State.

To build the start configuration for our MD calculations, we use a $5 \times 5 \times 5$ lattice simulation box of pure ZrO₂. We assume the lattice to be cubic and of the fluorite type (see Figure 1) with a lattice constant of 5.0×10^{-10} m, so that the initial box encloses 1000 oxygen atoms and 500 zirconium atoms.

We randomly swap five zirconium atoms with five cerium atoms so that $x_{CeO_2} \approx 0.01$. After that, we randomly swap zirconium atoms with scandium atoms until $x_{Sc_2O_3} \approx 0.1$. To guarantee the electroneutrality of the system, we randomly remove one oxygen atom for every two scandium atoms in the system. The resulting configuration is given in Table 1.

We describe the interaction between the atoms in the system with the Buckingham potential and a Coulomb term:

$$u(r_{ij}) = A_{ij} e^{r_{ij}/\rho_{ij}} - \frac{C_{ij}}{r_{ij}^6} + \frac{q_i q_j}{4\pi\epsilon_0 r_{ij}} \quad (8)$$

Here, we use values from the literature^{21,22} for the coefficients ρ_{ij} , C_{ij} , and A_{ij} to describe the interactions between the ions. These values are given in Table 2, where e is the elementary charge. The ions are seen as point charges with a valency of +4 for Zr and Ce, respectively, -2 for O, and +3 for Sc.

We carry out our study in the canonical ensemble with the density corresponding to a thermodynamic state at zero

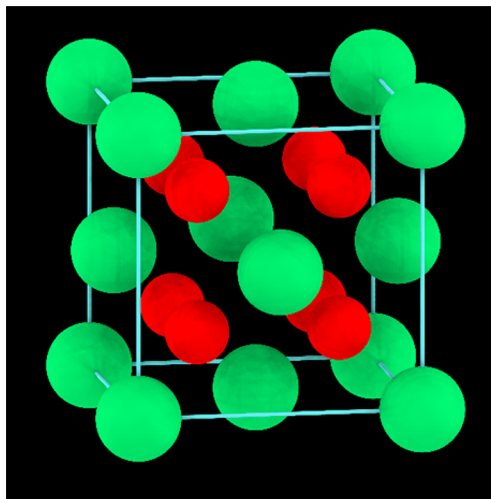


Figure 1. 10Sc1CeSZ cubic structure. In green are the Zr, Ce, or Sc atoms. O atoms or V_O vacancies are in red. The image was generated using OVITO.²⁷

Table 1. 10Sc1CeSZ Composition Analyzed in This Work

system	N_{Zr}	N_{Ce}	N_{Sc}	N_O	$x_{Sc_2O_3} \times 10^2$	$x_{CeO_2} \times 10^2$
10Sc1CeSZ	403	5	92	954	10.13	1.10

Table 2. Parameters A_{ij} , ρ_{ij} , and C_{ij} for the Buckingham Potential^a

	A_{ij} (J)	ρ_{ij} (10^{-10} m)	C_{ij} (10^{-60} J m ⁶)
Zr ⁴⁺ –O ²⁻	985.869e	0.376	0
Ce ⁴⁺ –O ²⁻	1013.6e	0.3949	0
Sc ³⁺ –O ²⁻	1299.4e	0.3312	0
O ²⁻ –O ²⁻	22764.3e	0.149	27.89e

^aThe values for the Zr⁴⁺–O²⁻ and O²⁻–O²⁻ interactions are taken from the work of Dwivedi and Cormack.²¹ The values for the Ce⁴⁺–O²⁻ and Sc³⁺–O²⁻ interactions are taken from the work of Lewis and Catlow.²² Here, e is the elementary charge.

pressure and different temperatures (1100 K, 1200 K, ..., 1500 K). We select this temperature range because it is difficult to measure the ionic conductivity of 10Sc1CeSZ for temperatures above 1100 K with, e.g., impedance spectroscopy, and, to our knowledge, there are no studies of the ionic conductivity for temperatures above 1300 K.

2.3. Computational Details. All of our calculations are strictly classical, and we carry them out using LAMMPS.²⁸ We use the computation methodology described in our previous works.^{26,29} For all simulations, periodic boundary conditions apply. We use a cutoff radius for the non-Coulomb contributions of 10×10^{-10} m. We integrate the Coulomb energy with the Ewald sum using an accuracy of 1×10^{-4} for the root-mean-square force error in the real and K -space, resulting in an Ewald parameter of approximately 0.3×10^{-10} m for all simulations. We conduct all simulations with a time step of 0.5×10^{-15} s. For each simulation, the equilibration run is 1×10^{-9} m long and the production run is 0.5×10^{-9} s long. For our calculations, we use the position and velocities of the atoms at each time step of the production run. We apply a cutoff radius of 10.2×10^{-10} m divided into 150 bins for the computation of the RDFs.

To calculate the lattice constant a , simulations in the Nosé–Hoover NpT ensemble are performed. The time span is 0.1 ×

10^{-12} s for the temperature relaxation and 1×10^{-12} s for the pressure relaxation. To calculate the RDFs, the MSD of the anions, and the correlation functions, we conduct simulations in the Nosé–Hoover NVT ensemble using the last configuration of the production run from the NpT simulations but adjusting the density in such a way that it corresponds to the calculated mean value of the lattice constant a . Here, the time span for the temperature relaxation is also 0.1×10^{-12} s.

We conduct independent simulations using 10 different 10Sc1CeSZ configurations for each temperature. As an indicator for the reproducibility of our results, we estimate the error for each simulation with well-known methods summarized by Allen and Tildesley.³⁰ The values presented throughout this paper are the mean values of the 10 independent simulations. Following the discussion of Pranami and Lamm,³¹ the uncertainties are calculated on the basis of a one-sided Student's distribution given by a 95% confidence interval. In the Supporting Information, we show that the simulations reached thermodynamic equilibrium and that the chosen number of independent simulations is appropriated, and we also provide simulation sample data.

3. RESULTS AND DISCUSSION

3.1. Structural Properties. We summarize in Table 3 the calculated lattice constant a and the calculated coefficient of

Table 3. Calculated Lattice Constant a and Coefficient of Thermal Expansion α for 10Sc1CeSZ, as Well as Calculated Coordination Number Z_O and Correlation Factor f_O for the Oxygen Sublattice in 10ScCeSZ, at Different Temperatures and Zero Pressure

T (K)	a (10^{-10} m)	α (10^{-6} K $^{-1}$)	Z_O	f_O
1100	5.11518(15)	8.444(48)	5.918(45)	0.6621(26)
1200	5.11948(11)	8.437(48)	5.908(38)	0.6615(22)
1300	5.12380(13)	8.430(48)	5.897(41)	0.6608(24)
1400	5.12813(10)	8.423(48)	5.885(37)	0.6602(21)
1500	5.13245(10)	8.416(48)	5.874(33)	0.6595(19)

thermal expansion (CTE) α for different temperatures. The extrapolated mean value for the lattice constant at 298 K is

$$a(298 \text{ K}) = 5.10231(31) \times 10^{-10} \text{ m} \quad (9)$$

and the relative deviation to the experimental value of $5.0956(1) \times 10^{-10}$ m, taken from the work of Omar et al.,³² is 0.13%, which is small but not within the error bars of the experimental value.

In the study of Heel et al.,³³ experimental values of the CTE are given for two different temperature ranges: 10.6×10^{-6} K $^{-1}$ at 473–923 K and 12.5×10^{-6} K $^{-1}$ at 923–1253 K. Heel et al.³³ also give a mean value for the CTE of 11.4×10^{-6} K $^{-1}$. The relative deviation between the simulated CTE and the experimental value at 1100 K is 48%. We calculate values of the lattice constant between 1100 and 1500 K using the mean experimental CTE (see the Supporting Information). The relative deviation between these values and the simulated lattice constant is 0.33% at 1100 K and 0.46% at 1500 K. The chosen parametrization, therefore, gives an acceptable description of the lattice constant of 10Sc1CeSZ and its temperature dependency despite the high relative deviation between the MD results and the experimental values of the CTE.

We plot in Figure 2 the calculated RDF between anions and the cations and the anions at 1100 and 1500 K. The RDFs for Zr–O, Ce–O, and Sc–O are similar, but the distance from the zirconium and scandium cations to the oxygen anions is slightly shorter than the distance between the cerium cations and the oxygen anions. Following the discussion of Shimojo et al.³⁴ for YSZ, the doping of cerium results in a shifting of the oxygen anions from their tetrahedral site. We calculate the first coordination number for Sc–O, Zr–O, and Ce–O considering only the first peak of the RDFs for the weighted integral (see Supporting Information). The coordination number for Ce–O is the highest. This is due to the larger ionic radius of cerium (185×10^{-12} m) in comparison to that of scandium (88.5×10^{-12} m) or zirconium (86×10^{-12} m), as discussed by Norberg et al.³⁵ for this kind of doped zirconias. The peak of

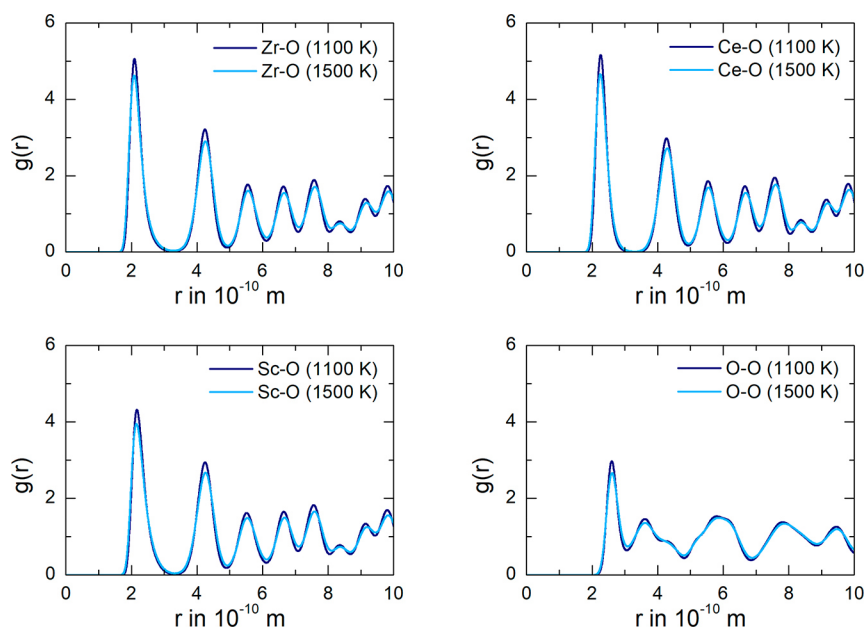


Figure 2. Calculated RDFs for the ion pairs Zr–O, Sc–O, Ce–O, and O–O in 10Sc1CeSZ at 1100 K (dark blue lines) and 1500 K (light blue lines) and zero pressure.

the local maxima for the RDF for Sc–O is smaller than that for Zr–O. However, the coordination numbers $Z_{\text{Sc-O}}$ and $Z_{\text{Zr-O}}$ are similar within the statistical uncertainty, since the RDFs for Sc–O are broader than the RDFs for Zr–O. Finally, the peak of the local maxima for all RDFs decreases at the higher temperature. This results in a smaller coordination number in all cases.

The calculated coordination number Z_{O} for the oxygen sublattice in 10Sc1CeSZ and the corresponding correlation factor f_{O} calculated with eq 4 are given in Table 3 for different temperatures. We test the null hypothesis that the values of the coordination number Z_{O} and of the correlation factor f_{O} do not differentiate from their mean value at different temperatures, i.e., that the values can be seen as temperature independent within the statistical uncertainty despite the appreciable decreasing tendency of Z_{O} and increasing tendency of f_{O} for higher temperatures. The detailed results from these tests are given in the Supporting Information and show that the null hypothesis has to be rejected, as some values cannot statistically be taken as temperature independent.

3.2. Diffusivities and Ionic Conductivity. Figure 3 is the Arrhenius plot for the Brownian diffusion coefficients of the

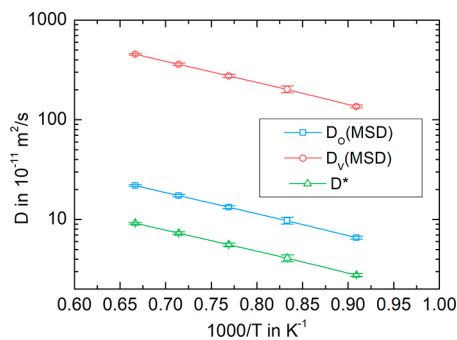


Figure 3. Brownian diffusion coefficients for the oxygen anions $D_{\text{O}}^{\text{MSD}}$ (blue squares) and for the vacancies $D_{\text{V}}^{\text{MSD}}$ (red circles) and tracer diffusion coefficient D^* (green triangles).

oxygen anions $D_{\text{O}}^{\text{MSD}}$ and the vacancies $D_{\text{V}}^{\text{MSD}}$ and for the tracer Diffusion coefficient D^* . As expected from the jump balance, the Brownian diffusion coefficient of the vacancies is bigger

than the Brownian diffusion coefficient of the oxygen anions. Furthermore, the progression of the tracer diffusion coefficient is similar to the progression of the other diffusion coefficients in the plot. In this case, all three diffusion coefficients can be described with an activation energy:

$$E_{\text{A}}^{\text{MSD}} = 0.4281(81)e \text{ J} \quad (10)$$

To our knowledge, there are no experimental data nor other calculation results for these quantities in 10Sc1CeSZ, so we cannot confirm the accuracy of our results.

The autocorrelation function (ACF) of the microflux of the oxygen anions normalized with the value $\langle J_{\text{O}}(0)J_{\text{O}}(0) \rangle_{T=1500\text{K}}$ is plotted for 1100 and 1500 K in Figure 4 (left). To evaluate the integral of the ACF with the Green–Kubo relation, we use the approach given in our previous work²⁶ with an averaging interval of $1\text{--}2 \times 10^{-12}$ s. This assumption is adequate, since the ACF decayed to zero at around 0.4×10^{-12} s in all cases. The Arrhenius plot of the ionic conductivity σ_{O} is given in Figure 4 (right) in comparison with experimental data of Lee et al.,³⁶ Liu et al.,⁷ and Arachi et al.⁹ To our knowledge, these are the only studies giving experimental data of the conductivity at this temperature range. The relative deviation in log scale is 10% for 1100 K, 6% for 1200 K, and 5% for 1300 K in comparison to the experimental values of Lee et al.³⁶ and Liu et al.,⁷ in comparison to the experimental values of Arachi et al.,⁹ it is 18% for 1100 K and 14% for 1200 K. The relative deviation of the absolute values should be significantly higher. However, the experimental values from different studies also show a similar discrepancy to each other. Therefore, we believe that the values calculated demonstrate that this approach is acceptable for the ionic conductivity at temperatures above 1200 K and that the comparison in the log scale is appropriate. Nevertheless, the calculation with the proposed force field parametrization is not suitable for temperatures below 1200 K due to the high relative deviation.

Taking into account the experimental values above 1200 K from the work of Lee et al.,³⁶ we calculate a mean activation energy of $0.51(24)e \text{ J}$. The activation energy calculated in this work of $0.331(21)e \text{ J}$ lies within the error bars of the calculated value from the experimental data of Lee et al.³⁶ Furthermore, the relative deviation between our calculated value and the

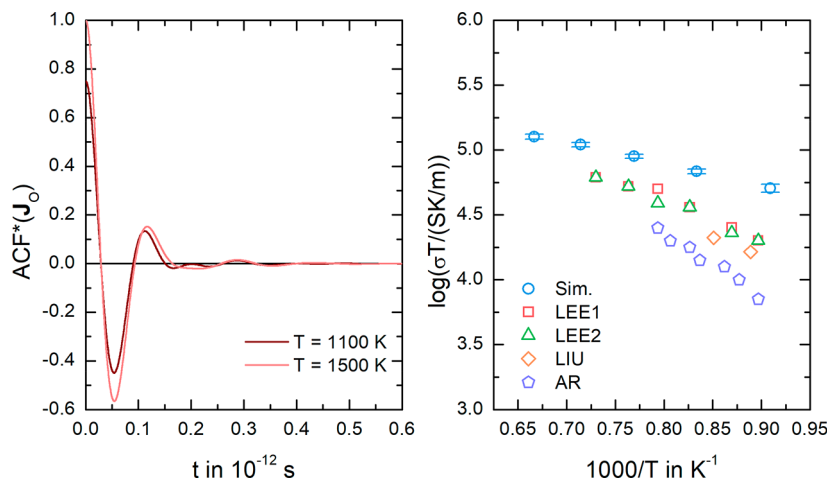


Figure 4. (left) Calculated ACF of the microflux of the oxygen anions normalized with the value $\langle J_{\text{O}}(0)J_{\text{O}}(0) \rangle_{T=1500\text{K}}$. (right) Calculated Arrhenius plot of the ionic conductivity σ (blue circles) in comparison with experimental data: LEE1 (red squares) and LEE2 (green triangles) from the work of Lee et al.,³⁶ LIU (orange diamonds) from the work of Liu et al.,⁷ and AR (violet pentagons) from the work of Arachi et al.⁹

Table 4. Calculated Nernst–Planck Diffusion Coefficient D_0 of 10Sc1CeSZ for Different Temperatures and Zero Pressure

T (K)	1100	1200	1300	1400	1500
D_0 (10^{-10} m ² /s)	4.78 (34)	6.47 (27)	8.48 (29)	10.46 (41)	12.08 (56)

experimental value of the activation energy for the grain ionic conductivity from the work of Wang et al.³⁷ of 0.363 eV is only 9%, so our approach provides a good description of the energy barriers for the ionic conductivity of 10Sc1CeSZ for temperatures between 1200 and 1500 K.

To calculate the ionic conductivity, the anion microflux is defined as the sum of the velocities of all oxygen anions.²⁶ The ACF of the anion microflux comprises, therefore, a term corresponding to the velocity auto correlation function (VACF). In the linear approximation, the diffusivities calculated from the VACF are equivalent to those calculated from the MSD. Thus, there is a relative high probability that the Brownian diffusion coefficients and the tracer diffusion coefficients calculated from the MSD of the anions in this study are as effectively described as the calculated ionic conductivity for temperatures above 1200 K (see Figure 3). Finally, the calculated Nernst–Planck diffusion coefficient D_0 for 10Sc1CeSZ is given in Table 4 for different temperatures. Here, the activation energy 0.335(21) eV is almost equal to the activation energy of the ionic conductivity in spite of the concentration dependency in eq 7.

4. CONCLUSIONS

The main goal of this study is to calculate the diffusivities and ionic conductivity of the oxygen anions in 10Sc1CeSZ. We select this material because it has a higher ionic conductivity than the standard material for SOFC applications, YSZ. We perform our calculations with the MD package LAMMPS²⁸ using the methodology reported in our previous work.^{26,29} We use the Buckingham potential to describe the interatomic contributions with a parametrization from the works of Dwedi and Cormack²¹ for the Zr–O and O–O interactions and a parametrization from Lewis and Catlow²² for the Sc–O and Ce–O interactions. The calculated lattice constant is in agreement with experimental data. For temperatures between 1200 and 1500 K, the calculated conductivity values are comparable to experimental data from the literature and the activation energy deviates only 9% from the experimental value for grain ionic conductivity, meaning that our approach effectively describes the energy barriers. In this case, there is quite a high probability that these statements are also true for the Brownian diffusion coefficient, the tracer diffusion coefficient, and the Nernst–Planck diffusion coefficient. To our knowledge, there are no experimental data for these diffusivities in the literature.

■ ASSOCIATED CONTENT

■ Supporting Information

The Supporting Information is available free of charge on the ACS Publications website at DOI: 10.1021/acs.jced.7b01094.

System equilibration; estimation of the number of independent simulations; sample data for D_0^{MSD} and L_{OO} ; calculated coordination numbers $Z_{\text{Zr-O}}$, $Z_{\text{Ce-O}}$, and $Z_{\text{Sc-O}}$; statistical analysis of the temperature dependence of Z_0 and f_0 (PDF)

■ AUTHOR INFORMATION

Corresponding Author

*E-mail: kabelac@ift.uni-hannover.de. Web page: www.ift.uni-hannover.de.

ORCID

Gerardo Valadez Huerta: 0000-0002-4858-5314

Present Address

†L.R.: Institut für Elektrische Energiesysteme. Fachgebiet Elektrische Energieversorgung, Gottfried Wilhelm Leibniz Universität Hannover, Appelstraße 9A, D-30167 Hannover, Germany.

Author Contributions

The manuscript was written through contributions of all authors. All authors have given approval to the final version of the manuscript.

Notes

The authors declare no competing financial interest.

■ ACKNOWLEDGMENTS

We would like to thank again our colleague Sheridan Renzi for the English correction throughout the whole manuscript.

■ ABBREVIATIONS

SOFC, solid oxide fuel cell; YSZ, yttrium(III) oxide stabilized zirconium dioxide; 10Sc1CeSZ, 10 mol % scandium dioxide–1 mol % cerium dioxide stabilized zirconium dioxide; MD, molecular dynamics; RDF, radial distribution function; MSD, mean square displacement; ACF, autocorrelation function; CTE, coefficient of thermal expansion

■ REFERENCES

- (1) Singhal, S. C. Advances in solid oxide fuel cell technology. *Solid State Ionics* **2000**, *135*, 131–305.
- (2) Kharton, V. V.; Marques, F. M. B.; Atkinson, A. Transport properties of solid oxide electrolyte ceramics: a brief review. *Solid State Ionics* **2004**, *174*, 135–149.
- (3) Mahato, N.; Banerjee, A.; Gupta, A.; Omar, S.; Balani, K. Progress in material selection for solid oxide fuel cell technology: A review. *Prog. Mater. Sci.* **2015**, *72*, 141–337.
- (4) Bredikhin, I.; Bredikhin, S.; Kveder, V. Optimization of the Charge Transfer Process in Composite Ni/YSZ Cermet Anodes. *ECSS Trans.* **2009**, *25*, 1967–1974.
- (5) Dasari, H. P.; Ahn, J. S.; Ahn, K.; Park, S.-Y.; Hong, J.; Kim, H.; Yoon, K. J.; Son, J.-W.; Lee, H.-W.; Lee, J.-H. Synthesis, sintering and conductivity behavior of ceria-doped Scandia-stabilized zirconia. *Solid State Ionics* **2014**, *263*, 103–109.
- (6) Tu, H.; Liu, X.; Qingchun, Y. Synthesis and characterization of scandia ceria stabilized zirconia powders prepared by polymeric precursor method for integration into anode-supported solid oxide fuel cells. *J. Power Sources* **2011**, *196*, 3109–3113.
- (7) Liu, M.; He, C. R.; Wang, W. G.; Wang, J. X. Synthesis and characterization of 10Sc1CeSZ powders prepared by a solid-liquid method for electrolyte-supported solid oxide fuel cells. *Ceram. Int.* **2014**, *40*, 5441–5446.
- (8) Kumar, A.; Jaiswal, A.; Sanbui, M.; Omar, S. Scandia stabilized zirconia-ceria solid electrolyte ($x\text{Sc}1\text{CeSZ}$, $5 < x < 11$) for IT-SOFCs: Structure and conductivity studies. *Scr. Mater.* **2016**, *121*, 10–13.
- (9) Arachi, Y.; Asai, T.; Yamamoto, O.; Takeda, Y.; Imanishi, N.; Kawate, K.; Tamakoshi, C. Electrical Conductivity of $\text{ZrO}_2\text{-Sc}_2\text{O}_3$

Doped with HfO₂, CeO₂ and Ga₂O₃. *J. Electrochem. Soc.* **2001**, *148*, A520–A523.

(10) Liu, M.; He, C.; Wang, J.; Wang, W. G.; Wang, Z. Investigation of (CeO₂)_x(Sc₂O₃)_(0.11-x)(ZrO₂)_{0.89} ($x = 0.01–0.10$) electrolyte materials for intermediate temperature solid oxide fuel cell. *J. Alloys Compd.* **2010**, *502*, 319–323.

(11) Preis, W.; Egger, A.; Waldhäusl, J.; Sitte, W.; de Carvalho, E.; Irvine, J. T. S. Bulk and Grain Boundary Conductivities as Function of Temperature and Oxygen Partial Pressure of Scandia-Stabilized Zirconia Co-Doped with Yttria and Ceria. *ECS Trans.* **2009**, *25*, 1635–1642.

(12) Orlovskaya, N.; Lukich, S.; Subhash, G.; Graule, T.; Kuebler, J. Mechanical properties of 10 mol% Sc₂O₃-1 mol% CeO₂-89 mol% ZrO₂ ceramics. *J. Power Sources* **2010**, *195*, 2774–2781.

(13) Fleischhauer, F.; Bermejo, R.; Danzer, R.; Mai, A.; Graule, T.; Kuebler, J. High Temperature mechanical properties of zirconia tapes used for electrolyte supported solid oxide fuel cells. *J. Power Sources* **2015**, *273*, 237–243.

(14) Fleischhauer, F.; Terner, M.; Bermejo, R.; Danzer, R.; Mai, A.; Graule, T.; Kuebler, J. Fracture toughness and strength distribution at room temperature of zirconia tapes used for electrolyte supported solid oxide fuel cells. *J. Power Sources* **2015**, *275*, 217–226.

(15) Omar, S.; Bonanos, A. Ionic conductivity ageing behavior of 10 mol.% Sc₂O₃-1 mol.% CeO₂-ZrO₂ ceramics. *J. Mater. Sci.* **2010**, *45*, 6406–6410.

(16) Omar, S.; Belda, A.; Escardino, A.; Bonanos, N. Ionic conductivity ageing investigation of 1Ce10ScSZ in different partial pressures of oxygen. *Solid State Ionics* **2011**, *184*, 2–5.

(17) Laguna-Bercero, M. A.; Orera, V. M. Micro-spectroscopic study of the degradation of scandia and ceria stabilized zirconia electrolytes in solid oxide electrolysis cells. *Int. J. Hydrogen Energy* **2011**, *36*, 13051–13058.

(18) Chang, K.-S.; Tung, K.-L. Oxygen-Ion Transport in a Dual-Phase Scandia-Yttria-Stabilized Zirconia Solid Electrolyte: A Molecular Dynamics Simulation. *ChemPhysChem* **2009**, *10*, 1887–1894.

(19) Xu, J.; Bai, S.; Higuchi, Y.; Ozawa, N.; Sato, K.; Hashida, T.; Kubo, M. Multi-nanoparticle model simulations of the porosity effect on sintering processes in Ni/YSZ and Ni/ScSZ by the molecular dynamics method. *J. Mater. Chem. A* **2015**, *3*, 21518–21527.

(20) Xue, Q.; Huang, X.; Wang, L.; Dong, J.; Xu, H.; Zhang, J. Effects of Sc doping on phase stability of Zr_{1-x}Sc_xO₂ and phase transition mechanism: First-principles calculations and Rietveld refinement. *Mater. Des.* **2017**, *114*, 297–302.

(21) Dwivedi, A.; Cormack, A. N. A computer simulation study of the defect structure of calcia-stabilized zirconia. *Philos. Mag. A* **1990**, *61*, 1–22.

(22) Lewis, G. V.; Catlow, C. R. A. Potential models for ionic oxides. *J. Phys. C: Solid State Phys.* **1985**, *18*, 1149–1161.

(23) Martin, M. Diffusion in Oxides. In *Diffusion in Condensed Matter: Methods, Materials, Models*; Heitjans, P., Kärger, J., Eds.; Springer: Berlin, Heidelberg, 2013.

(24) Mehrer, H. Diffusion: Introduction and Case Studies in Metals and Binary Alloys. In *Diffusion in Condensed Matter: Methods, Materials, Models*; Heitjans, P., Kärger, J., Eds.; Springer: Berlin, Heidelberg, 2013.

(25) Kjelstrup, S.; Bedeaux, D.; Johanessen, E.; Gross, J. *Non-Equilibrium Thermodynamics for Engineers*; World Scientific: Hackensack, NJ, London, 2010.

(26) Valadez Huerta, G.; Kelle, A.; Kabelac, S. A Phenomenological Study of Yttria-Stabilized Zirconia at 1300 K with the Green–Kubo Formulation and Equilibrium Molecular Dynamics. *Chem. Phys.* **2017**, *485–486*, 108–117.

(27) Stukowski, A. Visualization and analysis of atomistic simulation data with OVITO – the Open Visualization Tool. *Modell. Simul. Mater. Sci. Eng.* **2010**, *18*, 015012.

(28) Plimpton, S. Fast Parallel Algorithm for Short-Range Molecular Dynamics. *J. Comput. Phys.* **1995**, *117*, 1–19.

(29) Valadez Huerta, G.; Siemen, M.; Kabelac, S. Approach to the Coulomb Contribution of Thermodynamic Properties from the Mean

Electrostatic Potential of the Ions in (ZrO₂)_{1-x}(Y₂O₃)_x. *J. Phys. Chem. C* **2018**, *122*, 62–70.

(30) Allen, M. P.; Tildesley, D. J. *Computer simulation of liquids*; Oxford Science Publications: Oxford, New York, 1994.

(31) Pranami, G.; Lamm, M. H. Estimating Error in Diffusion Coefficients Derived from Molecular Dynamics Simulations. *J. Chem. Theory Comput.* **2015**, *11*, 4586–4592.

(32) Omar, S.; Najib, W. B.; Bonanos, N. Conductivity ageing studies on 1M10ScSZ (M⁴⁺ = Ce, Hf). *Solid State Ionics* **2011**, *189*, 100–106.

(33) Heel, A.; Vital, A.; Holtappels, P.; Graule, T. Flame spray synthesis and characterization of stabilized ZrO₂ and CeO₂ electrolyte nanopowders for SOFC applications at intermediate temperatures. *J. Electroceram.* **2009**, *22*, 40–46.

(34) Shimojo, F.; Tsuneyasu, O.; Tachibana, F.; Koboyashi, M.; Okazaki, H. Molecular Dynamics Studies of Yttria Stabilized Zirconia. I. Structure and Oxygen Diffusion. *J. Phys. Soc. Jpn.* **1992**, *61*, 2848–2857.

(35) Norberg, S. T.; Hull, S.; Ahmed, I.; Eriksson, S. G.; Marrochelli, G.; Madden, P. A.; Li, P.; Irvine, J. T. S. Structural Disorder in Doped Zirconias, Part I: The Zr_{0.8}Sc_{0.2-x}Y_xO_{1.9} (0.0 ≤ x ≤ 0.2) System. *Chem. Mater.* **2011**, *23*, 1356–1364.

(36) Lee, D.-S.; Kim, W. S.; Choi, S. H.; Kim, J.; Lee, H.-W.; Lee, J.-H. Characterization of ZrO₂ co-doped with Sc₂O₃ and CeO₂ electrolyte for the application of intermediate temperature SOFCs. *Solid State Ionics* **2005**, *176*, 33–39.

(37) Wang, Z.; Cheng, M.; Bi, Z.; Dong, Y.; Zhang, H.; Zhang, J.; Feng, Z.; Li, C. Structure and impedance of ZrO₂ doped with Sc₂O₃ and CeO₂. *Mater. Lett.* **2005**, *59*, 2579–2582.

A Diffusivity Study of $(\text{Sc}_2\text{O}_3)_{0.1}(\text{CeO}_2)_{0.01}(\text{ZrO}_2)_{0.89}$ between 1100 and 1500 K at Zero Pressure with Molecular Dynamics

*Gerardo Valadez Huerta, Lucas Reus, Stephan Kabelac**

Institut für Thermodynamik, Gottfried Wilhelm Leibniz Universität Hannover, Callinstraße 36,
D-30167 Hannover, Germany.

*kabelac@ift.uni-hannover.de, www.ift.uni-hannover.de

2.3 Computational Details. We plot in Figure S1 the calculated internal energy U of the system over the equilibration time for one of the ten independent simulations in the NpT and NVT ensemble. From the progression of the internal energy U , we assume that the system reaches thermodynamic equilibrium in all cases.

For each temperature, we test the two-sided null hypothesis $H_{01}: X = X_0$ vs. $H_{11}: X \neq X_0$ at the significance level $\alpha = 0.05$ and type 2 error $\beta = 0.1$ for $X = a, D_0^{MSD}, L_{OO}$, and we calculate the sample size n_X given by:

$$n_X \geq \left(\frac{(u_{1-\alpha/2} + u_{1-\beta})\sigma_X}{\Delta X} \right)^2.$$

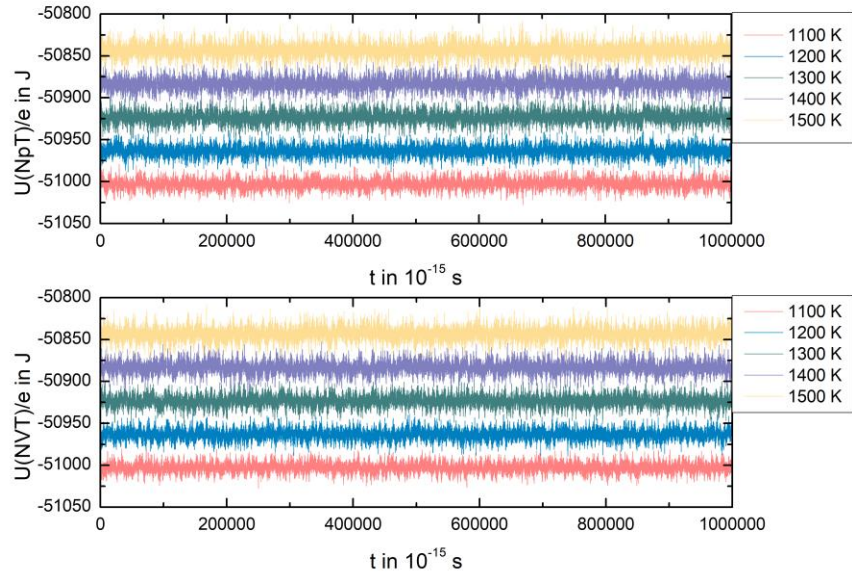


Figure S1. Calculated internal energy U of one system configuration over the equilibration time for a NpT and a NVT simulation, as well as for different temperatures.

Here, u_{1-Y} is the Y -quantile of the standard normal distribution, σ_X the standard deviation and $\Delta X = X - X_0$. For ΔX , we use the length of the error bars of the mean value of X . The resulting sample sizes have to be higher than 6 in all cases. Therefore, the hypothesis H_{01} cannot be rejected if the mean value is calculated from ten independent simulations.

Table S1. Calculated values for the MSD-Diffusion coefficient D_0^{MSD} and the phenomenological coefficient L_{00} for five of the ten independent simulations at 1100 K and 1500 K. Following the discussion of G. Pranami and M. H. Lamm,^{S1} we do not determine the uncertainty for each D_0^{MSD} , since this is only possible for a sample of values obtained from various independent simulations.

Conf.	D_0^{MSD} (1100 K)	D_0^{MSD} (1500 K)	L_{00} (1100 K)	L_{00} (1500 K)
	$10^{-11} \text{ m}^2/\text{s}$		$10^{-6} \text{ mol}^2 \cdot \text{K} \cdot (\text{J} \cdot \text{s} \cdot \text{m})^{-1}$	
A	6.248	0.224	1.45(41)	3.85(66)
B	6.521	0.212	1.37(57)	3.55(90)
C	6.470	0.210	1.19(68)	3.45(67)
D	6.958	0.219	1.42(75)	3.12(81)
E	6.672	0.220	1.37(49)	3.41(67)

Finally, we give exemplarily in Table S1 the simulated values of D_O^{MSD} and L_{OO} for five of the ten independent simulations at 1100 K and 1500 K, in order to give the readers some information about the statistics of the simulations.

Table S2. Calculated lattice constant of 10Sc1CeSZ using the experimental mean value for the CTE of $11.4 \cdot 10^{-6} \text{ K}^{-1}$ and the experimental value for the lattice constant at room temperature of $5.09 \cdot 10^{-10} \text{ m}$. Both values taken from Heel et al.^{S2}.

T in K	a in 10^{-10} m
1100	5.1266
1200	5.1325
1300	5.1384
1400	5.1444
1500	5.1503

3.1 Structural Properties. We summarize in Table S2 the lattice constant of 10Sc1CeSZ calculated from the experimental values given by Heel et al.^{S2} for different temperatures.

Table S3. Calculated coordination numbers Z_{Zr-O} , Z_{Ce-O} and Z_{Sc-O} at different temperatures and zero pressure.

T in K	Z_{Zr-O}	Z_{Ce-O}	Z_{Sc-O}
1100	7.598(84)	7.963(99)	7.70(42)
1200	7.598(71)	7.959(88)	7.69(41)
1300	7.598(78)	7.950(94)	7.68(41)
1400	7.598(69)	7.943(87)	7.67(41)
1500	7.596(63)	7.934(81)	7.66(41)

In Table S3, the simulated coordination numbers Z_{Zr-O} , Z_{Ce-O} and Z_{Sc-O} are summarized at different temperatures.

We test the null hypothesis H_{0i} at a significance level of $\alpha = 0.05$ to see, that the values of the coordination number $Z_O(T)$ and of the correlation factor $f_O(T)$ do not differentiate from the mean values \bar{Z}_O and \bar{f}_O at different temperatures $H_{02}: \bar{Z}_O = Z_O(T)$ vs $H_{12}: \bar{Z}_O \neq Z_O(T)$ and $H_{03}: \bar{f}_O = f_O(T)$ vs $H_{13}: \bar{f}_O \neq f_O(T)$. For this purpose, we calculate the values

$$z_X = \frac{\bar{X} - X(T)}{\sigma_X} \sqrt{n_X},$$

where $X = Z_O, f_O$. The resulting values for z_X are given in Table S4. We reject the hypothesis H_{02} and H_{03} , if $|z_X| > u_{0.975} = 1.96$.

Table S4. Calculated values z_{Z_O} and z_{f_O} for different temperatures.

T in K	1100	1200	1300	1400	1500
$z_{Z_O} \approx z_{f_O}$	2.77	1.44	0.07	1.41	2.87

REFERENCES

- (S1) Pranami, G.; Lamm, M. H. Estimating Error in Diffusion Coefficients Derived from Molecular Dynamics Simulations. *J. Chem. Theory Comput.* **2015**, *11*, 4586-4592.
- (S2) Heel, A.; Vital, A.; Holtappels, P.; Graule, T. Flame spray synthesis and characterization of stabilized ZrO_2 and CeO_2 electrolyte nanopowders for SOFC applications at intermediate temperatures. *J. Electroceram.* **2009**, *22*, 40-46.

IV

Article

Impact of Multi-Causal Transport Mechanisms in an Electrolyte Supported Planar SOFC with $(\text{ZrO}_2)_{x-1}(\text{Y}_2\text{O}_3)_x$ Electrolyte

Gerardo Valadez Huerta * , Vincent Flasbart, Tobias Marquardt, Pablo Radici 
and Stephan Kabelac

Institut für Thermodynamik, Gottfried Wilhelm Leibniz Universität Hannover, Callinstraße 36,
D-30167 Hannover, Germany; flasbart@stud.uni-hannover.de (V.F.); marquardt@ift.uni-hannover.de (T.M.);
radici@ift.uni-hannover.de (P.R.); kabelac@ift.uni-hannover.de (S.K.)

* Correspondence: valadez@ift.uni-hannover.de; Tel.: +49-511-762-5663

Received: 12 May 2018; Accepted: 14 June 2018; Published: 16 June 2018



Abstract: The calculation of the entropy production rate within an operational high temperature solid oxide fuel cell (SOFC) is necessary to design and improve heating and cooling strategies. However, due to a lack of information, most of the studies are limited to empirical relations, which are not in line with the more general approach given by non-equilibrium thermodynamics (NET). The SOFC 1D-model presented in this study is based on non-equilibrium thermodynamics and we parameterize it with experimental data and data from molecular dynamics (MD). The validation of the model shows that it can effectively describe the behavior of a SOFC at 1300 K. Moreover, we show that the highest entropy production is present in the electrolyte and the catalyst layers, and that the Peltier heat transfer is considerable for the calculation of the heat flux in the electrolyte and cannot be neglected. To our knowledge, this is the first validated model of a SOFC based on non-equilibrium thermodynamics and this study can be extended to analyze SOFCs with other solid oxide electrolytes, with perovskites electrolytes or even other electrochemical systems like solid oxide electrolysis cells (SOECs).

Keywords: entropy production; SOFC; electrochemistry; fuel cell; solid-state ionics

1. Introduction

Fuel cells are an alternative technology for power generation [1]. High temperature solid oxide fuel cells (SOFCs) have high efficiency and are, together with the polymer-electrolyte membrane fuel cell (PEMFC), the most promising type [2,3]. Some of the main advantages of SOFCs are the high tolerance to CO and their flexibility with the purity of the H_2 needed, in comparison to PEMFCs [4,5]. SOFC systems with pre- or internal reforming can work with common fuels in the actual infrastructure and also work in a future hydrogen network [6–8]. Depending on the electrolyte material and thickness, SOFCs are operated at a temperature between 700 °C and 1100 °C [9,10].

Consistent simulation data is beneficial considering the effort needed to obtain reliable results for different electrolytes through experimental research [11,12]. Many 2D-models or 3D-models of SOFCs exist in the literature [13–19], but only few are founded within the theory of non-equilibrium thermodynamics (NET) [20]. This theory includes possible coupled transport mechanisms driven by multiple gradients and does not claim mono-causal transport mechanisms as the classical kinetic equations [21–23]. Coupled transport mechanisms are; e.g., the Peltier effect—where a gradient in the electric potential drives a heat flux. The classical Fourier equation, used in many simulation models, only accounts for a heat flux due to a temperature gradient [24,25]. The coupling effects are small in

many technical systems and neglecting them still gives reliable simulation results [26]. Since most simulation models have empirical parameters to be fitted to the individual application, a deficit in the kinetic equation does not become apparent immediately. It results in “effective” transport coefficients. A well-known case is the simulation of multi-component diffusion with Fick’s law instead of using the Maxwell–Stefan equations [27,28].

In NET [22,23] the fluxes J_i of extensive thermodynamic properties are assigned to more than one generalized force X_j [21]. The force X_j is a gradient of an intensive property like temperature, chemical potential, etc. For the fluxes J_i , we can write the following phenomenological equations:

$$J_i \approx \sum_j L_{ij} X_j, \quad (1)$$

where L_{ij} are the phenomenological coefficients, also called Onsager-coefficients or conductivities. This approximation is the result of a Taylor expansion of the entropy in dependency on the deviations from equilibrium of all variables and the assumption that all processes occur near equilibrium [29]. Only in this case, the Onsager relations for the phenomenological coefficients $L_{ij} = L_{ji}$ apply [30]. The entropy production rate $\dot{\sigma}$ is given by the fluxes and the corresponding forces:

$$\dot{\sigma} = \sum_i J_i X_i. \quad (2)$$

This fundamental relationship between the local entropy production rate $\dot{\sigma}$ and the fluxes is extremely valuable for understanding dissipative phenomena and for possibly improving the efficiency of the cell by lowering the entropy production.

A 1D SOFC-model dealing with the transport mechanisms across the cell and using NET is given by S. Kjelstrup and D. Bedeaux [20]. In this model, empirical coefficients are used to calculate the conductivities L_{ij} and to describe the bulk-phases and the catalyst layers CLs. The assumption of infinite surfaces and a small heat conductivity in their model approach leads to temperature jumps in the CLs. However, the authors do not calculate the entropy production rate. The studies of A. Sciacovelli and V. Verda [31,32], as well as the recent studies of J. J. Ramírez-Minguela et al. [33,34], deal with the 3D calculation of the entropy production rate in a SOFC. They only use empirical equations and do not conduct any validation. Other studies regarding the entropy production are limited to the system level [35].

Since the validation of all details in the typical standard simulation approach for a SOFC is not yet completed [36,37], it is the aim of this paper to compare standard kinetic equations against the more general NET approach. Especially for electrochemical systems showing increasingly strong gradients due to very thin functional layers, it seems advisable to check the validity of mono-causal kinetic equations. In this study, we conduct experiments on a single SOFC and develop a 1D-model of the cell in steady state. We evaluate the cell experimentally with electrochemical impedance spectroscopy (EIS) and measure the voltage (E)-current(j)-characteristic. The model is based on NET, except for the CLs, where we assume them to be isotherm and calculate the reaction rate using Butler–Volmer kinetics. For an overall simulation model based on the NET-approach all conductivities L_{ij} need to be known [38]. These coefficients can be estimated from known (effective) standard transport coefficients [20,39,40], for example:

$$L_{qq} = \frac{\lambda}{(k_B \beta)^2} + \frac{\kappa \pi^2}{k_B \beta}, \quad (3)$$

where the conductivity L_{qq} describes the heat transport in a solid conductor, λ the heat conductivity, κ the electronic conductivity and π the peltier coefficient. Furthermore, $\beta = (k_B T)^{-1}$ is the reciprocal of the temperature and k_B the Boltzmann constant (1.3806×10^{-23} J/K). As the measured transport coefficients depend significantly on the exact individual nature of the sample; e.g., the grain size and

boundaries [41,42]—care must be taken when using relations like Equation (3). To overcome these problems, the direct calculation of the conductivities can be done using MD [43–45].

We believe that the processes across the cell are the most relevant to give insights of the coupled mechanisms and, thus, we limit our study to the spatial dimension perpendicular to the cell area. The coefficients to describe the electrolyte are taken from our previous MD study [40]. These values agree with the experimental data and are calculated from a single “experiment”. Furthermore, we can evaluate Equation (1) without any transformation. Unfortunately, the values are given only for 1300 K and, thus, we limit our study to this temperature.

The novelty of our study lies mostly on the following features:

- We expand the gas diffusion layers’ (GDLs’) NET models of S. Kjelstrup and D. Bedeaux [20] accounting for diffusion.
- We give a detailed description of the transport mechanisms in YSZ electrolytes based on NET using the phenomenological coefficients calculated with MD.
- Our NET model is validated with our own experimental data.
- We discuss in detail the influence of the coupled mechanisms and calculate each contribution to the entropy production rate in each layer.

2. Materials and Methods

2.1. Materials and Experimental Methods

We conduct all measurements with an Evaluator-HT test facility from FuelCon AG, Germany. We use a SOFC of type KeraCell II manufactured by KERAFOIL GmbH, Germany. The KeraCell II is an electrolyte supported cell (ESC) with an 8YSZ electrolyte and an electrolyte thickness of 1.6×10^{-4} m. The NiO/GDC anode and the ScSZ/LSM cathode GDLs are 0.4×10^{-4} m thick. We conduct our measurements after a first commissioning of the cell. Here, the first step is to heat the cell to 1123 K. The heating process is done with a 1 K/min ramp function in order to achieve a homogenous temperature field across the cell. After heating, the temperature of the cell is held at 1123 K for several hours before the anode material is reduced to Ni/GDC.

We conduct our EIS-measurements with a ModuLab XM ECS from the company AMETEK GmbH at atmospheric pressure and different oven temperatures (1023 K, 1073 K, 1123 K, 1173 K and 1300 K). The EIS-measurements are galvanostatic with a current amplitude of $\pm 280 \times 10^{-3}$ A in a frequency range of 0.1 Hz to 100 kHz. We choose the equivalent circuit given in Figure 1. We use three elements in series. The first element is a resistance to describe the ohmic losses from the electrolyte. In the second and the third element, we use a resistance and a constant phase element (CPE) in parallel to describe the losses in the catalyst layers (CLs). We fit our impedance spectra with the equivalent circuit using the software XM-studio of the analyzer. From this fitting, we get the electrolyte resistance R^e and the polarization resistances R_p^i .

We conduct an extra measurement of the E - j -characteristic of the cell with an oven temperature of 1300 K. This measurement is galvanostatic in a range of 0 to 8000 A/m².

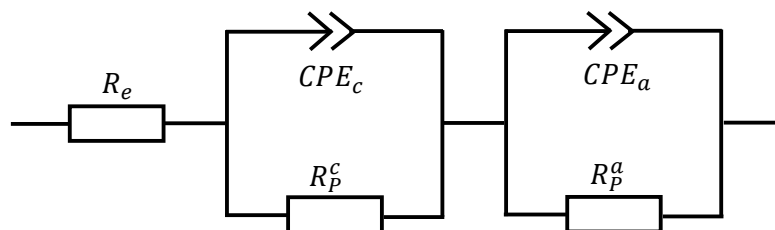


Figure 1. Equivalent electronic circuit.

2.2. Theoretical Methods

2.2.1. SOFC-System

We define y as the spatial coordinate perpendicular to the SOFC active area and divide the cell in the following regions: the anode GDL, the anode CL, the electrolyte, the cathode CL and the cathode GDL. The anode GDL has a thickness of Δy_a , the electrolyte a thickness of Δy_e and the cathode diffusion layer a thickness of Δy_c . In Figure 2, the resulting system including all the heat and molar fluxes is depicted. Since we only consider one spatial direction, the fluxes can be written as scalars and not as vectors.

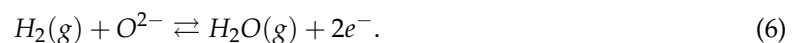
The oxygen molar flux $J_{O_2}^c$ coming from the gas channel flows through the cathode diffusion layer and into the CL. Here, an oxygen atom reacts with two electrons to build oxygen anions during the oxygen reduction reaction (ORR):



The oxygen anions are then transported through the solid oxide electrolyte. In this work, we study only YSZ-electrolytes. The doping of Y_2O_3 in ZrO_2 to form YSZ results in vacancies [46]. This defect formation can be described by the following reaction in Kröger–Vink notation:



with the electro-neutrality condition $[Y'] = 2[V_O^{\bullet\bullet}]$. The anion flux $J_{O^{2-}}^e$ is transported through these defects in the opposite direction of the electric current density j carrying two negative electric charges. From the gas channel through the anode GDL, the hydrogen molecules are transported as part of a molar flux $J_{H_2}^a$ to the anode CL, where they react with the anions. From this hydrogen oxidation reaction (HOR), water and two free electrons result:



The electrons flow opposite to j from the anode to the cathode in an external electronic circuit.

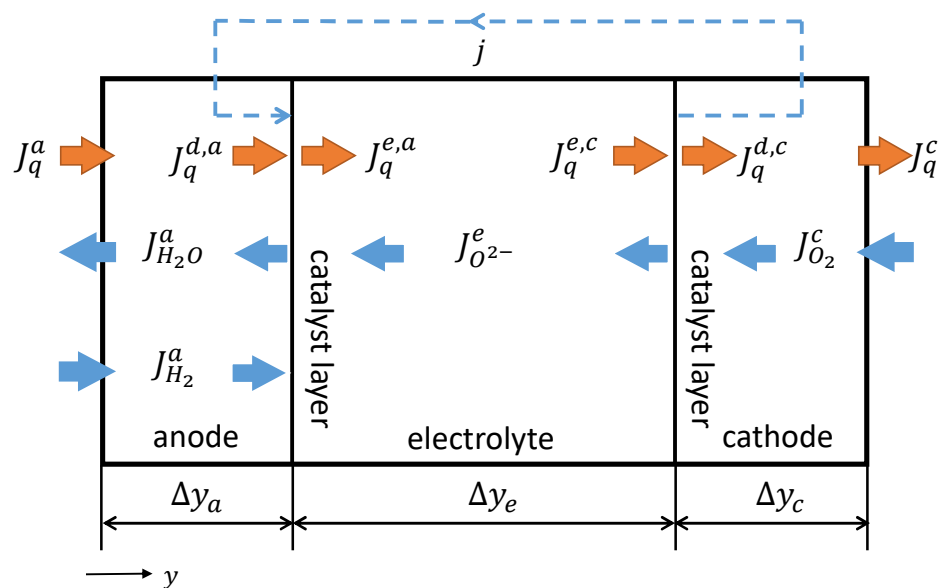


Figure 2. Solid oxide fuel cell (SOFC) including the electric current density j , all heat fluxes J_q^i and all molar fluxes J_k^i . The spatial coordinate y is defined perpendicular to the cell area.

We define all heat fluxes in the direction of the spatial coordinate y . The heat flux $J_q^a(y)$ flows through the anode GDL. At the CL, the heat flux $J_q^a(\Delta y_a)$ is equal to $J_q^{d,a}$. Due to the half-cell reaction, heat may be released at the CL, so that the heat J_q^a flowing from the anode to the electrolyte is not necessarily equal to $J_q^{d,a}$. From then on, the heat $J_q^e(y)$ with $J_q^e(\Delta y_a) = J_q^{d,a}$ flows through the electrolyte and, at the CL, $J_q^e(\Delta y_a + \Delta y_e)$ is equal to $J_q^{e,c}$. Again, the heat released from the cathode reaction results in a non-equality between $J_q^{e,c}$ and $J_q^{d,c}$. Finally, the heat flux $J_q^c(y)$ with $J_q^c(\Delta y_a + \Delta y_e) = J_q^{d,c}$ is transported further through the cathode diffusion layer.

We only consider a H_2, H_2O -ideal gas mixture at the anode side and an O_2, N_2 -ideal gas mixture at the cathode side. The thermodynamic state point is given by $T = 1300$ K and $p = p^o = 1$ bar, and we only consider steady state conditions.

2.2.2. Mathematical Description of the GDLs

Our start point is the energy balance for the anode GDL and the cathode GDL:

$$0 = \frac{dJ_q^a}{dy} + j \frac{d\phi}{dy} + J_{H_2}^a \frac{dH_{H_2}}{dy} - J_{H_2O}^a \frac{dH_{H_2O}}{dy}, \quad (7)$$

$$0 = \frac{dJ_q^c}{dy} + j \frac{d\phi}{dy} - J_{O_2}^c \frac{dH_{O_2}}{dy}, \quad (8)$$

where ϕ describes the electric potential. Heat J_q^i and electric power $j \cdot \phi$ are transported through the GDLs, while the gas components k enter or leave them with the molar enthalpy H_k . The molar enthalpy of ideal gases is only dependent on the temperature and can be expressed differentially as $dH_k = C_{p,k}(T)dT$, where $C_{p,k}(T)$ is the molar isobaric heat capacity of species k . We define all molar fluxes relative to the spatial direction (see Figure 2) and, considering the component balances $2J_{H_2}^a = -2J_{H_2O}^a = j/F$ and $-4J_{O_2}^c = j/F$, we get:

$$0 = \frac{dJ_q^a}{dy} + j \left[\frac{d\phi}{dy} + \frac{1}{2F} [C_{p,H_2}(T) + C_{p,H_2O}(T)] \frac{dT}{dy} \right], \quad (9)$$

$$0 = \frac{dJ_q^c}{dy} + j \left[\frac{d\phi}{dy} + \frac{1}{4F} C_{p,O_2}(T) \frac{dT}{dy} \right], \quad (10)$$

where F is the Faraday constant (96,485 C/mol). All thermodynamic properties for the ideal gases are calculated with the equations of Kabelac et al. [47]. To describe the fluxes and thermodynamic forces we use the following kinetics [20]:

$$J_q^i = -\lambda^i \frac{dT}{dy} + \pi^i j \quad (11)$$

$$j = -\frac{\pi^i}{r^i} \frac{1}{T} \frac{dT}{dy} - \frac{1}{r^i} \frac{d\phi}{dy}, \quad (12)$$

$$J_k^i = -D_k \frac{dc_k}{dy}, \quad (13)$$

where the upper script $i = a, c$ denotes the anode or the cathode, r^i the area specific resistance and D_k the effective diffusion coefficient of species k . The derivation of Equations (11) and (12) using non-equilibrium thermodynamics can be found in the work of S. Kjelstrup and D. Bedeaux [20].

The area specific resistance r^i is described by following the Arrhenius equation:

$$r^i / T = r_0^i \cdot e^{\frac{E_{Ar}^i}{RT}}. \quad (14)$$

Here, $E_{A,r}^i$ is the activation energy and r_0^i the pre-exponential factor. To give Equation (14) theoretical support, we firstly assume that all phenomenological coefficients L_{ij} may have an Arrhenius behavior. The coefficient $L_{\phi\phi}$, which describes the electronic transport, is related to the electronic conductivity κ as follows:

$$F^2 L_{\phi\phi}^i = \kappa^i T. \quad (15)$$

Equation (15) can be derived from Equation (1) following the steps given in our previous work [48]. As a consequence, the following Arrhenius equation arises:

$$\kappa^i T = \kappa_0^i \cdot e^{-\frac{E_{A,r}^i}{RT}}. \quad (16)$$

This result is supported by experimental data [49]. The electronic conductivity behaves inversely proportionally to the area specific resistance; i.e., $\kappa \sim 1/r^i$ and the proportionality factor is of mere geometrical nature. Therefore, Equation (14) follows directly from Equation (16) having the same activation energy, different pre-exponential factor, and inverse temperature dependency.

As can be taken from Equation (11) and from Equation (12), the Peltier coefficient π^i not only describes the heat transported due to charge transport, but also the contribution of a temperature gradient to the effective electric resistance.

The effective diffusion coefficient in Equation (13) also comprises multicomponent diffusion [24]. The Dusty gas model should give a better approximation than the one implemented in our model, because it accounts Knudsen diffusion [38]. However, following the discussion of R. Suwanwarangkul et al. [27], our model may also give satisfactory results within the simulation conditions (see below). We integrate Equation (13) to describe the concentration profile of hydrogen c_{H_2} and water c_{H_2O} at the anode GDL and oxygen c_{O_2} at the cathode GDL:

$$c_{H_2}(y) = c_{H_2}^0 - \frac{jy}{2FD_{H_2}}, \quad (17)$$

$$c_{H_2O}(y) = c_{H_2O}^0 + \frac{jy}{2FD_{H_2O}}, \quad (18)$$

$$c_{O_2}(y) = c_{O_2}^0 - \frac{j}{4FD_{O_2}}(y_c - y). \quad (19)$$

Here, we use the component balances, the superscript 0 denotes the gas channel and $y_c = \Delta y_a + \Delta y_e + \Delta y_c$. Finally, we calculate the entropy production rate from Equation (2) as follows:

$$\dot{\sigma}^i = -J_q^i \frac{1}{T^2} \frac{dT}{dy} - j \frac{1}{T} \frac{d\phi}{dy} - R \sum_k J_k^i \frac{1}{c_k} \frac{dc_k}{dy}, \quad (20)$$

where R is the ideal gas constant (8.3144 J/(molK)). From the Equations (13) and (17)–(19), a concentration dependent term is given for the anode and for the cathode:

$$\sum_k J_k^a \frac{1}{c_k} \frac{dc_k}{dy} = -\left(\frac{j}{2F}\right)^2 \left[\frac{1}{c_{H_2} D_{H_2}} + \frac{1}{c_{H_2O} D_{H_2O}} \right], \quad (21)$$

$$\sum_k J_k^c \frac{1}{c_k} \frac{dc_k}{dy} = -\left(\frac{j}{4F}\right)^2 \frac{1}{c_{O_2} D_{O_2}}. \quad (22)$$

2.2.3. Mathematical Description of the CLs

We assume constant temperature at the CL and its surroundings, but with a jump in the electric potential and the heat flux. To describe the potential jumps we begin by applying the Nernst-Equation

to calculate the open circuit voltage (OCV) $\Delta\phi_0^i$ for the anode half reaction (4) and for the cathode half reaction (6):

$$\Delta\phi_0^a = \frac{1}{2F} \left[G_{H_2O}^o(T) - G_{H_2}^o(T) + RT \ln \left(\frac{x_{H_2O}^R}{x_{H_2}^R} \right) \right], \quad (23)$$

$$\Delta\phi_0^c = \frac{1}{2F} \left[0.5 \cdot G_{O_2}^o(T) + \frac{RT}{2} \ln(x_{O_2}^R) \right], \quad (24)$$

where G_i^o describes the standard molar free enthalpy and the superscript R denotes the CLs. These equations result from the electrochemical equilibrium condition assuming $2F\Delta\phi_0^i = \tilde{\mu}_{O_2^-} - 2\tilde{\mu}_{e^-}$, where $\tilde{\mu}_k$ is the electrochemical potential of the charged species k . The mole fractions x_k^R are calculated from Equations (17) to (19) evaluated at $y^R = \Delta y_a$ for H_2 and H_2O and at $y^R = \Delta y_a + \Delta y_c$ for O_2 , and using the transformation $x_k^R = c_k(y^R)RT/p$. We define following Butler–Volmer equations for the ORR (4) and the HOR (6):

$$\dot{\zeta}_r^i = \frac{j_0^i}{2F} \left(e^{-\frac{\alpha^i 2F}{RT} \eta^i} - e^{\frac{(1-\alpha^i) 2F}{RT} \eta^i} \right), \quad (25)$$

The rate of reaction $\dot{\zeta}_r^i$ is imposed by the current density j , which determines the number of charges to be transferred per time unit. We can define $j = 2F\dot{\zeta}_{ORR}^i$ and $j = -2F\dot{\zeta}_{HOR}^a$ from a charge balance. For each reaction, an anodic and a cathodic barrier must be overcome, which are described by exponential terms. The charge transfer coefficient α^i determines the proportion of anodic or cathodic losses to the total losses, and the over-voltages η^i play the role of an activation energy. The exchange current density j_0^i describes the current, which in equilibrium flows equally in both directions of the half reaction. A more detailed discussion, can be found in [50]. We calculate j_0^i with an approach from Yonekura et al. [51]:

$$j_0^a = \left(x_{H_2}^R \right)^{0.41} \left(x_{H_2O}^R \right)^{0.4} \gamma^a e^{\frac{E_{A,j_0}^a}{RT}}, \quad (26)$$

$$j_0^c = \left(x_{O_2}^R \right)^{0.3} \gamma^c e^{\frac{E_{A,j_0}^c}{RT}}, \quad (27)$$

where γ^i are pre-exponential factors. The exchange current density j_0^i is related to the experimentally measurable polarization resistance R_p^i as follows:

$$j_0^i = \frac{RT}{2R_p^i F}. \quad (28)$$

The potentials at the reaction layers are given by:

$$\phi^{e,a} = \phi^{d,a} - \Delta\phi_0^a - \eta^a, \quad (29)$$

$$\phi^{d,c} = \phi^{e,c} + \Delta\phi_0^c + \eta^c. \quad (30)$$

To calculate the heat fluxes, we use the entropy balances for each CL:

$$J_q^{e,a} = J_q^{d,a} - T \frac{j}{2F} (S_{H_2O}(T) - S_{H_2}(T) - S_{O_2^-}(T) + 2S_{e^-}(T)) + T\dot{S}_{irr}^a, \quad (31)$$

$$J_q^{d,c} = J_q^{e,c} - T \frac{j}{2F} \left(S_{O_2^-}(T) - \frac{1}{2} S_{O_2}(T) - 2S_{e^-}(T) \right) + T\dot{S}_{irr}^c. \quad (32)$$

Here, S_k is the molar entropy of species k , \dot{S}_{irr}^i the area specific entropy production rate. From the literature [39], we assume that $S_{O_2^-} = 42 \text{ J}/(\text{molK})$ and $S_{e^-} = 1 \text{ J}/(\text{molK})$. Finally, we can write with the overvoltage η^i from Equation (25) the following equation:

$$\dot{S}_{irr}^i = -\eta^i \cdot \dot{\zeta}_r^i / T. \quad (33)$$

2.2.4. Mathematical Description of the Solid Oxide Electrolyte

To calculate the fluxes, we can write from Equation (1) following set of phenomenological equations:

$$J_q^e/k_B = -L_{qq} \frac{d\beta}{dy} - \sum_k L_{qk} \cdot \beta \cdot \frac{d\mu_k}{dy} - L_{q\varphi} \cdot \beta \cdot F \cdot \frac{d\varphi}{dy}, \quad (34)$$

$$J_k^e/k_B = -L_{kk} \frac{d\beta}{dy} - \sum_k L_{kk} \cdot \beta \cdot \frac{d\mu_k}{dy} - L_{k\varphi} \cdot \beta \cdot F \cdot \frac{d\varphi}{dy}, \quad (35)$$

$$j/(k_B F) = -L_{\varphi q} \frac{d\beta}{dy} - \sum_k L_{\varphi k} \cdot \beta \cdot \frac{d\mu_k}{dy} - L_{\varphi\varphi} \cdot \beta \cdot F \cdot \frac{d\varphi}{dy}, \quad (36)$$

where φ the electrostatic potential in YSZ. The current density j describes the flux of electrons transported along with the ionic fluxes J_k^e with $k = Z, Y, O$ for Zr^{4+} , Y^{3+} and O^{2-} . The conductivities L_{kk} are given by the auto correlation function (ACF) of the micro ionic fluxes [40] and $L_{\varphi\varphi}$ by the current ACF [45]. Due to polarization, the micro ionic fluxes may not necessarily be proportional to j , resulting in coefficients with completely different natures. The coupled effect between the electron and the ionic transport is then given by the conductivities $L_{k\varphi}$. For 1300 K, no cation diffusion in YSZ occurs; i.e., $L_{ZZ} = L_{YY} = 0$ [52]. Furthermore, Valadez Huerta et al. [46] compare their classical MD calculations of the Coulomb energy in YSZ with *ab-initio* calculations and do not find any substantial differences, concluding that polarization effects can be neglected. With these assumptions, we can write $J_{O^{2-}}^e = j/(z^*F)$ and

$$J_q^e/k_B = -L_{qq} \frac{d\beta}{dy} - L_{qO} \cdot \beta \cdot \frac{d\mu_{O^{2-}}}{dy} - L_{q\varphi} \cdot \beta \cdot F \cdot \frac{d\varphi}{dy}, \quad (37)$$

$$J_{O^{2-}}^e/k_B = -L_{Oq} \frac{d\beta}{dy} - L_{OO} \cdot \beta \cdot \frac{d\mu_{O^{2-}}}{dy} - L_{O\varphi} \cdot \beta \cdot F \cdot \frac{d\varphi}{dy}, \quad (38)$$

$$j/(k_B z^* F) = -L_{\varphi q} \frac{1}{z^*} \frac{d\beta}{dy} - L_{\varphi O} \cdot \frac{\beta}{z^*} \cdot \frac{d\mu_{O^{2-}}}{dy} - L_{\varphi\varphi} \cdot \frac{\beta}{z^*} \cdot F \cdot \frac{d\varphi}{dy} \quad (39)$$

with the valency $z^* = -2$. Equations (38) and (39) are equivalent. Equating the coefficients and using the Onsager relations $L_{O\varphi} = L_{\varphi O}$ and $L_{q\varphi} = L_{\varphi q}$, we get $L_{\varphi\varphi} = (z^*)^2 L_{OO}$, $L_{\varphi O} = z^* L_{OO}$ and $L_{Oq} = z^* L_{Oq}$. As a result, only the conductivities L_{OO} and $L_{Oq} = L_{qO}$ are necessary to describe the anionic conduction and heat transport. Using the definition of the electric potential $\phi = \tilde{\mu}_{O^{2-}}/(z^*F)$ with $\tilde{\mu}_{O^{2-}} = \mu_{O^{2-}} + z^*F \cdot \varphi$, two independent phenomenological equations arise:

$$J_q^e = -L_{qq} \frac{1}{T^2} \frac{dT}{dy} - L_{qO} \frac{z^*F}{T} \frac{d\phi}{dy}, \quad (40)$$

$$J_{O^{2-}}^e = -L_{Oq} \frac{1}{T^2} \frac{dT}{dy} - L_{OO} \frac{z^*F}{T} \frac{d\phi}{dy}. \quad (41)$$

We can write for the entropy production rate in analogy to Equation (20)

$$\dot{\sigma}^e = -J_q^e \frac{1}{T^2} \frac{dT}{dy} - J_{O^{2-}}^e \frac{z^*F}{T} \frac{d\phi}{dy} \quad (42)$$

and for the energy balance

$$0 = \frac{dJ_q^e}{dy} - J_{O^{2-}}^e z^* F \frac{d\phi}{dy}. \quad (43)$$

2.2.5. Computational Details

We conduct our calculation with MatLab[®] Version R2017a. We solve the equations consecutively from the anode to the cathode using the Runge–Kutta (4,5) method [53]. We assume as initial conditions $T(0) = 1300$ K and $\phi(0) = 0$ V. To reproduce the isothermal operational modus, we iterate numerically using the Newton–Raphson method. Thereby, the heat flux J_q is a variable with a start value of 1000 W/m² until the temperature at $y = \Delta y_a + \Delta y_e + \Delta y_c$ reaches $T(0)$ with an accuracy of 10^{-34} K.

The parameters used to describe the GDLs and the CLs are given in Table 1. The parameters needed to describe the exchange current density j_0^i in Equations (26) und (27) are derived directly from experiments (see next section). In the case of the electrolyte ($\Delta y^e = 160 \times 10^{-6}$ m), we analyze different YSZ compositions and take the values for the phenomenological coefficients from our previous work (see Table 2) [40].

Table 1. Parameters used in the simulation for the GDLs and the CLs. Values taken from Hajimolana et al. [25], Kjelstrup and Bedeaux [20], and Costamagna et al. [24].

Parameter	Anode GDL	Anode CL	Cathode CL	Cathode GDL	Reference
Δy_i in 10^{-6} m	40	-	-	40	-
r_0^i in 10^{-6} $\Omega\text{m}/\text{K}$	1/95	-	-	1/42	[25]
$E_{A,r}^i/R$	1150	-	-	1200	[25]
λ^i in W/mK	2	-	-	2	[20]
π^i/T_{cell} in J/(CK)	-5.4×10^{-4}	-	-	-6.2×10^{-4}	[20]
$D_{H_2} = D_{H_2O}$ in m ² /s	2.1×10^{-5}	-	-	-	[24]
D_{O_2} in m ² /s	-	-	-	5.4×10^{-6}	[24]
α^i	-	0.5	0.3	-	[24]

Table 2. Parameters used in the phenomenological equations to describe the electrolyte. The values are taken from the MD study of Valadez Huerta et al. [40].

YSZ	L_{OO} in $10^{-7} \text{mol}^2\text{K}(\text{Jms})^{-1}$	L_{qq} in 10^6 W/m	RL_{oq} in W/m
YSZ08	6.22(79)	6.21(25)	-0.81(69)
YSZ12	4.10(57)	5.37(27)	-0.77(75)
YSZ16	2.85(36)	4.85(34)	-0.55(56)
YSZ20	1.95(55)	4.54(29)	-0.48(36)

3. Results and Discussion

3.1. EIS Measurements

We plot exemplarily in Figure 3a the impedance spectrum of the cell at a cell temperature of 1117 K. The measured cell temperature is not equal to the oven temperature due to heat losses. For the impedance spectrum in Figure 3, we calculate for the CPE at the anode an angle of 60.33° and at the cathode an angle of 83.52° despite the apparent circular progression of the curve. Therefore, our assumption of CPEs instead of perfect capacities is more accurate. In Figure 3b, we plot the Arrhenius plot for the specific resistance r^e and the exchange current densities $j_0^{c,0}$ and $j_0^{a,0}$. From these Arrhenius plots, we get the pre-exponential factors $r_0^e = 9.28(27) \times 10^{-5}$ Ωm , $\gamma^a = 24(37) \times 10^6$ A/m² and $\gamma^c = 1.82(67) \times 10^{11}$ A/m², and the activation energies $E_{A,r}^e = 0.7816(65)e$ J, $E_{A,j_0}^c = 1.62(10)e$ J and $E_{A,j_0}^a = 0.75(43)e$ J, where e is the elementary charge (1.6022×10^{-19} C). Here, the deviation describes the error due to the linear regression with a 95% confidence interval. The noise in the current results in a poorly defined spectrum at low frequencies; i.e., a low linearity and a high error in the values for the anode CL. The specific resistance r^e at a cell temperature of 1300 K is $0.0622(40)$ Ωm . The value calculated from the coefficient L_{OO} for YSZ08 is $0.0561(71)$ Ωm . The relative deviation between both values is only $\sim 10\%$ indicating that our approach effectively describes the electrolyte ionic conductivity. At this point it should be mentioned that the effective resistance may also include

a Peltier contribution given by the temperature gradient and the phenomenological coefficient L_{Oq} (see Equation (40)), which is not included in the coefficient L_{OO} . This will be discussed later on in more detail.

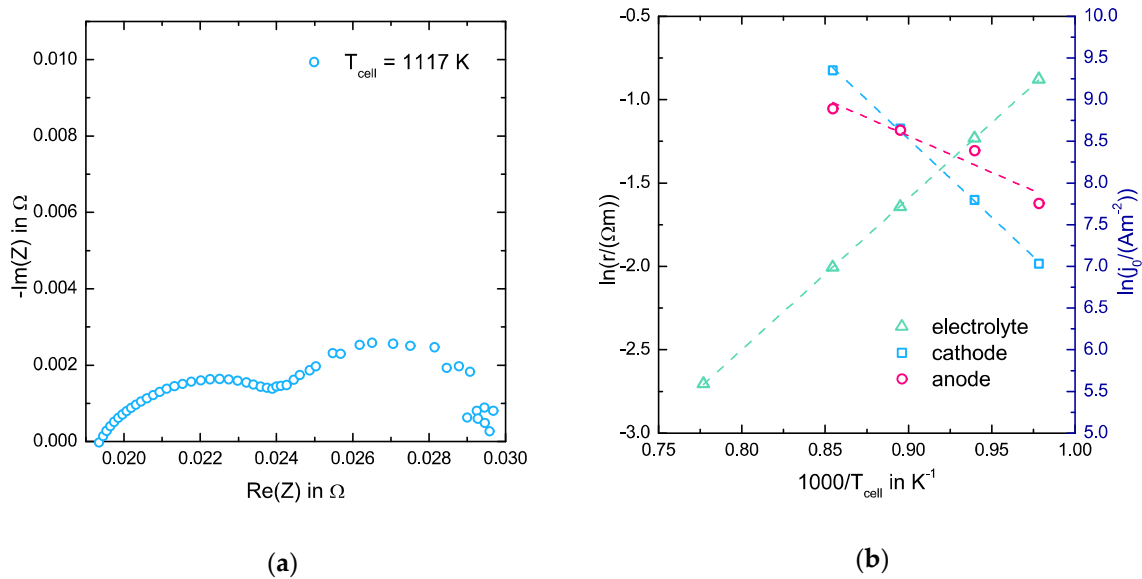


Figure 3. (a) Impedance spectrum at a cell temperature of 1117 K and (b) Arrhenius plot for the specific resistance r for the electrolyte and the exchange current density j_0 for the anode and the cathode.

3.2. Model Validation

In Figure 4, we plot the measured (Exp) and the simulated E - j -characteristic (Sim1) for $T_{cell} = 1287$ K. We use in Sim1 the specific resistance $r^e(1287 \text{ K}) = 0.0667(44) \text{ } \Omega\text{m}$ calculated from the experimental Arrhenius curve and assume $L_{Oq} = L_{qO} = 0$. The OCV value of the Sim1 curve deviates only 1.2% from the experimental value. It can be concluded from Equations (22) and (23) that gas leakages or uncertainties in the gas mixture concentration during the experiment may explain the deviation of the OCV to the theoretical value. Furthermore, losses due to a low electronic conductivity or a thermal gradient across the cell may also contribute to this deviation, since for $j = 0 \text{ A/m}^2$ our model does not account such phenomena. We calculate the negative slope for each curve and assume it as the area specific resistance (ASR). The ASR is $1.5457(98) \times 10^{-5} \text{ } \Omega\text{m}^2$ for the experimental curve and $1.5696(10) \times 10^{-5} \text{ } \Omega\text{m}^2$ for the Sim1 curve. The relative deviation of the ASR between the experimental curve and Sim1 is only $\sim 1.5\%$. Not only the losses due to the resistance in the electrolyte contribute to the ASR, but also the losses in the catalyst layer given by the reaction kinetics, as it can be taken from Equation (29). The low deviation means a successful implementation of Equations (26) and (27) using the experimental parameters for γ^i and $E_{A,0}^i$, despite the high error bars in the activation energy E_{A,j_0}^a and the pre-exponential factor γ^a . Furthermore, the relative deviation between the experimental voltage and the simulated voltage is only of $\sim 1.3\%$ for $j = 8000 \text{ A/m}^2$. V. Evely et al. [54] reported model predictions within 3% to 6% of the cell voltage from different literature sources and, therefore, we can say that our simulation model effectively describes the E - j -characteristic for 1287 K.

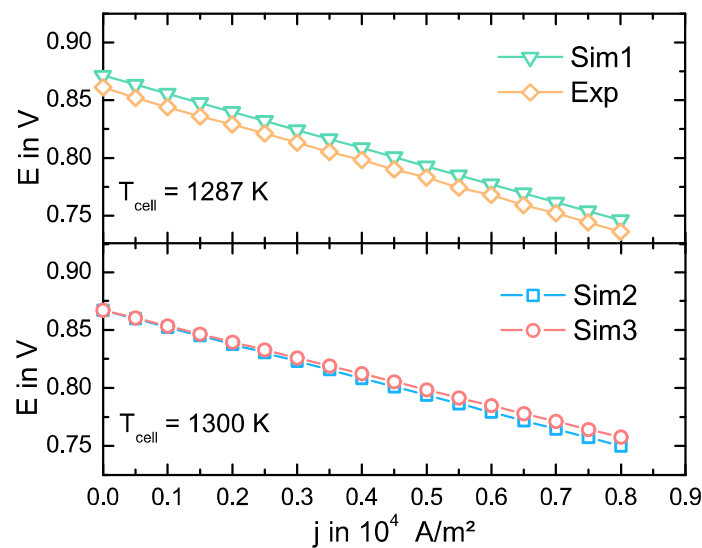


Figure 4. Experimental (Exp) and simulated voltage (E)-current(j)-characteristic (Sim1) at $T_{cell} = 1287$ K (upper diagram), and simulated E - j -characteristics (Sim2 and Sim3) at $T_{cell} = 1300$ K (lower diagram). We use the value $r^e(1287\text{ K}) = 0.0667(44)\ \Omega\text{m}$ in Sim1 and the value $r^e(1300\text{ K}) = 0.0622(40)\ \Omega\text{m}$ in Sim2. Both values are calculated from the experimental Arrhenius curve. In Sim3, we use the phenomenological coefficients for YSZ08 from Valadez Huerta et al. [40].

To further validation, we calculate the E - j -characteristic using $r^e(1300\text{ K}) = 0.0622(40)\ \Omega\text{m}$ (Sim2) as well as the phenomenological coefficients for YSZ08 (Sim3) at 1300 K respectively and plot the results in Figure 4. From the discussion above, we can assume that the progression of the Sim2 curve may provide a satisfactory approach for the progression of the E - j -characteristic at 1300 K, because the simulation model, which is based on the same assumptions, effectively describes the E - j -progression for 1287 K. For that reason, we can use the Sim2 curve as a reference to evaluate the progression of the Sim3 curve. In this case and because of the same model framework, the OCV values are equal. The calculated ASR is $1.46524(80) \times 10^{-5}\ \Omega\text{m}^2$ for the Sim2 curve and $1.37117(80) \times 10^{-5}\ \Omega\text{m}^2$ for the Sim3 curve. The discrepancy between both ASRs of $\sim 6.4\%$ is mostly accounted by the relative deviation between the resistance calculated using L_{OO} and the value from the experimental Arrhenius curve. Furthermore, the relative deviation of the voltage E between the Sim2 and the Sim3 curves is only $\sim 1\%$ for a current density of $8 \times 10^3\ \text{A/m}^2$, meaning our model gives a satisfactory description of the cell up to this current density.

3.3. Simulation Results

In Figure 5a, the simulated temperature profile across the SOFC at 1300 K is depicted for various YSZ-electrolytes and $j = 1000\ \text{A/m}^2$ and $8000\ \text{A/m}^2$. The temperature gradient is negative in the GDLs and positive in the electrolyte. In all cases, the progression of the temperature can be seen as linear. A higher current density and a higher electrolyte Y_2O_3 concentration result in higher absolute values for the temperature gradient in all of the bulk phases. Furthermore, a minimum at the anode and a maximum at the cathode can be observed. To explain these effects, we plot in Figure 5a the results of a simulation for YSZ08 and YSZ20 at $j = 8000\ \text{A/m}^2$, where we neglect all Peltier (coupling) mechanisms. Here, all absolute values of the temperature gradients are lower than for the original conditions. In the YSZ20 electrolyte case, the one in the anode is positive and the one in the electrolyte does not progress linearly, experiencing a maximum at $y = 1.8 \times 10^{-4}\ \text{m}$. From a comparison with the previous results, the high absolute values for the temperature gradients may result from a Seebeck mechanism. While J_{O-2}^e , L_{Oq} and z^* are negative in Equation (41), L_{OO} is positive. A high potential loss in the electrolyte results in a high negative value of the potential gradient and the negative Ohmic term

decreases. To counter this and to assure a constant anion flux, the temperature gradient has to have a high positive value. This may explain not only the pronounced temperature progression, but also its dependency on the current density, since a higher anion flux gives a higher counter effect. A calculation without these coupled mechanisms results in a significantly different temperature progression.

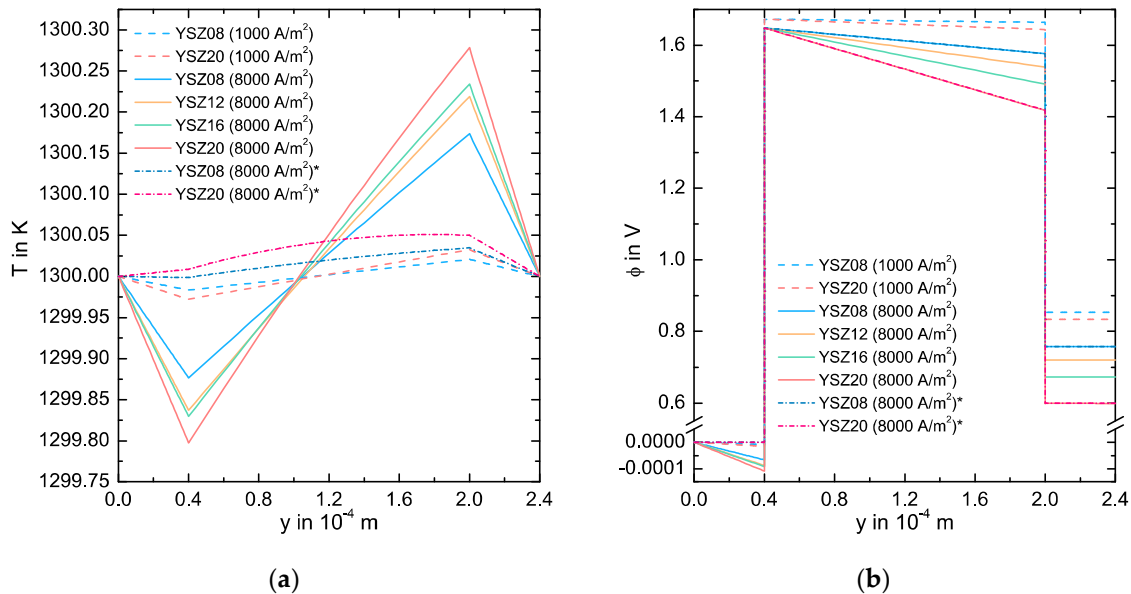


Figure 5. (a) Simulated temperature and (b) electric potential profile across the SOFC at 1300 K for various YSZ-electrolytes and the current densities $j = 1000 \text{ A/m}^2$ and $j = 8000 \text{ A/m}^2$. For the simulated curves marked with *, we neglect all Peltier type coupled mechanisms.

In Figure 5b, we plot the profile of the electric potential across the cell. In all bulk phases, the potential decreases. The progression also shows two jumps: a positive at the anode CL and a negative at the cathode CL. These jumps result from the equilibrium potentials $\Delta\phi_0^a = -1.68 \text{ V}$ and $\Delta\phi_0^c = -0.81 \text{ V}$, and from the activation losses in each electrode. We calculate the over-potentials $\eta^a = 3.4 \cdot 10^{-3} \text{ V}$ and $\eta^c = -9.3 \times 10^{-4} \text{ V}$ for 1000 A/m^2 , and $\eta^a = 0.027 \text{ V}$ and $\eta^c = -7.3 \times 10^{-3} \text{ V}$ for 8000 A/m^2 . As expected, η^a is positive, η^c is negative and their magnitude does not depend on the electrolyte type. The potential losses in the bulk phases increase for a higher current density and for a higher Y_2O_3 concentration in the electrolyte. Since the potential losses in the anode GDL and in the cathode GDL are too small, the progression of the curve is mostly defined by the losses in the electrolyte. To give a more detailed discussion, Figure 5b also includes results for simulations neglecting all Peltier mechanisms. The progression of the potential in the electrolyte is not substantially different from the original results and the losses are mainly Ohmic. However, the potential losses in the GDLs are mainly given by the temperature gradient rather than by the electric resistance. To justify this statement, we can argue analogous to the discussion of the pronounced temperature gradient by using Equation (12). We can calculate the effective specific resistance $r^e(1300 \text{ K}) \approx 0.05621 \text{ } \Omega\text{m}$ using the potential gradient across the electrolyte and the current density. This value deviates only $\sim 0.2\%$ from the one calculated with the conductivity L_{00} . Therefore, the potential losses due to the coupled effects do not significantly affect the progression of the E - j characteristic and the direct comparison between L_{00} and r^e in Section 3.1 is appropriate.

We plot in Figure 6 the heat flux J_q across the cell. We only calculate the net heat flux in the y -direction. It increases in the electrolyte with a slope dJ_q^e/dy , which becomes higher for higher current densities and higher potential losses due to energy conservation (see Equation (43)). Furthermore, it remains almost constant at the GDLs. The heat flux shows a negative jump at the anode CL and a positive jump at the cathode CL, meaning the anode half reaction is endothermic and the cathode

half reaction is exothermic. This is in agreement with the study of K. Fischer and J. R. Seume [55]. Both jumps increase for a higher current density due to the higher activation losses, yet they remain almost the same for the different electrolytes. Independent of the current density, the heat flows across the anode GDL and across the cathode GDL in y -direction for YSZ08, but across the electrolyte opposite to this direction. As expected from classical behavior, the heat flows from a higher to a lower temperature. However, the heat is transported from a low to a high temperature in electrolytes with a higher Y_2O_3 concentration, contradicting Fourier conduction behavior. In Figure 6, the heat flux resulting from a simulation without any coupled effects is given for the cases of an YSZ08 and an YSZ20 electrolyte at 8000 A/m^2 . Due to energy conservation, the progression of these curves is almost equal to the progression of the original curves. However, the amount and sign of the heat flux is different. If the coupled mechanisms are considered, the heat transported is higher in all layers. On one hand, the higher heat flux at the GDLs results from the higher temperature gradient, since the Peltier-effect may reduce it (see Equation (11)). On the other hand, the higher heat flux in the electrolyte results from the potential gradient, since the positive temperature gradient may diminish it (see Equation (40)). This effect is most pronounced for a higher Y_2O_3 concentration in the electrolyte and a higher current density due to the higher potential losses. As it can be seen from the YSZ20 case, if the coupled mechanisms are neglected, not only the amount of heat transported may be underestimated, but also the direction of the heat flux. This may lead to the wrong decisions regarding the material design or heating/cooling strategies of SOFCs, such as which gas inlet flow may be used for cooling the cell to minimize thermal stress.

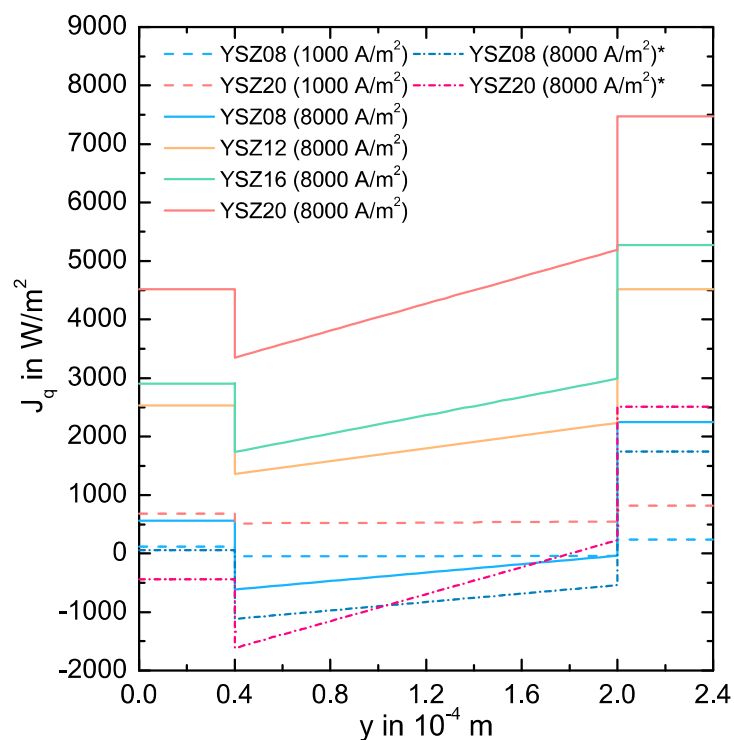


Figure 6. Simulated heat flux $J_q(y)$ across the SOFC at 1300 K for various YSZ-electrolytes and the current densities $j = 1000 \text{ A/m}^2$ and $j = 8000 \text{ A/m}^2$. For the simulated curves marked with *, we neglect all Peltier type coupled mechanisms.

In Figure 7, the heat contribution $\dot{\sigma}_Q$, the potential contribution $\dot{\sigma}_\phi$ and the diffusion contribution $\dot{\sigma}_c$ to the local entropy production rate $\dot{\sigma}$ are depicted for each layer for different electrolyte compositions at 1000 A/m^2 and 8000 A/m^2 . $\dot{\sigma}_Q$ is the term given by the temperature gradient (see Equations (20) and (42)), $\dot{\sigma}_\phi$ the term given by the potential gradient (see Equations (20) and (42)),

and $\dot{\sigma}_c$ the concentration dependent term (see Equations (20)–(22)). We also plot two simulation results neglecting all Peltier mechanisms. We normalize all terms with the value $\dot{\sigma}_{i,0}$ at the beginning of each layer, because the magnitude of the values is of a different order for each case (see Table 3) and, thus, a direct comparison is difficult.

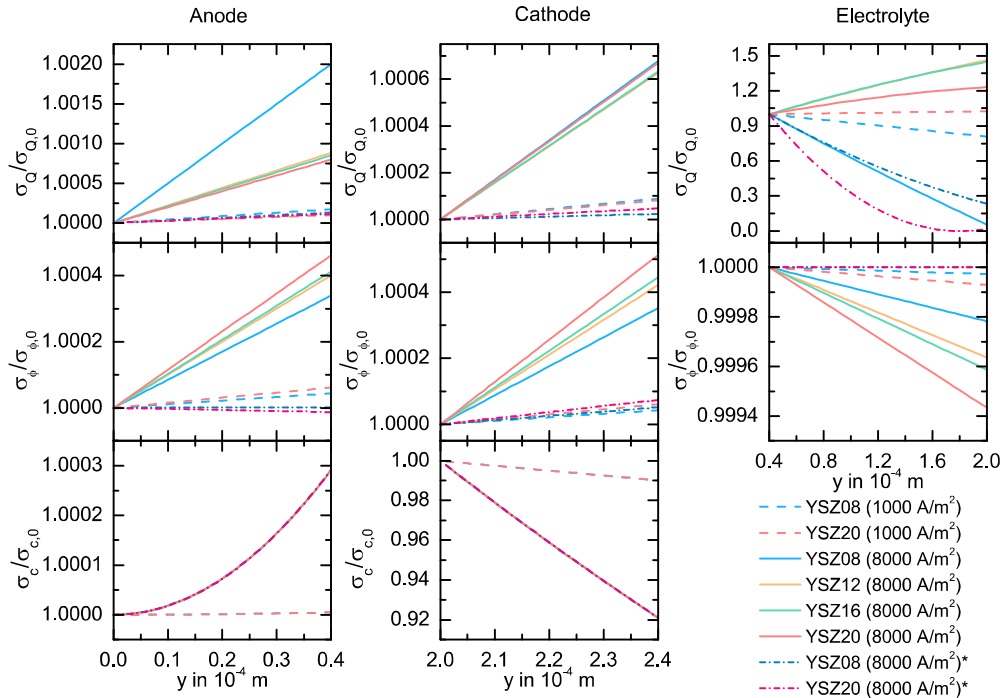


Figure 7. Simulated local entropy production rate contributions $\dot{\sigma}_Q$ (heat flux contribution), $\dot{\sigma}_\phi$ (potential contribution) and $\dot{\sigma}_c$ (diffusion contribution) in the anode GDL, in the cathode GDL and in the electrolyte. We normalized the values with $\dot{\sigma}_{i,0} = \dot{\sigma}_i(y = 0)$ for the anode, $\dot{\sigma}_{i,0} = \dot{\sigma}_i(y = 2 \times 10^{-4} \text{ m})$ for the cathode and (c) $\dot{\sigma}_{i,0} = \dot{\sigma}_i(y = 0.4 \times 10^{-4} \text{ m})$ for the electrolyte (see Table 3). The curves are given for a SOFC at 1300 K, for various YSZ-electrolytes and two current densities, $j = 1000 \text{ A/m}^2$ and $j = 8000 \text{ A/m}^2$. For the simulated curves marked with *, we neglect all Peltier type coupled mechanisms.

Table 3. Values of the entropy production rate used for the normalization in Figure 7. For the values marked with *, we neglect all Peltier type coupled mechanisms.

YSZ j	Anode GDL	Electrolyte	Cathode GDL
	$\dot{\alpha}_i(y = 0 \text{ m})$ W/(m ² K) $i = Q \text{CE} C$	$\dot{\alpha}_i(y = 0.4 \times 10^{-4} \text{ m})$ W/(m ² K) $i = Q \text{CE}$	$\dot{\alpha}_i(y = 2 \times 10^{-4} \text{ m})$ W/(m ² K) $i = Q \text{CE} C$
YSZ08 1000 A/m ²	0.03 0.17 4.60	0.007 43.24	0.074 0.25 5.37
YSZ20 1000 A/m ²	0.28 0.29 4.60	−0.12 138.6	0.40 0.39 5.37
YSZ08 8000 A/m ²	1.02 10.26 294.20	0.70 2767	5.77 16.58 369.73
YSZ12 8000 A/m ²	6.11 13.54 294.20	−2.04 4204	14.65 20.91 369.73
YSZ16 8000 A/m ²	7.33 14.16 294.20	−2.82 6033	18.27 22.35 369.73
YSZ20 8000 A/m ²	13.55 16.84 294.20	−6.64 8871	30.77 26.55 369.73
YSZ08* 8000 A/m ²	0.001 0.001 294.20	0.20 2760	0.90 0.003 369.73
YSZ20* 8000 A/m ²	0.06 0.001 294.20	0.57 8846	1.86 0.003 369.73

The absolute values for $\dot{\sigma}_{Q,0}$ in all layers become higher for increasing current density and increasing Y₂O₃ content. Due to the Peltier effect, most of the values are negative across the electrolyte. These negative contributions are smaller than the potential contribution and a positive local entropy

production rate is always ensured. The heat flux contributions are only positive for YSZ08 and, clearly, for the cases assuming no Peltier effect. For these latter cases, the absolute values for $\dot{\sigma}_{Q,0}$ are smaller than for the original cases. The values for $\dot{\sigma}_{Q,0}$ are proportional to the temperature gradient (see Equations (20) and (42)) and, thus, all these dependencies can be explained following the above discussion. The absolute values for $\dot{\sigma}_{Q,0}$ are higher across the GDLs than across the electrolyte in each case, resembling the results for the heat flux in Figure 6. Looking at Figure 7, the value of the heat flux contribution $\dot{\sigma}_Q$ in the GDLs increases slightly in the y -direction. If we assume a constant temperature gradient, the temperature and the heat flux progression may define the progression of $\dot{\sigma}_Q$. Here, the dependency on the Y_2O_3 concentration is not well defined and, thus, we cannot find a direct correlation to the curves for the temperature or the heat flux. Therefore, the resulting behavior may be given from a combination of both effects. This may also explain the low changes in the progression of the curves for lower current densities and for the cases neglecting all coupled mechanisms. However, these changes are smaller than 0.2% of the initial value. As already discussed, the negative potential gradient in the electrolyte and a high current density result into an increasing heat flux due to energy conservation. Together with the increasing temperature appearing in the denominator of the term $\dot{\sigma}_Q$ in Equation (43), the negative progression of J_q^c results in a decreasing progression of $\dot{\sigma}_Q$ for YSZ08. This trend changes for higher Y_2O_3 concentrations because the heat flux becomes increasing positive due to the Peltier effect. This behavior is observed for both current densities studied here. For an YSZ08 electrolyte, the value can decrease by 30% across the electrolyte and, for higher compositions, the value can increase by 150% depending on the current density. Additionally, the progression for $\dot{\sigma}_Q$ is not well predicted if the coupled effects are neglected, resulting in a strong decaying tendency independent of the electrolyte.

The values $\dot{\sigma}_{\phi,0}$ increase for higher current density and higher Y_2O_3 composition in all bulk phases, but its dependency on the electrolyte composition is not given in the GDLs if the Peltier effect is neglected. The dependency on the current density and on the Y_2O_3 composition is given by Equation (20), where $\dot{\sigma}_{\phi,0}$ is negatively proportional to the product between j and the potential gradient divided by the temperature. The low values for $\dot{\sigma}_{\phi,0}$ in the GDLs for the cases assuming no Peltier effect result from the low potential gradients. As expected from the similar progression of the potential with and without any Peltier mechanisms, all $\dot{\sigma}_{\phi,0}$ values in the electrolyte are similar for both cases. Furthermore, this contribution is the highest across the cell. For all curves in Figure 7, the slightly increasing or decreasing progression of $\dot{\sigma}_\phi$ is given by the temperature. This statement is justified, since the dependency on the spatial dimension, on the current density, on the Y_2O_3 composition and on whether the Peltier mechanisms are taken into account, is in agreement with the results depicted in Figure 5.

As expected from Equations (21) and (22), the values of $\dot{\sigma}_{c,0}$ depend only on the current density and not on the YSZ composition of the electrolyte. Since the temperature and potential differences at the GDLs are very low, the diffusion process provides the major contribution to the local entropy production rate. This contribution is lower at the anode GDL than at the cathode GDL. Here, the losses due to the oxygen diffusion are higher than the losses due to the diffusion of hydrogen and water at the anode GDL. The non-linearity of the increasing progression of $\dot{\sigma}_c$ at the anode can be accounted for by the superposition of a decreasing hydrogen concentration and an increasing water concentration across the GDL. This effect is not present at the cathode GDL, where the increasing oxygen concentration in the y -direction results in a decreasing progression of $\dot{\sigma}_c$.

The jump in the entropy production rate per area at the anode CL is $2.6 \times 10^{-3} \text{ W/m}^2\text{K}$ for 1000 A/m^2 and $0.17 \text{ W/m}^2\text{K}$ for 8000 A/m^2 , and at the cathode CL $7.1 \times 10^{-4} \text{ W/m}^2\text{K}$ for 1000 A/m^2 and $0.045 \text{ W/m}^2\text{K}$ for 8000 A/m^2 . These jumps do not depend substantially on the Y_2O_3 concentration of the electrolyte. To make a comparison between the entropy production at the CLs and at the bulk phases, non-specific values are needed. If we consider an YSZ12 cell with a $4 \text{ cm} \times 4 \text{ cm}$ active area working at 8000 A/m^2 and use the values given in Table 3 as an estimate for the entropy production rate contributions, it results in an entropy production rate of $4.60 \times 10^{-5} \text{ W/K}$ in the GDLs,

of 1.08×10^{-3} W/K in the electrolyte, and of 3.44×10^{-4} W/K at the CLs. This means that 3% of the losses would originate in the GDLs, 73% in the electrolyte, and 24% at the CLs. These values are expected for an ESC like the one studied here.

4. Summary and Conclusions

The main goal of this study is the 1D-calculation of the local entropy production rate across an electrolyte supported planar SOFC at 1300 K and atmospheric pressure. We describe all bulk phases using non-equilibrium thermodynamics. While we use empirical coefficients from the literature to describe the GDLs, the phenomenological coefficients from our previous MD study [40] are used to characterize the cell with various electrolytes of different Y_2O_3 content. We describe the CLs using the Butler–Volmer ansatz. We conduct EIS measurements in a YSZ08 SOFC to derive the parameters to describe the exchange current densities $j_0^{i,0}$. Moreover, we measure the E - j -characteristic and use this data to validate our model. Here, we show that the Butler–Volmer kinetics is well parametrized and implemented. Furthermore, the relative deviation of $\sim 6.4\%$ between the ASR of both curves is mainly due to the deviation of the electrolyte resistance calculated with L_{00} to the experimental value of $\sim 10\%$. For a current density of 8000 A/m^2 the relative deviation between both E - j -characteristics is only $\sim 1\%$, so that our approach effectively describes the SOFC. The temperature gradient across each layer is higher for a higher Y_2O_3 electrolyte concentration and a higher current density. This effect results from the coupled mechanisms and, thus, if the Peltier effect is neglected, the temperature profile across the cell is not properly described. From the potential profile, we conclude that the highest contribution to the electric potential losses are in the electrolyte. These losses are higher for a higher Y_2O_3 concentration and no substantial differences arise, if the simulation does not consider any coupled effects. Using the entropy balance for the calculation of the heat flux at the CLs, it results in an endothermic half reaction at the anode and an exothermic half reaction at the cathode. Moreover, the description of the transport mechanisms across a SOFC using NET cannot be avoided, since the heat flux in the electrolyte is mainly given by the Peltier effect. If this effect is neglected, the heat flux will not be properly described. Finally, we calculate the heat flux contribution, the potential contribution, and the diffusion contribution to the local entropy production rate. The entropy production rate across the electrolyte is mostly given by the ionic conduction, since the Peltier heat transfer from lower to higher temperature would reduce the entropy production. While the temperature and the heat flux define the progression of $\dot{\sigma}_Q$ across the electrolyte, the potential contribution profile is mainly given by the temperature. Despite the appreciable increasing or decreasing tendency of the contributions to the entropy production rate, a substantial change along the y -direction can be observed only for the heat flux contribution in the electrolyte. If we neglect the Peltier effect, the values for the heat flux and potential contribution are underestimated in the GDLs and a different profile of the heat flux contribution to the local entropy production rate is predicted across the electrolyte. Finally, the entropy production rate of a cell is the highest in the electrolyte (73%) followed by the contribution in both GDLs with (24%).

Author Contributions: G.V.H. and S.K. conceived the idea and the theoretical background. T.M. and P.R. conceived, designed, and performed the experiments. G.V.H., T.M. and P.R. analyzed the data. G.V.H. and V.F. developed the mathematical framework, conducted the validation and the simulation, and evaluated the computational data. S.K. supervised the work. G.V.H. wrote the paper, and made the figures. G.V.H. and S.K. revised the paper. All authors approved the last version of the paper.

Acknowledgments: The Deutsche Forschungsgemeinschaft (DFG) provided the experimental setup and materials as part of the major research instrumentation program with contract number INST 187/630-1 FUGG. The German Academic Exchange Service (DAAD) funded the work conducted by P. Radici as part of a PhD program. We would like to thank our colleague Sheridan Renzi for the kind corrections of the English language throughout this paper.

Conflicts of Interest: The authors declare no conflict of interest. The founding sponsors had no role in the design of the study; in the collection, analyses, or interpretation of data; in the writing of the manuscript, and in the decision to publish the results.

References

1. Das, V.; Padmanaban, S.; Venkitusamy, K.; Selvamuthukumaran, R.; Blaabjerg, F.; Siano, P. Recent advances and challenges of fuel cell based power system architectures and control—A review. *Renew. Sustain. Energy Rev.* **2017**, *73*, 10–18. [[CrossRef](#)]
2. Boudghene Stambouli, A.; Traversa, E. Solid oxide fuel cells (SOFCs): A review of an environmentally clean and efficient source of energy. *Renew. Sustain. Energy Rev.* **2002**, *6*, 433–455. [[CrossRef](#)]
3. Ostergaard Gadsboll, R.; Thomsen, J.; Bang-Moller, C.; Ahrenfeldt, J.; Henriksen, U.B. Solid oxide fuel cells powered by biomass gasification for high efficiency power generation. *Energy* **2017**, *131*, 198–206. [[CrossRef](#)]
4. Wang, S.; Jiang, S.P. Prospects of fuel cell technologies. *Natl. Sci. Rev.* **2017**, *4*, 761–780. [[CrossRef](#)]
5. Litzelman, S.J.; Lemmon, J.P. The Promise and Challenges of Intermediate Temperature Fuel Cells. *ECS Trans.* **2015**, *68*, 39–47. [[CrossRef](#)]
6. Sengodan, S.; Lan, R.; Humphreys, J.; Dongwei, D.; Xu, W.; Wang, H.; Tao, S. Advances in reforming and partial oxidation of hydrocarbons for hydrogen production and fuel cell applications. *Renew. Sustain. Energy Rev.* **2018**, *82*, 761–780. [[CrossRef](#)]
7. Valadez Huerta, G.; Álvarez Jordán, J.; Dragon, M.; Leites, K.; Kabelac, S. Exergy analysis of the diesel pre-reforming solid oxide fuel cell system with anode off-gas recycling in the SchIBZ project. Part I: Modeling and validation. *Int. J. Hydrogen Energy* **2018**. [[CrossRef](#)]
8. Nehter, P.; Wildrath, B.; Bauschulte, A.; Leites, K. Diesel Based SOFC Demonstrator for Maritime Applications. *ECS Trans.* **2017**, *78*, 171–180. [[CrossRef](#)]
9. Santos, T.H.; Grilo, J.P.F.; Loureiro, F.J.A.; Fagg, D.P.; Fonseca, F.C.; Macedo, D.A. Structure, densification and electrical properties of Gd³⁺ and Cu²⁺ co-doped ceria solid electrolytes for SOFC applications: Effects of Gd₂O₃. *Ceram. Int.* **2018**, *44*, 2745–2751. [[CrossRef](#)]
10. Irshad, M.; Siraj, K.; Raza, R.; Ali, A.; Tiwari, P.; Zhu, B.; Rafique, A.; Ali, A.; Ullah, M.K.; Usman, A. A Brief Description of High Temperature Solid Oxide Fuel Cell's Operation, Materials, Design, Fabrication Technologies and Performance. *Appl. Sci.* **2016**, *6*, 75. [[CrossRef](#)]
11. Steele, B.C.H.; Heinzl, A. Materials for fuel-cell technologies. *Nature* **2001**, *414*, 345–352. [[CrossRef](#)] [[PubMed](#)]
12. Lee, K.H.; Strand, R.K. SOFC cogeneration system for building applications, part 1: Development of SOFC system-level model and the parametric study. *Renew. Energy* **2009**, *34*, 2831–2838. [[CrossRef](#)]
13. Peksen, M. Safe heating-up of a full scale SOFC system using 3D multiphysics modelling optimization. *Int. J. Hydrogen Energy* **2018**, *43*, 354–362. [[CrossRef](#)]
14. Peksen, M.; Al-Masri, A.; Peter, R.; Blum, L.; Stolten, D. Recent Developments in 3D Multiphysics Modelling of Whole Fuel Cell Systems for Assisting Commercialization and Improved Reliability. *ECS Trans.* **2017**, *75*, 15–22. [[CrossRef](#)]
15. Dokmaingam, P.; Areesinpitak, S.; Laosiripojana, N. Transient Modeling of Tubular-Designed IIR-SOFC Fueled by Methane, Methanol, and Ethanol. *Eng. J.* **2017**, *21*, 235–249. [[CrossRef](#)]
16. Hering, M.; Brouwer, J.; Winkler, W. Dynamic model of a micro-tubular solid oxide fuel cell stack including an integrated cooling system. *J. Power Sources* **2017**, *342*, 504–514. [[CrossRef](#)]
17. Wang, X.; Zhang, T.; Kang, J.; Zhao, L.; Guo, L.; Feng, P.; Zhou, F.; Ling, Y. Numerical modeling of ceria-based SOFCs with bi-layer electrolyte free from internal short circuit: Comparison of two cell configurations. *Electrochim. Acta* **2017**, *138*, 728–738. [[CrossRef](#)]
18. Song, T.W.; Sohn, J.L.; Kim, J.H.; Kim, T.S.; Ro, S.T.; Suzuki, K. Performance analysis of a tubular solid oxide fuel cell/micro gas turbine hybrid power system based on a quasi-two dimensional model. *J. Power Sources* **2005**, *142*, 30–42. [[CrossRef](#)]
19. Bove, R.; Lunghi, P.; Sammes, N.M. SOFC mathematic model for systems simulations—Part 2: Definition of an analytical model. *Int. J. Hydrogen Energy* **2005**, *30*, 189–200. [[CrossRef](#)]
20. Kjelstrup, S.; Bedeaux, D. Jumps in electric potential and in temperature at the electrode surfaces of the solid oxide fuel cell. *Physica A* **1997**, *244*, 213–226. [[CrossRef](#)]
21. Kjelstrup, S.; Bedeaux, D. *Non-Equilibrium Thermodynamics of Heterogeneous Systems*; World Scientific: Singapore, 2017; pp. 1–6, ISBN 13 978-981-277-913-7.
22. Onsager, L. Reciprocal Relations in Irreversible Processes. I. *Phys. Rev.* **1931**, *37*, 405–426. [[CrossRef](#)]
23. Onsager, L. Reciprocal Relations in Irreversible Processes. II. *Phys. Rev.* **1931**, *38*, 2265–2279. [[CrossRef](#)]

24. Costamagna, P.; Selimovic, A.; Del Borghi, M.; Agnew, G. Electrochemical model of the integrated planar solid oxide fuel cell (IP-SOFC). *Chem. Eng. J.* **2004**, *102*, 61–69. [[CrossRef](#)]
25. Hajimolana, S.A.; Hussain, M.A.; Ashri Wan Daud, W.M.; Soroush, M.; Shamiri, A. Mathematical modeling of solid oxide fuel cell: A review. *Renew. Sustain. Energy Rev.* **2011**, *15*, 1893–1917. [[CrossRef](#)]
26. Nazari, A.; Farhad, S. Heat generation in lithium-ion batteries with different nominal capacities and chemistries. *Appl. Therm. Eng.* **2017**, *125*, 1501–1517. [[CrossRef](#)]
27. Suwanwarangkul, R.; Croiset, E.; Fowler, M.W.; Douglas, P.L.; Entchev, E.; Douglas, M.A. Performance comparison of Fick's, dusty gas and Stefan-Maxwell models to predict the concentration overpotential of a SOFC anode. *J. Power Sources* **2003**, *122*, 9–18. [[CrossRef](#)]
28. Taylor, R.; Krishna, R. *Multicomponent Mass Transfer*; John Wiley & Sons, Inc.: New York, NY, USA, 1993; pp. 124–138, ISBN 978-047-157-417-0.
29. Benfenati, F.; Beretta, G.P. Ergodicity, Maximum Entropy Production, and Steepest Entropy Ascent in the Proofs of Onsager's Reciprocal Relations. *J. Non-Equilib. Thermodyn.* **2018**, *43*, 101–110. [[CrossRef](#)]
30. Alahverdyan, A.E.; Nieuwenhuizen, T.M. Steady adiabatic state: Its thermodynamic, entropy production, energy dissipation, and violation of Onsager relations. *Phys. Rev. E* **2000**, *62*, 845–850. [[CrossRef](#)]
31. Sciacovelli, A.; Verda, V. Entropy generation analysis in a monolithic-type solid oxide fuel cell (SOFC). *Energy* **2009**, *34*, 850–865. [[CrossRef](#)]
32. Sciacovelli, A.; Verda, V. Entropy Generation Minimization in a Tubular Solid Oxide Fuel Cell. *J. Energy Resour. Technol.* **2010**, *132*, 012601. [[CrossRef](#)]
33. Ramírez-Minguela, J.J.; Rangel-Hernández, V.H.; Alfaro-Ayala, J.A.; Uribe-Ramírez, A.R.; Mendoza-Miranda, J.M.; Belman-Flores, J.M.; Ruiz-Camacho, B. Energy and entropy study of a SOFC using biogas from different sources considering internal reforming of methane. *Int. J. Heat Mass Transf.* **2018**, *120*, 1044–1054. [[CrossRef](#)]
34. Ramírez-Minguela, J.J.; Mendoza-Miranda, J.M.; Rodríguez-Muñoz, J.L.; Perez-García, V.; Alfaro-Ayala, J.A.; Uribe-Ramírez, A.R. Entropy Generation Analysis of a Solid Oxide Fuel Cell by Computational Fluid Dynamics. Influence of Electrochemical Model and Its Parameters. *Therm. Sci.* **2018**, *22*, 577–589.
35. Choudhary, S.; Sanja, S. Thermodynamic assessment of SOFC-ICGT hybrid cycle: Energy analysis and entropy generation minimization. *Energy* **2017**, *134*, 1013–1028. [[CrossRef](#)]
36. Timurkutluk, B.; Mat, M.D. A review on micro-level modeling of solid oxide fuel cells. *Int. J. Hydrogen Energy* **2016**, *41*, 9968–9981. [[CrossRef](#)]
37. Peksen, M. Numerical thermomechanical modelling of solid oxide fuel cells. *Prog. Energy Combust. Sci.* **2015**, *48*, 1–20. [[CrossRef](#)]
38. Siemer, M.; Marquardt, T.; Valadez Huerta, G.; Kabelac, S. Local Entropy Production Rates in a Polymer Electrolyte Membrane Fuel Cell. *J. Non-Equilib. Thermodyn.* **2017**, *42*, 1–30. [[CrossRef](#)]
39. Kjelstrup, S.; Seip Forland, K. The Transported Entropy of Oxygen Ion in Yttria-Stabilized Zirconia. *J. Electrochem. Soc.* **1991**, *138*, 2374–2376. [[CrossRef](#)]
40. Valadez Huerta, G.; Kelle, A.; Kabelac, S. A phenomenological study of yttria stabilized zirconia at 1300 K with the Green-Kubo formulation and equilibrium molecular dynamics. *Chem. Phys.* **2017**, *485*, 108–117. [[CrossRef](#)]
41. Ahamer, C.; Opitz, A.K.; Rupp, G.M.; Feig, J. Revisiting the Temperature Dependent Ionic Conductivity of Yttria Stabilized Zirconia (YSZ). *J. Electrochem. Soc.* **2017**, *164*, F790–F803. [[CrossRef](#)]
42. Grosso, R.L.; Muccillo, E.N.S. Sintering, phase composition and ionic conductivity of zirconia-scandia-ceria. *J. Power Sources* **2013**, *233*, 6–13. [[CrossRef](#)]
43. Liu, X.; Martín-Calvo, A.; McGarrity, E.; Schnell, S.K.; Calero, S.; Simon, J.M.; Bedeaux, D.; Kjelstrup, S.; Bardow, A.; Vlugt, T.J.H. Fick Diffusion Coefficients in Ternary Liquid Systems from Equilibrium Molecular Dynamics Simulations. *Ind. Eng. Chem. Res.* **2012**, *51*, 10247–10258. [[CrossRef](#)]
44. Gao, C.Y.; Limmer, D.T. Transport Coefficients from Large Deviation Functions. *Entropy* **2017**, *19*, 571. [[CrossRef](#)]
45. Dufty, J.; Wrighton, J.; Luo, K.; Trickey, S.B. On the Kubo-Greenwood model for electron conductivity. *Contrib. Plasma Phys.* **2018**, *58*, 150–154. [[CrossRef](#)]
46. Valadez Huerta, G.; Siemen, M.; Kabelac, S. Approach to the Coulomb Contribution of Thermodynamic Properties from the Mean Electrostatic Potential of the Ions in $(\text{ZrO}_2)_{1-x}(\text{Y}_2\text{O}_3)_x$. *J. Phys. Chem. C* **2018**, *122*, 62–70. [[CrossRef](#)]

47. Kabelac, S.; Siemer, M.; Ahrendts, J. Thermodynamische Stoffdaten für Biogase. *Forschung im Ingenieurwesen* **2005**, *70*, 46–55. [[CrossRef](#)]
48. Valadez Huerta, G.; Reus, L.; Kabelac, S. A Diffusivity Study of $(\text{Sc}_2\text{O}_3)_{0.1}(\text{CeO}_2)_{0.01}(\text{ZrO}_2)_{0.89}$ between 1100 and 1500 K at Zero Pressure with Molecular Dynamics. *J. Chem. Eng. Data* **2018**, *63*, 1955–1960. [[CrossRef](#)]
49. Preis, W.; Egger, A.; Waldhäusl, J.; Sitte, W.; de Carvalho, E.; Irvine, J.T.S. Bulk and Grain Boundary Conductivities as Function of Temperature and Oxygen Partial Pressure of Scandia-Stabilized Zirconia Co-Doped with Yttria and Ceria. *ECS Trans.* **2009**, *25*, 1635–1642. [[CrossRef](#)]
50. Atkins, P.; de Paula, J. *Physical Chemistry*; Oxford University Press: Oxford, UK, 2006; pp. 935–938, ISBN 0-7167-8759-8.
51. Yonekura, T.; Tachikawa, Y.; Yoshizumi, T.; Shiratori, Y.; Ito, K.; Sasaki, K. Exchange Current Density of Solid Oxide Fuel Cell Electrode. *ECS Trans.* **2011**, *35*, 1007–1014. [[CrossRef](#)]
52. Kilo, M.; Taylor, M.A.; Argirusis, C.; Borchardt, G.; Jackson, R.A.; Schulz, O.; Martin, M.; Weller, M. Modeling of cation diffusion in oxygen ion conductors using molecular dynamics. *Solid State Ion.* **2004**, *175*, 823–827. [[CrossRef](#)]
53. Shampine, L.F.; Reichelt, M.W. The MATLAB ODE Suite. *SIAM. J. Sci. Comput.* **1997**, *18*, 1–22. [[CrossRef](#)]
54. Eveloy, V.; Karunkeyoon, W.; Rodgers, P.; Al Alili, A. Validation of Solid Oxide Fuel Cell Thermodynamic Models for System-level Integration. *Int. J. Therm. Environ. Eng.* **2016**, *11*, 25–32. [[CrossRef](#)]
55. Fischer, K.; Seume, J.R. Impact of the Temperature Profile on Thermal Stress in a Tubular Solid Oxide Fuel Cell. *J. Fuel Cell Sci. Technol.* **2009**, *6*, 011017. [[CrossRef](#)]



© 2018 by the authors. Licensee MDPI, Basel, Switzerland. This article is an open access article distributed under the terms and conditions of the Creative Commons Attribution (CC BY) license (<http://creativecommons.org/licenses/by/4.0/>).

Curriculum Vitae

Personal data

Name: Dipl.-Ing. Gerardo Valadez Huerta
Birthday/place: 31.10.1987 in Puebla, Mexico

Scientific career

03/2013 - today **Research assistant / PhD student , Institute for Thermodynamics**, Gottfried Wilhelm Leibniz University of Hanover

- MD simulation of metal oxides
- Modelling and simulation of fuel cell systems in the SchIBZ-project 03BI206K funded by the German Federal Ministry of Economics and Technology
- Teaching assistant for the lectures: Thermal separation processes (2013), Thermodynamics of chemical processes (2014), Fuel cell and fuel cell systems (2015), Thermodynamics I and II (2015/2016), Refrigeration and Cryotechnology (2017)

07/2010 - 03/2011 & 10/2011 - 02/2013 **Student employee / Research Assistant, Institute for Thermodynamics**, Braunschweig University of Technology

- MD simulation of solids
- Assistance in the project Az-27385-20/0 funded by the German Federal Environmental Foundation in system modelling and simulation of refrigeration cycles
- Teaching assistant for the lecture Thermodynamics of mixtures (2011-2013)

Education

10/2006-07/2012 **Study in mechanical engineering**, Braunschweig University of Technology

- Graduation to Diplom (Univ.); Mark: 1.7
- Specialization: Energy and process engineering
- Diploma thesis: *Molecular dynamics simulation of the properties of soldering material* (Institute for Thermodynamics); Mark: 1.3.
- Student project: *Simulation of crystallization fouling with population balances* (Institute for Chemical and Thermal Process engineering) Mark: 1.0

07/2012 **CCP5 Summer School**, University of Cardiff

- Extending the knowledge in the field of MD and MC simulation
- Acquisition of basics in DFT calculation